BASE PRESSURE EFFECTS ON AEROFOILS

IN TRANSONIC FLOW

A thesis submitted in accordance with the requirements
of the University of Liverpool for the degree of
Doctor in Philosophy

by

FARIS FAKHRI ABDUL-KADIR

Mechanical Engineering Department

University of Liverpool

November 1976

ACKNOWLEDGEMENTS

The author wishes to express his gratitude and thanks to:-

The Iraqi Government (Ministry of Higher Education) for providing the financial support.

Dr. J.C. Gibbings and Professor J.F. Norbury whose supervision, guidance and constant encouragement made this project possible.

Mr. J. Patterson, who not only assisted with the experimental work, but tolerated high temperatures and noise levels to do so.

Miss D. Wright for typing the manuscript.

SUMMARY

The effects of free stream Mach number, angle of incidence and base bleed on the base pressure of a symmetrical blunt-base aerofoil in the transonic range, $0.6 \leq M_{e\infty} \leq 1.3$, were investigated. The tests were carried out in a 4" x 4" transonic slotted wind tunnel.

At zero incidence, a minimum value of base pressure was obtained when the Mach number just ahead of the base was approximately equal to 1.42. The effect of increasing incidence was to increase the base pressure when the flow was attached.

With base bleed bleed, the base pressure was increased until it reached an optimum value.

At zero incidence, the flow around the base was investigated. Correlations were obtained for the reattachment pressure and position and for the base pressure with base bleed.

Most of the assumptions used by theories for base pressure were found to be invalid.

The boundary layer velocity profile just after separation can be calculated using an analysis based on the stream-tube method.

The free shear layer velocity profile can be calculated using the modified Nash method.

CONTENTS

NOTATION

C	Crocco's number $= \left(\frac{\gamma-1}{2} M^2 \,/\, 1 + \frac{\gamma-1}{2} M^2\right)^{1/2}$
C_D	Total drag coefficient = $D/\rho_{e\infty} u_{e\infty}{}^2 h$
C_{Df}	Skin friction drag coefficient = $\int_0^{CH} (\tau_w/\rho_{e\infty} u_{e\infty}{}^2 h)dx$
C_{DB}	Base pressure drag coefficient = - C_{PB}
C_{DP}	Pressure drag coefficient based on trailing edge height
C_{DW}	Wave drag coefficient based on trailing edge height
CH	Chord length
C_{PB}	Base drag coefficient = $(P_b - P_\infty)/\frac{1}{2}\rho_{e\infty} u_{e\infty}{}^2$
$(C_{PB})_{LIM}$	Limit base drag coefficient (obtained when the flow approaching the trailing edge has zero boundary layer thickness
C_q	Base bleed coefficient = $\dot{m}/\rho_{e\infty}.u_{e\infty}.2h.S$
C_{qb}	= $\dot{m}_b/\rho_{e\infty}.u_{e\infty}.2h.S$
d	Transition wire diameter
D	Total drag
h	Semi-thickness of the trailing edge; equivalent to the back step height.
H	Shape factor = θ/δ^*
l	Splitter plate length
L	Free shear layer length
L_{SW}	Slotted wall length
m	Power law exponent of the boundary layer velocity profile (eqn. 2.20)

$\bar{m}$	Mass transported from external stream to the viscous region (eqn. 3.21)
$\dot{m}$	Rate of base bleed calculated from the orifice readings (Kg/sec)
$\dot{m}_b$	Rate of base bleed calculated by assuming that the velocity distribution of the base bleed along the span is uniform and equal to the velocity near the centre-line (kg/sec)
M	Mach number
$\bar{M}_{el}$	Mach number at 0.03" upstream of the trailing edge
M_{el}	Mach number at 0.4" upstream of the trailing edge
M_p	Mach number calculated from P_{tp} and P_{sp}
M_s	Mach number calculated from P_{sp} and the true total pressure
N	Reattachment parameter (eqn. 3.16)
P	Static pressure
P_{sp}	Static pressure measured by either pitot-static probe or the static probe
P_{tp}	Total pressure measured by the pitot-static probe
R_e	Reynolds number based on the chord length
S	Span
T	Static temperature
TH	Tunnel height
u,v	Velocity along the x and y direction respectively
u_R	Reference velocity
x,y	Free shear layer co-ordinates

$\bar{x}$ Distance between the origin of the equivalent asymptotic shear layer and the separation point (eqn. 3.13)

Z Distance along the span

γ Specific heat ratio

$\bar{\gamma}$ Local angle between external stream and the x-axis at $y = \delta$ (eqn. 3.21)

α Angle of incidence

$\bar{\alpha}$ Slotted walls divergence angle

β Angle formed by taking a straight line between the corner and the reattachment point

$\bar{\beta}$ Boattail angle

δ Boundary layer thickness = $y_{u=0.99} - y_{u=0.01}$

δ^* Boundary layer displacement thickness

θ Boundary layer momentum thickness

δ_1, δ_2 Boundary layer thickness before and after expansion

δ^*_1, δ^*_2 Boundary layer displacement thickness before and after expansion

θ_1, θ_2 Boundary layer momentum thickness before and after expansion

ε Eddy viscosity

$\eta = y/2\sqrt{\zeta}$

$\eta_0 = \delta_2/2\sqrt{\zeta}$

$\eta_{\theta 2} = \theta_2/2\sqrt{\zeta}$

$\zeta = \int \frac{\varepsilon}{u_R} dx$

ν	Prandtl-Meyer angle
ρ	Density
ϕ	Free shear layer velocity ratio = u_2/u_{e2}
ϕ_2	Velocity ratio of the boundary layer just after expansion
λ	= $1 - \phi_D$
τ_w	Wall shear stress
τ_D	Shear stress along the dividing streamline
τ_{1D}	Shear stress along the dividing streamline at the constant pressure region

SUFFICES

0	Stagnation conditions
1	Conditions upstream of the separation point
2	Conditions downstream of the separation point
b	Base pressure conditions (equivalent to 2)
℄	Conditions along the centreline of the model in the wake
D	Conditions along the dividing streamline
e	Inviscid external stream conditions
i	Incompressible equivalent
$\dot{m}_b$	Conditions with base bleed rate $\dot{m}_b$
opt.	Conditions with optimum value of base pressure with base bleed
r	Reattachment conditions
∞	Free stream conditions calculated from plenum chamber pressure. (In the theory, ∞ conditions are assumed to be equivalent to 1 conditions)

INTRODUCTION

The turbulent base flow over a two dimensional body with a blunt trailing edge has, for a long time, been a problem of interest that has been studied by both analysis and experiment. In an effort to define the aerofoil with sharp trailing edge, Nash[54] argued that for the aerofoil to be 'aerodynamically sharp', the trailing edge thickness must be of the same order or less than the total boundary momentum thickness at the trailing edge. He defined the aerofoil with a blunt trailing edge as that with $h/CH > 0.01$.

While potential flow theories give zero drag for all shapes, experiments show that blunt edge bodies have a large profile drag which cannot be explained by the effects of the friction forces on their surfaces.

It was recognised that an essential feature of the flow past a blunt edge aerofoil is the flow separation at the trailing edge and the existence of a low pressure region behind the separation point as compared with the pressure in the undisturbed stream. This low pressure, the base pressure, is the cause of the greater part of the total drag especially at transonic and supersonic speeds.

To investigate the parameters effecting the two dimensional turbulent base pressure, numerous experimental data were obtained as described in Chapter 1. Previous experimental results had shown that at subsonic speeds, the base pressure was periodic because of the vortex formation downstream of the separation point. As the flow speed was increased, the vortex formation was reduced and eventually suppressed at supersonic speeds and the flow was then considered steady.

At transonic speeds, there were few experimental results with no available data on the effect of the angle of incidence and the base bleed on the base pressure at these speeds.

In recent years, the interest the base pressure problem was extended to the case of the high-speed gas-turbine blade. The cooling air, which is needed to cool the blades, is passed through the blade and injected through either holes or a slot in the trailing edge back to the main flow. This means that the trailing edge has to be made thicker and the knowledge of the base drag becomes necessary in the determination and improvement of the turbine's overall efficiency.

Because the flow over a symmetrical aerofoil at an angle of incidence resembles that over a turbine blade, the interest in the effect of incidence on the base pressure became greater.

Many theories were developed for the steady base pressure at zero incidence, see Chapter 3. All these theories simplify the problem by employing many assumptions.

The purpose of the present work is to:-

i) Investigate the effect of various parameters on the transonic base pressure thus filling the gap in the experimental data at transonic speeds.

ii) Investigate the flow around the trailing edge at zero incidence to obtain a better understanding of the transonic base flow and to investigate the validity of the assumption and correlations used in the theory.

iii) Obtain the total drag by measuring the wake profile and compare the values of the various drag components.

CHAPTER ONE

SURVEY OF PREVIOUS EXPERIMENTS ON TWO-DIMENSIONAL BASE PRESSURE

1.1 Experiment at Subsonic and Transonic Speeds

Experimental results for base pressure for subsonic flow over aerofoils were collected by Hoerner[1,2] who found that the base drag data could be correlated in terms of skin friction drag of the aerofoil upstream of the trailing edge and gave the correlation

$$C_{PB} = - \frac{0.135}{\sqrt[3]{C_{Df}}} \qquad (1.1)$$

Hoerner also analysed measurements of the base drag of backward facing steps and found that for this case the base drag could be correlated by;

$$C_{PB} = - \frac{0.1}{\sqrt[3]{C_{Df}}} \qquad (1.2)$$

From the above results it could be seen that for given free stream conditions the base pressure at subsonic speeds of the blunt trailing edge aerofoil was less than that of a back step. Hoerner attributed the discrepancy to the existance of a Karman vortex sheet in the wake of the aerofoil, whereas in the case of a back step the presence of a downstream wall prohibited the formation of any such vortex system.

To support this argument, the use of a splitter plate was later demonstrated by Roshko[3,4] to have the effect of reducing the base

drag of a bluff cylinder body and was able to show that as the splitter plate was moved downstream from the body the base pressure rose and the shedding frequency of the periodic vortices decreased.

Bearman[5] investigated the effect of varying the length of a splitter plate, attached to the centre-line of an aerofoil, on the base drag. He found that the base pressure rose rapidly as the length of the splitter plate was increased but reached a local maximum when the splitter plate length was approximately equal to the trailing edge thickness (l/2h = 1.0). After this point the base pressure decreased until l/2h was approximately equal to 1.5 and then the base pressure began to rise again. The results of Nash et al[6] showed similar features.

Chapman et al[7] suggested that if the periodic vortex formation was suppressed, the subsonic base flow would be quite similar to that of steady base flow at supersonic speed. Therefore, if the splitter plate was long enough, the periodic vortex shedding could be wholly suppressed and the base flow would then be steady. Arie and Rouse[8] reported that a splitter plate ten times the height of the base was necessary before the base pressure was insensitive to further increase in length, while Tanner[9] concluded from his results, which were obtained by measurements on several wedges under nominally two-dimensional test conditions, that for a splitter plate of length equal to four times its body thickness, the periodic vortex shedding was wholly suppressed and the base pressure remained practically constant when l/2h was increased above the value of four.

Nash et al[6] carried out measurements on the base pressure at

subsonic and transonic speed. Using a stroboscope in conjunction with a schlieren optical system, he was able to observe the formation of the vortex street. He concluded from these observations that as the free stream Mach number approached unity, the periodic effects collapsed and subsequently the flow closely resembled the ideal steady base flow. This could explain the reason why at supersonic speeds the splitter plate has a very small influence on the base pressure.

Tests on aerofoils in the transonic speed range[6,10,11,12,13,14] showed a qualitative agreement in which the base drag varied very little with Mach number in the subsonic range until the free stream Mach number had a value of around 0.9 to 0.95, then the base drag increased sharply until it reached a maximum after which it decreased.

Using a series of aerofoils with different angles of sweepback, Rogers et al[13] showed that the free stream Mach number at which the base drag increased sharply in the transonic speed range could be delayed. When the base drag results were plotted against $[M_\infty \cos \omega]$, where ω was the angle of sweep, they collapsed to a single curve which suggested that the base flow behaved in many respects in the manner required by the simple-sweep theory.

Tanner's[10] results showed that for transonic speed there was an appreciable influence of the boundary layer upon the base drag. The latter decreased as the boundary layer thickness increased.

1.2 Experiments at Supersonic Speeds

All the early studies[15,16] for supersonic base pressure were carried out with the free stream Mach number as the only variable and

the general trend was that base pressure (P_b/P_∞) decreased with M_∞.

The effect of the boundary layer approaching the base was considered by Chapman[17]. In his analysis he assumed that in general it was expected that P_b/P_∞ followed the functional equation

$$\frac{P_b}{P_\infty} = f(M_{e\infty}, \frac{\theta_1}{h}, \bar{\beta}, \alpha) \qquad (1.3)$$

For zero angle of incidence and zero boat tail angle he assumed that the turbulent boundary layer just ahead of the base was equal to that which had developed over a flat plate of length equal to the chord length of the aerofoil and thus was able to write

$$\frac{\theta_1}{h} = f\left(\frac{CH}{h} \frac{1}{R_e^{1/5}}\right)$$

for the turbulent boundary layer.

Therefore the equation could be written as

$$\frac{P_b}{P_\infty} = f\left(M_{e\infty}, \frac{CH}{h} \frac{1}{R_e^{1/5}}\right) \qquad (1.3a)$$

He concluded that for a specific free stream Mach number, the Reynolds number had little effect on (P_b/P_∞) if the boundary layer approaching the base was turbulent. His experimental results confirmed this.

Kurzweg[18], in his studies of the variation of (P_b/P_∞) with (R_e), pointed out that the base pressure for a specific free stream Mach

number was not only dependent on the nature of the boundary layer approaching the base (turbulent or laminar) but also was strongly dependent on the position of the boundary layer transition from laminar to turbulent as, presumably, this effected the value of θ_1 for the turbulent boundary layer at the base.

The result of Kurzweg[18], Bogdonoff[20] and Kavanau[21], all obtained with bodies of revoltuion at Mach numbers of about three, showed a similar variation of P_b/P_∞ with (R_e) as was predicted by Crocco's theory[19]* and there was a marked minimum value of P_b/P_∞ which occurred at $(R_e = 1.5 \times 10^6)$.

Holder and Chadd[22] and Van Hise[23] carried out similar tests on a two-dimensional case for a free stream Mach number ranging from 1.95 to 2.92 and found similar results in which there was a minimum value of P_b/P_∞ and at the value of $(R_e = 1 \text{ to } 2 \times 10^6)$, the base pressure ratio became constant with respect to (R_e) when the transition point became fixed.

Since the boundary layer thickness was a function of the body geometry (i.e. the pressure gradients acting on the boundary layer) as well as (R_e), the effect of (θ_1/h) on the base pressure was investigated.

Experimental results[24] behind a two-dimensional step at Mach number 1.86 showed that when the ratio of boundary layer thickness to base height was halved there was very little change in the base pressure ratio. A physical argument[22] was given for this. The argument was that at the corner the flow was accelerated so that the

---

* See Section 3.2.

part of the boundary layer after expansion, which had high velocity gradients, was really much thinner than the boundary layer just before the base. This was particularly true for a turbulent boundary layer where the part of the boundary layer which had high velocity gradients was small to start with so that the flow downstream of the base could almost be treated as if there was no boundary layer upstream of it. Therefore, the effect of the boundary layer was negligible.

Hastings[25] results showed that this was not the case. He carried out tests on base pressure for a back step at Mach numbers of 1.5, 2.0 and 3.1 and the effect of boundary layer thickness was investigated by varying the step height. His results showed that base pressure ratio was very much dependent on the ratio of the boundary layer momentum thickness to the step height (θ_1/h). The trend was that as θ_1/h was increased from a very small value, the base pressure ratio increased rapidly. The rate of this increase diminishes with increasing θ_1/h and when the value of θ_1/h reached unity there was very little effect of further boundary layer thickness increments on the value of base pressure.

Nash[54] analysed Hasting's results and suggested the correlation for supersonic flows;

$$(C_{Pb})_{LIM} - C_{Pb} = 0.175 \left(\frac{\theta_1}{2h}\right)^{\frac{1}{2}} \qquad (1.4)$$

where $(C_{Pb})_{LIM}$ is the value of base drag with zero boundary layer thickness (i.e. limit base drag) and was assumed to vary with free

stream Mach numbers according to the following approximate relation

$$(C_{Pb})_{LIM} = -(3.627-4.458M_{e\infty}+1.877M_{e\infty}^{2}-0.246M_{e\infty}^{3}) \quad (1.5)$$

The effect of boat tail angle on the base pressure was investigated by Chapman[26]. He showed that for a turbulent boundary layer and a boat tail angle, $\bar{\beta}$, in the range of 0^{o} to 20^{o} there was very little change in the value of base pressure ratio.*

Fuller and Reid[27] gave more reliable results as they used the same basic section with different boat tail angles. Their results showed a slight increase in base pressure as $\bar{\beta}$ was increased from 0^{o} to 8^{o}. This was thought to be due to the fact that as $\bar{\beta}$ was increased the trailing edge thickness was decreased and therefore the ratio (θ_1/h) increased giving a higher base pressure value.

The effect of incidence on the base pressure was also investigated[26]. The results showed that for Mach numbers of 1.5, 2.0 and 3.1, and an angle of incidence, α, of 0 to 5^{o} there was very little change in base pressure. Coin[28] and Love[29] showed similar results. It was concluded from the above results that the influence of the boat tail and incidence angles on the base pressure was mainly in the way they altered the ratio of the boundary layer thickness to trailing edge height at separation.

Some results[18] have shown the change in boundary layer velocity profile, by changing the boundary layer temperature profile, which

---

* This could be misleading since the results were for wings with different sections and different maximum thicknesses.

caused the base pressure to vary in spite of constant values of $M_{e\infty}$ and R_e. It was demonstrated by these results that the base pressure was reduced when the temperature of the body was low so giving a cooling effect to the boundary layer and increased when the temperature of the body was increased.

1.3 Experiments on Reduction of Base Drag

Because the base drag constitutes an appreciable part of the total drag, particularly at transonic and supersonic speeds, various methods have been used to reduce the base drag. The oldest and best known methods were the use of splitter plates and of base bleed, but recently it was demonstrated that the shape of the base had an effect on the base drag. These methods are discussed in this section.

1.3.1 The Splitter Plate

As already mentioend in Section (1.1), because of the presence of a periodic vortex street in the wake behind the two-dimensional body with its kinetic energy content, the base drag could be reduced by suppressing this vortex shedding. The use of a thin splitter plate attached to the centre-line of the base had the effect of suppressing the vortex shedding. If the plate was long enough, the shedding could be wholly eliminated and the wake was then steady.

At subsonic speeds, a large reduction of base drag was obtained by this method. A reduction of about 50% of base drag was obtained by employing a long thin splitter plate with wedges of various angles[9]. Similar reductions in base drag were obtained for two-

dimensional bodies[5].*

At transonic speeds, results[6] showed that with a long thin splitter plate a maximum reduction of about 60% in the base drag of an aerofoil was obtained even for a high subsonic speed. But for a Mach number of about unity the base drag with splitter plate was only slightly less than that without the plate (about 10%). This was because the periodicity of the base flow rapidly decreased at M=1 approximately[6] and the strength of the vortex street further decreased with increasing Mach number. That was why the splitter plate as a device for reducing the base drag was less effective at supersonic Mach numbers than at subsonic speeds.

Results[5,6] showed that for subsonic and transonic speeds, the base pressure had local maximum value when ($1/2h \simeq 1.0$) and that for ($1.0 \leqslant 1/2h \leqslant 2.0$) the base pressure was decreasing. This led many authors[6,14] to believe that a splitter plate having a length ($1/2h = 1.0$) would be the most practical for reducing the base drag since a longer thin splitter plate which gave greater base pressure ($1/2h \geqslant 3.0$) would not be structurally strong enough due to its length. This practical problem of not using a long thin splitter plate was overcome by the use of a long thick splitter plate. These relatively thick splitter plates gave an additional advantage since the pressure acting on the end face of the thick plate was higher than the base pressure and therefore the effective base drag was lower than that of a thin splitter plate of equivalent length. Results showed that it was possible to get still more reduction in base drag

---

* A similar reduction in the base drag of circular cylinders was obtained by this method[3].

by the use of splitter wedges[30].

1.3.2 Base Bleed

Bearman[92,93] investigated, for incompressible flow, the effect of bleeding air through a slot at the base of a two-dimensional wing on the base pressure and on the vortex shedding. The base pressure drag decreased with increasing bleed rate (C_q) until the base pressure reached a local maximum at a value of C_q = 0.1 - 0.14 approximately depending on the slot width. Greater slot widths seemed to give the maximum increase in base pressure. From his observation on the vortex formation, it seemed that the effect of the base bleed was to suppress the vortex formation, similar to the effect of a splitter plate.

Bardminarayanau[31] measured the base pressure of a two-dimensional body at a Mach number of 2.0 with and without base bleed. These results indicated that the base bleed effected the entire flow in the mixing region and that a small quantity of air injected into the dead air region effected the base pressure significantly causing a maximum increase of about 24% in the base pressure when the boundary layer approaching the base was turbulent. Similar results[32,33] were obtained for supersonic flows over a back step.

So far there appears to be no available data on the effect of base bleed on the base pressure in the transonic range.

1.3.3 Additional Methods for Reducing Base Drag in Two-Dimensional Flow

Experimental measurements[81] in incompressible flow on rectangular wings, having serrated trailing edges, have shown that the serrated

separation line inhibited the periodic vortex formation and thus created a steady base flow with lower base drag. Results[30] from experimental investigation at subsonic, transonic and supersonic Mach numbers on rectangular wings have also shown that the base drag can be greatly reduced by using a serrated trailing edge instead of a straight trailing edge.

Measurements[14] in the transonic range on two-dimensional models with a different trailing edge configuration have also shown a reduction in base drag by using these configurations instead of a straight trailing edge.

Measurements[6] on an aerofoil with a half round base in the transonic range have shown that up to $M_\infty = 0.55$, the base drag was considerably lower for the half round base than that for the rectangular base. In the Mach number range from $0.6 \leqslant M_{e\infty} \leqslant 0.9$ the opposite was true, while for $0.9 \leqslant M_{e\infty} \leqslant 1.2$ the base drag for both trailing edge shapes was almost the same. The conclusion was that the rounding of the blunt base seemed to be unfavourable for base drag reduction in the transonic range.

It is reported in Ref. 54 that the use of a base with a ventilated cavity can also give a reduction in base drag.

CHAPTER TWO

THE NATURE OF THE FLOW

For steady base flow, the flow on either side of the plane symmetry in the wake behind isolated base is assumed to be similar to the flow past a back step. Fig. 1 shows sketches of the flow. The flow separates at S and reattaches at the point R. Thus a dead-air region (SRA) is formed where the velocity is low and the pressure is assumed to be constant everywhere in this region and equal to the base pressure.

Because of the viscous-inviscid interaction between the external stream and fluid inside the dead-air region, a mixing layer which is called the free shear layer is developed by entraining fluid from the dead-air region. Since the mass in this region must be conserved, a recompression is needed at the reattachment zone to slow down and eventually reverse part of the free shear layer back to the dead-air region. This is why the base pressure essentially must be lower than that of the free stream pressure.

If there is no base bleed, then the separation streamline must be the same as the reattachment streamline. This streamline (the line SR) is called the dividing streamline.

2.1 The Flow Expansion and Separation at the Corner

The features which distinguish boundary layer separation at a sharp edge from the usual boundary layer separation are the sign and

magnitude of the pressure gradient. In the classical separation the shear stress is zero at the point of separation and the pressure gradient is adverse causing the boundary layer to thicken, whilst at a sharp corner the shear stress at separation is high but finite and the pressure gradient is favourable causing the boundary layer thickness to decrease.

The expansion at the corner is assumed to be rapid and to occur in a very short distance. The boundary layer velocity profile and dimensions are effected by the rapid expansion and separation. To evaluate this effect, the stream tube method is employed in which the expansion along any streamline is assumed to be isentropic* and the rate of mass flow between any two streamlines is assumed to remain constant throughout the expansion process.

Fig. 2 shows the boundary layer, of initial thickness δ_1, approaching the base to form there a new boundary layer thickness δ_2 just after separation. To find the velocity profile for the new boundary layer after expansion, the flow along any streamline AA' is assumed isentropic.

$$\frac{P_b}{P_1} = \frac{P_b}{P_\infty} = \left(\frac{1 + \frac{\gamma-1}{2} M_1^2}{1 + \frac{\gamma-1}{2} M_2^2} \right)^{\gamma/\gamma-1} \qquad (2.1)$$

where M_1 = Mach number of the streamline AA' just before expansion and

M_2 = Mach number of streamline AA' just after expansion.

If the total temperature is conserved along the boundary layer

---

* This assumption is reasonable since the expansion process occurs in a very short distance.

then

$$\frac{u_1}{u_{e1}} = \frac{C_1}{C_{e1}} \quad \text{and} \quad \frac{u_2}{u_{e2}} = \frac{C_2}{C_{e2}} \tag{2.2}$$

where C = Crocco's number $= \left(\frac{\frac{\gamma-1}{2} M^2}{1 + \frac{\gamma-1}{2} M^2} \right)^{1/2}$

If the initial profile of the boundary layer just before expansion is given as:-

$$\frac{u_1}{u_{e1}} = \left(\frac{y_1}{\delta_1}\right)^{1/7} \tag{2.3}$$

then for any base pressure ratio P_b/P_∞, the velocity along any streamline can be found from equation (2.1), (2.2) and (2.3). To find the position y_2 of the streamline AA' after expansion, the continuity equation is used,

$$\int_0^{y_1} \rho_1 u_1 \, dy = \int_0^{y_2} \rho_2 u_2 \, dy$$

$$\therefore \frac{y_2}{\delta_1} = \left(\frac{P_\infty}{P_b}\right)^{\frac{\gamma+1}{2\gamma}} \int_0^{y_1/\delta_1} \frac{M_1}{M_2} \, d\left(\frac{y_1}{\delta_1}\right) \tag{2.4}$$

Thus the boundary layer velocity profile after expansion is calculated once the base pressure ratio (P_∞/P_b) is known.

The change in the momentum thickness of the boundary layer due to the expansion is calculated by the simple approximate relation given by Nash[50]

$$\frac{\theta_2}{\theta_1} = \left[\frac{M_{e\infty}}{M_{e2}} \quad \frac{1 + \frac{\gamma-1}{2} M_{e2}^2}{1 + \frac{\gamma-1}{2} M_{e\infty}^2} \right]^3 \tag{2.5}$$

Roberts[62] gives a more accurate but complex relation using the stream tube method which is found to differ very little from that calculated by eqn. (2.5). White[64] using the momentum-integral equation and integrating it across a pressure difference gives the relation

$$\frac{\theta_2}{\theta_1} = \left(\frac{C_{e2}}{C_{e\infty}}\right)^{3.2} \left(\frac{1 - C_{e2}^2}{1 - C_{e\infty}^2}\right)^{1.4} \tag{2.6}$$

Fig. 3 shows the values of $\frac{\theta_2}{\theta_1}$ for different values of $\left(\frac{P_b}{P_\infty}\right)$ for (M_∞ = 1.0 and 1.3) calculated from equation (2.5) and (2.6).

In the past it has been assumed that when a supersonic flow passes over a rearward facing step or a blunt trailing edge aero-foil, the separation occurs smoothly from the corner of the step. It has also been assumed that the subsequent mixing region and the dividing streamline also originates from this point. The subsonic portion of the boundary layer provides a channel through which pressure signals from the base region downstream of the corner can propogate upstream. These pressure signals may be felt at a distance

of the order ($M_{e\infty}$ δ_1) (Ref. 65) upstream of the corner. Therefore a significant pressure drop will be experienced ahead of the corner causing the expansion process to start there and not at the corner as all theories assume.

Because the flow will start to turn towards the horizontal surface ahead of the corner the wall shear stress will increase very rapidly. R.C. Ackerberg[66] in his theoretical analysis for incompressible flow approaching the corner found that the skin friction is proportional to the inverse eighth power of the distance from the edge ($\tau_w \propto (-x)^{-\frac{1}{8}}$) with a singularity point at the corner with infinite wall shear stress.*

A significant step in understanding the supersonic base separation has been made by Weinbaum[67] and Weiss and Weinbaum[68] who developed a theory for the expansion and separation process that occurs at a blunt base trailing edge. These authors adopt an inviscid rotational model for the supersonic portion of the expanding boundary layer flow. The assumption is made that the origin of the expansion fan is positioned at the corner and that separation occurs at the trailing edge. The supersonic portion of the boundary layer is assumed to consist of an infinite number of layers with slightly different Mach numbers separated by slip lines. Fig. 4A shows two of these layers interacting with an expansion wave ABC.

From their theoretical analysis they concluded that for the final deflection angles (Ω_2 and Ω_3) and the final pressures (P_2 and P_3) to be equal, there exists a reflected wave (BF) at the slip line.

---

* This is only a theoretical model since experiments showed that at the separation point the wall shear stress is finite.

When $M_i > \sqrt{2}$ the reflected wave is an expansion wave and for $M_i < \sqrt{2}$ the reflected wave is a compression wave. These reflected waves, when reaching the sonic line, will be reflected as waves of the opposite family. Thus for high Mach numbers ($M_i > \sqrt{2}$), they reflect at the sonic line as compression waves and these waves will coalesce, typically 5 to 10 boundary layer thicknesses downstream of the corner, to form a lip shock (Fig. 4B).

Contrary to the prediction of the inviscid theory just mentioned, Harnma's[69] detailed experiment indicated that the lip shock formation distance was less than a boundary layer thickness and that the foot of the shock appeared to be located beneath the corner and adjacent to the base wall. Moreover, the accompanying static pressure measurements on the base wall showed that the pressure reached a minimum at a small distance and then increased again to the base pressure value.

These results suggest that the flow adjacent to the base must be turned sharply, over expanded initially, and then compressed and separated from the base face in the region of rapidly increasing pressure as shown in Fig. 4C. Dewey[70] in his experiment for hypersonic flow over a cylinder showed a similar pressure distribution where the pressure initially decreased to a minimum value and then increased to a constant value at separation.

Donaldson[71] measured the free shear layer very close to the base and the apparent displacement of the mixing region can only be achieved by a flow deflection much greater than would be expected from the inviscid rotational theory. The difference was significantly

large to suggest to the author that at very small distances behind the base the neglect of the viscous forces is not justified and that even with a supersonic outer flow these forces are sufficient to have an appreciable effect on the outer flow and in particular may cause the separation point to be on the rear face of the base and not at the corner as it is suggested by the inviscid theory.

To try to explain these experimental results Weinbaum[72] modified his original model by assuming that a thin layer exists adjacent to the wall where the flow is slow and can be treated as a Stokes type flow in which the viscous term is high and the inertia term can be neglected in the momentum equation. His mathematical solution led him to the following conclusions:-

i) The separation point is as the rear face of the base in a region of adverse pressure gradient and not at the corner in a favourable pressure gradient as the inviscid theory has assumed.

ii) The separation streamline is not a straight line but has significant curvature near the separation point.

2.2 Free Shear Layer Development

The development of the free shear layer with zero initial boundary layer thickness is similar to that of uniform jet mixing with fluid at rest. The velocity profile of the latter is similar at any position in the x-direction and can be approximated by the asymptotic error function velocity profile (see Section 3.1.1, Eqn. 3.5).

To take into account the effect of a finite initial boundary layer thickness, Kirk[49] has proposed a method in which the real shear layer can be replaced by an equivalent asymptotic shear layer developing over a greater distance with zero initial boundary layer thickness (Section 3.1.2).

When the flow has a finite initial boundary layer thickness, the shear layer velocity profile becomes similar and asymptotic only after a distance of many boundary layer thicknesses downstream from the separation point. Therefore, there exists a region near the separation point where the free shear layer velocity profiles are not similar but are a function of the distance from the base.

Denison and Baum[73] tackled the problem of the free shear layer development in the non-similar velocity profile region. In their analysis, which is for the Laminar shear layer, the assumption is made that at separation the boundary layer has a Blasius profile. Knowing these initial conditions, the solution for the shear layer velocity profile is obtained by a numerical integration of the shear layer momentum equation.

Kubota and Dewey[74] proposed a simple method in which the momentum integral method is used to describe the development of the constant pressure, Laminar free mixing with finite initial thickness. Their technique is to divide the velocity profile of the free shear layer into two parts, one above and one below the zero streamline (i.e. the dividing streamline). Each part is represented by a simple analytical function containing parameters that may vary with the distance in the x-direction. These profiles are substituted in a number of moment of

momentum equations equal to the number of these parameters. These equations are integrated across the shear layer and the boundary conditions are applied at the inner and outer edges. The simplest analytical solution is employed in which the incompressible velocity profiles above and below the dividing streamline are assumed to be quadratic functions.* Therefore, the shear layer velocity profile is given as follows:-

Above the dividing streamline

$$\frac{u}{u_e} = f = a_o + a_1 \bar{\eta}_i + a_2 \bar{\eta}_i^2 \qquad (2.7)$$

Below the dividing streamline

$$\frac{u}{u_e} = g = b_o + b_1 \hat{\eta}_i + b_2 \hat{\eta}_i^2 \qquad (2.8)$$

where $\bar{\eta}_i = \frac{y_i}{\bar{\delta}_i}$, $\hat{\eta}_i = \frac{y_i}{\hat{\delta}_i}$

$\bar{\delta}_i$ = Incompressible shear layer thickness above the dividing streamline,

$\hat{\delta}_i$ = Incompressible shear layer thickness below the dividing streamline,

a_o, a_1, a_2, b_o, b_1 and b_2 are constants.

---

* This means that at separation, the initial boundary layer has a quadratic profile. For a turbulent boundary layer this is quite a poor assumption.

The boundary conditions are

$$\left.\begin{aligned} \text{at } \bar{\eta}_i &= 1\,, \quad f = 1, \quad \frac{\partial f}{\partial \bar{\eta}_i} = 0 \\ \hat{\eta}_i &= -1\,, \quad g = 0, \quad \frac{\partial g}{\partial \hat{\eta}_i} = 0 \end{aligned}\right\} \tag{2.9}$$

The two expressions for the velocity profile are related by the requirement that the velocity and its derivatives must be continuous at the joining point (i.e. at the diving streamline where y = 0). Therefore,

$$\frac{\partial f}{\partial \bar{\eta}_i} = \frac{\bar{\delta}_i}{\hat{\delta}_i} \frac{\partial g}{\partial \hat{\eta}_i} \quad \text{and} \quad f = g = \phi_D \tag{2.10}$$

Equations (2.7), (2.8), (2.9) and (2.10) give

$$\left.\begin{aligned} f &= 1 - \lambda(1-\bar{\eta}_i)^2 \\ g &= (1-\lambda)(1+\hat{\eta}_i)^2 \\ \hat{\delta}_i &= \frac{1-\lambda}{\lambda}\,\bar{\delta}_i \end{aligned}\right\} \tag{2.11}$$

where $\lambda = 1 - \phi_D$

The momentum equation is transformed into the incompressible plane and integrated across the shear layer. The expressions in Eqn. (2.11) are substituted in the momentum integral equation. The solution gives the variation of ϕ_D with the distance (x) from the base. The solution

for a laminar shear layer is

$$\frac{\nu_e x}{u_{e2}\theta_2^2} = f(\lambda) \tag{2.12}$$

where

$$F(\lambda) = \frac{225}{4}\left[\frac{1}{5}\frac{(1-\lambda)^3}{(3-9\lambda+4\lambda^2)^2} - \frac{1}{55}\frac{(\lambda+3)(1-\lambda)}{(3-9\lambda+4\lambda^2)}\right.$$

$$\left. + \frac{4}{55\sqrt{33}}\left(\ln\left|\frac{8\lambda-9+\sqrt{33}}{8\lambda-9-\sqrt{33}}\right| + \ln\frac{\sqrt{33}+1}{\sqrt{33}-1}\right)\right] \tag{2.12a}$$

Since for the present investigation, the free shear layer is turbulent, the L.H.S. of eqn. (2.12) is slightly modified to

$$\frac{\int_0^x \varepsilon\, dx}{u_{e2}\theta_2^2} = F(\lambda) \tag{2.13}$$

where ε = free turbulent eddy viscosity

$$= \frac{1}{4\sigma^2} u_{e2} x \ *$$

and σ = rate of spread of shear layer (see Appendix 1).

Therefore, eqn. (2.13) becomes

$$\frac{x^2}{\sigma^2\theta_2^2} = \frac{8}{4} f(\lambda) \tag{2.14}$$

---

* See Section ~~3.7.7~~ 3.1.1. This is valid only for the case of a turbulent shear layer with similar profiles. Since we are treating the case of a turbulent shear layer with non-similar profiles, there is an element of error introduced here.

At any position (x), given the initial boundary layer momentum thickness (θ_2), the velocity along the dividing streamline ϕ_D and the shear layer velocity profile in the incompressible plane can be calculated using eqn. (2.14) and (2.11). The velocity profile can be transformed to the compressible plane.

Nash[75] treated the problem of the development of the free shear layer with finite initial thickness in a different way. Following Korst's approximation, the momentum equation can be written as[36,37,38]

$$u_R \frac{\partial u}{\partial x} = \varepsilon \frac{\partial^2 u}{\partial y^2} \tag{2.15}$$

where u_R is some reference velocity.

Nash argued that since u_R is some mean value between zero and u_{e2}, it is assumed that

$$u_R = \frac{u_{e2}}{2} \tag{2.16}$$

By making the transformations

$$\zeta = \int \frac{\varepsilon}{u_R} dx \, , \quad \phi = \frac{u_2}{u_{e2}} \tag{2.17}$$

Eqn. (2.15) becomes

$$\frac{d\phi}{d\zeta} = \frac{d\phi^2}{dy^2} \tag{2.18}$$

Thus, the momentum equation, simplifies to the one dimensional diffusion equation for which standard solution is available[39]. The following boundary and initial conditions are used:-

$$\phi = 1 \quad \text{for} \quad \zeta = 0, \quad \delta < y < \infty$$

$$\phi = \phi_2(y) \quad \text{for} \quad \zeta = 0, \quad 0 < y < \delta$$

Then the solution of eqn. (2.18) for the velocity profile at any streamwise position of the free shear layer is given by

$$\phi = \frac{1}{2}\left[1 + \text{erf}(\eta - \eta_o)\right] + \frac{1}{\sqrt{\pi}} \int_0^{\eta_o} \phi_2(y)\, e^{-(\alpha-\eta)^2}\, d\alpha \qquad (2.19)$$

where

$$\eta = \frac{y}{2\sqrt{\zeta}}, \quad \eta_o = \frac{\delta_2}{2\sqrt{\zeta}} \qquad (2.19a)$$

Since the boundary layer at separation is turbulent, the assumption is made that the boundary layer just after separation has a 1/m th power law velocity profile. Therefore:-

$$\phi_2(y) = \left(\frac{y}{\delta_2}\right)^{\frac{1}{m}} \qquad (2.20)$$

Eqn. (2.19) becomes

$$\phi = \frac{1}{2}\left[1 + \text{erf}(\eta - \eta_o)\right] + \frac{1}{\sqrt{\pi}\ \eta_o^{\ 1/m}} \int_0^{\eta_o} \alpha^{\frac{1}{m}}\, e^{-(\alpha-\eta)^2}\, d\alpha \qquad (2.21)$$

For a complete solution, the problem is to specify the variation of (ε) with respect to (x) in order to determine the value of η_o and thus the velocity profile (ϕ) at that position. The eddy viscosity model employed is

$$\varepsilon = K u_{e_2} \Big/ \left[\frac{d\phi}{dy}\right]_{y=o} \tag{2.22}$$

where K is a constant determined from the asymptotic shear layer.

Equations (2.22) and (2.21) give the variation of (η_o) with respect to (x) as*

$$\frac{x}{\sigma\delta_2} = F(\eta_o) \tag{2.23}$$

where

$$F(\eta_o) = \frac{1}{\eta_o} - \int_o^{1/\eta_o} \left[1 - e^{-\eta_o{}^2} - \frac{2}{\eta_o{}^{1/m}} \int_o^{\eta_o} \alpha^{\frac{m+1}{m}} e^{-\alpha^2}\, d\alpha\right] d\left(\frac{1}{\eta_o}\right) \tag{2.23a}$$

Nash found that eqn. (2.23), with m = 7, gave the best fit to the experimental results of Chapman and Korst[105]. These results were for incompressible flow where the initial boundary layer has a $\frac{1}{7}$ th power law velocity profile.

For the present case, Nash's method is modified since there is no reason why the above results cannot be applied to the compressible

---

* See Ref. 75 for more details.

flow with a different value of m. Table (1) gives the variation of (η_o) with $\left[\frac{x}{\sigma\delta 2}\right]$ for different values of (m) according to eqn. (2.23). Fig. 5 shows the effect of $\frac{x}{\sigma\delta_2}$ on the shear layer thickness δ using eqn. (2.23) and eqn. (2.21) with m = 11. To transform δ_2 to the incompressible plane, we use the Stewardson transformation

$$dy = \frac{\rho_e}{\rho} dy_i$$

$$\delta_2 = \int_0^{\delta_{i2}} \frac{\rho_{e2}}{\rho_2} dy_i = \int_0^{\delta_{i2}} \frac{1 - C_{e2}{}^2 \phi^2}{1 - C_{e2}{}^2} dy_i$$

$$= \frac{1}{1-C_{e2}{}^2} \int_0^{\delta_{i2}} \left[1 - C_{e2}{}^2 \left(\frac{y_i}{\delta_{i2}}\right)^{\frac{2}{m}} \right] dy_i$$

Therefore,

$$\frac{\delta_2}{\delta_{i2}} = \frac{2 + m - m\, C_{e2}{}^2}{(1 - C_{e2}{}^2)(2 + m)} \qquad (2.24)$$

In the incompressible plane, the boundary layer thickness and momentum thickness are related by

$$\theta_{i2} = \frac{m}{(m+1)(m+2)} \delta_{i2} \qquad (2.25)$$

By using the Stewardson transformation, the momentum thickness in the incompressible plane remains equal to that in the compressible

plane. Therefore,

$$\theta_{i2} = \theta_2 \tag{2.26}$$

Eqn. (2.19), (2.20), (2.21) and (2.22) gives

$$\frac{x}{\sigma\theta_2} = \frac{(m+1)(m+2)}{m} \cdot \frac{(2+m-mC_{e2}^{\ 2})}{(1-C_{e2}^{\ 2})(2+m)} F(\eta_o) \tag{2.27}$$

Therefore, given the initial boundary layer thickness, eqns. (2.23) & (2.27) gives the value of η_o at any x. This value is substituted in eqn. (2.21) to evaluate the velocity profile at that particular value of x.

The position and the velocity of the dividing streamline can be calculated using the following analysis:

Defining θ_x as the momentum thickness of the shear layer at any position in the x-direction. Therefore

$$\theta_x = \int_{-\infty}^{y_R} \left[\frac{\rho_2 u_2}{\rho_{e2} u_{e2}} - \frac{\rho_2 u_2^{\ 2}}{\rho_{e2} u_{e2}^{\ 2}} \right]_x dy \tag{2.28}$$

where y_R is some reference value in the inviscid external flow.

At x = 0, θ_x will be equal to θ_2, the boundary layer momentum thickness just after expansion. Eqn. (2.28) becomes

$$\theta_2 = \int_{-\infty}^{y_R} \left[\frac{\rho_2 u_2}{\rho_{e2} u_{e2}} \right]_{x=0} dy - \int_{-\infty}^{y_R} \left[\frac{\rho_2 u_2^{\ 2}}{\rho_{e2} u_{e2}^{\ 2}} \right]_{x=0} dy \tag{2.29}$$

By the definition of the dividing streamline,

$$\int_{-\infty}^{y_R} \left(\frac{\rho_2 u_2}{\rho_{e2} u_{e2}}\right)_{x=0} dy = \int_{y_D}^{y_R} \left(\frac{\rho_2 u_2}{\rho_{e2} u_{e2}}\right)_x dy \qquad (2.30)$$

where y_D is the dividing streamline co-ordinate.

Since the pressure in the mixing region is constant then the shear layer momentum is conserved. Therefore,

$$\int_{-\infty}^{y_R} \left(\frac{\rho_2 u_2^2}{\rho_{e2} u_{e2}^2}\right)_{x=0} = \int_{-\infty}^{y_R} \left(\frac{\rho_2 u_2^2}{\rho_{e2} u_{e2}^2}\right)_x dy \qquad (2.31)$$

Equations (2.29), (2.30) and (2.31) give

$$\theta_2 = \int_{-\infty}^{y_R} \frac{\rho_2 u_2}{\rho_{e2} u_{e2}} dy - \int_{-\infty}^{y_D} \frac{\rho_2 u_2}{\rho_{e2} u_{e2}} dy - \int_{-\infty}^{y_R} \frac{\rho_2 u_2^2}{\rho_{e2} u_{e2}^2} dy \qquad (2.32)$$

$$\eta_{\theta 2} = (1-C_{e2}^2) \left[\int_{-\infty}^{\eta_R} \frac{\phi}{1-C_{e2}^2 \phi^2} d\eta - \int_{-\infty}^{\eta_D} \frac{\phi}{1-C_{e2}^2 \phi^2} d\eta - \int_{-\infty}^{\eta_R} \frac{\phi^2}{1-C_{e2}^2 \phi^2} d\eta \right] \qquad (2.33$$

where $\eta_{\theta 2} = \frac{\theta_2}{2\sqrt{\zeta}}$, $\eta_d = \frac{y_d}{2\sqrt{\zeta}}$, C_{e2} = Crocco's number,

$$\phi = \frac{u_2}{u_{e2}} \text{ (eqn. 2.21)} \qquad (2.33a)$$

If $\eta_{\theta 2}$, ϕ and M_{e2} are known then η_D and ϕ_D can be calculated using eqn. (2.33) and eqn. (2.21) respectively.

From equations (2.24), (2.25) and (2.26) and from the definition of $\eta_{\theta 2}$ we obtain,

$$\eta_{\theta 2} = \frac{\theta_2}{2\sqrt{\zeta}} = \eta_o \frac{\theta_2}{\delta_2}$$

$$= \eta_o \frac{m}{(m+1)(m+2)} \frac{(1-C_{e2}^2)(2+m)}{(2+m-mC_{e2}^2)} \qquad (2.34)$$

Fig. 6 shows the effect of M_{e2} on the variation of ϕ_D with $\frac{x}{\sigma\theta_2}$ when (m = 11) using eqns. (2.34), (2.33), (2.23) and (2.21)

Camarta[82] proposed a method for dealing with the problem. The initial boundary layer is assumed to have a $\left(\frac{1}{m}\right)$th power law velocity profile. Near the base, the initial boundary layer profile is not wholly effected by the mixing process. Thus, the shear layer profile can be divided into two regions. The lower region is the part of the initial boundary layer which is effected by the mixing and is assumed to have an asymptotic error function velocity profile. The upper region is the part of the initial boundary layer which is not yet effected by the mixing and therefore the $\left(\frac{1}{m}\right)$th power law velocity profile is returned in this region.

The joining point of the two regions is a function of $\left(\frac{x}{\delta_2}\right)$. An empirical relation is used to specify the joining point position.

Because the two regions have different velocity profiles, the shear layer profile has a kink at the joining point where the velocity gradient is not continuous.

Gerhart and Korst[83] proposed a similar but more complex method in which the lower region of the shear layer profile is assumed to be linear. The joining point of the two regions is found from the argument that the momentum of the shear layer remains constant with respect to (x) thus, the empirical relation of Camarta is avoided.

2.3 The Reattachment Region

After separation, the free shear layer will develop and will continue to thicken and entrain air from the dead-air region under constant pressure. The dividing streamline in the mixing region is almost straight. Eventually, the reattachment region is reached where the pressure starts to rise to reverse the air entrained by the shear layer back to the dead-air region until the dividing streamline reattaches.

To obtain an idea of the geometric configuration of the dividing streamline near the reattachment point, Cheng[76] assumes the flow to be incompressible and uses the full Navier-Stokes equations. The solution of these equations is assumed analytic. This solution shows that in the region very near to the reattachment point, the dividing streamline shape is parabolic having an infinite slope at the reattachment point. This corresponds to the requirement of potential flow at such a stagnation point[87].

Although our present interest is with the compressible flow, it is thought that in the neighbourhood of the reattachment point the dividing streamline has very low velocities anyway and that the incompressible treatment of Cheng is valid there even for a high speed external flow.

The reattachment criterion used by Chapman[7] and Korst[36] is simply that the reattachment pressure is equal to the free stream static pressure.

Various correlations are given to improve the reattachment criterion. In all these correlations, which are for supersonic flow, the assumption is made that (P_r) is either a function of $M_{e\infty}$ and P_b or a function of $M_{e\infty}$ and some free shear layer parameter in which the free shear layer is assumed to have the asymptotic profile.

The first improvement on the Chapman and Korst reattachment criterion is due to Nash[50] who introduced the parameter N(see section 3.1.3, eqn. 3.16) to account for the fact that P_r is actually smaller than P_∞. For supersonic flow, Nash employs (N = .35) while Cook[53] uses (N = 0.5). Experimental results[33,23,25,77] have shown that the value of N is between (0.1) and (0.5) for supersonic flow.

Roberts[63] gives a correlation which is valid for $M_{e2} > 2.0$.

The Mach number M_{er} based on the value of P_r is given as,

$$M_{er} = M_{e\infty} \Big/ .799 + .156\, M_{e2} - .08237\, M_{e2}^2 + .009564\, M_{e2}^2 \quad (2.35)$$

Page[78] has tackled the problem in a different way and has given the following correlation for $1.95 < M_{e2} < 4.13$

$$\frac{\nu_r - \nu_2}{\nu_\infty - \nu_2} = 0.5 \left[1 - \cos\left(180\phi_D - 1.8\right)\right] \qquad (2.36)$$

where ϕ_D is calculated by the equivalent asymptotic shear layer (eqn. ~~3.5~~ 3.14).

Batham[79] gives another correlation,

$$\frac{P_\infty - P_r}{\frac{1}{2}\rho_\infty u_\infty^2} = K\sqrt{\tau_D \Big/ \left(\tfrac{1}{2}\rho_\infty u_\infty^2 \sqrt{M_{e2}^2 - 1}\right)}$$

where τ_D = the shear stress at the dividing streamline of the free shear layer with zero initial thickness (given in Ref. 80). K = a constant that can be evaluated from experiment.

CHAPTER THREE

THEORIES FOR STEADY TRANSONIC AND SUPERSONIC BASE PRESSURE

A common feature of the theoretical methods for predicting base pressure is the assumption that the base pressure depends on the pressure recovery which can be sustained by the wake or by the re-attaching shear layer. The final recovery pressure far downstream is assumed known; frequently it is either equal to or approximated by the free stream static pressure. The base pressure is then found by subtracting from this known pressure the computed pressure rise occuring between the base and the reattachment point.

These methods can be divided into two groups: those which employ the Chapman-Korst model which depends on dividing the base flow into separate flow regions and those which employ integral techniques. These two groups will now be discussed.

3.1 Theories Employing the Chapman-Korst Flow Model

Chapman[17] studied the supersonic base pressure problem for both two-dimensional and axisymmetric inviscid flow. His purpose was to develop an understanding of the problem in its simplest form and also to study the effects of variations in profile shape on the base pressure. In addition to excluding viscosity and hence the boundary layer on the body, Chapman also excludes consideration of the mixing of the dead-air with the outside free streamline. He assumes that a

dead-air region of constant pressure equal to the base pressure exists just behind the base and is terminated by a single trailing shock wave.

For the two-dimensional case he assumes an inviscid flow passing over a semi-infinite two-dimensional flat horizontal surface which has a step in it (Fig. 7A). To construct the flow pattern in the neighbourhood of the base, the assumption is made that the inviscid flow expands through a centred Prandtl-Meyer expansion wave at the corner to form the dead-air region (ABC). The line (AB) represents the inviscid free streamline which separates the dead-air region from the external flow.

The flow is terminated by a single shock wave (BE) where the flow is turned back to the free stream conditions through an angle equal to the corner expansion angle. For a specific free stream Mach number $M_{e\infty}$ (which is assumed to be equal to the value just upstream of the corner M_{e1}), the maximum possible turning angle, and thus the lowest possible base pressure, is determined simply by the requirement that this maximum limit angle must be equal to the maximum deflection angle possible for a trailing shock wave to occur at that particular Mach number. The base pressure value at this maximum angle is called the limiting base pressure. Fig. 7B shows the limiting base pressure coefficient (C_{PB}) as a function of ($M_{e\infty}$) assuming the above argument to be correct.

On the basis of this analysis, Chapman concludes that a purely inviscid flow theory cannot possibly be satisfactory for predicting the base pressure and the shaded area in Fig. 7B represents the region of

possible values for this pressure. As we shall see in the following sections, the base pressure is in fact determined by the viscous-inviscid interation which occurs between where the flow separates from the corner and where it reattaches.

Chapman[34,35] considers the problem of laminar mixing of the compressible air stream, separating at the corner of a two-dimensional body, with the dead-air region. He assumes that the flow has zero boundary layer thickness at separation.

3.1.1 Theory of Korst

Korst[36] developed a theory for transonic and supersonic turbulent flow in which the flow model is the same as in the theory of Chapman for supersonic laminar flow. Since this flow model forms a basis for most theoretical work and because the assumptions made by the theory are to be compared with the present experiment, the theory is explained in detail. The Chapman-Korst analysis is based on dividing the flow into four regions. The flow mechanism in each region is formulated as follows.

The flow approaching the corner is assumed to be uniform flow with zero boundary layer thickness.

The expansion of the flow around the corner is assumed to occur rapidly and isentropically. For supersonic flow, this occurs through a centred Prandtl-Meyer expansion originating from the corner. Therefore,

$$\frac{P_b}{P_1} = \frac{P_b}{P_\infty} = \frac{\left(1 + \frac{\gamma-1}{2} M_{e\infty}^2\right)^{\gamma/\gamma-1}}{\left(1 + \frac{\gamma-1}{2} M_{e2}^2\right)} \qquad (3.1)$$

In the mixing region, the free shear layer is assumed to develop at a constant pressure equal to the base pressure, P_b.

The velocity profile at any position along the shear layer is obtained from eqn. (2.21).

Since the boundary layer thickness at separation is zero then $\eta_o = 0$ and eqn. (2.21) becomes

$$\phi = \frac{1}{2}(1+\text{erf}\eta) \tag{3.2}$$

It is recognised that the development of the turbulent free shear layer with zero initial boundary layer thickness is identical to the case of uniform free jet turbulent mixing with fluid at rest which has been dealt with theoretically[40,41,42,43]. All the theories assume that free shear layer velocity profiles are similar. Tollmien[40] uses Prandtl's mixing length concept to study the incompressible mixing of a two-dimensional jet with a free boundary. His solution for the free shear layer velocity profile is in the form

$$\phi = f\left(\frac{\sigma y}{x}\right) \tag{3.3}$$

where σ is the rate of spread of the shear layer which is a constant defined by eqn. (3.4).

Abramovich[41] extended Tollmien's results to cover the case of compressible flow up to the speed of sound. He found that compressibility has only a slight effect on the velocity profile. Experimental results[46,47,48] have shown that the free shear layer velocity profile

at supersonic speeds differs little in form from that at low speeds and the only effect of compressibility is to effect the value of σ. (See Appendix 1 on the effect of Mach number on the value of σ). Gortler[42] used Prandtl's new theory[45] of free turbulence in which the free turbulent eddy viscosity is defined as follows

$$\varepsilon = \frac{1}{4\sigma^2} \cdot u_e \cdot x \qquad (3.4)$$

Substituting eqn. (3.4) in the momentum equation, Gortler obtained an infinite series for the solution for the velocity profile. The first two terms of this series gave

$$\phi = \frac{1}{2}\left[1 + \text{erf}\,\frac{\sigma y}{x}\right] \qquad (3.5)$$

Eqn. (3.5) is known to be in good agreement with the measured mean velocity near the centre of the shear layer, with slight deviation towards the edges. Because eqn. (3.5) approaches the edges of the shear layer asymptotically, it is referred to as the asymptotic error function velocity profile. Table 2 gives this velocity profile.

Eqn. (3.5) can be identified to eqn. (3.2) by putting,

$$\eta = \frac{\sigma y}{x} \qquad (3.6)^*$$

---

* It must be emphasised that eqn. (3.6) is valid only when the initial boundary layer thickness is zero and the free shear velocity profile, eqn. (3.2), can then be approximated by the asymptotic error function profile, eqn. (3.5).

To find the velocity along the dividing streamline, ϕ_D, in the constant pressure region, a different approach from that of Korst is used to give the same result. If the initial boundary layer thickness is zero then $\eta_{\theta 2} = 0$ and the free shear layer has the asymptotic velocity profile. Therefore, eqn. (2.33) becomes:-

$$0 = (1-C_{e2}^2) \left[\int_{-\infty}^{\eta_R} \frac{\phi}{1-C_{e2}^2\phi^2} d\eta - \int_{-\infty}^{\eta_D} \frac{\phi}{1-C_{e2}^2\phi^2} d\eta - \int_{-\infty}^{\eta_R} \frac{\phi^2}{1-C_{e2}^2\phi^2} d\eta \right] \quad (3.7)$$

where ϕ and η are given by eqn. (3.5) and eqn. (3.6) respectively.

If M_{e2} is given, then eqn. (3.7) can be integrated numerically to obtain the position and the velocity of the dividing streamline.

Fig. 8 shows the theoretical variation of ϕ_D with M_{e2} for zero initial boundary layer thickness according to eqn. (3.7).

In the recompression region, the pressure rises in order to reverse back to the dead-air region that air entrained by the free shear layer. If the flow is supersonic, the corresponding recompression waves will coalesce to form a trailing shock.

As did Chapman, Korst made two assumptions for this region. The first is that the free stream static pressure (P_∞) is equal to the reattachment pressure (P_r). The second is that the compression process is isentropic.

The Mach number along the dividing streamline is given by:-

$$M_{eD}^2 = \frac{\phi_D^2 M_{e2}^2}{1 + \frac{\gamma-1}{2} M_{e2}^2 (1-\phi_D^2)} \quad (3.8)$$

Since the compression process is assumed isentropic, the flow along the dividing streamline is brought to rest according to;

$$\frac{P_r}{P_b} = \frac{P_\infty}{P_b} = (1 + \frac{\gamma-1}{2} M_{eD}^2)^{\gamma/\gamma-1} \qquad (3.9)$$

Eqns. (2.1), (2.19) and (2.20) give

$$M_{e\infty}^2 = (1-\phi_D^2)\, M_{e2}^2 \qquad (3.10)$$

and

$$\frac{P_b}{P_\infty} = \left[\frac{1 + \frac{\gamma-1}{2} M_{e\infty}^2}{1 + \frac{\gamma-1}{2} \frac{M_{e\infty}^2}{1-\phi_D^2}}\right]^{\gamma/\gamma-1} \qquad (3.11)$$

To evaluate the base pressure for a given free stream Mach number $M_{e\infty}$, the proceedure is as follows:-

i) Assume a value of (P_b/P_∞) and substitute this value in eqn. (3.1) to obtain M_{e2}.

ii) Use eqn. (3.7) to obtain ϕ_D.

iii) Substitute the value of ϕ_D in either eqn. (3.10) or eqn. (3.11). If both sides of the eqn. are not equal, assume another value of (P_b/P_∞) and repeat the procedure to iterate to the correct value of (P_b/P_∞). Few iterations are needed.

Thus for zero initial boundary layer thickness, Korst has constructed a simple method to evaluate the base pressure. Fig. 9 shows the variation of (P_b/P_∞) with $M_{e\infty}$ according to the above theory.

3.1.2 Extension of Korst Theory to Include the Effect of Finite Boundary Layer Thickness at Separation

The Chapman and Korst theories are confined to the case of zero initial boundary layer thickness at separation. Kirk[49] has proposed a means of including the effect of a finite boundary layer thickness in these theories. His method is to assume that the real free shear layer developing from a finite initial boundary layer thickness becomes asymptotic after a short distance after separation and can be replaced by an equivalent asymptotic free shear layer as illustrated in Fig. 10. The distance $\bar{x}$, between the shift in the origin of the equivalent asymptotic shear layer and the separation point is calculated by using the argument that at the separation point the momentum of the boundary layer is equal to that of the equivalent shear layer.

In his analysis, Kirk did not include the value of $\bar{x}$ in the final result. For the present case, the value of $\bar{x}$ is included by using a different approach from that used by Kirk. At $x = 0$,

$$\theta_2 = \int_{-\infty}^{\infty} \left[\frac{\rho_2 u_2}{\rho_{e2} u_{e2}} - \frac{\rho_2 u_2^2}{\rho_{e2} u_{e2}^2} \right]_{x=0} dy \qquad (3.12)$$

where the right hand side of this equation represents the equivalent shear layer momentum thickness.

Because the equivalent shear layer has an asymptotic error function velocity profile, eqn. (3.12) becomes

$$\frac{\sigma\theta_2}{\overline{x}} = (1-C_{e2}^2)\left[\int_{-\infty}^{\infty}\frac{\phi}{1-C_{e2}^2\phi^2}\,d\eta - \int_{-\infty}^{\infty}\frac{\phi^2}{1-C_{e2}^2\phi^2}\,d\eta\right] \quad (3.13)$$

where ϕ and η are given by eqn. (3.5) and eqn. (3.6) respectively. Fig. 77 shows the variation of $\frac{\sigma\theta_2}{\overline{x}}$ with M_{e2} according to eqn. (3.13).

Since at any distance x, the equivalent shear layer has the length $(x+\overline{x})$, eqn. (2.33) becomes

$$\frac{\sigma\theta_2}{(x+\overline{x})} = (1-C_{e2}^2)\left[\int_{-\infty}^{\eta_R}\frac{\phi}{1-C_{e2}^2\phi^2}\,d\eta - \int_{-\infty}^{\eta_D}\frac{\phi}{1-C_{e2}^2\phi^2}\,d\eta - \int_{-\infty}^{\eta_R}\frac{\phi^2}{1-C_{e2}^2\phi^2}\,d\eta\right] \quad (3.14$$

where ϕ and η are given by eqn. (3.5) and eqn. (3.6) respectively. The numerical integration of eqn. (3.14) together with eqn. (3.13) gives the variation of ϕ_D with $\frac{\sigma\theta_2}{x}$ for any value of M_{e2}.

Fig. 12 shows the effect of M_{e2} on the variation of ϕ_D with $\frac{x}{\sigma\theta_2}$ according to eqn. (3.14).

Therefore, ϕ_D is now a function of $\frac{\sigma\theta_2}{x}$ and M_{e2} in contrast to the case of zero initial boundary layer thickness where ϕ_D is a function of M_{e2} only.

For comparison, Fig. 13, shows the variation of ϕ_D with respect to $\frac{x}{\sigma\theta_2}$ for incompressible flow as calculated by the above method and the two methods described in Chapter 2.

The effect of the finite initial boundary layer thickness can now be included in Korst's theory using the above method. The base pressure is evaluated in the same way as before (section 3.1.1) except that ϕ_D is now calculated using eqn. (3.14) with x taken as the distance between the separation point and the beginning of the recompression region.

For simplicity, this distance is assumed to be equal to the distance between the separation and reattachment points (L).

For supersonic flow, the dividing streamline is assumed to be straight and parallel to the external flow. Thus,

$$L = \frac{h}{\sin(\nu_2 - \nu_\infty)} \tag{3.15}$$

3.1.3 Theory of Nash

In the theory of Nash[50] for turbulent base flow, the flow model is essentially the same as that used by Korst. It is possible to predict the influences of the initial boundary layer thickness and of the base bleed on the base pressure.

In all previous theories the reattachment pressure, P_r, is assumed to be equal to the free stream pressure or slightly less for the case of supersonic flow to take account of the pressure loss resulting from the passage of the external stream trhough the

trailing shock.

Nash however raises the doubt that reattachment can occur at zero pressure gradient. His doubt has been supported by both experimental evidence[31,33] and theoretical treatment of the reattachment process[19,51,52] where it has been shown that the reattachment point is reached before the pressure has risen to the free stream pressure. The reason for this is that a pressure rise is needed to rehabilitate the reattached boundary layer*. Therefore, it is apparent that reattachment takes place at a point of adverse pressure gradient and a substantial pressure recovery is achieved downstream of the reattachment point. Nash therefore, introduces a new parameter (N) in the analysis where (N) is defined as

$$N = \frac{P_r - P_b}{P_\infty - P_b} \qquad (3.16)$$

From experimental results for supersonic flow, Nash assumes the value of (N = .35) instead of unity as has been assumed by all previous theories.

If there is no base bleed into the dead-air region, the theory gives the solution for base pressure as,

$$\frac{\theta_2}{L} = E_1 \frac{A(A-B)}{B} \qquad (3.17)$$

where $A = \ln(\lambda_b)$

---

* See References 51 and 52.

$$\lambda_b = \left(1 + \frac{\gamma-1}{2} M_{e2}^2\right) \Big/ \left[1 + \frac{\gamma-1}{2} M_{e_2}^2 (1-\phi_m^2)\right]$$

$$\phi_m^2 = .348 + .018\, M_{e2}^{*}$$

$$B = \ln \left(\frac{P_r}{P_b}\right)^{\frac{\gamma-1}{\gamma}}$$

$$\frac{P_r}{P_b} = N\left[\left(\frac{P_\infty}{P_b}\right) - 1\right] + 1$$

$$E_1 = \frac{\sqrt{\pi}}{(\gamma-1)\,\sigma M_{e2}^2}$$

L = Free shear layer length.

For supersonic flow L is defined by eqn. (3.15). Then eqn. (3.17) becomes:-

$$\frac{\theta_2}{h} = E_2 \cdot \frac{A(A-B)}{B} \qquad (3.18)$$

where $E_2 = \left(\frac{M_{e2} T_{e2}}{M_{e\infty} T_{e\infty}}\right)^3 \frac{E_1}{\sin(\nu_2 - \nu_\infty)}$

---

* u_m is the velocity along the median streamline. This streamline (ψ_m) is generally different from the dividing streamline ψ_D. The two are related as follows:-

$$\psi_m - \psi_D = \rho_{e2}\, u_{e2}\, \theta_2$$

If the initial boundary layer thickness is zero then ψ_m and ψ_D are identical.

As the initial boundary layer thickness approaches zero, the base pressure tends to its limiting value $\left(\frac{P_b}{P_\infty}\right)_{LIM}$. From eqn. (3.18)

$$\left(\frac{P_b}{P_\infty}\right)_{LIM} = \frac{1}{1 + \frac{1}{N}\left[(\lambda_b)^{\gamma/\gamma-1} - 1\right]} \qquad (3.19)$$

3.1.4 Later Developments in the Theory Based on the Chapman-Korst Flow Model

Nash[54] later suggested that his value of 0.35 for N is not accurate and that N is a function of $M_{e\infty}$ and $\frac{\theta_2}{h}$. Other reattachment criterions are given in Section 2.3.

To avoid the necessaty of introducing a reattachment pressure parameter, McDonald[55] has suggested a method for dealing with the part of the pressure rise occuring downstream of the reattachment point. In McDonald's theory, which is for supersonic flow past a backstep, the analysis is the same as for the previous theories until the start of the pressure rise at the reattachment region. From this point, a momentum integral approach gives the velocity profile thickness parameters at the reattachment point. The pressure rise to P_r is assumed abrupt and therefore isentropic. The remaining pressure rise (P_∞-P_r) is related to the change in the shape factor (H) of the attached boundary layer between reattachment point and far downstream.

A similar approach is used by Reshotko and Tucker[56] for the separating boundary layer in adverse pressure gradients. However, an important difference exists between detaching and reattaching flows. Whereas in both cases the pressure rise is in the downstream

direction, the shape factor increases in the separating flow but decreases in the reattaching flow.

McDonald assumes that a certain pressure rise is associated with a given change of shape factor irrespective of the sign of the change. Although this argument does not seem satisfactory, it has received some confirmation from Curl[57]. McDonald[52], in a later paper, attempts to argue this on a firmer basis.

Thus, a simple result is used by McDonald which is that the rate of change in the shape factor of the reattaching boundary layer is merely minus that of the separating boundary layer. Therefore, Reshotko results can be used as follows:-

$$\frac{M_{e\infty}}{M_{er}} = \frac{f(H_{i\infty})}{f(H_{ir})} \qquad (3.20)$$

where

$$f(H_i) = \frac{H_i^2}{(H_i-1)^{\frac{1}{2}}.(H_i+1)}\, e^{1/H_i+1} \qquad (3.20a)$$

H_i = The incompressible shape factor.

H_i is related to H by the Stewartson transformation as

$$H = (1 + \tfrac{\gamma-1}{2} M_e^2)\, H_i + \tfrac{\gamma-1}{2} M_e \qquad (3.20b)$$

McDonald assumes that for a backstep, $H_{i\infty}$ is equal to that of flow over a flat plate. A mean value of $H_{i\infty} = 1.4$ is used.

The procedure to evaluate the base pressure for any $M_{e\infty}$ is as follows:-

i) Assume a value for $\frac{P_b}{P_\infty}$

ii) Use eqn. (3.1) to evaluate M_{e2}

iii) Use eqn. (3.14) to evaluate ϕ_D

iv) Use eqn. (3.8) and eqn. (3.9) to evaluate P_r and thus M_{er}

v) The velocity profile at reattachment is assumed to be asymptotic. Therefore H_{ir} can be evaluated

vi) Use eqn. (3.20) to evaluate $H_{i\infty}$. If $H_{i\infty}$ is not equal to 1.4, repeat the procedure (i) to (vi).

All the above theories do not show any difference between the flow past a backstep or an isolated base with no vertex formation. In fact, all these theories assume that the two types are similar and the results relating to one can be applied to the other. This assumption appears to have originated with the older theories like that of Chapman and Korst in which P_r is assumed to be equal to P_∞. Thus, the flow conditions downstream of the reattachment point are thought to be unimportant. This has received some confirmation by experiments which have shown that for supersonic flow the base pressure for the two cases are not very different.

As discussed above, there exists a considerable pressure rise after the reattachment point, thus, one expects that the flow field after reattachment plays an important role in the determination of the pressure field as a whole.

The essential differences between the step and the base flow lies in the development of the boundary layer after the reattachment point. In a backstep, there is a wall shear stress and the boundary layer must finally recover to that of a flat plate type far downstream. In an isolated base, there exists no shear stress on the centreline of the wake and the boundary layer must eventually have a value of ($H_\infty = 1$) far downstream.

In view of the above differences, it is difficult to see how the McDonald theory can be used for an isolated base since a value of ($H_{i\infty} = 1$) gives $f(H_{i\infty})$ equal to infinity.

3.2 Integral Method

All the above theories are incapable of predicting such important wake characteristics as the length of the recompression region, the location of the rear stagnation point, the reattachment pressure, the longitudinal pressure, variations in the reattachment region and most important of all, the difference in the flow behaviour after reattachment between an isolated base and a backstep. These theories are deficient because they disregard the essential viscous-inviscid interation which determines the reattachment process and thus the whole turbulent base flow.

In 1952, Crocco and Lees[19] developed a theory for the supersonic rear wake. The theory includes the effect of the viscous-inviscid interaction through the use of the integral continuity equation. Therefore, if γ is the angle which the external inviscid stream makes with the x-direction (Fig. 14), then the rate of mass

of fluid which is transported to the boundary layer is

$$\frac{d\overline{m}}{dx} = \rho_e u_e \left(\frac{d\delta}{dx} - \overline{\gamma}\right) \tag{3.21}$$

Integrating the continuity equation

$$\tan \overline{\gamma} = \frac{v_e}{u_e} = \frac{d\delta^*}{dx} - \left[\frac{d}{dx} (\log \rho_e u_e)\right] \int_o^\delta \frac{\rho u}{\rho_e u_e} dy \tag{3.21a}$$

In their analysis for supersonic two-dimensional turbulent base flow, the assumption is made that a single semi-empirical relation for the boundary layer parameters is valid for all flow regions from the separation point up to the wake. The momentum equation is used together with equation (3.21a) and the final equation shows the existence of a critical point after reattachment at which the pressure is still rising. This means that even after the reattachment point the pressure is less than the free stream pressure. To evaluate the base pressure, a value of P_b/P_∞ is assumed and the final equation is integrated from the separation point towards the wake. The correct base pressure value is the one that allows the flow to pass smoothly through the critical point.

The analysis also predicted the dependence of P_b/P_∞ on Re. Fig. 15 shows a sketch of this prediction. There four distinct regions.

Region A-B: P_b/P_∞ increases as R_e increases. The flow is wholly laminar in this region. As R_e increases, θ_1 and the

mixing rate decreases. The decrease in the mixing rate is apparently more than enough to offset the effect of the decrease in the boundary layer thickness thus the base pressure increases. Because of the low laminar mixing rate, the base pressure ratio is relatively high.

Region B-C: P_b/P_∞ decreases with increasing R_e. In this region the transition from laminar to turbulent flow starts to occur just ahead of the reattachment position and this position is moving towards the base. Therefore, the shear layers are partly turbulent and as R_e is increased, the large increase in the local mixing rate causes P_b/P_∞ to decrease. At point c the base pressure ratio has a minimum value where the hole shear layer is turbulent and the transition point is just ahead of the base.

Region C-D: P_b/P_∞ increases with increasing R_e. This is because as R_e increases, the transition point is moving away from the base towards the leading edge causing θ_1 and thus P_b/P_∞ to increase.

Region D-E: P_b/P_∞ decreases slightly with increased R_e. Here the transition point has reached a fixed point (namely the leading edge) and the flow is wholly turbulent. As R_e increases, θ_1 and therefore P_b/P_∞ decreases. Since for turbulent flow $\theta_1 \propto 1/R_e^{1/5}$, the rate of decrease in P_b/P_∞ is small.

In order to avoid the semi-empirical features of Crocco-Lees' method, a theoretical model was developed by Reeves and Lees[58,59] for the hypersonic laminar near wake behind blunt bodies. This model has improved the Crocco-Lees' solution through the use of an additional first moment of momentum equation with a suitable profile.

Alber and Lees[60] extended Reeves and Lees' model to the analysis of turbulent base flow for moderate supersonic flow. The effect of the free stream turbulence is now included in the solution by using an eddy viscosity model based on Prandtl's theory for incompressible free turbulence in which the length scale is not the width of the shear layer but the momentum thickness of this layer. The flow field is treated by dividing it into two distinct regions:-

The first is the mixing region in which the free shear layer develops and the mixing process is assumed to occur at constant pressure. The initial velocity profile for the shear layer is assumed to have a quadratic profile similar to that used in the analysis of Kubota and Dewery[74] (Section ~~3.2~~ 2.2).

The second is the wake region where the pressure is starting to rise and the flow is beginning to turn back to the free stream condition. In the wake region the velocity profiles are assumed to be similar and corespond to the solutions of the Falkner-Skon[61,62] equation of viscous flow in a pressure gradient with zero shear stress on the axis of symmetry.

The location of the point where the two regions join cannot be specified a priori but is uniquely determined by the condition that the flow must pass smoothly through the critical point. At

the joining point certain flow conditions at the beginning of the wake region must be equal to the flow conditions at the end of the constant pressure mixing region.*

* See Ref. 60 for further detail.

CHAPTER FOUR

DESCRIPTION OF THE RIG

The tests were carried out in a transonic wind tunnel with slotted walls.* The slotted wind tunnel has mainly two advantages over a closed or open wind tunnel.

If the model is placed in a closed wind tunnel with straight walls, bulging out of the streamlines is prevented by the direct guiding of the wall. Proceeding from the model outwards to the walls, the streamlines are gradually straightened out by the influence of the walls. The air flow between two adjacent streamlines must now squeeze through a smaller area than that of the real conditions giving rise to higher mean velocities around the model.

On the contrary, if the model is placed in an open jet wind tunnel the streamlines will bulge out more than those under real conditions because the free stream pressure must be reached at the free jet boundary. Thus, the air flows between adjacent streamlines have larger areas and consequently lower mean velocities around the model than the real conditions.

Therefore open or closed wind tunnels produce deformations around the model with opposite signs that require velocity corrections with opposing signs. If a slotted wind tunnel, having proper open-to-closed area ratio is employed, these deformations can be made to cancel each other.

As the flow Mach number reaches unity the slotted wind tunnel

---

* See Plate 1.

acts like a supersonic nozzle with the throat at the beginning of the slots. Thus we are able to obtain Mach numbers higher than unity in the slotted wind tunnel by just increasing the stagnation pressure of the flow.

The other advantage is in minimising the flow disturbances along the wind tunnel at transonic and supersonic speeds which result from the pressure wave reflections. A pressure wave is reflected from the solid wall and free jet boundary in like and unlike sense respectively. Again, by having a slotted wall with proper open-to-closed area ratio, some of the reflected waves are expected to cancel each other minimising the effect of these waves on the flow.

The general layout of the closed air circuit for the transonic wind tunnel is shown in Fig. 16. The air is passed through a filter and an intake value which is controlled by a remote control pressure regulator in the wind tunnel room. The air is compressed by a 4-stage turbo air compressor. Table 3 gives the compressor specifications. The compressed air is then passed through an after cooler and a settling chamber before entering the slotted wind tunnel. After leaving the tunnel, air is cycled back to the intake valve. An isolating valve is provided in the circuit which can be shut in an emergency by pressing a button in the remote pressure regulator. An after cooler by-pass is provided for fine temperature adjustment.

A pressure tapping is provided in the settling chamber for measuring the air total pressure. The settling chamber temperature is measured using a thermocouple.

At the entrance of the tunnel air is expanded between the subsonic liners and then flows over the model, through the slotted section. The test section is nominally 4" x 4" with slotted upper and lower surfaces and the area of the slotted section can be altered by varying the angle of the slotted wall. Schlieren glass windows are provided on the two solid side walls of the test section to enable visualisation of the flow.

The model is symmetrical about the centreline with pressure tappings on both upper and lower surfaces and at the base. To investigate the effect of base air bleed, the model is made hollow with an air inlet port through each side wall and a rectangular slot at the base for the bleed flow at outlet. The model can be set at different angles of incidence with respect to the tunnel. Thus, different Mach number distributions can be created on the upper and lower surfaces of the model and the flow over the model can then resemble that over turbine blades.

To measure the boundary layer velocity profile and to investigate the flow field near the base, pressure probes can be inserted inside the working section through the solid side wall. A traverse gear is designed for this purpose.

The slotted section, the model and the traverse gear have been designed by Malhotra[84].

4.1 Description of the Tunnel Working Section

Fig. 17 shows the general layout of the test section.* The slotted walls are geometrically similar to those designed by Bansal[85].

---

* See Plate 1C.

In each wall, there are three slots having a total open to closed area ratio of 1/14.

The angle of the slotted walls can be varied. This is to shift the sonic line backwards and forward.

4.2 Description of the Test Model

The flow approaching the base is desired to be uniform and parallel as a basic condition for the base pressure correlation. Thus, the supersonic part of the model is designed with a contour similar to that of a supersonic nozzle, in which the contour must first curve outward and then backward until it is parallel to the flow direction.

The supersonic contour obtained by Malhotra, with a final Mach number of 1.3 ahead of the trailing edge, can be approximated by the polynomial*,

$$y = .2637 + .0074\,x - .1001x^2 + .0719x^3 - .0223x^4 + .026x^5 \qquad (4.1)$$

The shape of the sonic line depends on the profile of the subsonic inlet and the angle of the slotted liners. The subsonic part of the model is a combination of an ellipse and a straight line.

Table 4 gives the model dimensions. Fig. 18 shows the model which is 6" long with maximum thickness of .528" and trailing edge thickness of 0.3".

---

* See Ref. 84 for further design details.

Fig. 19 shows the base geometry. The pressure tappings are shown in Fig. 20.

4.3 The Base Bleed Air Supply System

Fig. 21 shows the air supply system. Air from the reciprocating compressor passes through throttle valves, a pressure control valve and an orifice plate. The orifice plate is made according to B.S. specification[95] with inside and outside diameters of 27/32" and $1\frac{5}{8}$" respectively. A thermometer is used to measure the air total temperature downstream of the orifice.

4.4 Design and Description of the Pressure Probes

To measure the static pressure in transonic flow represents some difficulty since at high subsonic speed the flow over the probe becomes supersonic locally and the supersonic region terminates by a shock wave. As the flow Mach number is increased, the shock moves backward until it passes the static pressure tappings and the recorded pressure becomes lower than the true one. Therefore, as the flow Mach number approaches unity the instrument reading falls abruptly.

These effects can be reduced by using a probe with a fine tapered head. Experimental results[90] have shown that by using a conical probe, a correction of .002 to .004 is needed for the Mach number correction over the range of .98 → 1.2. For M = 1.6, experiments[91] have shown that the static pressure reading is independent of the nose shape when the static tappings are more than ten tube

diameters behind the shoulder of the nose.

For the wind tunnel calibration, a static pressure probe was used which has a conical nose with an apex angle of 10^{o} followed by a steel tube of diameter .066 (Fig. 22A). Four equally spaced holes each of .013" diameter are drilled at a distance of 1" from the nose.

A rectangular head pitot-static probe was used for the boundary layer traverse and the measurement of the axial pressure and velocity distribution on the centreline of the flow near the base. The static pressure reading was used only for the latter.

Although the use of a pitot-static probe is not suitable for transonic flow measurements, the employment of this probe for the base region investigations is justified since the flow to be investigated was of a low Mach number. Fig. 22B shows the pitot-static probe.

4.5 The Traverse Gear

The traverse gear was designed to be suitable for boundary layer traverse. The flow can be investigated across the height and the width of the tunnel and along the flow.

4.6 Calibration of the Pressure Probes

The probes were calibrated in the uniform flow in the otherwise empty test section.

Before the model was placed inside the tunnel, the static probe was aligned with the flow at the centreline of the tunnel. The pressure tappings were at the same streamwise position as that of the plenum chamber tappings.

It was assumed that there was no difference between the static pressure recorded by the plenum chamber tappings and the true static pressure of the undisturbed flow. Therefore, the pressure recorded by the probe was calibrated against the plenum chamber pressure. Fig. 23 shows the calibration curve for the static probe; the subsonic values of zero error confirm the corrections of equating the plenum and true static pressure at those Mach numbers though not necessarily for $M > 1$.

The pitot-static probe was calibrated in the same way. The pitot total pressure reading was calibrated against the settling chamber total pressure. Fig. 24 shows the calibration curve for the pitot-static probe.

4.7 Calibration of the Wind Tunnel Working Section

Before fitting the model, the wind tunnel was calibrated.

Fig. 25A shows the calibration curve for $M_{e\infty} = 1.3$ with two settings for the slotted walls. It can be seen that a wall divergence of $1^{o}\ 2'$ is giving a better Mach number distribution than that of parallel slotted walls. The angle was therefore chosen for the tunnel calibration.

Fig. 25B shows the calibration curves for the tunnel working section throughout the transonic range. The waviness of the curves at $M_{e\infty} > 1$ is due to the partial reflections of the pressure waves.

4.8 Calibration of the Rate of Basic Bleed

The air injected through the base bleed is found to have a non-uniform velocity distribution along the span with large boundary layers near the ends and a fairly uniform velocity distribution around the centreline (Fig. 26). Therefore, the rate of base bleed ($\dot{m}$) measured by the orifice plate is less than the value ($\dot{m}_b$) which is the rate of base bleed calculated with the assumption that the velocity distribution along the span is uniform and equal to the velocity near the centreline.

Since the base pressure tapping is situated near the centreline, the base pressure recorded is that which corresponds to a rate of base bleed equal to ($\dot{m}_b$). Therefore, $\dot{m}$ must be calibrated against $\dot{m}_b$.

The calibration was also carried out with different external flow Mach numbers, $M_{e\infty}$.

Fig. (27) shows the calibration curve of $\dot{m}$ with $\dot{m}_b$ for $M_{e\infty}$ = 0, 0.6 and 1.3. The calibration process was stopped when the injected air local Mach number reached unity.

It can be seen that the effect of $M_{e\infty}$ on the calibration curve is negligible.

CHAPTER FIVE

EXPERIMENTAL RESULTS AND DISCUSSION

5.1 Experimental Procedure

The aerofoil was aligned at zero angle of incidence by balancing the pressure recorded by the tappings on the upper and lower surfaces.

Two identical transition wires were fixed along the span on the upper and lower surfaces of the model at a distance of 0.475" from the leading edge. The size of the wires was above the value necessary for transition to occur at the position of the wire (Ref. 88). Two sets of wires of diameter .007" and .024" were used for the present investigations. The base pressure was investigated with the free stream Mach number in the range of $M_{e\infty}$ = .6 to 1.3. The boundary layer profile of the flow approaching the base was measured at 0.4" from the trailing edge.

5.2 Base Pressure Variation Along the Span at Zero Incidence

Fig. 28 shows the results of P_b/P_∞ along the span for $M_{e\infty}$ = 0.6, 1.0 and 1.3. It can be seen that the base pressure is uniform along the span and the flow near the centre of the span can be treated as a two-dimensional one.

5.3 The Base Pressure Variation

5.3.1 Effect of Reynolds Number

Fig. 29 shows the results of base pressure variation with the chord Reynolds number for $M_{e\infty}$ = .945 and 1.24.

It can be seen that P_b/P_∞ is independent of R_e for the range investigated. This result is expected since, for turbulent flow with fixed transition point, the boundary layer thickness is a function of $R_e^{-1/5}$, (See Section 1.1.2). Thus R_e will have a small effect on P_b/P_∞.

5.3.2 Effect of Free Stream Mach Number at Zero Incidence

Fig. 30 shows Mach number distribution on either surface of the model at zero angle of incidence for different values of $M_{e\infty}$.

Some of these results are plotted again in Fig. 31 to show the Mach number distribution near the base.

It can be seen that the low base pressure is felt upstream of the base even when $M_{e\infty}$ is supersonic*. Therefore, the expansion process is starting some distance upstream. This distance seems to diminish as $M_{e\infty}$ is increased.

The result of the variation of the base pressure with $M_{e\infty}$ is shown in Fig. 32. The values of Mach number on the blade surface at 0.4" and .03" from the base are included in the scale.

It is seen that as $M_{e\infty}$ is increased, P_b/P_∞ is decreased. When the local Mach number just upstream of the base reaches unity (at

---

* This is predicted (see Section 2.1). Gibbings[87] obtained similar results for incompressible flow.

$M_{e\infty}$ = .82, $\bar{M}_{e1}$ = 1.0), there is a sharp drop in the base pressure. This continues until P_b/P_∞ reaches a minimum value at $M_{e\infty}$ approximately equal to 1.15. Thereafter, P_b/P_∞ increases as $M_{e\infty}$ increases. The above results are explained by the following argument.

In Chapter 2, it is argued that the entrained air by the free shear layer causes P_b/P_∞ to be less than unity. This is because a recompression is needed at the reattachment region to reverse the entrained air back to the dead-air region to conserve the mass of the air in this region.

If the wall shear stress at separation is increased by thinning the boundary layer at the corner, the rate of the free shear layer entrainment is increased and consequently a lower value of P_b/P_∞ is needed to provide the enhanced back flow.

The fall in pressure that starts upstream of the base in low-speed flow results in a thinning of the boundary layer as it approaches the base. This thinning will enable the expansion of the external flow still to be present when that flow becomes supersonic.

For a small pressure fall near the base, the corresponding small change in the flow direction in the Prandtl-Meyer expansion is increased by a factor of the order 3.5 as the local Mach number changes from unity to about 1.3. Thus this enhanced flow curvature implies a corresponding marked increase in the thinning of the boundary layer and correspondingly a fall in the base pressure as the flow becomes supersonic locally.

The reason for the existence of a minimum value of P_b/P_∞ is not clear. Two arguments are given here for this.

The first argument is that it is interesting to note that the minimum value of P_b/P_∞ occurs when the Mach number just ahead of the trailing edge is approximately 1.42.

According to Weinbaum's analysis (see Section ~~2.7~~ 2.1), if the supersonic portion of the boundary layer is assumed to consist of an infinite number of layers with slightly different Mach numbers, then there will be waves reflecting from the slip lines that separate these layers (see Fig. 4A).

If $M_i < \sqrt{2}$ or $M_i > \sqrt{2}$, then the reflected waves are compression and expansion waves respectively. Since the base region is essentially a constant pressure region, then these waves will reflect at the sonic line as waves of different signs. Therefore, compression waves are reflected as expansion waves at the sonic line as shown in Fig. 33A. This will cause the sonic line and the flow to turn more towards the wake's centreline thus increasing the turning angle*. The increase in the degree of expansion will increase the thinning of the boundary layer at separation, as discussed above, and consequently P_b/P_∞ will decrease. This may be one of the reasons why the base pressure drops sharply when the flow becomes supersonic locally.

When $M_i > \sqrt{2}$, then the reflected expansion waves will reflect as compression waves at the sonic line as shown in Fig. 33B. This will cause the sonic line and the flow to turn away from the wake's centreline thus reducing the turning angle**. The reduction in the

---

* See Plate 4A.

** See Plate 2A.

degree of expansion, similar to that happening on an aerofoil at transonic speeds, will reduce the thinning of the boundary layer at separation and consequently P_b/P_∞ will increase.

The other argument for the reason of the existence of the minimum value of P_b/P_∞ is given as follows.

If the boundary layer is visualised to consist of a subsonic and supersonic regions with a hypothetical line, representing the sonic line, separating the two regions. As seen from the experimental results, the pressure drop to the base pressure is gradual with the expansion process starting some distance before the trailing edge.

As the pressure drops in the streamwise direction, the thickness of the subsonic region decreases. This causes the flow in the supersonic region to turn towards the surface thus, expanding to the same local pressure. The shape of the subsonic region is that which is required for pressure and velocity continuity at the sonic line. Fig. 34A shows the shape of the sonic line AB. As M_{e1} is increased, a point is reached where the initially subsonic region becomes supersonic at the throat causing it to increase its thickness with further decrease in pressure. This is clearly incompatable with the supersonic region, which must continue to turn towards the surface to decrease its pressure. The only solution for this is that the subsonic region throat occurs at the corner. At this stage, the sonic line is just missing the corner as shown in Fig. 34B.

If M_{e1} is further increased, by increasing the stagnation pressure, the sonic line now starts at a new position A' (Fig. 34C).

If we assume that P_b/P_∞ remains constant or decreases then, the curve A'B' will represent the new sonic line with point B' before the corner. As discussed before, this is not possible and the throat must be at the corner. Therefore, point A' is shifted in the x-direction to point A", where the xonic line A"B is now just missing the corner. This will cause the expansion process to occur in a shorter distance than before* thus giving rise to a higher transverse pressure gradient than before. Eventually a point is reached where the flow cannot sustain a further transverse pressure gradient and P_b/P_∞ has to increase to allow the sonic line to pass the corner with further increase in M_{el}.

5.3.3 Effect of Angle of Incidence

Fig. 35 shows the results of the effect of the incidence angle on the base pressure through the transonic range.

It is seen that at any angle of incidence, the variation of P_b/P_∞ with $M_{e\infty}$ is in qualitative agreement with that for zero incidence angle. The effect of increasing the incidence angle is to increase the base pressure, particularly at subsonic speeds, and to increase the value of $M_{e\infty}$ at which the base pressure starts to drop sharply from $M_{e\infty} = .82$ at $\alpha = 0$ to $M_{e\infty} = 1.0$ at $\alpha = 6^0$. To try to understand the behaviour of the flow at these incidence angles, the Mach number distributions on the upper surface of the model at different values of $M_{e\infty}$ are plotted in Fig. 36. The Mach number dis-

---

* See Fig. 31.

tributions on the upper and lower surfaces of the model for $M_{e\infty}$ = 0.6, 1.0 and 1.3 are plotted in Fig. 37.

It is seen from these distributions that at subsonic speeds ($M_{e\infty} < 1$), the flow on the upper surface reaches a relatively high supersonic speed and a shock wave is formed to compress the flow to the trailing edge conditions. At some value of $M_{e\infty}$, the shock wave interacts with the turbulent boundary layer and causes the flow to separate there*. A further increase in $M_{e\infty}$ causes the separation point to move towards the base. The separation ceases either when the pressure rise across the shock wave is smaller than that needed to separate the flow or when the flow on the upper surface is shock-free**.

Fig. 38 shows a schematic diagram of the flow possibilities on the upper surface. If the flow does not separate or the separation bubble reattaches upstream the trailing edge (Fig. 38A), then the flow will represent that of a trailing edge separating two air streams of different Mach numbers and boundary layer thicknesses.

If the separation bubble extends over the base and reattaches downstream the trailing edge, then the local pressure in the bubble at the base corresponds to either subsonic or supersonic speeds of the external flow at the same streamwise position as that of the base (Fig. 38B and Fig. 38C). The bubble cannot support any abrupt pressure change. The pressure rise along the bubble, which depends on the mixing rate and the bubble depth, must be gradual and usually small. Thus, it is expected that when the bubble reattaches downstream of the trailing edge, there will not be a large difference between the value of P_∞ and P_b.

---

* Pearcey[104] showed that a shock wave with a pressure rise ratio of 1.4 was needed to separate the turbulent boundary layer.

** See Plate 3.

Having discussed the possibilities of the flow pattern on the upper surface and examining the Mach number distribution on the model, the base pressure results are analysed as follows.

The general increase in the base pressure as the angle of incidence is increased is thought to be because the adverse pressure gradient on the upper surface will increase the boundary layer thickness there thus reducing the entrainment of the succeeding free shear layers. The base pressure remains relatively high as long as there is a separation on the upper surface and the bubble reattaches downstream of the trailing edge.

As the separation ceases, usually at high value of $M_{e\infty}$, the flow on the upper surface is attached and supersonic just ahead of the trailing edge and there is a sharp fall in P_b/P_∞ similar to the case of zero angle of incidence.

Therefore, the existence of the separation bubble explains the reason behind the increase in the value of $M_{e\infty}$ at which P_b/P_∞ starts to fall sharply when the angle of incidence is increased. The dotted lines in Fig. 35 correspond to the $M_{e\infty}$ values at which the flow separation on the upper surface cease. Table 5 gives the values of P_b/P_∞ and the values of M_{e1} on both surfaces for $M_{e\infty}$ = 0.6, 1.0 and 1.3 at different angles of incidence.

5.3.4 Effect of Boundary Layer Thickness Ahead of the Trailing Edge

The boundary layer ahead of the trailing edge at zero angle of incidence was measured at 0.4" from the trailing edge where the pressure gradient in the streamwise direction was very small (see

Fig. 30). Therefore the flow streamlines were assumed to be parallel to the model surface and the static pressure across the boundary layer was constant and equal to the pressure recorded by the surface tapping at that point.

Table 6 gives the boundary layer thicknesses and P_b/P_∞ for $M_{e\infty}$ = 0.6, 1.0 and 1.3 and for the two sets of transition wires used.

It is seen that for each set of transition wires, the boundary layer thickness is reduced as $M_{e\infty}$ is increased.

It can also be seen that for any value of $M_{e\infty}$ the effect of increasing the wire diameter is to increase the boundary layer thickness. This effect diminishes as $M_{e\infty}$ becomes supersonic.

Fig. 39A shows the results of the variation of P_b/P_∞ with $M_{e\infty}$ for the two sets of wires at zero angle of incidence.

It is seen that the effect of increasing the wire size is to increase the base pressure due to the increase in the boundary layer thickness. This is consistent with the previous discussion in Section 5.3.2. As $M_{e\infty}$ becomes supersonic, the effect of the wire size on the base pressure diminishes and eventually it disappears when P_b/P_∞ reaches its minimum value. This is partly because at supersonic speeds, the effect of the wire size on the boundary layer thickness has been reduced. But the total independence of P_b/P_∞ on the wire size when the minimum value of P_b/P_∞ is reached seems to suggest that at this value the effect of the boundary layer on the base pressure becomes secondary and some other flow mechanism dominates the base pressure value (see the discussion on the reason for the existence of a minimum value of P_b/P_∞ in Section 5.3.2).

Fig. 39B, Fig. 39C and Fig. 39D show the variation of P_b/P_∞ with $M_{e\infty}$ for the two sets of wires for $\alpha = 2^0$, 4^0 and 6^0 respectively. The boundary layer thicknesses at these angles were not measured. It is seen that for these angles of incidence, the base pressure is independent of the size of the transition wire.

5.3.5 Effect of Base Bleed

Fig. 40 shows the results of the effect of the base bleed on the base pressure for different values of $M_{e\infty}$ at zero angle of incidence. Fig. 41 shows the effect of base bleed on the base pressure for $M_{e\infty}$ = 0.6, 1.0 and 1.3 and for different angles of incidence. The general trend of these results is that as the rate of base bleed is increased, the base pressure is increased until the base pressure reaches an optimum value, $(P_b/P_\infty)_{opt}$. Thereafter, the base pressure decreases with further increase in base bleed.

The reason for the behaviour of the base pressure with base bleed in the above manner will be discussed later in Section 5.4.3(ii).

5.4 Flow Around the Trailing Edge at Zero Angle of Incidence

5.4.1 Flow Approaching the Trailing Edge

The boundary layer of the flow approaching the trailing edge was measured in the way mentioned in Section 5.3.4 at 0.4" upstream of the trailing edge. Fig. 42 shows the boundary layer velocity profile for $M_{e\infty}$ = 0.6, 1.0 and 1.3.

It is seen that the flow is turbulent and the results fit very

well with the 1/7th power law velocity profile.

5.4.2 Flow Expansion at the Trailing Edge

To measure the velocity profile of the flow at the corner is difficult. This is because as the expansion process starts ahead of the corner, there will be a transverse pressure gradient across the boundary layer at the corner. This is particularly true for high speeds where the flow just ahead of the corner reaches the sonic speed giving rise to expansion waves there. Therefore, the pitot measurements are not sufficient to give the velocity profile. However, at $M_{e\infty}$ = 0.6, the difference between the upstream pressure and the base pressure was small thus the pressure across the boundary layer at the corner was assumed to be constant and equal to the base pressure.

Fig. 43 shows the boundary layer velocity profile at the corner for $M_{e\infty}$ = .6 which fits very well with the 1/11th power law profile.

For comparison, the boundary layer velocity profile of the flow approaching the trailing edge is included in the figure. It is seen that even for a relatively low value of free stream Mach number, $M_{e\infty}$ = 0.6, and a relatively high value of base pressure ratio, P_b/P_∞ = .91, the effect of the corner expansion on the boundary layer velocity profile is large.

5.4.3 Axial Pressure and Mach Number Distributions Along the Centreline

The pitot static tube was used for the measurement of the distributions of the axial pressure and the Mach number along the centreline of the model in the wake.

5.4.3(i) Without Base Bleed

Fig. 44 shows the $P_{\mathbb{C}}$ and $M_{\mathbb{C}}$ distributions for $M_{e\infty}$ = 1.0 which is a typical result. The reattachment point is the point where the measured total and static pressures are equal. The definition of this point is located in the figure. The above results show that $M_{\mathbb{C}}$ is closely zero along the entire length of the dead-air region. Because of the flow circulation in the dead-air region, $M_{\mathbb{C}}$ will be negative in this region. The probe with the pitot head facing the flow cannot measure the negative $M_{\mathbb{C}}$.

Since the interest lies mainly in the $P_{\mathbb{C}}$ distribution and the value of the reattachment pressure, an assumed $M_{\mathbb{C}}$ distribution of zero in the dead-air region, is considered valid for the present investigations. Fig. 45 shows the $P_{\mathbb{C}}$ distributions for $M_{e\infty}$ = 0.6, 0.75, 0.9, 1.0 and 1.3. The reattachment points are shown on these distributions.

It is seen from these results that the pressure remains almost constant and equal to the base pressure for a distance of about x/2h = 2/3. Thereafter, the pressure starts to rise rapidly and the flow reattaches in a region where the pressure is still rising. There is an appreciable pressure to be recovered by the flow between the reattachment point and far downstream. Eventually, the rate of the pressure rise becomes smaller and the flow, presumably, will recover to the free stream conditions for downstream.

In all theories which are based on the Chapman-Korst model*, the assumption is made that the pressure remains constant for the whole length of

---

* See Section 3.1

the shear layer and that the recompression to the reattachment point occurs in a very short distance so that it can be considered isentropic.

The above results show that this is not the case. The recompression process is starting at an appreciable distance before the reattachment point thus this process cannot be considered isentropic particularly when the flow is turbulent.

Table 7 gives the present and some previous results for the reattachment pressure, P_r.

5.4.3(ii) With Bleed

The results in Section 5.3.5 have shown that the base pressure varies with the rate of base bleed in a certain manner. Fig. 46 shows a typical result which is for $M_{e\infty} = 1.3$.

To try to explain the behaviour of the base pressure with the base bleed, the P_{ℓ} and M_{ℓ} distributions for $M_{e\infty} = 1.3$ were measured for four different rates of base bleed that correspond to points A, B, C and D in Fig. 46.

Fig. 47 shows these results which can be explained by the following argument.

Fig. 47A (Plate 2A). No base bleed.

The free shear layer which is formed by the main flow will entrain air from the dead-air region. The mass in this region must be conserved therefore a recompression is needed to retard and eventually reverse

all the entrained air back to the region. This means that P_b is less than P_∞. Obviously, as the entrained mass is decreased, P_b/P_∞ will increase. Note here that the dividing streamline is the same as the reattachment streamline.

Fig. 47B, C (Plate 2B). P_b/P_∞ increases as the rate of base bleed increases.

The air injected into the base region will be opposed by the adverse pressure gradient in the recompression region. The adverse pressure force is greater than the momentum of the injected air therefore this air will be brought to rest before reaching the reattachment point.

Since the injected air must leave the dead-air region, it will be entrained by the main free shear layer. This means that less air is now needed to be reversed back to the dead-air region therefore, P_b/P_∞ will rise.

Note here that the dividing streamline is not the same as the reattachment point and the difference between the two streamlines will be proportional to the rate of the mass of the injected air.

Fig. 47D (Plate 2C) P_b/P_∞ decreases as the rate of base bleed increases.

The momentum of the injected air has now overcome the adverse pressure force thus some of the injected air

will 'escape' from the dead-air region and will not be entrained by the free shear layer.

P_b/P_∞ will now decrease for two reasons. Firstly, there will be less air 'trapped' in the dead-air region to be used by the main flow free shear layer. Secondly, there will now be four shear layers because of the two small dead-air regions which are formed between the injected air boundaries and the main flow free shear layers. Air will be entrained by these free shear layers and a recompression is needed to conserve the mass in the small dead-air regions.

From the above discussion it can be argued that $(P_b/P_\infty)_{opt}$ is directly dependent on the bleed momentum and not on the bleed mass. Therefore, it is expected that for any value of $M_{e\infty}$, the effect of increasing the slot height will be to increase the values of $(P_b/P_\infty)_{opt}$ and $(C_{qb})_{opt}$. This is because, for the same rate of bleed mass, the momentum of the bleed will now be less than that of the same base with smaller slot height. In addition, the increase in the slot height will reduce the height of the two small dead-air regions and less air will be entrained by shear layers of these regions giving rise to even higher values of $(P_b/P_\infty)_{opt}$.

As the ratio of the slot height to the base height tends to one, the value of $(P_b/P_\infty)_{opt}$ tends to one. Then, the base drag will be zero.

5.4.4 Free Shear Layer Development Without Base Bleed

Fig. 48A shows the results of the free shear layer velocity profile from the separation point up to the reattachment position for $M_{e\infty}$ = 0.6. Table 8 gives the free shear layer parameters. It is seen from these results that the shear layer velocity profile at the end of the constant pressure region is still developing and has not reached the similarity state. This is in contrast to all base pressure theories in which the free shear layer profile is assumed to be similar and can be approximated by the error function profile (see Section 3.1).

Similar results were obtained for $M_{e\infty}$ = 1.0 and 1.3. Fig. 48B shows the shear layer velocity profile at the end of the constant pressure region for these Mach numbers.

Previous experimental results[43] have shown that the error function profile is a good approximation to the free shear layer velocity profile when the value of θ_1/h is small. But, the present results suggest that when θ_1/h is relatively large*, the error function profile does not represent the shear layer velocity profile even at the end of the constant pressure region.

5.5 The Wake Traverse

The wake profile was measured at a distance of 2.5" (x/2h = 8.33) from the trailing edge for different values of $M_{e\infty}$ and α.

Fig. 49 shows the measured wake profile at α = 0 for $M_{e\infty}$ = 0.6,

---

* See Table 6 for the values of θ_1.

1.0 and 1.3 without base bleed and with optimum base bleed.

These results show that the flow has a relatively large boundary layer near the wall. Schlieren photographs(Plate 4) have shown that this is caused by the mixing of the air leaving the plenum chamber through the slots with the main flow. Similar results were obtained for the case of $\alpha = 2^{o}$ and 6^{o} (Fig. 50 and Fig. 51 respectively). Because of the interference of the air leaving the plenum chamber with the main flow, the exact shape of the wake profile without this interference and the exact value of the total drap coefficient, C_D, will not be known. However, it is thought that qualitative values of the total drag and the drag components can be obtained if the measured wake profile is approximated.

The approximation is done by assuming that the total and static pressures remain constant between the wall and the point where the flow from the plenum chamber is thought to start interferring with the main flow (the dotted lines in Figs. 49, 50 and 51). The approximate value of C_D is calculated using the analysis given in Appendix 2.

The skin friction drag coefficient, C_{Df}, is calculated using the analysis of Ref. 97.

The pressure drag coefficient, arising from the pressure distribution on the upper and lower surfaces of the model, can be divided into two parts.

$$C_{DP} = (C_{DP})_{nose} + (C_{DP})_{body}$$

where $(C_{DP})_{nose}$ = Value of C_{DP} between the leading edge and the point of maximum thickness.

$(C_{CP})_{body}$ = value of C_{DP} between the maximum thickness and the trailing edge.

Because of the absence of any pressure tappings in the nose of the model, the values of $(C_{CP})_{nose}$ cannot be calculated and can only be estimated from the results. Therefore:-

$$C_{DP} = C_D - (C_{DB} + C_{Df})$$

$$(C_{DP})_{nose} = C_D - \left[C_{DB} + C_{Df} + (C_{DP})_{body}\right]$$

where $C_{DB} = - C_{PB}$ and $(C_{DP})_{body}$ is calculated using the measured pressure distributions.

Table 9 gives the results of the drag components. It is seen that at $\alpha = 0$, the base drag constitutes a major part of the total drag (see the value of C_{DB}/C_D). For any specific $M_{e\infty}$, as α is increased, C_{DB} is reduced while C_{DP} is increased. Thus the value of C_{DB}/C_D becomes less.

The effect of base bleed on C_{Df} and C_{DP} is negligible. This is because the change in the surface pressure distribution was found to be small and confined to a small distance ahead of the base, $x/2h < 1.0$. Thus, the effect of the base bleed is to reduce the total drag by reducing the base drag only.

The wave drag, C_{DW}, is the drag component which is directly related to the loss in the stagnation pressure when the flow passes through the trailing shock.

An attempt is made to calculate C_{DW} but because of the uncertainty

of the measured wake profile shape near the slotted wall, the calculation is performed for the case of zero incidence only with and without base bleed. Table 9 gives these values of C_{DW}.

It can be seen that with optimum base bleed, C_{DW} is reduced by almost 50%. The reduction in C_{DW} with base bleed is expected since the effect of base bleed is to reduce the strength of the trailing shock by increasing P_b/P_∞.

CHAPTER SIX

CORRELATIONS AND COMPARISON OF THEORY WITH EXPERIMENTAL RESULTS

6.1 Correlations

6.1.1 Reattachment Correlations at Zero Angle of Incidence

Fig. 52 shows the results of the variation of M_{er} with M_{e2} (see Table 7). Results of M_{er} with base bleed are also included in the figure (see Fig. 47). It is seen that M_{er} is a function of M_{e2} only and not as has been suggested by previous correlations* that M_{er} is a function of M_{e2} and $M_{e\infty}$.

These results give a reattachment correlation valid for $M_{e2} \leq 4.36$ as

$$M_{er} = 0.86\, M_{e2} \tag{6.1}$$

At supersonic speeds, theory assumes that the distance L of the reattachment point is a function of the Prandtl-Meyer angle (see Eqn. 3.15). Experimental evidence suggests that this distance is a function of the boundary layer thickness as well.

Fig. 53 shows the results of the effect of the boundary -layer thickness on the location of the reattachment point. A correlation is given for this location which is :-

---

* See Section 2.3.

$$\sin\beta - \sin(\nu_2-\nu_\infty) = 2.26\left(\frac{\theta_2}{h}\right) - 13.75\left(\frac{\theta_2}{h}\right)^2 + 41.67\left(\frac{\theta_2}{h}\right)^3 \quad (6.2)$$

where β = angle formed by taking a straight line between the corner and the reattachment point

and θ_2 = boundary layer momentum thickness after expansion calculated by Eqn. 2.5

6.1.2 Correlations for Base Pressure with Base Bleed

The results of Section 5.3.5 are replotted. Fig. 54 shows the variation of $(P_b/P_\infty)_{opt}$ with P_b/P_∞ for different values of α, $M_{e\infty}$ and transition wires. The results suggest that $(P_b/P_\infty)_{opt}$ is a function of P_b/P_∞ only and the angle of incidence possibly having a weak effect. A correlation is obtained as:-

$$\left(\frac{P_b}{P_\infty}\right)_{opt} = -1.03\left(\frac{P_b}{P_\infty}\right)^3 + 2.3\left(\frac{P_b}{P_\infty}\right)^2 - 1.03\left(\frac{P_b}{P_\infty}\right) + 0.77 \quad (6.3)$$

The value of $(C_{qb})_{opt}$ is difficult to evaluate. This is because the curves that represent the variation of base pressure with base bleed are fairly flat near this value. But, the results suggest

that $(C_{qb})_{opt}$ decreases with increasing $M_{e\infty}$.

At zero angle of incidence, a straight line is assumed to represent the variation of $(C_{qb})_{opt}$ with $M_{e\infty}$. The straight line which gives the best fit to the experimental results in the range of $0.6 \leqslant M_{e\infty} \leqslant 1.3$ is defined by the equation (see Fig. 55).

$$(C_{qb})_{opt} = 0.113 - 0.096 \quad (M_{e\infty} - 0.6) \tag{6.3}$$

Fig. 56 shows the correlation of the effect of the base bleed on the base pressure up to the optimum conditions at zero angle of incidence which is:-

$$\left[\left(\frac{P_b}{P_\infty}\right)_{\dot{m}_b} - \frac{P_b}{P_\infty}\right] = \left[\left(\frac{P_b}{P_\infty}\right)_{opt} - \frac{P_b}{P_\infty}\right] \left[\sin\left(\frac{\pi}{2} \cdot \frac{\dot{m}_b}{(\dot{m}_b)_{opt}}\right)\right] \tag{6.4}$$

where $(\dot{m}_b)_{opt}$ is calculated using eqn. 6.3. It must be emphasised that all correlations for base pressure with base bleed are valid only when the ratio of the slot height to the trailing edge height is equal to 1/3.

6.1.3 Semi-empirical Relation for the Limit Base Pressure

A semi-empirical relation for the base pressure of a flow with zero boundary layer thickness at separation is obtained as follows.

Consider the flow expanding around the corner of a backstep to form the dead-air region SRA (Fig. 57).

PQ represents the position where the pressure starts to rise.

Following the analysis given by Childs et al[98] for the reattachment of the ramp caused separation where the momentum and continuity equations are applied to the control volume PQR, the following relation is obtained:-

$$\frac{P_r}{P_b} = 1 + \frac{2\gamma M_{e2}^2}{\sigma \tan(\nu_2 - \nu_\infty)} \left[\frac{1}{\Delta L} \int_{L1}^{L} \frac{\tau_D \sigma}{\rho_{e2} U_{e2}^2} dx + \frac{L1}{\Delta L} I_2 + (L1/\Delta L)^2 \cdot \frac{I_1^2}{(1-C_{e2}^2)\left[\sigma \tan(\nu_2 - \nu_\infty) - \frac{L1}{\Delta L} \cdot \frac{\phi_D}{0.564}\right]} \right] \quad (6.5)$$

where $\phi = (1 + \text{erf } \eta)$

$\eta = \sigma y/x$

$L = h/\sin(\nu_2 - \nu_\infty)$

$\Delta L = L - L1$

$$I_1 = (1 - C_{e2}^2) \int_{-\infty}^{\eta_D} \frac{\phi}{1 - C_{e2}^2 \phi^2} d\eta$$

$$I_2 = (1 - C_{e2}^2) \int_{-\infty}^{\eta_D} \frac{\phi^2}{1 - C_{e2}^2 \phi^2} d\eta$$

τ_D = Shear stress at the dividing streamline.

Assuming τ_D to vary lineary with x between L1 and L, then (see Appendix 3),

$$\int_{L1}^{L} \tau_D \, dx = \frac{\tau_{1D}}{2} (L-L1) = \frac{\Delta L}{2} \cdot \frac{\rho e_2 U_{e2}^2}{\sigma} I_2$$

where τ_{1D} = the dividing streamline shear stress at the end of the constant pressure region. For any value of M_{e2}, η_D and ϕ_D are given by eqn. 3.7 and eqn. 3.5 respectively.

Since,

$$\frac{P_r}{P_b} = \left(\frac{1 + \frac{\gamma-1}{2} M^2_{e2}}{1 + \frac{\gamma-1}{2} M^2_{er}} \right)^{\frac{\gamma}{\gamma-1}},$$

and $\nu = f(M_e)$

then eqn. 6.5 can be solved for $M_{e2}/M_{e\infty}$ (or P_b/P_∞) for any value of M_{e2} once M_{er} and ΔL are specified.

From experimental results,

$$M_{er} = 0.86 \, M_{e2}$$

and

$$L1 = \frac{4h}{3 \cos (\nu_2 - \nu_\infty)}$$

Fig. 58 shows the solution of eqn. 6.5 using the experimental results. This solution can be approximated by the polynomial

$$(-C_{PB})_{LIM} = 3.77 - 4.43\ M_{e\infty} + 1.89\ M_{e\infty}^{2} - 0.27\ M_{e\infty}^{3} \qquad (6.6)$$

For comparison, other relations for the limit base pressure are plotted in the same Figure. It can be seen that some of the experimental results with finite boundary layer thickness give lower values of C_{PB} than the values of $(C_{PB})_{LIM}$ calculated by either Korst's theory or Nash's relation which is obviously in contrast to the definition of $(C_{PB})_{LIM}$.

The present method gives values of $(C_{PB})_{LIM}$ which are lower than all the available experimental results of C_{PB} with finite boundary layer thickness. Some of the experimental results, which are interpolated to $\theta_1/h = 0$, are found to give values of $(C_{PB})_{LIM}$ equal to those which are calculated by the present method.

6.2 Comparison of Theory with Experimental Results

6.2.1 Boundary Layer Velocity Profile Just After Separation

The boundary layer velocity profile is calculated using the theoretical analysis of Section 2.1 together with the assumption that the boundary layer just before separation has a 1/7th power law profile.

Fig. 59 shows the theoretical boundary layer velocity profile just after expansion for $M_{e\infty} = 0.6$, 1.0 and 1.3.

It is seen that all these profiles show a great distortion from that of the 1/7th power law. At $M_{e\infty}$ = 0.6, the theoretical profile is in good agreement with the 1/11th power law while at $M_{e\infty}$ = 1.0 and 1.3, the 1/17th power law profile is a good fit to the theoretical profiles at these speeds.

The only available experimental result is for $M_{e\infty}$ = 0.6 which is in good agreement with the 1/11th power law profile (see Section 5.4.2). This means that the theoretical analysis gives a good agreement to the experimental results and the boundary layer velocity profile just after expansion can be calculated by the simple stream-tube method.

6.2.2 Free Shear Layer Velocity Profile

The free shear layer velocity profiles at the end of the constant pressure region are compared with the calculated profiles using the theoretical analysis (See Section 2.2).

Fig. 60 shows this comparison for $M_{e\infty}$ = 1.3. It is seen that the modified Kubotas's method gives a very poor agreement with the experimental results. This is thought to be mainly due to the poor assumption in this method that the turbulent boundary layer just after separation has a quadratic profile.

The modified Nash method, in which the boundary layer just after separation is assumed to have a 1/mth power law velocity -profile*, gives a better agreement with the results.

---

* This is a more realistic assumption than that of Kubota.

The agreement seems to improve as the value of m is increased from 7 to 17.

At $M_{e\infty}$ = 1.3, the stream-tube method gives m = 17 (see section 6.2.1). The figure shows that there is a good agreement between the theory, with m = 17, and the experimental results.

At $M_{e\infty}$ = 0.6 and 1.0, the stream-tube method gives m = 11 and 17 respectively.

Fig. 61 and Fig. 62 show a comparison between the theory and the experimental results for $M_{e\infty}$ = 1.0 and 0.6 respectively.

Again, there is a good agreement between the theory, with m = 11 and 17, with the experimental results for $M_{e\infty}$ = 0.6 and 1.0 respectively.

6.2.3 Base Pressure at Zero Angle of Incidence and Without Base Bleed

Fig. 63 and Fig. 64 show the comparison of the experimental results of P_b/P_∞ for $M_{e\infty}$ = 1.0 and 1.3 with the theoretical values using Korst and Nash theories. These theories were discussed in Chapter three.

In the theory of Korst, the effect of the boundary layer thickness is not included in the analysis and the base pressure is assumed to be a function of $M_{e\infty}$ only. While the theory of Nash includes this effect.

It is seen that both theories over-estimate the base pressure. Korst's theory underestimates the base drag for $M_{e\infty}$ = 1.3 and 1.0 by 19.4% and 40% respectively while Nash's theory gives a corresponding underestimation in base drag of 6.8% and 16.6%.

CHAPTER SEVEN

CONCLUSIONS AND PROPOSALS FOR FUTURE WORK

7.1 Conclusions

With turbulent flow over a symmetrical blunt trailing edge aerofoil in the transonic range, $0.6 \leqslant M_{e\infty} \leqslant 1.3$, the following conclusions can be drawn from the results of Chapters 5 and 6.

1) The base pressure is independent of the chord Reynolds number in the range of $2.9 \times 10^6 \leqslant R_e \leqslant 5.0 \times 10^6$.

2) At zero incidence, the effect of increasing $M_{e\infty}$ on the base pressure ratio, P_b/P_∞, is as follows: Initially P_b/P_∞ decreases slowly. As the local Mach number, $\bar{M}_{e1}$, just ahead of the separation point becomes supersonic, P_b/P_∞ decreases sharply and continues to do so until it reaches a minimum value when $\bar{M}_{e1}$ is approximately equal to 1.42. Thereafter, P_b/P_∞ increases with further increase in $M_{e\infty}$.

3) The effect of $M_{e\infty}$ on P_b/P_∞ with the angle of incidence in the range $2^o \leqslant \alpha \leqslant 6^o$ is qualitatively similar to that at zero incidence.

Generally for the same free stream conditions, the effect

of increasing α is to increase P_b/P_∞ when the flow is attached on both surfaces just ahead of the trailing edge.

When the flow separates on the suction surface and reattaches downstream of the base, the base pressure remains relatively low and decreases very slowly with increasing $M_{e\infty}$. This also has the effect of delaying the value of $M_{e\infty}$ at which P_b/P_∞ starts to drop sharply from $M_{e\infty} = .82$ at $\alpha = 0$ to $M_{e\infty} = 1.0$ at $\alpha = 6^0$.

4) At zero incidence, for the same free stream conditions, the effect of increasing the transition wire diameter is to increase P_b/P_∞. However, the rate of this increase in P_b/P_∞ diminishes with increasing $M_{e\infty}$ and eventually ceases when the minimum value of P_b/P_∞ is reached. Over the range, $2^0 \leqslant \alpha \leqslant 6^0$, there is very little effect of the size of the transition wires on P_b/P_∞.

5) At any angle of incidence and free stream conditions, the effect of increasing the base bleed rate on the base pressure is as follows: Initially, the base pressure increases rapidly. The rate of this increase diminishes until an optimum base pressure ratio, $(P_b/P_\infty)_{opt}$, is reached. Thereafter, the base pressure decreases with further increase in base bleed rate.

6) It has been found that $(P_b/P_\infty)_{opt}$ is a function of the base pressure ratio without base bleed, P_b/P_∞, (see eqn. 6.3).
It is expected that for the same free stream conditions and angle of incidence, $(P_b/P_\infty)_{opt}$ will increase when the ratio of the slot height to the base height is increased.

7) At zero incidence, the following conclusions are drawn on the behaviour of the flow in the base region:

a) The expansion process around the base starts ahead of the corner. The boundary layer profile is distorted from that of the 1/7th power law before expansion to that of a power law with a higher exponent value just after expansion.
A simple method, based on the stream-tube analysis, can be used to calculate the boundary layer profile just after expansion if the base pressure ratio is known.

b) For a flow with a relatively thick boundary layer before separation, the free shear layer velocity profile does not reach the similarity state even at the end of the constant pressure region. Thus, the error function velocity profile is not a good representation of the real velocity profile.

Instead, the velocity profile can be calculated to a reasonable approximation using Nash's modified method. This method is modified by taking the initial boundary layer profile to be of that of a power law of index 1/m, where m ≥ 7 and by taking into account the compressibility effect.
Using the above method, with m calculated by the stream-tube method, is found to give a good fit to the experimental results.

c) The constant pressure region ends at a distance approximately equal to x/2h = 2/3, from the base. The recompression process starts at an appreciable distance before the reattachment point which suggests that the recompression process cannot be considered isentropic.
The flow reattaches at a point where the pressure is still rising and there is an appreciable pressure to be recovered downstream of the reattachment point.
The reattachment pressure is found to be a function of the base pressure only, (see eqn. 6.1).

d) At supersonic speeds, the distance of the reattachment point is found to be a function

of the boundary layer thickness as well as the Prandtl-Meyer angles, (see eqn. 6.2).

From the above conclusions, it can be seen that most of the assumptions made in the theories for steady base pressures are invalid.

8) The theory under-estimates the base drag. Because of the absence of more reliable theories, Nash's theory can be used to give approximate results.

9) The wake profile is difficult to measure because of the interference of the air from the plenum chambers with the main flow.

However, when the measured wake profile is approximated, it is found that the base drag constitutes a major part of the total drag and the effect of the base bleed is to reduce the total drag by reducing the base drag only.

7.2 Proposals for Future Work

i) Since the model used for the present experiment had a rectangular base, it will be of great practical interest to compare the present results of base pressure and surface pressure distribution near the base with those of similar models having round bases with different radiuses of curvature.

ii) There is an appreciable pressure rise downstream of the reattachment point. The parameters

affecting this pressure rise are not known. Previous work[52,55] had suggested that this pressure rise is needed to rehabilitate the reattaching boundary layer. Therefore, an experimental investigation on the behaviour of the reattaching boundary layer with pressure rise downstream of the reattaching point is needed to verify this.

iii) In the discussion, see 5.4.3 (ii), it is argued that the optimum base pressure with base bleed is expected to increase as the ratio of the slot height to the base height is increased. Experimental evidence is needed to support this.

It will be interesting to compare the effect of injecting air through a base with one slot to that with a number of holes having a total area equal to the slot area thereby altering the total amount of entrainment.

iv) In view of the invalidity of most of the assumptions made in the theory, a new theoretical approach is needed.

REFERENCES

1. Hoerner S.F. — Base drag and thick trailing edge. J. Aero. Sci., Vol. 17, pp.622-628, (1950).

2. Hoerner S.F. — Fluid dynamic drag. Published by the author, (1958).

3. Roshko A. — On the drag and shedding frequency of 2-dimensional bluff bodies. NACA TN-3169, (1954).

4. Roshko A. — On the wake and drag of bluff bodies. J. Aero. Sci., Vol. 22, p.124, (1955).

5. Bearman P.W. — Investigation of the flow behind a 2-dimensional model with a blunt trailing edge. J.F.M., Vol. 21, pp. 241-255, (1965).

6. Nash J.F. Quincey V.G. and Callinan J. — Experiments on 2-dimensional base flow at subsonic and transonic speeds. ARC R&M 3427, (1966).

7. Chapman D.R. Kuehn D.M. and Larson H.K. — Investigation of separated flows in supersonic and subsonic streams with emphasis on the effect of transion. NACA TN 3869 (1957).

8. Arie M. and Rouse H. — Experiments on 2-dimensional flow over a normal wall. J.F.M., Vol. 1, Part 2, p.129, (1956).

9. Tanner M. — The wake pressure behind wedges as influenced by splitter plates and suction. AGARD CP.4, pp. 887-909, (1966).

10. Tanner M. — Experimental investigations of the drag of wings with a blunt trailing edge at transonic speeds. AGARD CP.83, pp. 8-1 to 8-6, (1971).

11. Saltzman E.J. — Base pressure coefficients obtained from the X-15 airplane for Mach numbers up to 6. NASA TN-D-2420, (1964).

12. Morrow J.D. and Katz E. — Flight investigation at Mach numbers from 0.6 to 1.7 to determine drag and base pressures at a blunt trailing edge aerofoil and drag of diamond and circular arc aerofoils at zero lift. NACA TN-3548, (1955).

13. Rogers E.W.E., Berry C.J. and Quincey V.G. — Test at transonic speeds on wings with wedge sections and sweep varying between 0 to 60°. ARC R&M 3348 (1963).

14. Pollock N. — Some effects of base geometry on a 2-dimensional base drag at subsonic and transonic speeds. Note ARL/Aero. 316, Aero. Res. Laboratories (Australia), (1969).

15. Charters A.C. and Turetsky R.A. — Determination of base pressure from free flight data. B.R.L. Report 653, (1948).

16. Faro T.D.V. — Experimental determination of base pressures at supersonic velocities. Bumblebee Series Report No. 106, (1949).

17. Chapman D.R. — An analysis of base pressure at supersonic velocities and comparison with experiment. NACA TN-2137, (1950).

18. Kurzweg H.H. — Interrelationship between boundary layer and base pressure. J. Aero. Sci., Vol. 18, pp. 743-748, (1951).

19. Crocco L. and Lees L. — A mixing theory in the interaction between dissipated flow and nearly isentropic streams. J. Aero. Sci., Vol. 19, pp. 649-676, (1952).

20. Bogdonoff S.M. — A preliminary study of a Reynolds number effects on base pressure at M = 2.95. J. Aero. Sci., Vol. 19, pp. 201-206, (1952).

21. Kavanau L.L. — Some base pressure results at intermediate Reynolds numbers with M = 2.84. J. Aero. Sci., Vol. 21, pp. 257-260, (1954).

22. Holder D.W. and Gadd G.E. — The interaction between shock waves and boundary layers and its relation to base pressure in supersonic flow. The international symposium on boundary layer effects in aerodynamics, N.P.L., pp. (8-1), to (8-65), (1955).

23. Van Hise V. — Investigation of variation in base pressure over the Reynolds number range in which wake transition occurs for 2-dimensional bodies at M from 1.95 to 2.92. NASA TN-D-167, (1959).

24. Beastall D. and Eggink H. — Some experiments on breakaway in supersonic flow. Part I, RAE Tech. Note, Aero. 2041, (1950). Part II, RAE Tech Note, Aero. 2061, (1950).

25. Hastings R.C. — Turbulent flow past 2-dimensional base in supersonic streams. ARC R&M 3401, (1965).

26. Chapman D.R., Wimbrow W.R. and Kester R.H. — Experimental investigation of base pressure on blunt trailing edge wings at supersonic velocities. NACA TN-2611, (1952).

27. Fuller L. and Reid J. — Experiments on 2-dimensional base flow at M = 2.4. ARC R&M 3064, (1956).

28. Coin K.L. — Effects of plan form aerofoil section and angle of attack on the pressures along the base of blunt trailing edge wing at M = 1.41, 1.62 and 1.96. NACA RML52D21, (1952).

29. Love E.S. — Base pressures at supersonic speeds on 2-dimensional aerofoils and on bodies of revolution with and without fins having turbulent boundary layer. NACA TN-3819, (1957).

30. Tanner M. — New investigations for reducing the base drag of wings with a blunt trailing edge. AGARD CP-124, pp. 12-1 to 12-9, (1973).

31. Badrinarayanau M.A. — An experimental investigation of base flows at supersonic speeds. J. of the Aeron. Society, Vol. 65, p. 475, (1961).

32. Ginoux J.J. — Effect of gas injection in separated supersonic flows. TCEA TN-7, (1962).

33. Sirieix M. — Pression de culot et processus de melange turbulent en ecoulement supersonique plan. Recherche Aeronaut No. 78, (1960).

34. Chapman. D.R. — Laminar mixing of a compressible fluid. NACA Report R-958.

35. Chapman D.R. — Theoretical analysis of heat transfer in regions of separated flow. NACA TN-3792, (1956).

36. Korst H.H. — A theory for base pressure in transonic and supersonic flow. J. of Applied Mechanics, Vol. 23, pp. 593-600, (1956).

37. Korst H.H., Page R.H. and Childs M.E. — Compressible 2-dimensional jet mixing at constant pressure. Univ. of Illinois, ME-TN-392-1, OSR-TN-54-82, Contract No. AF 18 (600). (Ref. 3 from NASA CR-419, (1966)).

38. Pai S.I. — Two-dimensional mixing of a compressible fluid. J. Aero. Sci., Vol. 16, pp. 463-469, (1949).

39. Grank J. — The mathematics of diffusion. Oxford University Press, (1957).

40. Tollmien W. — Calculation of turbulent expansion processes. NACA TM-1085, (1945).

41. Abramovich G.N. — The theory of free jet of a compressible gas. NACA TM-1058, (1944).

42. Gortler H. — See Ref. 96, pp. 104-106.

43. Crane L.J. — The laminar and turbulent mixing of jets of compressible fluid. Part II: The mixing of two semi-infinite streams. J.F.M., Vol. 3, p.81, (1957).

44. Prandtl L. — See Ref. 96, pp. 52-56.

45. Prandtl L. — See Ref. 96, pp. 103-104.

46. Gooderum P.B., Wood G.P. and Brevoort M.J. — Investigation with an interferometer of the turbulent mixing of free supersonic jet. NACA Rep. 963, (1950).

47. Johannesen N.H. — The mixing of free axially symmetrical jets of Mach No. 1.4. ARC R&M 3291, (1957).

48. Charwat A.F. and Yakura — An investigation of two-dimensional supersonic base pressure. J. Aero. Sci., Vol. 25, p.122, (1958).

49. Kirk F.N. — An approximate theory of base pressure in two-dimensional flow at supersonic speed. RAE. Tech. Note No. Aero. 2377, (1959).

50. Nash J.F. — An analysis of two-dimensional turbulent base flow including the effect of the approaching boundary layer. ARC R&M 3344, (1963).

51. Green J.E. — Two-dimensional turbulent reattachment as a boundary layer problem. AGARD CP-4, pp. 393-427, (1966).

52. McDonald H. — The turbulent supersonic base pressure problem: A comparison between theory and some experimental evidence. The Aeron. Quart., Vol. 17, pp. 105-126, (1966).

53. Cook J.C. — Separated supersonic flow. ARC 24935, (1963).

54. Nash J.F. — A discussion of two-dimensional turbulent base flows. ARC R&M 3468, (1967).

55. McDonald H. — Turbulent shear layer reattachment with special emphasis on the base pressure problem. Aero. Quart., Vol. 15, pp. 247-280, (1964).

56. Reshotko E. and Tucker M. — Effect of a discontinuity on turbulent boundary layer thickness parameters with application to shock-induced separation. NACA TN-3454, (1954).

57. Curle N. — Laminar boundary layer equations. Oxford University Press, (1962).

58. Lees L. and Reeves B. — Supersonic separated and reattaching laminar flows: I,General theory and application to adiabatic boundary layer/shock wave interactions. AIAA Journal, Vol. 2, pp. 1907-1920, (1964).

59. Reeves B. and Lees L. — Theory of laminar near wake of blunt bodies in hypersonic bodies. AIAA Journal, Vol. 3, pp. 2061-2074, (1965).

60. Alber I.E. and Lees L. — Integral theory for supersonic turbulent base flows. AIAA Journal, Vol. 6, pp. 1343-1351, (1968).

61. Stewartson K. — Further solutions of Falkner-Skan equations. Proc. Cambridge Phil. Soc., 50, pp. 454-465, (1954).

62. Kennedy E.D. — Wake like solutions of the laminar boundary layer equations. AIAA Journal, Vol. 2, pp. 225-231, (1964).

63. Roberts J.B. — On the prediction of base pressure in two-dimensional supersonic turbulent flow. ARC R&M 3434, (1966).

64. White R. — Effect of sudden expansions or compressions on the turbulent boundary layer. AIAA Journal, Vol. 4, pp. 2232-2233, (1966).

65. Weiss R.F. and Nelson W. — Upstream influence of base pressure. AIAA Journal, Vol. 6, pp. 466-471, (1968).

66. Ackerberg R.C. — Boundary layer separation at a free streamline. J.F.M., Vol. 44, p.211, (1970).

67. Weinbaum S. — Rapid expansion of a supersonic boundary layer and its application to near wake. AIAA Journal, Vol. 4, pp. 217-226, (1966).

68. Weiss R.F. and Weinbaum S. — Hypersonic boundary layer separation and the base flow problem. AIAA Journal, Vol. 4, p. 1321, (1966).

69. Hamma F.R. — Experimental studies on the lip shock. AIAA Journal, Vol. 5, pp. 51-56, (1967).

70. Dewey C.F. — The near wake of a blunt body at hypersonic speeds. AIAA Journal, Vol. 3, pp. 1001-1010, (1965).

71. Donaldson I.S. — On the separation of supersonic flow at a sharp corner. AIAA Journal, Vol. 5, pp. 1086-1088, (1967).

72. Weinbaum S. — On the singular points in the laminar two-dimensional near wake flow field. J.F.M., Vol. 33, pp. 39-63, (1968).

73. Denison M.R. and Baum E. — Compressible free shear layer with finite initial thickness. AIAA Journal, Vol. 1, pp. 342-249, (1963).

74. Kubota T. and Dewey C.F. — Momentum integral methods for the laminar free shear layer. AIAA Journal, Vol. 2, pp. 625-629, (1964).

75. Nash J.F. — The effect of an initial boundary layer on the development of a turbulent free shear layer. ARC CP-682, (1963).

76. Cheng S.I. — Flow aroud an isolated stagnation point in the near wake. AVCO Corp., Research and advanced development division TM-63-23, (see Ref. 94, pp. 233-236).

77. Gadd G.E., Holder D.W. and Regan J.D. — Base pressure in supersonic flow. ARC CP-271, (1955).

78. Page R.H., Kessler T.J. and Hill W.G., JR. — Reattachment of two-dimensional supersonic turbulent flow. ASME paper No. 67-FE-20, (1967).

79. Batham J.P. — Reattachment criterion for turbulent supersonic separated flows. AIAA Journal, Vol. 7, pp. 154-156, (1969).

80. Korst H.H. and Chow W.L. — Non-isentropic turbulent jet mixing between two compressible streams at constant pressure. NASA CP-419, (1966).

81. Tanner M. — A method for reducing the base drag of wings with blunt trailing edge. Aero. Auart., Vol. 23, pp. 15-23, (1972).

82. Camarata F.J. — A method for determining the effect of initial boundary layer on turbulent free shear layer velocity profiles. Transactions of ASME. J. of Basic Engineering, Vol. 93, pp. 713-715, (1971).

83. Gerhart P.M. and — Korst H.H. — On the free shear layer downstream of a backstep in supersonic flow. Transactions of ASME. J. of Fluid Eng., Vol. 95, pp. 361-366, (1973).

84. Malhotra J.P. — Transonic base flow past blunt trailing edge. M.Eng. thesis, Univ. of Liverpool, (1974).

85. Bansal F.C. — The development of a transonic liner for a 3" x 3" wind tunnel. M.Eng. thesis, Univ. of Liverpool, (1970).

86. Chow. W.L. — Recompression of a two-dimensional supersonic turbulent free shear layer. NASA CR 118331.

87. Gibbings J.C. and Sproston J.L. — The hydrograph method of aerofoil and cascade design for incompressible flow, Part 5: The symmetrical aerofoil with blunt base. Liverpool University report.

88. Gibbings J.C. — On boundary layer transition wires. ARC CR-462, (1959).

89. Tanner M. — The pressure at the reattachment point in subsonic two-dimensional steady base flow. Aero. Quart. Vol. XXVII Part 7, (1976). pp. 55-65.

90. Sutton E.P. — The development of slotted working section liners for transonic operation of RAE Bedford 3ft. wind tunnel. ARC R&M 3085.

91. Holder D.W., North R.J. and Chinneck A. — Experiments with static tubes in supersonic air streams. Parts I and II. ARC R&M 2782, (1953).

92. Bearman P.W. — Investigation into the effect of base bleed on the flow behind a two-dimensional model with a blunt trailing edge. AGARD CP-4, pp. 485-507, (1966).

93. Bearman P.W. — The effect of base bleed on the flow behind a two-dimensional model with a blunt trailing edge. Aero. Quart., Vol. 18, pp.207-214, (1967).

94. Berger S.A. — Laminar wakes. American Elsevier Publishing Co. Inc., New York, (1971).

95. — B.S. 1042: Part 1 (1964).

96. Abramovich G.N. — The theory of turbulent jets. Published by the Masschusetts Institute of Technology, (1963).

97. Reshotko E. and Tucker M. — Approximate calculation of the compressible turbulent boundary layer with heat transfer and arbitrary pressure gradient. NACA TN 4154, (1957).

98. Childs M.E., Paynter G.C. and Redeker E. — The prediction of separation and reattachment flow characteristics for two-dimensional supersonic and hypersonic turbulent boundary layer. AGARD CP-8/4 (1966), pp 325-352.

99. Tanner M. — Theoretical prediction of base pressure for steady base flow. Progress in Aero. Sci., Vol. 14, (1973), pp. 177-225.

100. Korst H.H. and Tripp W. — The pressure on a blunt trailing edge separating two supersonic two-dimensional air streams of different Mach numbers and stagnation pressures but identical stagnation temperatures. Proceedings of 5th Midwestern Conference on Fluid Mechanics, (1957), pp. 187-199.

101. Channapragada R.S. — Compressible jet spread parameter for mixing zone analysis. AIAA Journal, Vol. 1, (1963), pp. 2188-2190.

102. Mager A. — Transformation of the compressible turbulent boundary layer. J. Aero. Sci., Vol. 25, (1958), pp. 305-311.

103. Baur R.C. — Another estimate of the similarity parameter for turbulent mixing. AIAA Journal, Vol. 6, (1968), pp. 925-927.

104. Pearcey H.H. — Some effects of shock-induced separation of turbulent boundary layers in transonic flow past aerofoils. ARC R&M No. 3108, (1959).

105. Chapman A.J. and Korst H.H. — Free jet boundary with consideration of initial boundary layer. Proc. 2nd. U.S. National Congress of Applied Mechanics, Michigan, June, (1954).

106. Maydew R.C. and Reed J.F. — Turbulent mixing of compressible free jets, AIAA Journal, pp-1443-1444, (1963).

APPENDIX 1

RATE OF SPREAD OF THE FREE SHEAR LAYER

After the separation from a corner, the free shear layer will develop. When the shear layer reaches the similarity state, its velocity profile can be approximated by that of the error function profile where,

$$\phi = \tfrac{1}{2}(1+\mathrm{erf}\,\eta)$$

and $$\eta = \sigma y/x$$

σ is called the similarity parameter of the mixing region or the rate of spread of the shear layer. For incompressible flow the value of $\sigma_i = 12$ generally is used and this seems to be a good value for conditions which correspond to the mixing between a uniform stream and fluid at rest.

Various experiments* have shown that σ increases when the Mach number is increased. From a limited number of experiments, Korst and Tripp[100] suggested an empirical linear relationship,

$$\sigma/\sigma_i = 1 + 0.23\, M_{e2} \qquad (A1)$$

The relationship has been used by many theories for steady base pressure[36, 50] and by the present calculations.

McDonald[55] takes account of the experimental results obtained

* These experiments are quoted in Ref. 99.

in Ref.106 and develops the equation

$$\sigma/\sigma_i = (1 + \frac{\gamma-1}{2} M_{e2}^2)\ (1 + 0.035\ M_{e2}^2) \qquad (A2)$$

In a latter paper, McDonald[52] suggests a different relationship,

$$\sigma/\sigma_i = \left[(1 + \frac{\gamma-1}{2} M_{e2}^2)\ (1 + 0.035\ M_{e2}^2)\right] / (1 + 0.004\ M_{e2}^4) \qquad (A3)$$

In an analysis given by Channapragada[101] the shear stress is based on Prandtl's mixing length hypothesis. Using the Howarth transformation and following Mager[102] assumption that the shear stress is unaffected by the transformation, Channapragada develops the formula

$$\sigma/\sigma_i = \rho/\rho_{ref} \qquad (A4)$$

where ρ_{ref} is the density of some reference conditions. The final equation is

$$\sigma/\sigma_i = R_1\ (\ 1 + \frac{\beta_1}{Z}\ )^{-1} \qquad (A5)$$

where $Z = 1 + \frac{\gamma-1}{2} M_{e1}^2$

$$\beta_1 = \frac{\text{Total temperature of the fluid}}{\text{Total temperature in the dead-air region}}$$

R_1 = Divergence factor (a function of M_{e2}).

Alber and Lee's[60] uses eqn. A4 with ρ_{ref} taken as the density at the dead-air region. For adiabatic flow

$$\sigma/\sigma_i = \rho/\rho_{ref} = 1 + \frac{\gamma-1}{2} M_{e2}^2 \qquad (A6)$$

Further contributions to the effect of M_{e2} on σ have been given by Baur[103].

Experimental results have shown a great discrepancy and it is difficult to say which of the above semi-empirical methods gives the best agreement with the results.

There appear to be two major causes for the descrepancies in the results. The first cause may be attributed to the fact that in many measured cases the flow has not reached the similarity state because of the pressure of a relatively large boundary layer at separation. The second cause may be attributed to the use, by several experimentalists, of various velocity profile techniques in order to determine the spreading parameter.

APPENDIX 2

CALCULATION OF THE TOTAL DRAG

Fig. 65 shows the control volume ABCD which encloses the model.

Air enters the control volume through AB, where the flow is uniform everywhere. Air leaves the control volume through CD where the wake profile is measured. Air 'spilles' out through AC and AD with a velocity V.

MAS and MOM represents the base bleed mass and momentum rates respectively.

The continuity equation requires that

$$MAS + \int_B^A \rho_\infty u_\infty dy = \int_D^C \rho u dy + \int_{AC} 2\rho v dx \qquad (A7)$$

The momentum equation in the x-direction requires that

$$F_x = \left[MOM + \int_B^A \rho_\infty u_\infty^2 dy\right] - \left[\int_D^C \rho u^2 dy + \int_{AC} 2u_\infty \rho v dx\right] \qquad (A8)$$

where F_x represents the total force in the x-direction. Equations A7 and A8 give

$$F_x = MOM - (u_\infty . MAS) + \int_B^A \rho u(u_\infty - u) dy \qquad (A9)$$

But

$$F_x = D + \int_D^C P\,dy - \int_B^A P_\infty\,dy \qquad \text{(A10)}$$

where

D = Total drag

Equations (A9) and (A10) give

$$C_D = \frac{1}{\rho_\infty u_\infty{}^2 h}\left[\text{MOM} - (u_\infty.\text{MAS}) + \int_B^A \rho u(u_\infty - u)dy + \int_B^A (P_\infty - P)\,dy\right] \qquad \text{(A11)}$$

APPENDIX 3

CALCULATION OF SHEAR STRESS ALONG THE DIVIDING STREAMLINE IN THE CONSTANT PRESSURE REGION

Continuity equation

$$\frac{\partial}{\partial x}(\rho u) + \frac{\partial}{\partial y}(\rho v) = 0 \qquad \text{(A12)}$$

Momentum equation

$$\rho u \frac{\partial u}{\partial x} + \rho v \frac{\partial u}{\partial y} = -\frac{\partial P}{\partial x} + \frac{\partial \tau}{\partial y} \qquad \text{(A13)}$$

Since the pressure is constant, $\partial P/\partial x = 0$.

Integrate eqn. A13 from $-\infty$ to y_D and use eqn. A12 to obtain

$$\tau_{1D} = \int_{-\infty}^{y_D} \rho u \frac{\partial u}{\partial x}\, \partial y + \int_{-\infty}^{y_D} u \frac{\partial}{\partial x}(\rho u)\, dy$$

$$= \int_{-\infty}^{y_D} \frac{\partial}{\partial x}(\rho u^2)\, \partial y$$

$$= \frac{\partial}{\partial x}\left[\frac{x}{\sigma}(\rho_{e2}\, u_{e2}^2) \int_{-\infty}^{\eta_D} \frac{\rho u^2}{\rho_{e2} u_{e2}^2}\, d\eta \right]$$

$$= \frac{\rho_{e2}\, u_{e2}^2}{\sigma}\, I_2 \qquad \text{(A14)}$$

where

$$I_2 = \int_{-\infty}^{\eta_D} \frac{\rho u^2}{\rho_{e2}\, u_{e2}^2}\, d\eta = (1 - C_{e2}^2) \int_{-\infty}^{\eta_D} \frac{\phi^2}{1 - C_{e2}^2\, \phi^2}\, d\eta$$

APPENDIX 4

FORTRAN PROGRAM FOR THE CALCULATION OF THE FREE SHEAR LAYER PROFILE FOR A GIVEN VALUE OF m AND η_o (EQUATION 2.21)

```
C     TO START THE PROGRAM,INPUT P AND EN
C     P=m.POWER LAW EXPONENT FOR BOUNDARY LAYER PROFILE JUST AFTER
C     EXPANSION
C     EN=η0.(SEE TABLE 1)
C     EM2(JJ)=U/UE=VELOCITY RATIO OF THE FREE SHEAR LAYER
C     Y(JJ)=η. FUNCTION OF DISTANCE(Y) ACROSS THE FREE SHEAR LAYER
      DIMENSION H(200),H1(200),H2(200),H3(200),H4(200),H5(200),H6(200),X
     *(200),XX(200),EM1(200),EM2(200),Y(200),HH(200),X1(200),YY(200)
C     CALCULATION OF ERROR FUNCTION FOR ANY VALUE
      REAL L
      L=0,005
      X(97)=0.
      H(97)=0.
      DO 2 I=97,193
      H1(I)=2./(1,7728*EXP(X(I)**2.))
      H2(I)=-(2.*X(I)*H1(I))

      H3(I)=-(2.*X(I)*H2(I)+2.*H1(I))
      H4(I)=-(2.*X(I)*H3(I)+4.*H2(I))
      H5(I)=-(2.*X(I)*H4(I)+6.*H3(I))
      H6(I)=-(2.*X(I)*H5(I)+8.*H4(I))
      I1=I+1
      X(I1)=X(I)+L
      H(I1)=H(I)+L*H1(I)+(((L**2.)*H2(I))/2.)+(((L**3.)*H3(I))/6.)+(((L*
     **4.)*H4(I))/24.)+(((L**5.)*H5(I))/120.)+(((L**6.)*H6(I))/720.)
      IF (X(I1).LT.0,296) GOTO 2
      L=0,05
    2 CONTINUE
      L=-0,005
      D=ABS(L)
      H(1)=0.
      X(1)=0.
      DO 3 II=1,96
      H1(II)=2./(1,7728*EXP(ABS(X(II))**2.))
      H2(II)=-(2.*X(II)*H1(II))
      H3(II)=-(2.*X(II)*H2(II)+2.*H1(II))
      H4(II)=-(2.*X(II)*H3(II)+4.*H2(II))
      H5(II)=-(2.*X(II)*H4(II)+6.*H3(II))
      H6(II)=-(2.*X(II)*H5(II)+8.*H4(II))
      II1=II+1
      X(II1)=X(II)+L
      H(II1)=H(II)-D*H1(II)+(((D**2.)*H2(II))/2.)-(((D**3.)*H3(II))/6.)+
     +(((D**4.)*H4(II))/24.)-(((D**5.)*H5(II))/120.)+(((D**6.)*H6(II))/7
     +20.)
```

```
      IF (X(III),GT,-0,296) GOTO 3
      L=-0,05
      D=ABS(L)
    3 CONTINUE
      DO 4 II=1,97
      I=98-II
      HH(I)=H(II)
      X1(I)=X(II)
    4 CONTINUE
      DO 5 I=1,97
      H(I)=HH(I)
      X(I)=X1(I)
    5 CONTINUE
C       END OF ERROR FUNCTION CALCULATION
C
C       INPUT THE VALUES OF P,EN
    1 READ (5,100) P,EN
  100 FORMAT (2F10,6)
      WRITE (6,199)
  199 FORMAT (15H DISTANCE Y(JJ),15X,23H VELOCITY RATIO EM2(JJ))

C
C.      CALCULATION OF THE INTEGRAL TERM IN EQUATION 2,21
      N=EN*10,
      MM=(N+39)/2
      EM1(1)=0,
      XX(1)=0,
      DO 6 J=2,N
      XX(J)=XX(J-1)+0,1
    6 CONTINUE
      PP=XX(N)**(1,/P)
      Y(1)=-2,1
      EM2(1)=0,
      DO 24 JJ=2,MM
      Y(JJ)=Y(JJ-1)+0,2
      DO 7 J=2,N
      XY=ABS(XX(J)-Y(JJ))
      IF (XY,GT,10,) GOTO 9
      EM1(J)=(XX(J)**(1,/P))/(2,7183**(ABS(XX(J)-Y(JJ))**2,))
      GOTO 7
    9 EM1(J)=0,0
    7 CONTINUE
      EK1=0,
      N2=N-2
      DO 8 J=1,N2,2
      CALL AREA (EM1,XX,EK1,J)
    8 CONTINUE
      EK1=EK1/(SQRT(22,/7,)*PP)
C       END OF INTEGRAL TERM CALCULATION
CC
C       CALCULATION OF ERROR FUNCTION TERM IN EQUATION 2,21
      YY(JJ)=Y(JJ)-XX(N)
      IF (YY(JJ),GT,2,1) GOTO 14
```

```
      DO 10 I=1,193
      IF (YY(JJ).GT.X(I)) GOTO 10
      EH=H(I)
      GOTO 22
   10 CONTINUE
   14 EH=1.
   22 CONTINUE
C        END OF ERROR FUNCTION TERM CALCULATION
C
C        SUMMING UP THE TERMS OF EQUATION 2,21
         EM2(JJ)=(.5*(1.+EH))+EK1
C        PRINTING THE VALUES OF Y(JJ) AND EM2(JJ)
         WRITE (6,245) Y(JJ),EM2(JJ)
  245 FORMAT (F13.6,20X,F13.6)
      IF (EM2(JJ).GT.0.99) GOTO 30
   24 CONTINUE

   30 CONTINUE
      STOP
      END
C
C
      SUBROUTINE AREA (EM1,XX,EK1,J)
      DIMENSION EM1(200),XX(200)
      Z1=(EM1(J+1)-EM1(J))/(XX(J+1)-XX(J))
      V1=(EM1(J+2)-EM1(J+1))/(XX(J+2)-XX(J+1))
      B1=(1./(XX(J+2)-XX(J)))*(V1-Z1)
      C1=Z1-(B1*(XX(J+1)+XX(J)))
      H1=EM1(J)-(B1*(XX(J)**2))-(C1*XX(J))
      A1=((B1/3.)*(XX(J+2)**3-XX(J)**3))+((C1/2.)*(XX(J+2)**2-XX(J)**2))
      A1=A1+(H1*(XX(J+2)-XX(J)))
      EK1=EK1+A1
      RETURN
      END
      FINISH
```

APPENDIX 5

FORTRAN PROGRAM FOR THE CALCULATION OF THE VARIATION OF $\eta_o (0.1 \leq \eta_o \leq 23.9)$ WITH $x/\sigma\delta_2$ FOR A GIVEN VALUE OF m (EQUATION 2.23)

```
C       TO START THE PROGRAM,INPUT P
C       P=m. (POWER LAW EXPONENT FOR THE BOUNDARY LAYER VELOCITY PROFILE
C            JUST AFTER EXPANSION)
C       XXX(J)=XX(J)=η0
C       EKK1=F(η0)=X/σδ2
        DIMENSION XX(500),XXX(500),EM1(500),EMM1(500)
C       INPUT P
        READ (5,100) P
  100 FORMAT (F10.6)
    1 CONTINUE
C       SETTING THE VALUE OF (XX(J)=XXX(J)) BETWEEN 0.1 AND 23.9
        XX(1)=0.0
        EM1(1)=0.0
        DO 2 J=2,481
        XX(J)=XX(J-1)+0.05
        IF (J.GT.200) GOTO 150
        EM1(J)=(XX(J)**((1.+P)/P))/(2.7183**(XX(J)**2.))
        GOTO 2
  150 EM1(J)=0.0
    2 CONTINUE
C       END OF XX(J) SETTING
C       CALCULATION OF THE INTEGRAL TERM IN EQUATION 2.23 FOR A GIVEN XX(J)
        EK1=0.0
        DO 4 J=1,479,2
        CALL AREA (EM1,XX,EK1,J)
        IF (J.GT.200) GOTO 160
        EK2=(1./(2.7183**(XX(J+2)**2.)))+((2.*EK1)/(XX(J+2)**(1./P)))
        GOTO 170
  160 EK2=(2.*EK1)/(XX(J+2)**(1./P))
  170 CONTINUE
        EM1(J+1)=(1.-EK2)
    4 CONTINUE
        DO 6 J=2,480,2
        J1=(J+2)/2
        EMM1(J1)=EM1(J)
        XXX(J1)=XX(J+1)
    6 CONTINUE
        DO 8 J1=2,241
        JJ=243-J1
        EM1(JJ)=EMM1(J1)
        XX(JJ)=1./XXX(J1)
    8 CONTINUE
        DO 9 J=2,241
        JJ=J
        EM1(J)=EM1(JJ)
        XX(J)=XX(JJ)
    9 CONTINUE
```

```
      EK1=0.
      DO 10 J=1,239,2
      CALL AREA (EM1,XX,EK1,J)
C     END OF THE INTEGRAL TERM CALCULATION
      XXX(J+2)=1./XX(J+2)
C     PRINTING THE VALUES OF XXX(J) AND EKK1
      EKK1=(XX(J+2)-EK1)
      WRITE (6,200) XXX(J+2),EKK1
   10 CONTINUE
  200 FORMAT (F8.2,F14.5)
   12 CONTINUE
      STOP
      END
      SUBROUTINE AREA (EM1,XX,EK1,J)
      DIMENSION EM1(500),XX(500)
      Z1=(EM1(J+1)-EM1(J))/(XX(J+1)-XX(J))
      V1=(EM1(J+2)-EM1(J+1))/(XX(J+2)-XX(J+1))
      B1=(1./(XX(J+2)-XX(J)))*(V1-Z1)
      C1=Z1-(B1*(XX(J+1)+XX(J)))
      H1=EM1(J)-(B1*(XX(J)**2))-(C1*XX(J))
      A1=((B1/3.)*(XX(J+2)**3-XX(J)**3))+((C1/2.)*(XX(J+2)**2-XX(J)**2))
      A1=A1+(H1*(XX(J+2)-XX(J)))
      EK1=EK1+A1
      RETURN
      END
      FINISH
END JOB
```

Table 1. Variation of η_o with $x/\sigma\delta_2$.(eqn.2.23)

η_o	$F(\eta_o) = x/\sigma\delta_2$					
	m=7	m=9	m=11	m=13	m=15	m=17
0.0	∞	∞	∞	∞	∞	∞
0.1	9.7964	9.8374	9.8646	9.8841	9.8986	9.9099
0.3	3.1398	3.1787	3.2045	3.2230	3.2368	3.2476
0.5	1.8191	1.8553	1.8795	1.8967	1.9096	1.9197
0.7	1.2599	1.2935	1.3160	1.3320	1.3441	1.3535
0.9	0.9538	0.9850	1.0059	1.0209	1.0322	1.0409
1.1	0.7623	0.7913	0.8108	0.8248	0.8352	0.8434
1.3	0.6321	0.6591	0.6773	0.6903	0.7001	0.7077
1.5	0.5382	0.5634	0.5804	0.5926	0.6018	0.6089
1.7	0.4677	0.4912	0.5071	0.5186	0.5272	0.5339
1.9	0.4128	0.4350	0.4500	0.4606	0.4687	0.4750
2.1	0.3691	0.3899	0.4040	0.4141	0.4217	0.4277
2.3	0.3334	0.3531	0.3664	0.3759	0.3832	0.3888
2.5	0.3038	0.3224	0.3350	0.3441	0.3509	0.3563
2.7	0.2789	0.2966	0.3085	0.3171	0.3236	0.3287
2.9	0.2577	0.2744	0.2858	0.2940	0.3002	0.3051
3.1	0.2394	0.2553	0.2662	0.2749	0.2799	0.2846
3.3	0.2234	0.2386	0.2490	0.2565	0.2622	0.2666
3.5	0.2094	0.2240	0.2339	0.2411	0.2465	0.2507
3.7	0.1970	0.2110	0.2205	0.2273	0.2326	0.2367
3.9	0.1860	0.1994	0.2085	0.2151	0.2201	0.2240
4.1	0.1761	0.1889	0.1977	0.2041	0.2089	0.2127
4.3	0.1672	0.1795	0.1880	0.1941	0.1988	0.2024
4.5	0.1591	0.1710	0.1792	0.1851	0.1896	0.1931
4.7	0.1518	0.1633	0.1712	0.1769	0.1812	0.1846
4.9	0.1451	0.1562	0.1638	0.1693	0.1735	0.1768
5.1	0.1390	0.1497	0.1571	0.1624	0.1665	0.1697
5.3	0.1333	0.1437	0.1508	0.1560	0.1600	0.1631
5.5	0.1281	0.1382	0.1451	0.1501	0.1539	0.1569
5.7	0.1233	0.1331	0.1398	0.1447	0.1484	0.1513
5.9	0.1189	0.1283	0.1348	0.1396	0.1432	0.1460

Table 1.(Continued)

η_o	$F(\eta_o) = x/\sigma\delta_2$					
	m=7	m=9	m=11	m=13	m=15	m=17
6.1	0.1147	0.1239	0.1302	0.1348	0.1383	0.1411
6.3	0.1109	0.1198	0.1259	0.1304	0.1338	0.1365
6.5	0.1073	0.1159	0.1219	0.1263	0.1296	0.1322
6.7	0.1039	0.1123	0.1181	0.1224	0.1256	0.1281
6.9	0.1007	0.1089	0.1146	0.1187	0.1219	0.1243
7.1	0.0977	0.1057	0.1112	0.1153	0.1183	0.1207
7.3	0.0949	0.1027	0.1081	0.1120	0.1150	0.1174
7.5	0.0923	0.0999	0.1051	0.1090	0.1119	0.1142
7.7	0.0898	0.0972	0.1023	0.1061	0.1089	0.1111
7.9	0.0874	0.0947	0.0997	0.1033	0.1061	0.1083
8.1	0.0852	0.0923	0.0971	0.1007	0.1034	0.1056
8.3	0.0831	0.0900	0.0947	0.0982	0.1009	0.1030
8.5	0.0811	0.0878	0.0925	0.0959	0.0985	0.1005
8.7	0.0791	0.0857	0.0903	0.0936	0.0962	0.0982
8.9	0.0773	0.0838	0.0882	0.0915	0.0940	0.0959
9.1	0.0756	0.0819	0.0862	0.0894	0.0919	0.0938
9.3	0.0739	0.0801	0.0844	0.0875	0.0899	0.0918
9.5	0.0723	0.0784	0.0826	0.0856	0.0880	0.0898
9.7	0.0708	0.0767	0.0808	0.0838	0.0861	0.0879
9.9	0.0694	0.0752	0.0792	0.0821	0.0844	0.0861
10.1	0.0680	0.0737	0.0776	0.0805	0.0827	0.0844
10.3	0.0667	0.0722	0.0761	0.0789	0.0811	0.0828
10.5	0.0654	0.0708	0.0746	0.0774	0.0795	0.0812
10.7	0.0642	0.0695	0.0732	0.0759	0.0780	0.0797
10.9	0.0630	0.0682	0.0719	0.0745	0.0766	0.0782
11.1	0.0618	0.0670	0.0706	0.0732	0.0752	0.0768
11.3	0.0608	0.0658	0.0693	0.0719	0.0739	0.0754
11.5	0.0597	0.0647	0.0681	0.0707	0.0726	0.0741
11.7	0.0587	0.0636	0.0670	0.0694	0.0713	0.0728
11.9	0.0577	0.0625	0.0658	0.0683	0.0701	0.0716

Table 1. (Continued)

η_o	$(Fn_o) = x/\sigma\delta_2$					
	m=7	m=9	m=11	m=13	m=15	m=17
12.1	0.0568	0.0615	0.0648	0.0672	0.0690	0.0704
12.3	0.0559	0.0605	0.0637	0.0661	0.0679	0.0693
12.5	0.0550	0.0595	0.0627	0.0650	0.0668	0.0682
12.7	0.0542	0.0586	0.0617	0.0640	0.0658	0.0671
12.9	0.0533	0.0577	0.0608	0.0630	0.0647	0.0661
13.1	0.0526	0.0569	0.0599	0.0621	0.0638	0.0651
13.3	0.0518	0.0560	0.0590	0.0612	0.0628	0.0641
13.5	0.0510	0.0552	0.0581	0.0603	0.0619	0.0632
13.7	0.0503	0.0544	0.0573	0.0594	0.0610	0.0623
13.9	0.0496	0.0537	0.0565	0.0586	0.0601	0.0614
14.1	0.0490	0.0529	0.0557	0.0577	0.0593	0.0605
14.3	0.0483	0.0522	0.0549	0.0569	0.0586	0.0597
14.5	0.0477	0.0515	0.0542	0.0562	0.0577	0.0589
14.7	0.0471	0.0508	0.0535	0.0553	0.0569	0.0581
14.9	0.0465	0.0502	0.0528	0.0547	0.0562	0.0573
15.1	0.0459	0.0495	0.0521	0.0540	0.0554	0.0566
15.3	0.0453	0.0489	0.0514	0.0533	0.0547	0.0559
15.5	0.0448	0.0483	0.0508	0.0526	0.0540	0.0551
15.7	0.0442	0.0477	0.0502	0.0520	0.0534	0.0545
15.9	0.0437	0.0472	0.0496	0.0514	0.0527	0.0538
16.1	0.0432	0.0466	0.0490	0.0507	0.0521	0.0531
16.3	0.0427	0.0461	0.0484	0.0501	0.0515	0.0525
16.5	0.0422	0.0455	0.0478	0.0495	0.0508	0.0519
16.7	0.0418	0.0450	0.0473	0.0490	0.0503	0.0513
16.9	0.0413	0.0445	0.0468	0.0484	0.0497	0.0507
17.1	0.0409	0.0440	0.0462	0.0479	0.0491	0.0501
17.3	0.0404	0.0435	0.0457	0.0473	0.0486	0.0495
17.5	0.0400	0.0431	0.0452	0.0468	0.0480	0.0490
17.7	0.0396	0.0426	0.0447	0.0463	0.0475	0.0485
17.9	0.0392	0.0422	0.0443	0.0458	0.0470	0.0479

Table 1. (Concluded)

η_o	$(F\eta_0) = x/\sigma\delta_2$					
	m=7	m=9	m=11	m=13	m=15	m=17
18.1	0.0388	0.0417	0.0438	0.0453	0.0465	0.0474
18.3	0.0384	0.0413	0.0434	0.0449	0.0460	0.0469
18.5	0.0380	0.0409	0.0429	0.0444	0.0455	0.0464
18.7	0.0377	0.0405	0.0425	0.0439	0.0451	0.0459
18.9	0.0373	0.0401	0.0421	0.0435	0.0446	0.0455
19.1	0.0370	0.0397	0.0416	0.0431	0.0442	0.0450
19.3	0.0366	0.0393	0.0412	0.0426	0.0437	0.0446
19.5	0.0363	0.0390	0.0408	0.0422	0.0433	0.0441
19.7	0.0359	0.0386	0.0405	0.0418	0.0429	0.0437
19.9	0.0356	0.0382	0.0401	0.0414	0.0425	0.0433
20.1	0.0353	0.0379	0.0397	0.0410	0.0421	0.0429
20.3	0.0350	0.0376	0.0393	0.0407	0.0417	0.0425
20.5	0.0347	0.0372	0.0390	0.0403	0.0413	0.0421
20.7	0.0344	0.0369	0.0386	0.0399	0.0409	0.0417
20.9	0.0341	0.0366	0.0383	0.0396	0.0406	0.0413
21.1	0.0338	0.0363	0.0380	0.0392	0.0402	0.0409
21.3	0.0336	0.0360	0.0376	0.0389	0.0398	0.0406
21.5	0.0333	0.0357	0.0373	0.0385	0.0395	0.0402
21.7	0.0330	0.0354	0.0370	0.0382	0.0391	0.0399
21.9	0.0328	0.0351	0.0367	0.0379	0.0388	0.0395
22.1	0.0325	0.0348	0.0364	0.0376	0.0385	0.0392
22.3	0.0323	0.0345	0.0361	0.0372	0.0381	0.0388
22.5	0.0320	0.0342	0.0358	0.0369	0.0378	0.0385
22.7	0.0318	0.0340	0.0355	0.0366	0.0375	0.0382
22.9	0.0315	0.0338	0.0352	0.0363	0.0372	0.0379
23.1	0.0313	0.0335	0.0349	0.0360	0.0369	0.0376
23.3	0.0311	0.0332	0.0347	0.0358	0.0366	0.0373
23.5	0.0308	0.0329	0.0344	0.0355	0.0363	0.0370
23.7	0.0306	0.0327	0.0341	0.0352	0.0360	0.0367
23.9	0.0304	0.0324	0.0339	0.0349	0.0357	0.0364

Table 2. Error function velocity profile.(eqn.3.5)

η	ϕ		η	ϕ
-2.1	0.0016		0.9	0.8984
-2.0	0.0024		1.0	0.9213
-1.9	0.0037		1.1	0.9400
-1.8	0.0056		1.2	0.9551
-1.7	0.0082		1.3	0.9669
-1.6	0.0119		1.4	0.9761
-1.5	0.0170		1.5	0.9830
-1.4	0.0240		1.6	0.9881
-1.3	0.0331		1.7	0.9918
-1.2	0.0449		1.8	0.9944
-1.1	0.0600		1.9	0.9963
-1.0	0.0787		2.0	0.9976
-0.9	0.1020		2.1	0.9984
-0.8	0.1290			
-0.7	0.1612			
-0.6	0.1981			
-0.5	0.2398			
-0.4	0.2858			
-0.3	0.3357			
-0.2	0.3887			
-0.1	0.4438			
0.0	0.5000			
0.1	0.5562			
0.2	0.6113			
0.3	0.6643			
0.4	0.7142			
0.5	0.7602			
0.6	0.8019			
0.7	0.8388			
0.8	0.8710			

Table 3. Four stage Turbo Comressor specifications

Mass flow (lb/sec)	10
Inlet pressure (p.s.i. absolute)	14.7
Delivery pressure (p.s.i. gauge)	30.0
Speed (r.p.m.)	8750
Horse power	930

Table 4. (See Fig.18)

X inches	Y inches	Y (Calculated from eqn.4.1) inches
0.000	0.000	
0.027	0.070	
0.101	0.133	
0.223	0.189	
0.378	0.228	
0.555	0.253	
0.631	0.259	
0.750	0.264	
Straight up to X = 2.750"		
2.750	0.264	0.264
2.884	0.263	0.263
2.938	0.262	0.262
3.031	0.259	0.259
3.135	0.256	0.255
3.229	0.252	0.251
3.329	0.246	0.246
3.429	0.240	0.241
3.529	0.235	0.235
3.629	0.229	0.230
3.674	0.226	0.227
3.774	0.222	0.222
3.874	0.218	0.217
3.974	0.213	0.212
4.074	0.209	0.207
4.174	0.204	0.202
4.274	0.200	0.198
4.374	0.196	0.194
4.474	0.191	0.190
4.567	0.188	0.186
4.667	0.183	0.183
4.767	0.179	0.179
4.867	0.175	0.175
4.967	0.171	0.170
5.015	0.169	0.167
5.115	0.165	0.164
5.215	0.163	0.161
5.315	0.159	0.160
5.356	0.158	0.157
5.456	0.156	0.154
5.556	0.153	0.153
5.653	0.152	0.152
5.753	0.151	0.151
5.853	0.150	0.151
5.956	0.150	0.152
6.000	0.150	0.153

Table 5. Values of P_b/P_∞ for different values of $M_{e\infty}$ and α ($\dot{m}=0$)

α	$M_{e\infty}$	M_{e1}		P_b/P_∞
		Upper surface	Lower surface	
0°	0.6	0.645	0.645	0.91
	1.0	1.150	1.150	0.515
	1.3	1.360	1.360	0.46
2°	0.6	0.660	0.645	0.92
	1.0	1.300	1.040	0.52
	1.3	1.380	1.290	0.485
4°	0.6	0.662	0.640	0.94
	1.0	1.340	0.980	0.59
	1.3	1.470	1.110	0.515
6°	0.6	0.665	0.610	0.955
	1.0	*	0.920	0.725
	1.3	1.550	0.950	0.525

* It is difficult to evaluate this value since the flow is seperating just before the trailing edge (Fig.37C)

$M_{e\infty}$	Wire diameter = 0.007"				Wire diameter = 0.024"			
	δ_1 in.	δ_1^* in.	θ_1 in.	P_b/P_∞	δ_1 in.	δ_1^* in.	θ_1 in.	P_b/P_∞
0.6	0.20	0.029	0.0174	0.87	0.32	0.040	0.028	0.91
1.0	0.14	0.027	0.014	0.48	0.16	0.033	0.017	0.515
1.3	0.12	0.024	0.0123	0.49	0.15	0.027	0.015	0.46

Table 6. Boundary layer dimensions at 0.4" upstream the trailing edge

($\dot{m} = 0$, $\alpha = 0$)

Table 7.

Reference	$M_{e\infty}$	P_b/P_∞	P_r/P_∞	M_{e2}	M_{er}
Tanner[89]	0.10	0.9972	0.9998	0.12	0.10
	o.10	0.9957	0.9987	0.13	0.11
Nash[6]	0.40	0.98	1.01	0.44	0.38
	0.80	0.89	1.02	0.91	0.78
	0.95	0.78	0.99	1.16	0.96
	1.00	0.65	0.90	1.34	1.09
	1.10	0.52	0.70	1.58	1.38
Chow[86]	2.00	0.36	0.60	2.66	2.33
Rom (given in ref. 86)	2.24	0.30	0.50	3.02	2.69
Hastings[25]	1.56	0.46	0.75	2.07	1.75
	2.41	0.25	0.48	3.33	2.89
	3.10	0.18	0.40	4.36	3.74
Present results	0.60	0.91	0.98	0.71	0.63
	0.75	0.86	0.94	0.90	0.81
	0.90	0.70	0.83	1.20	1.05
	1.00	0.52	0.77	1.50	1.20
	1.30	0.46	0.59	1.83	1.67
	1.30	0.49	0.70	1.79	1.55

Table 8. Free shear layer parameters for $M_{\infty} = 0.6$ ($\alpha = 0$, d=0.024")

Distance from base(x/2h)	θ in.	δ^* in.	H
0	0.0247	0.0384	1.56
1/3	0.0277	0.0498	1.79
2/3	0.0318	0.0578	1.81
1.0	0.0391	0.0822	2.10
1.5	0.0520	0.1164	2.24

α	$M_{e\infty}$	C_D	C_{DB}	C_{Df}	C_{DP}	$(C_{DP})_{body}$	$(C_{DP})_{nose}$	C_{DB}/C_D	C_{DW}
0°	0.6	0.725	0.515	0.155	0.055	0	0.055	0.71	0
	* 0.6	0.475	0.240	0.155	0.080	0	0.080	0.51	0
	1.0	0.870	0.740	0.115	0.015	0	0.015	0.85	0.25
	* 1.0	0.580	0.465	0.115	0	0	0	0.80	0.136
	1.3	0.640	0.440	0.100	0.100	0	0.100	0.69	0.30
	* 1.3	0.500	0.310	0.100	0.090	0	0.090	0.62	0.14
2°	0.6	0.730	0.330	0.150	0.250	0.31	-0.060	0.45	—
	* 0.6	0.650	0.200	0.150	0.300	0.31	-0.010	0.31	—
	1.0	1.26	0.73	0.11	0.42	0.35	0.07	0.58	—
	* 1.0	0.96	0.40	0.11	0.45	0.35	0.10	0.42	—
	1.3	0.85	0.41	0.095	0.345	0.16	0.185	0.48	—
	* 1.3	0.73	0.25	0.095	0.385	0.16	0.225	0.34	—
6°	0.6	1.00	0.20	0.145	0.655	1.53	-0.875	0.20	—
	* 0.6	0.95	0.17	0.145	0.635	1.53	-0.895	0.18	—
	1.0	0.95	0.43	0.1	0.42	1.76	-1.34	0.45	—
	* 1.0	0.78	0.28	0.1	0.40	1.76	-1.36	0.36	—
	1.3	0.63	0.40	0.085	0.145	1.33	-1.185	0.64	—
	* 1.3	0.50	0.23	0.085	0.185	1.33	-1.145	0.46	—

* With optimum base bleed

Table 9. Drag coefficients

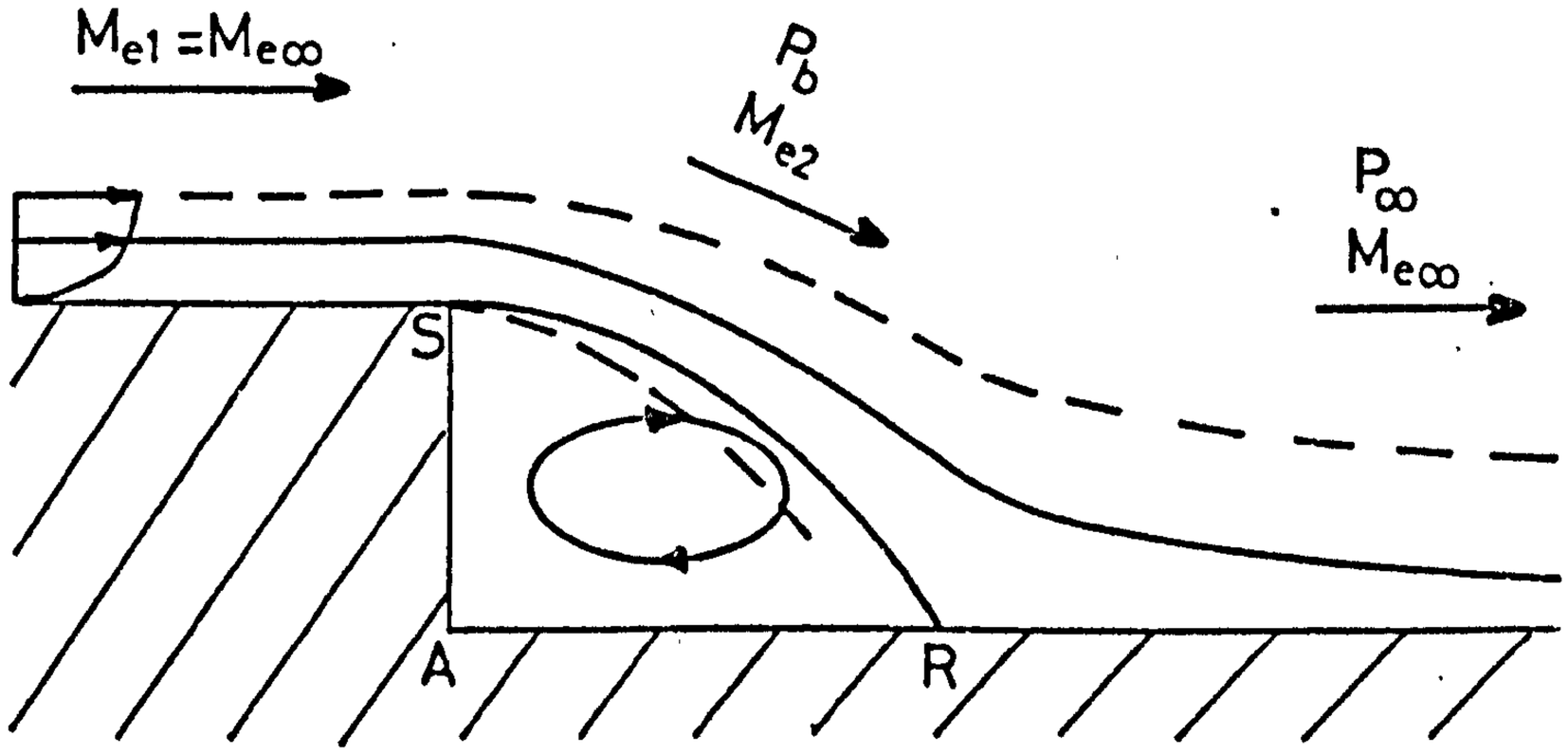

(A). Subsonic flow over a step.

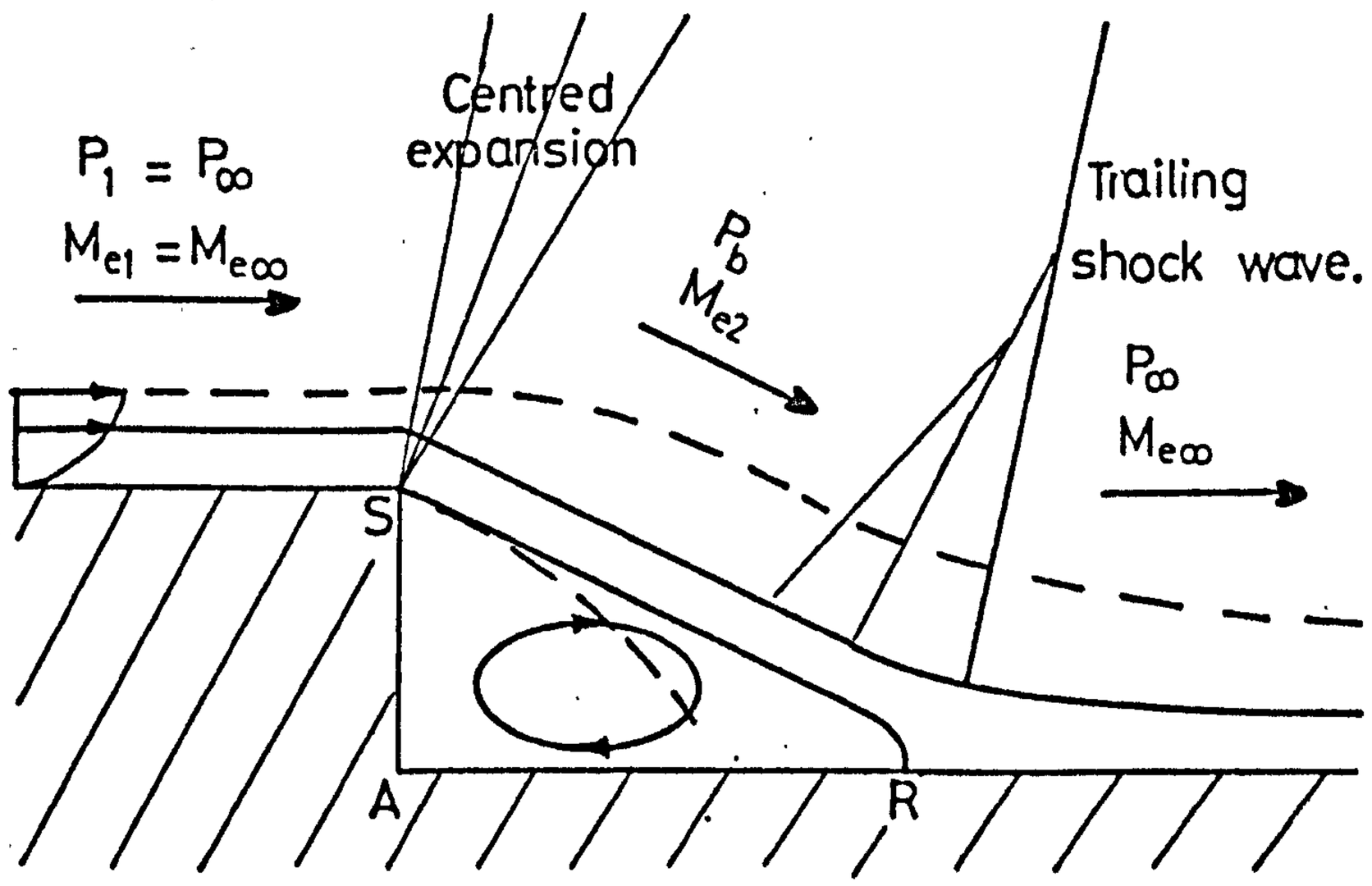

(B). Supersonic flow over a step.

— — — — shear layer edge

FIG.1. SKETCH OF THE BASE FLOW.

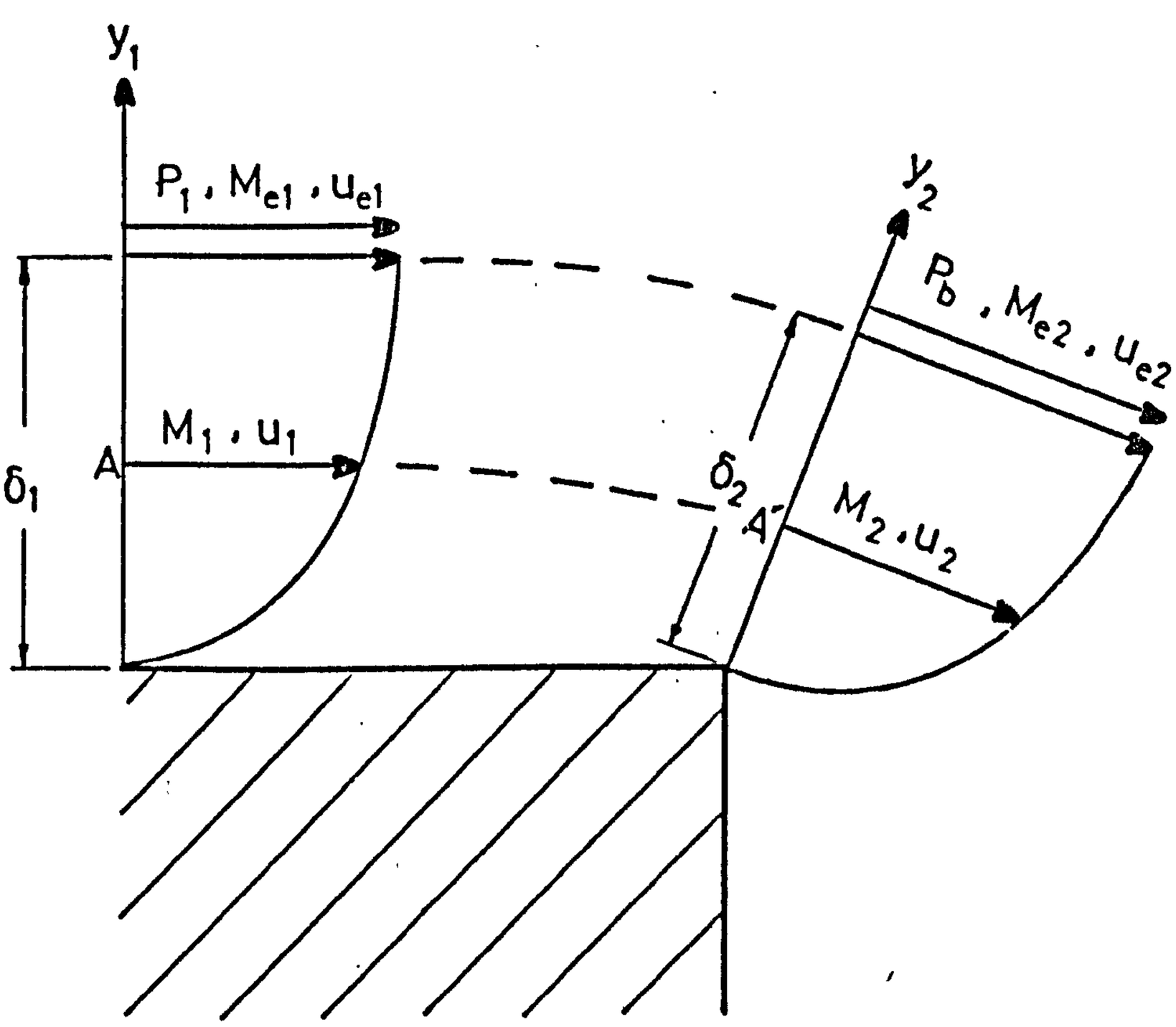

FIG.2. FLOW MODEL AT THE EXPANSION CORNER.

FIG.3. CHANGE OF BOUNDARY LAYER MOMENTUM THICKNESS DUE TO EXPANSION AROUND A CORNER.

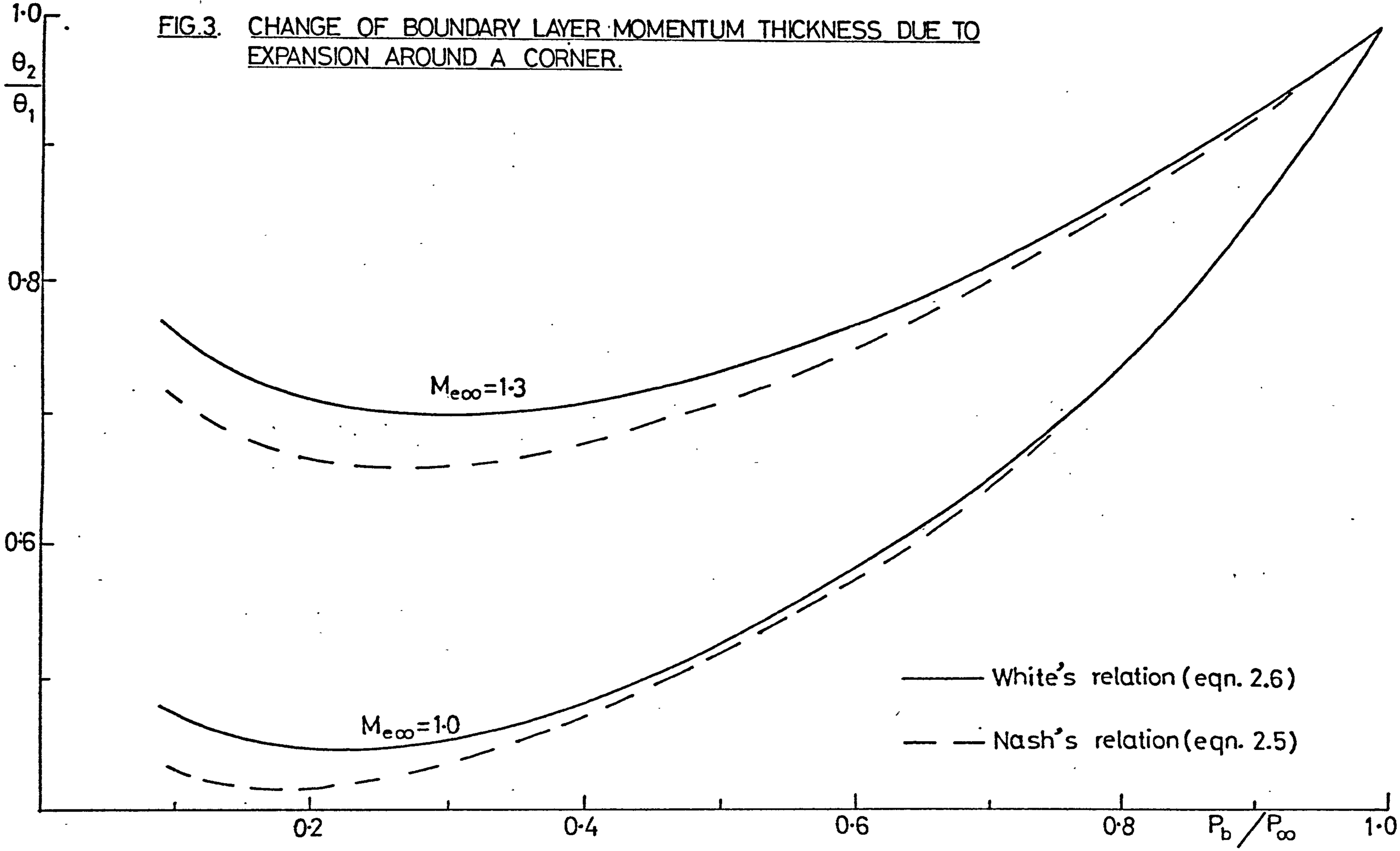

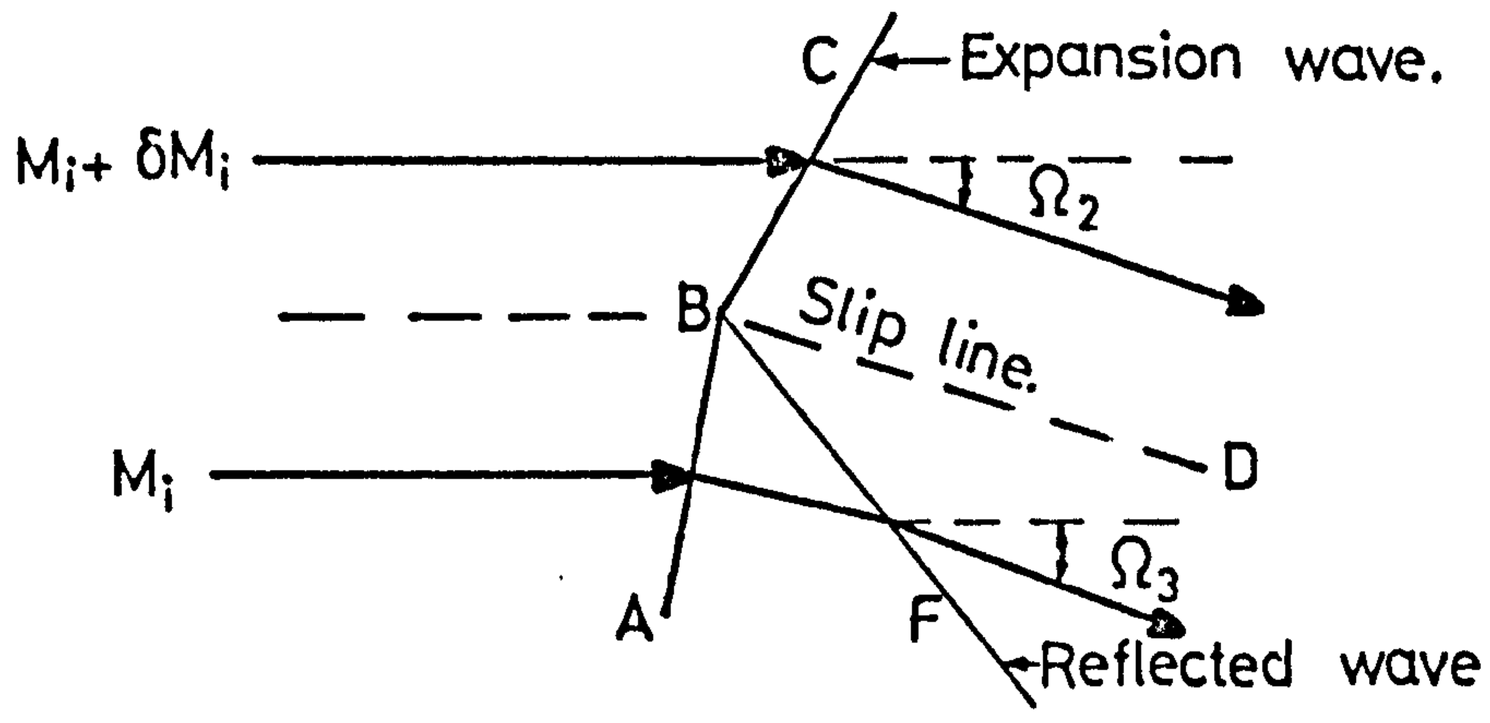

FIG.4.a. SCHEMATIC FOR THE INTERACTION OF AN EXPANSION WAVE AT A WEAK MACH NUMBER DISCONTINUITY. (REF. 68)

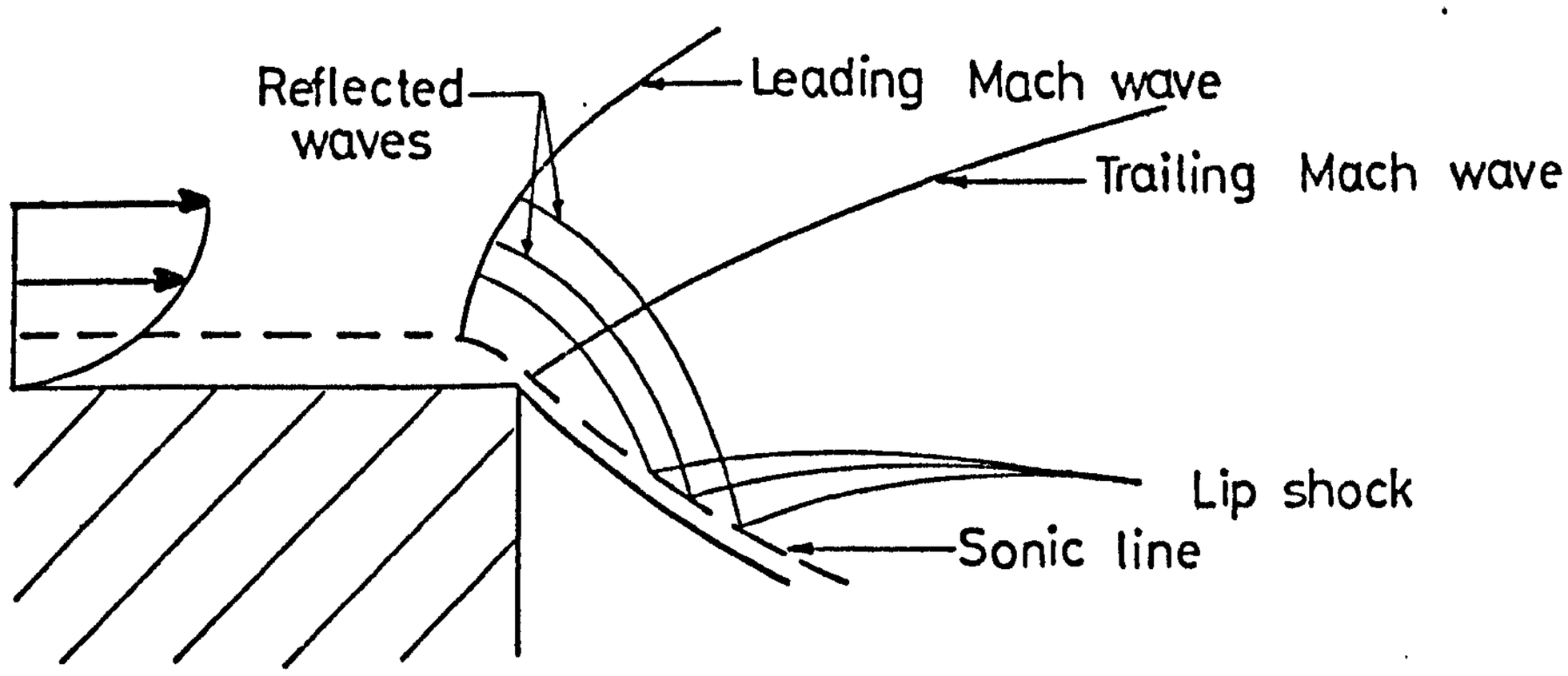

FIG.4.b. SCHEMATIC DIAGRAM OF THE EXPANSION REGION. (REF. 68)

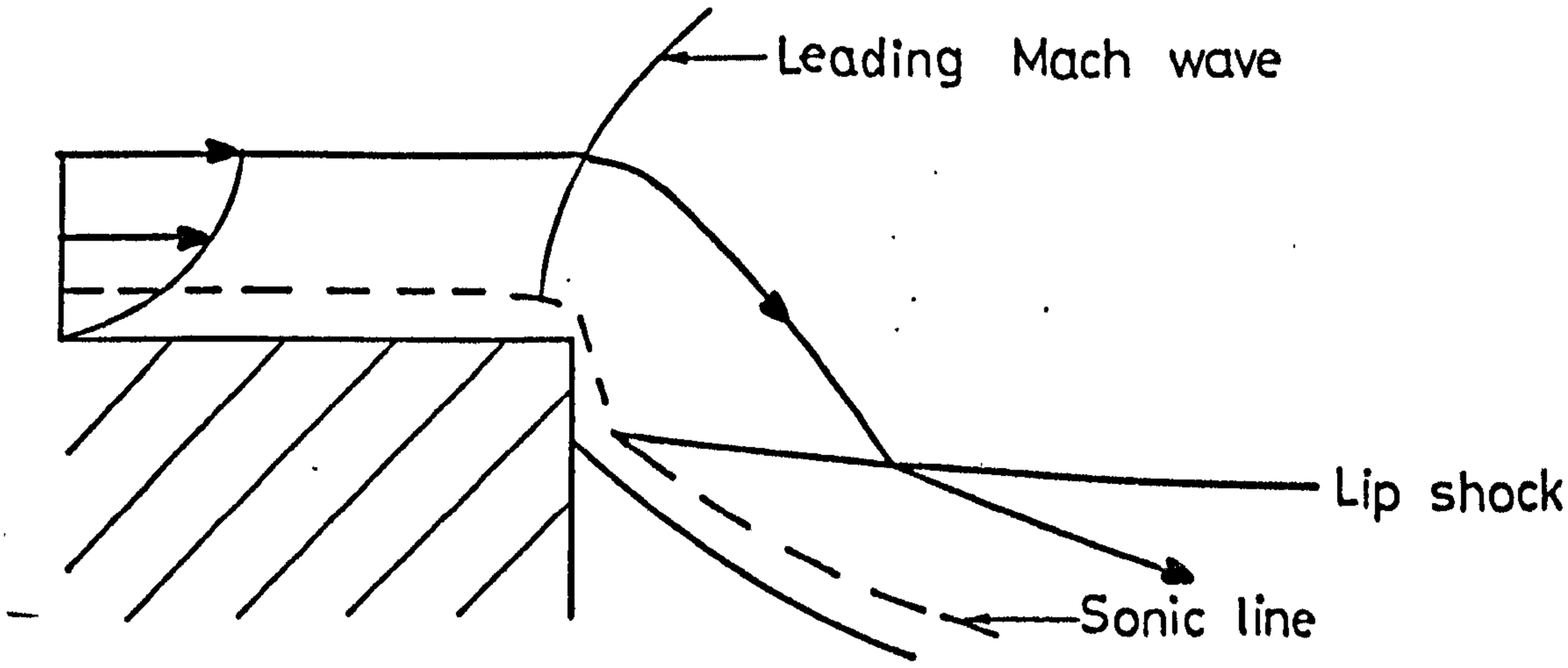

FIG.4.c. FLOW BEHAVIOUR NEAR SEPARATION. (REF. 69)

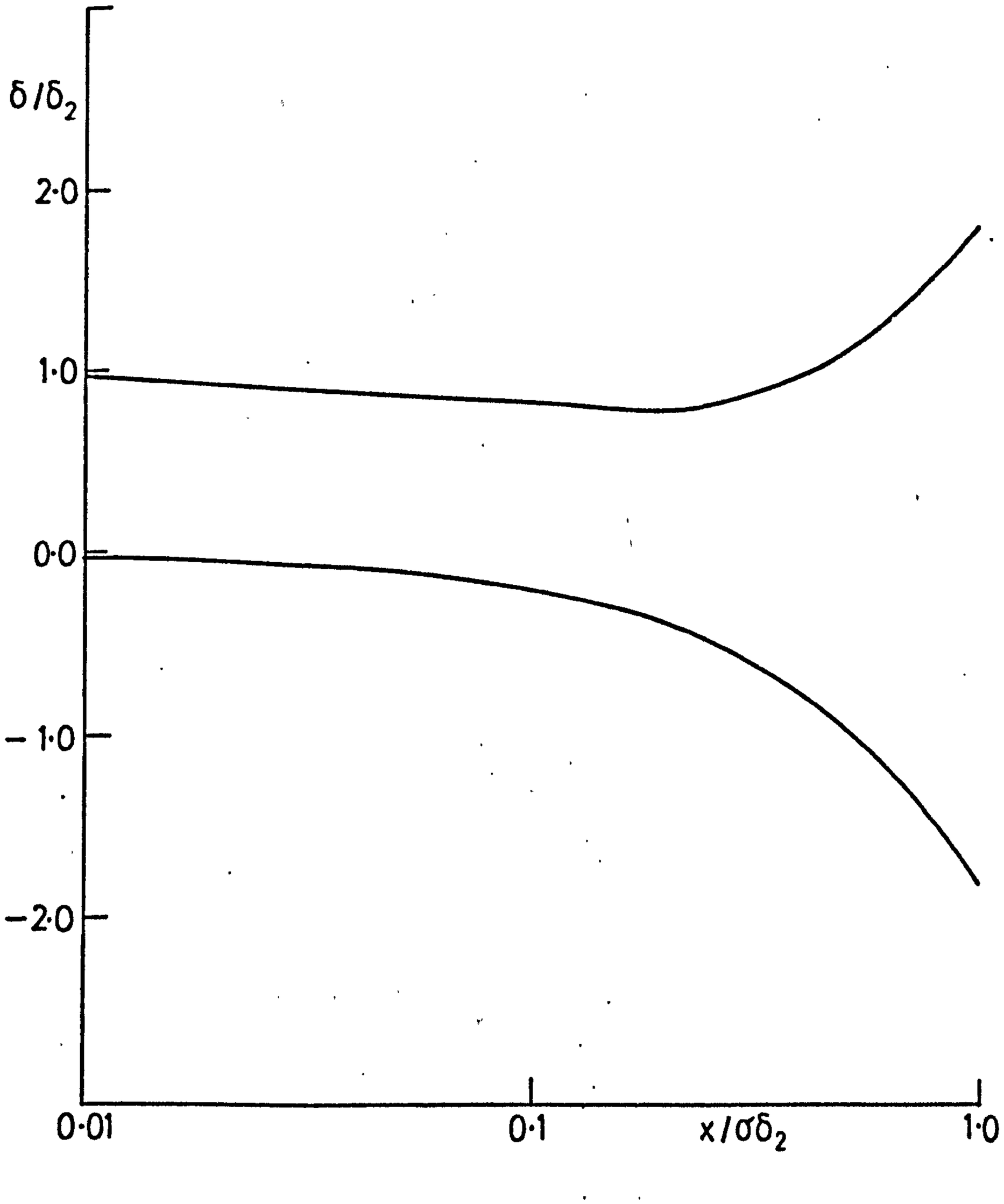

FIG.5. VARIATION OF SHEAR LAYER THICKNESS WITH DISTANCE. (EQUATIONS 2·21 & 2·23.)

FIG.6. EFFECT OF COMPRESSIBILITY ON THE VARIATION OF ϕ_D WITH $\frac{x}{\sigma\theta_2}$ USING MODIFIED NASH METHOD WITH m=11.

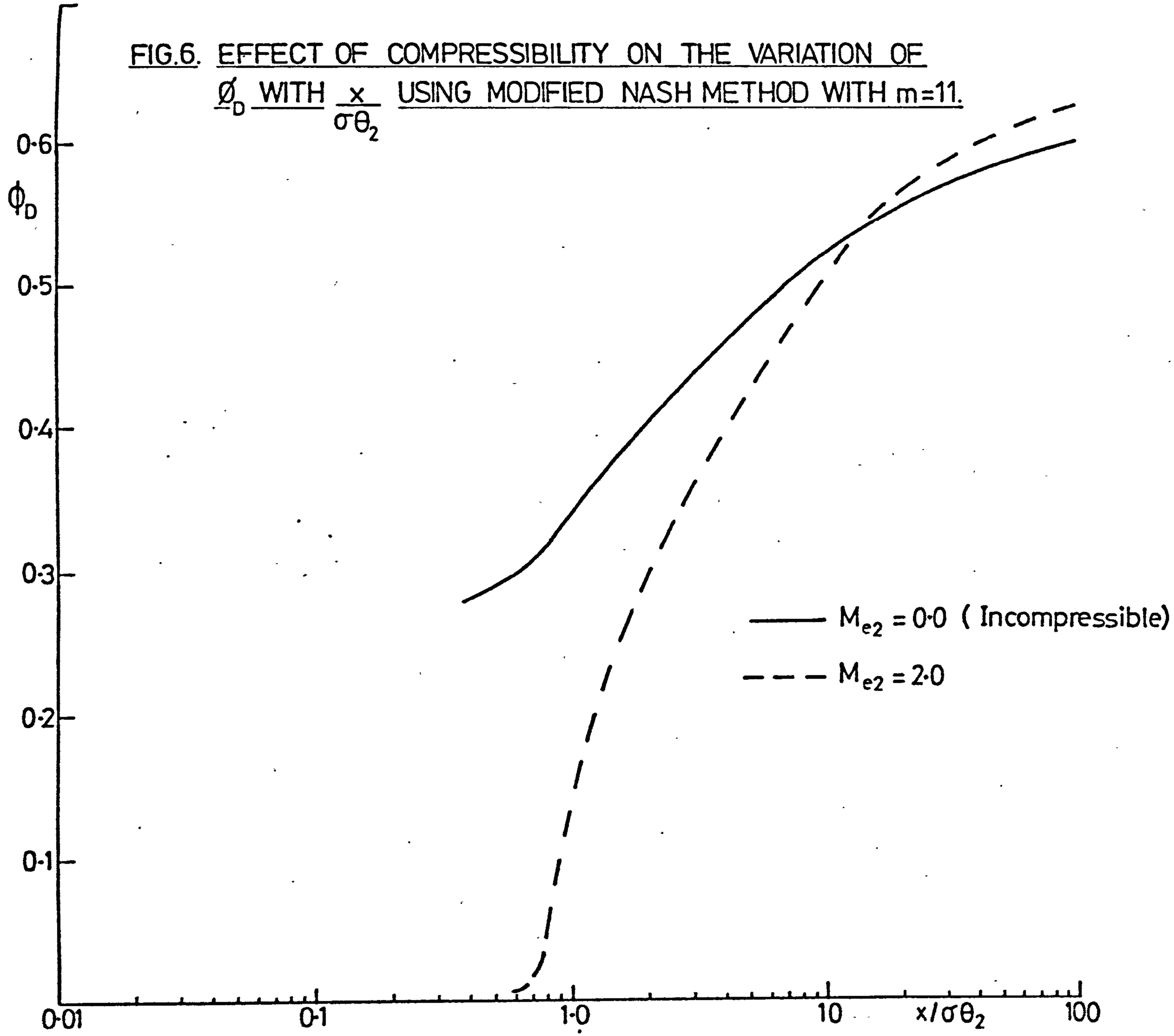

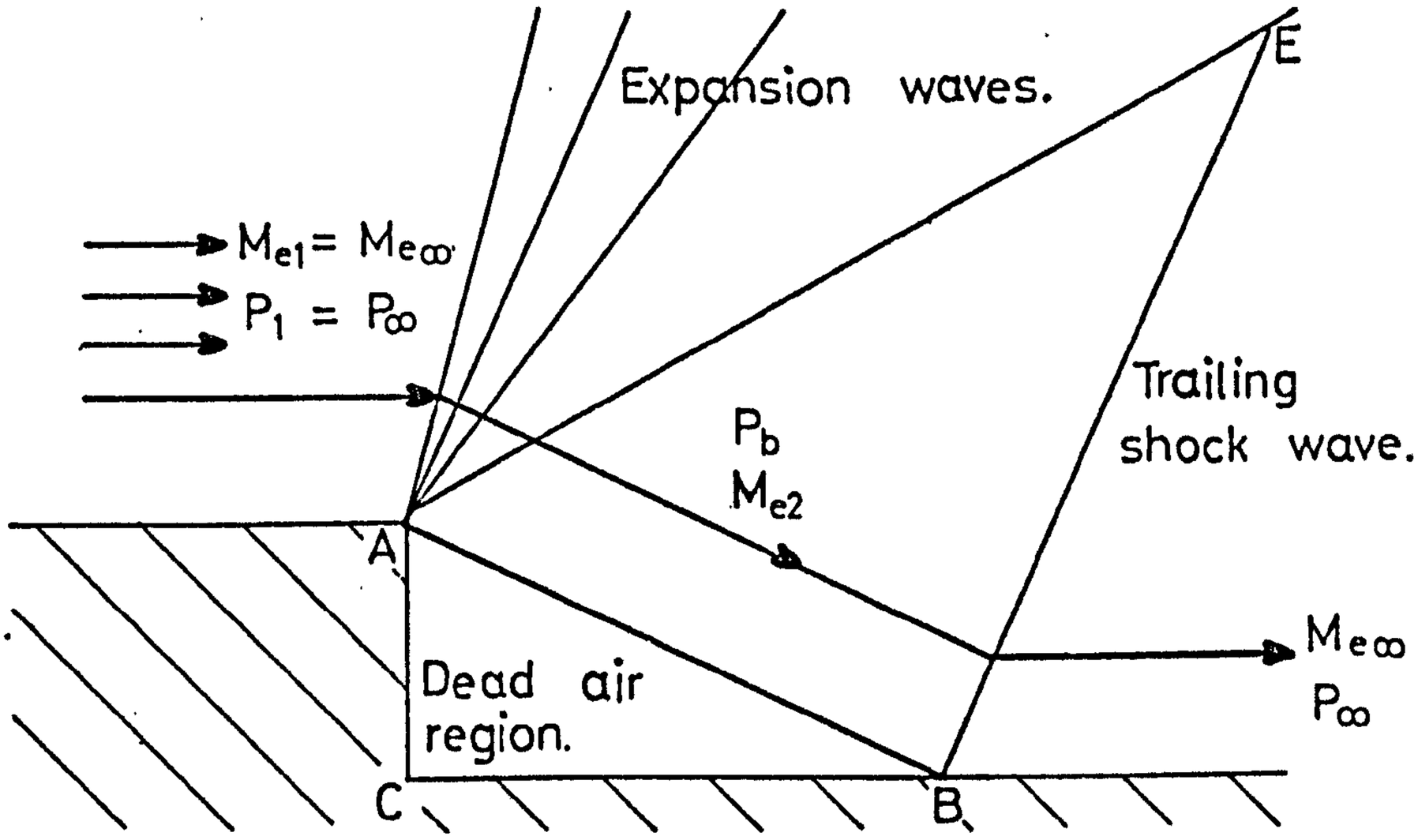

FIG.7.a. SUPERSONIC INVISCID FLOW OVER TWO-DIMENSIONAL STEP. (REF. 17.)

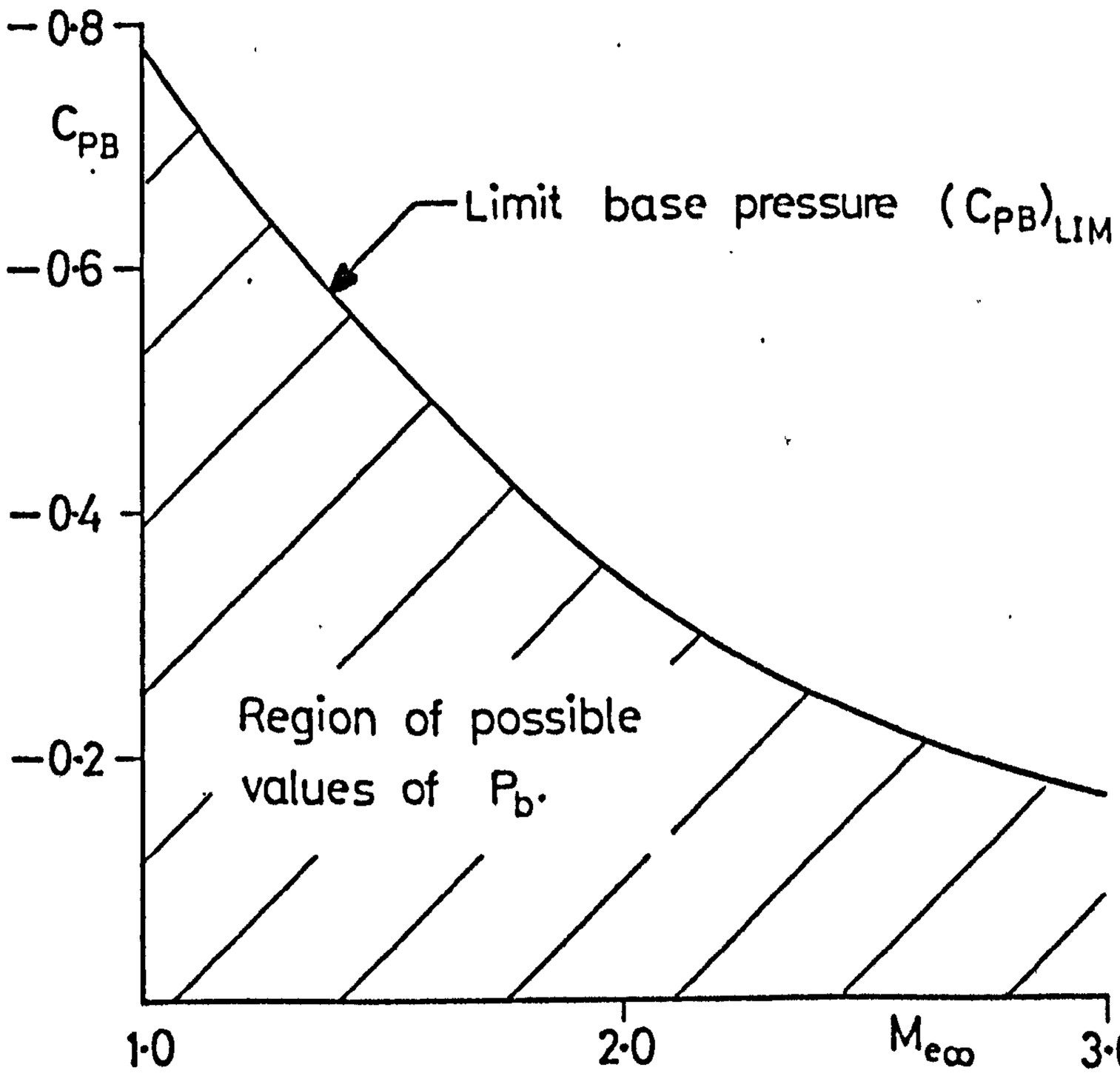

FIG.7.b. BASE PRESSURE FOR TWO-DIMENSIONAL SUPERSONIC INVISCID FLOW. (REF: 17.)

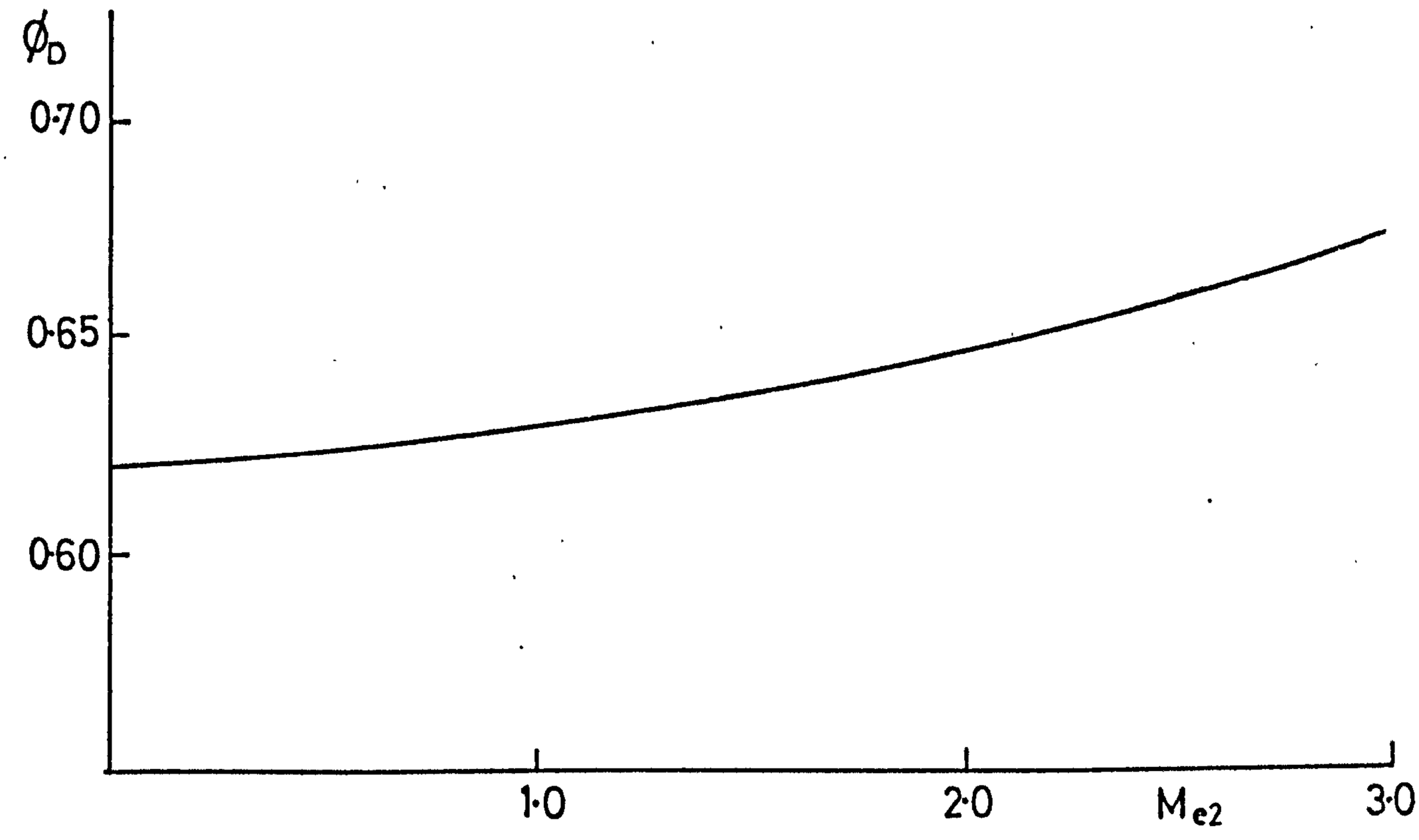

FIG.8. VARIATION OF ϕ_D WITH $M_{e\infty}$ FOR ASYMPTOTIC SHEAR LAYER WITH ZERO INITIAL B.L. THICKNESS. (Eqn. 2·18.)

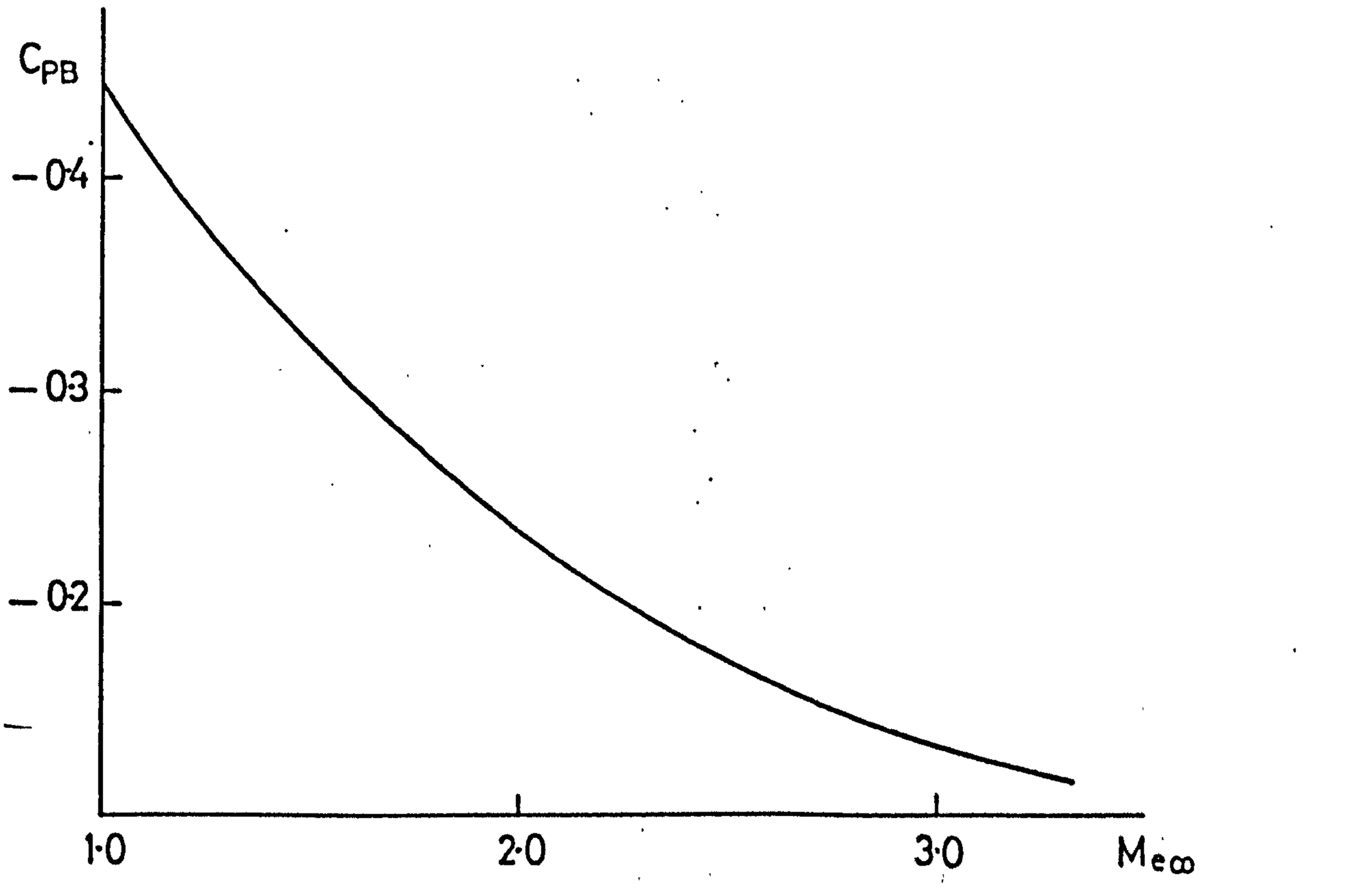

FIG.9. THEORETICAL BASE PRESSURE ACCORDING TO KORST. (REF. 36.)

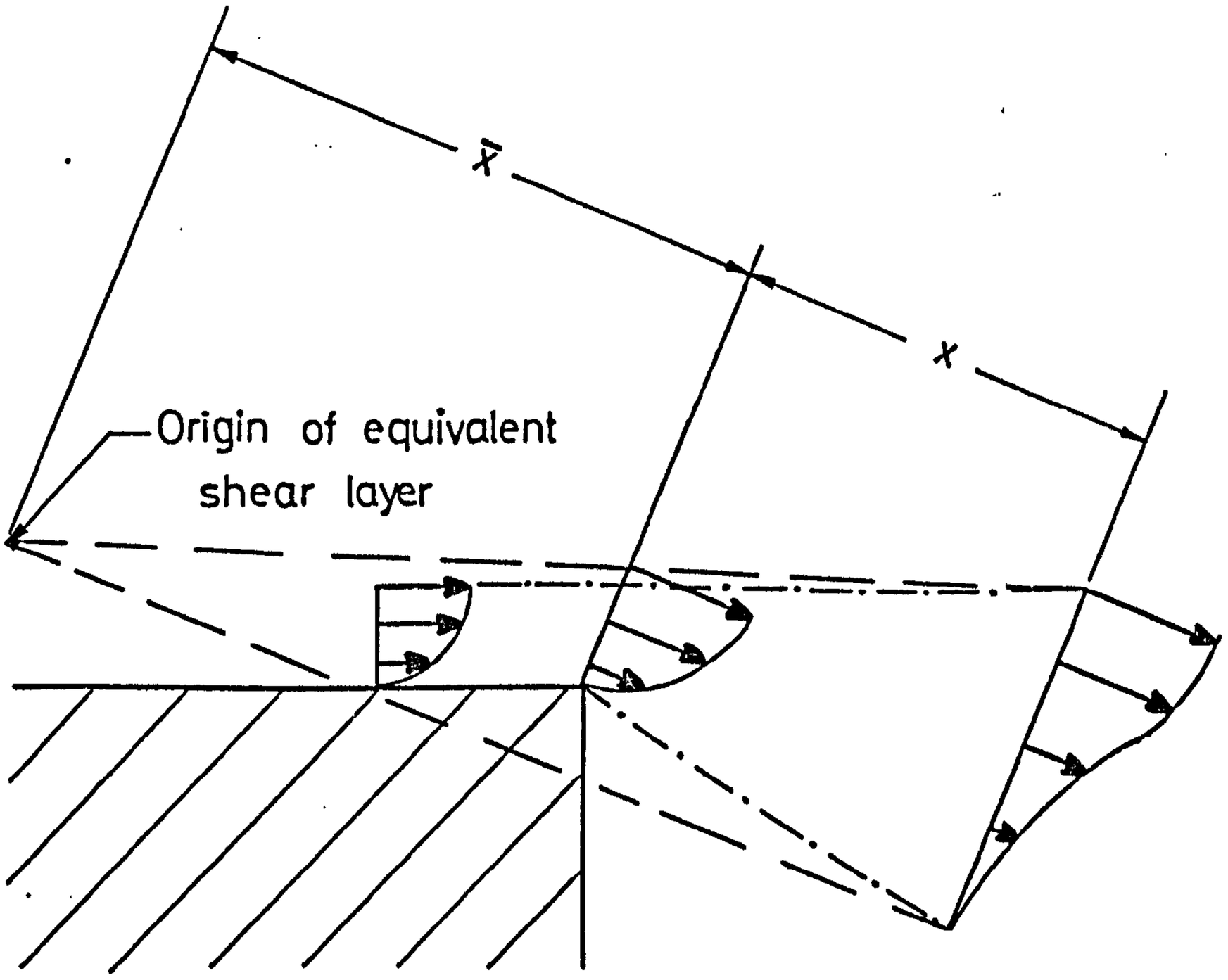

—·—·— Real shear layer

— — — Equivalent shear layer

FIG.10. EFFECT OF THE INITIAL BOUNDARY LAYER ON THE FREE SHEAR LAYER DEVELOPMENT.

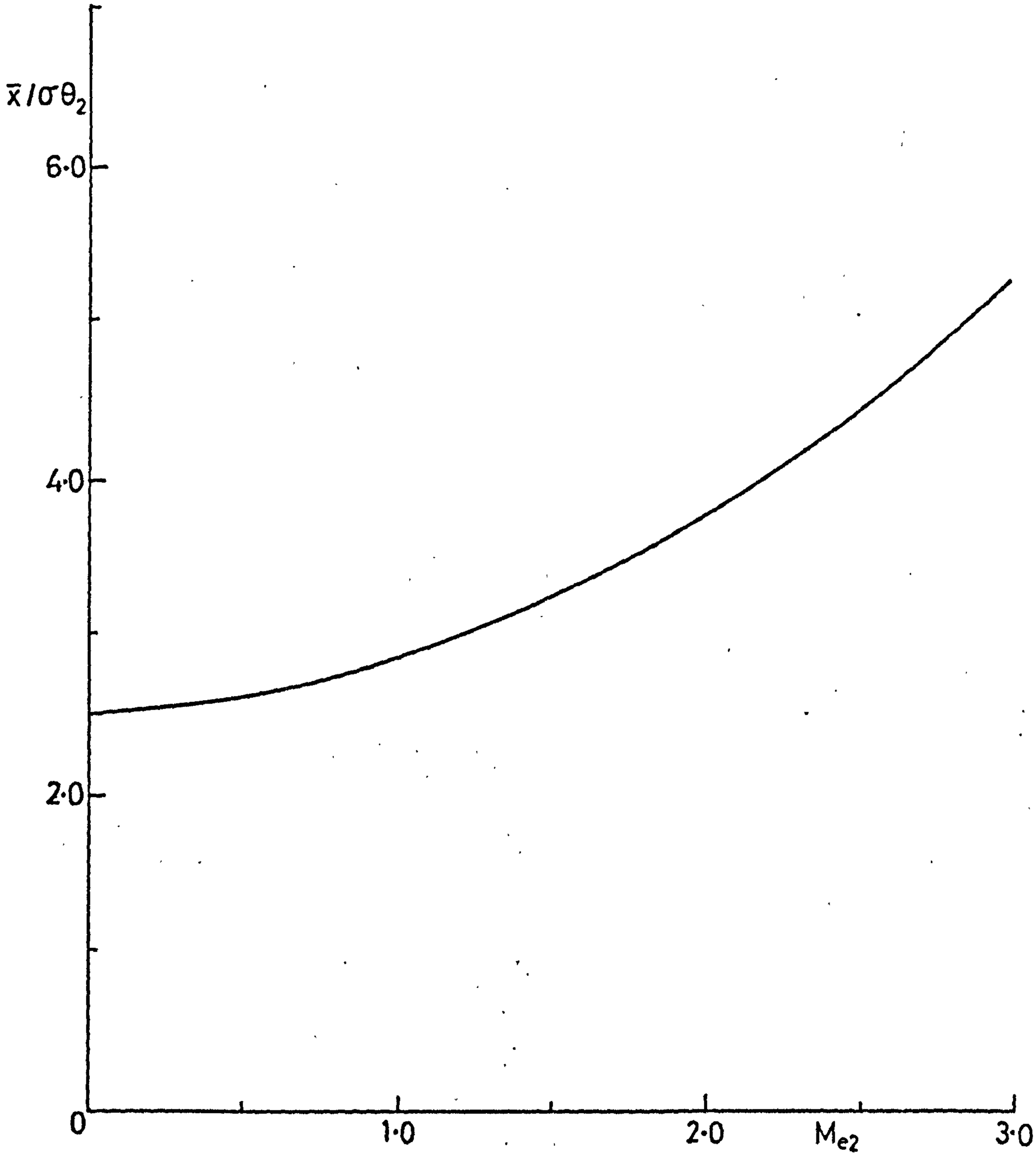

FIG. 11. EFFECT OF M_{e2} ON $\bar{x}$. (Eqn. 3·13.)

FIG.12 EFFECT OF COMPRESSIBILITY ON THE VARIATION OF ϕ_D WITH $\frac{x}{\sigma\theta_2}$ FOR THE EQUIVALENT ASYMPTOTIC TURBULENT FREE SHEAR LAYER. (Eqn. 3·14)

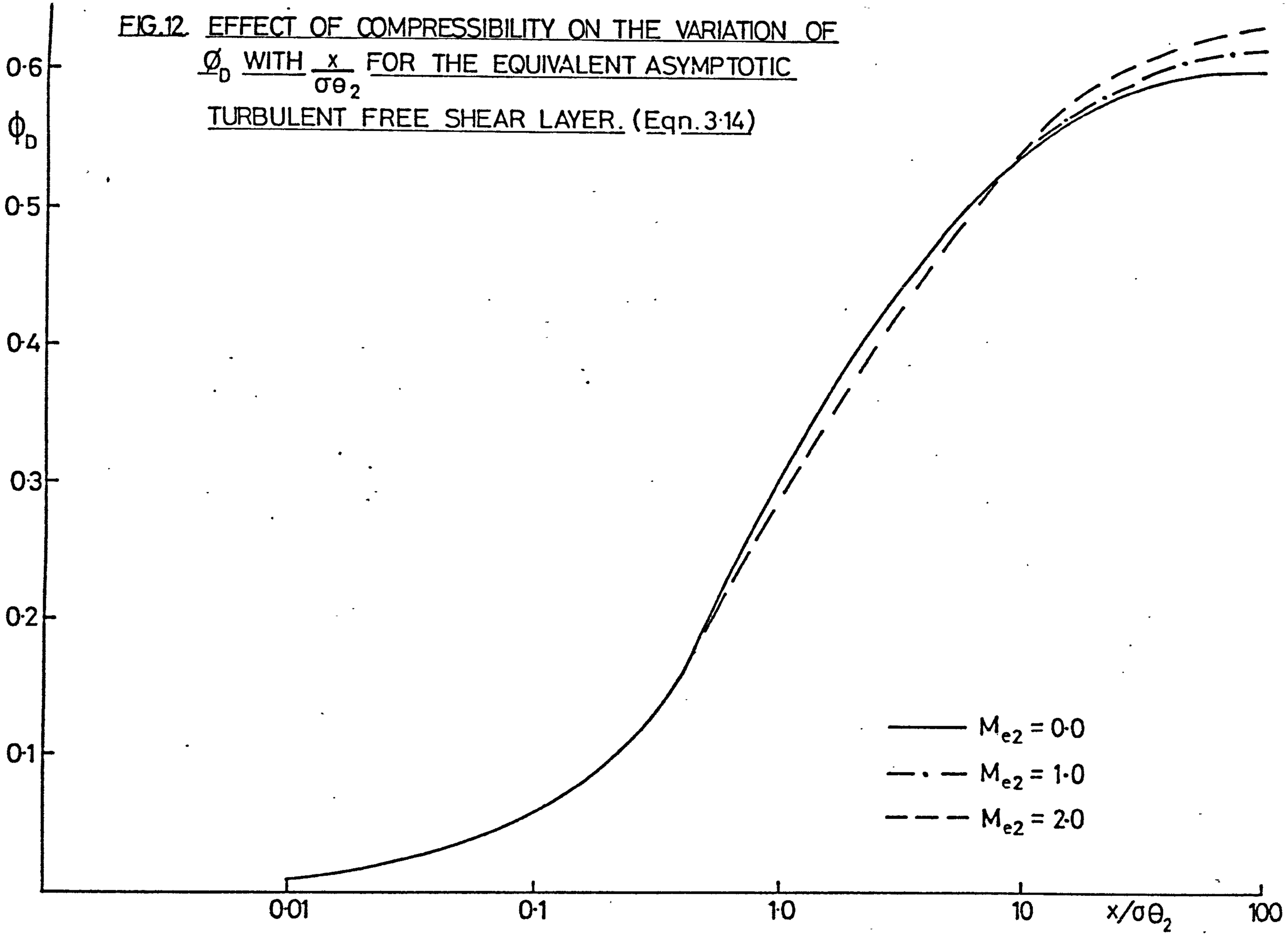

FIG.13. COMPARISON OF VARIOUS METHODS FOR THE VARIATION OF ϕ_D WITH $\frac{x}{\sigma\theta_2}$ FOR INCOMPRESSIBLE TURBULENT FREE SHEAR LAYER.

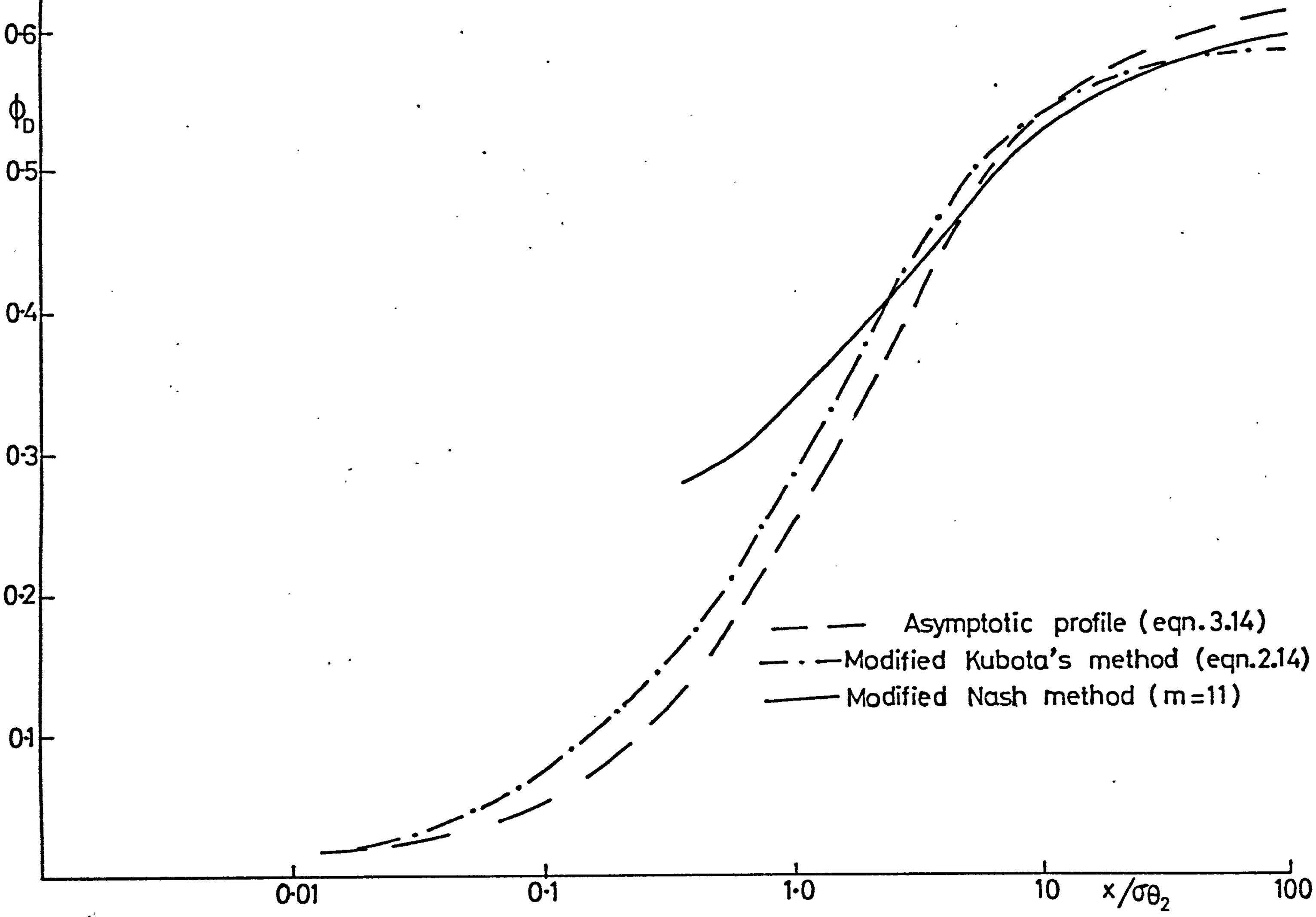

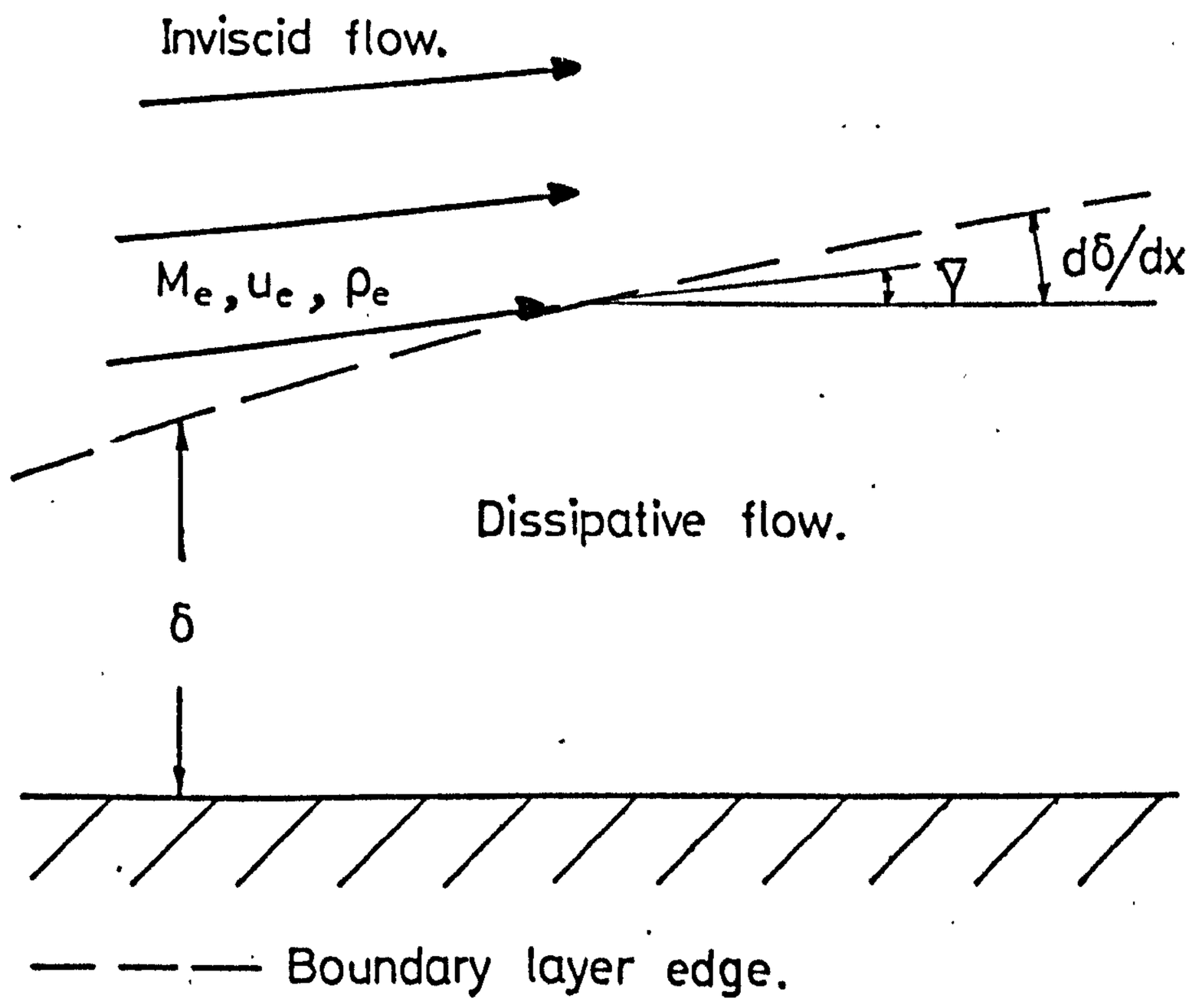

FIG.14. THE TWO FLOW REGIONS. (REF. 19.)

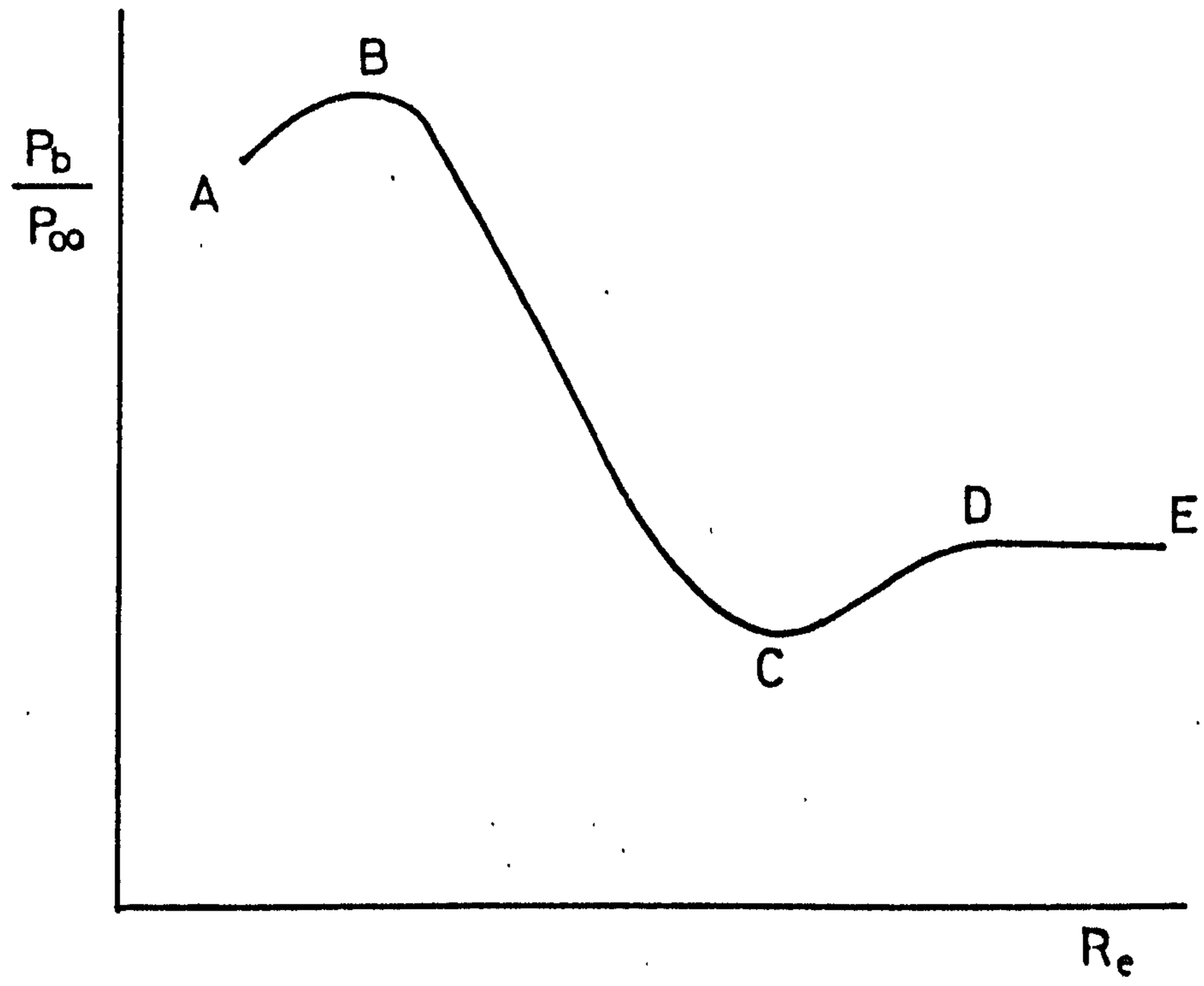

FIG.15. VARIATION OF (P_b/P_∞) WITH (R_e). [REF.19]

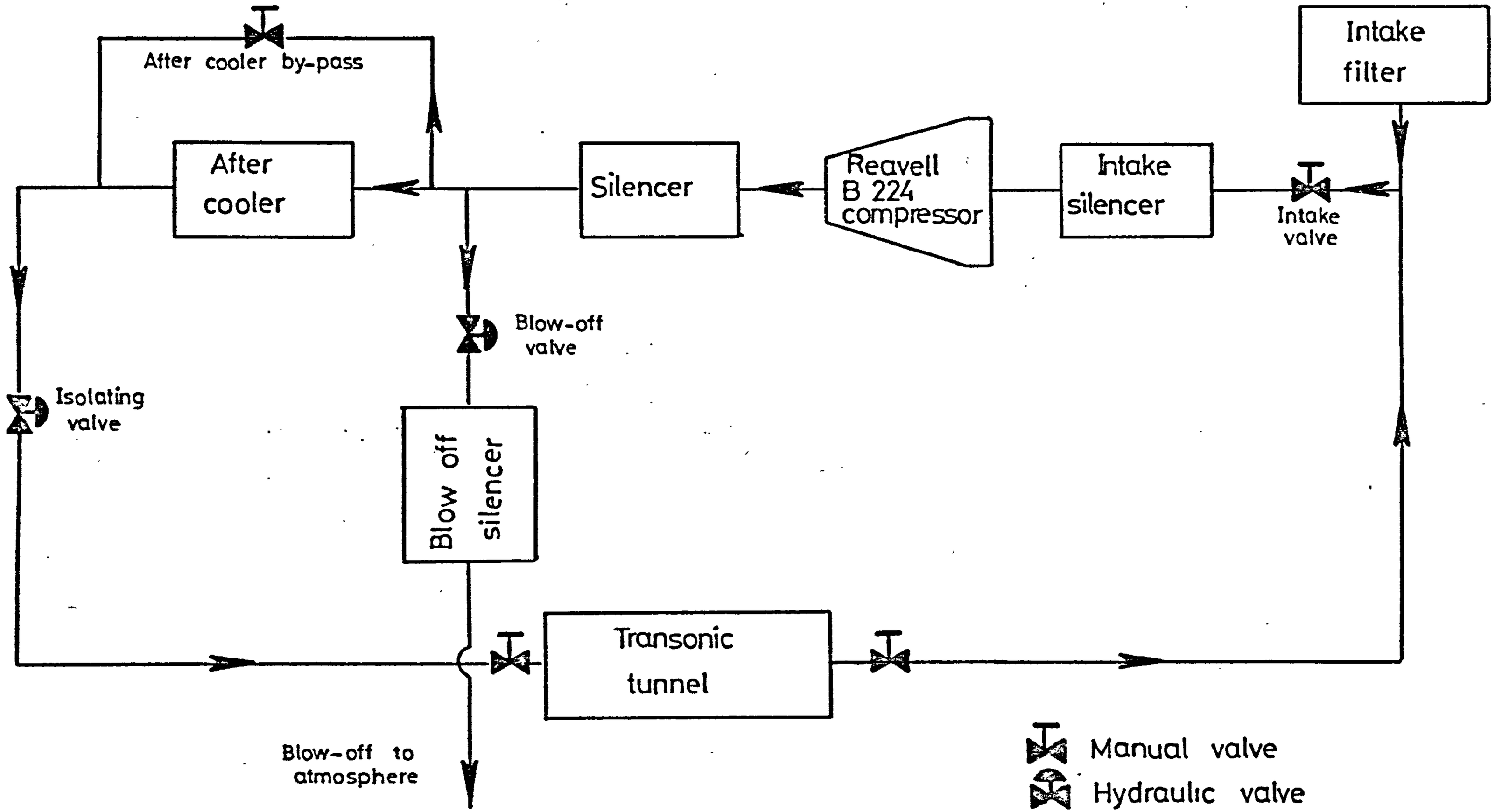

FIG. 16. TRANSONIC TUNNEL AIR CIRCUIT.

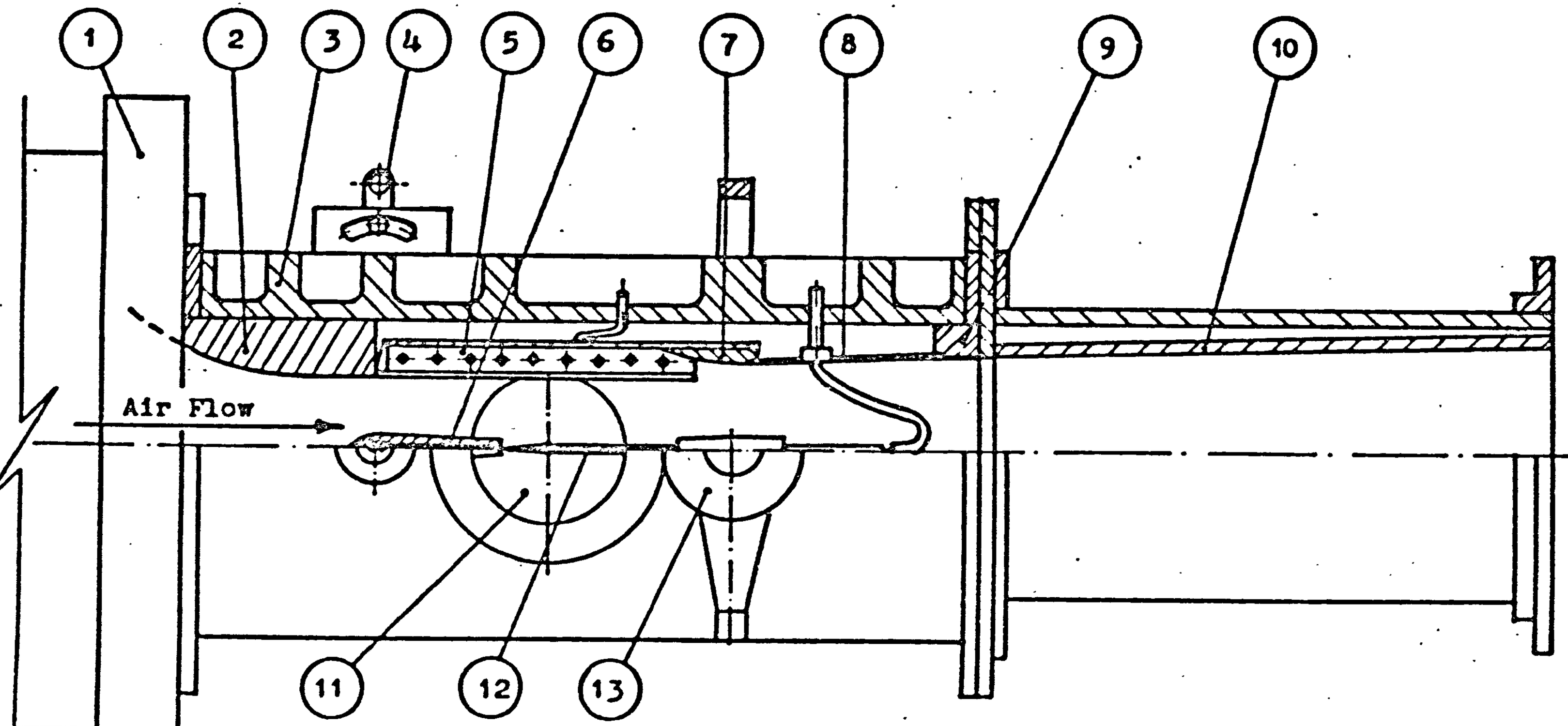

1. Settling Chamber. 2. Subsonic Liner. 3. Housing. 4. Blade Adjustment Gear.
5. Slotted Test Section. 6. Blade. 7. Slotted Wedge. 8. Transition Plate.
9. Transition Liner. 10. Diffuser. 11. Schlieren Glass Window. 12. Probe.
13. Traverse Gear.

General Layout of 4" High Speed Wind Tunnel.

Fig. 17.

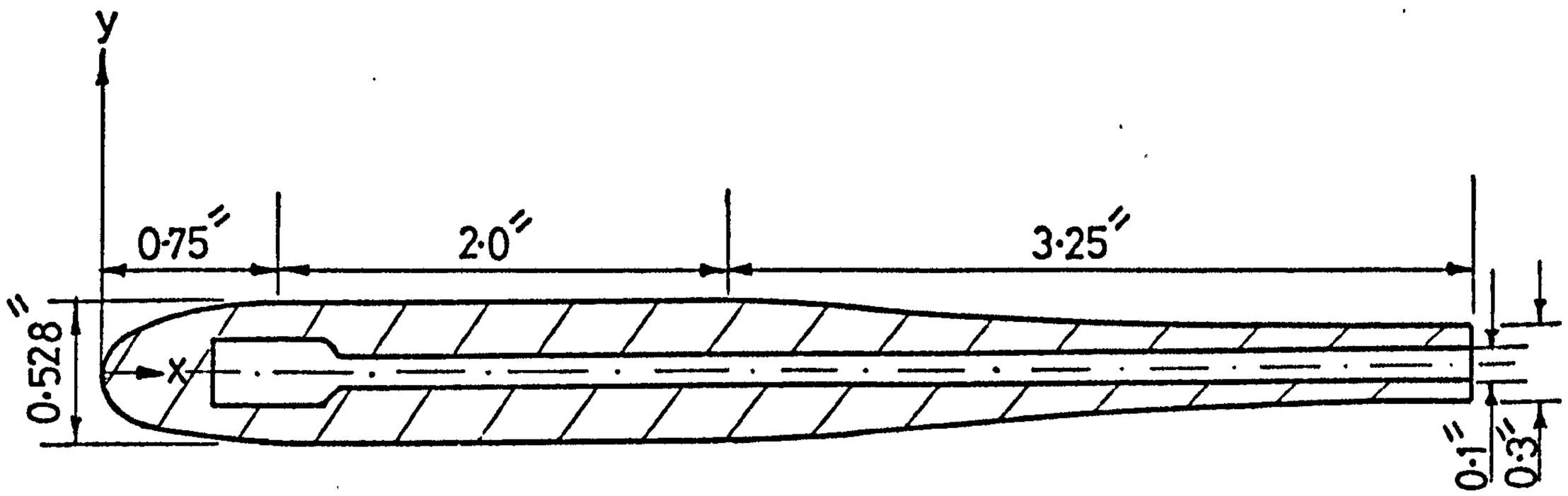

FIG.18. THE MODEL CROSS-SECTION.

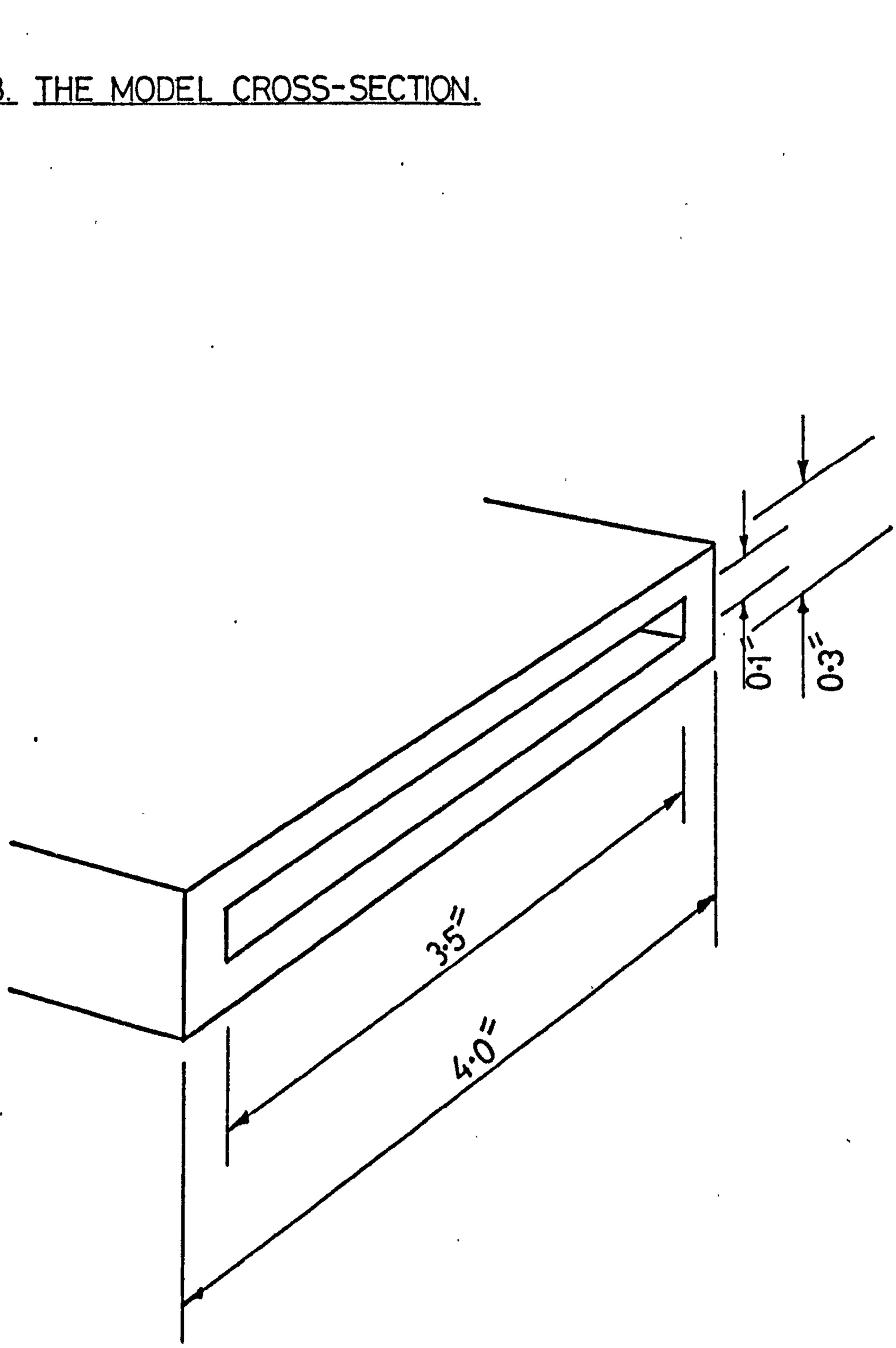

FIG.19. THE BASE GEOMETRY.

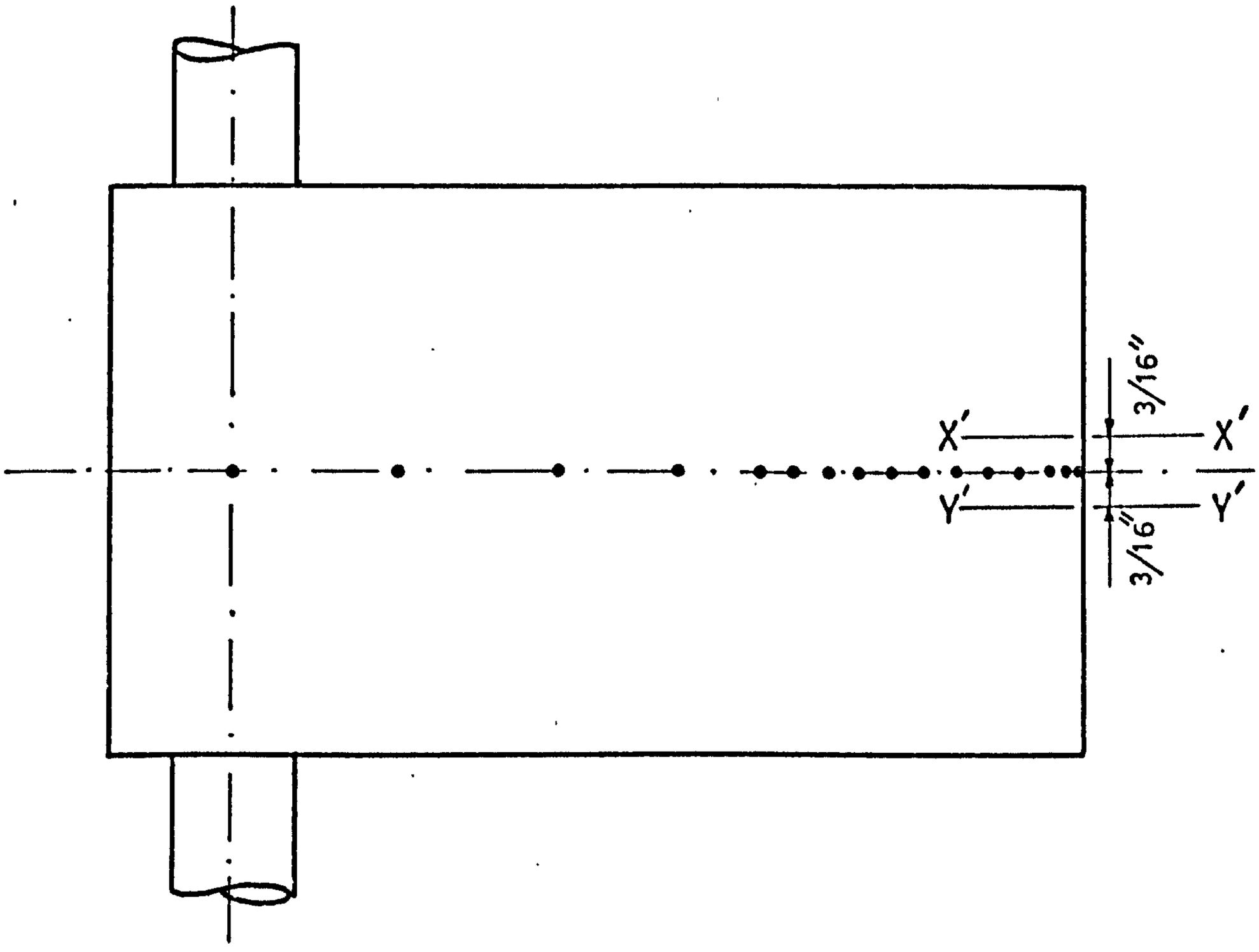

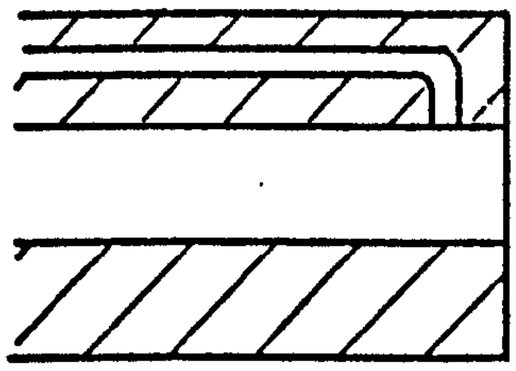

YY' view showing slot tapping.

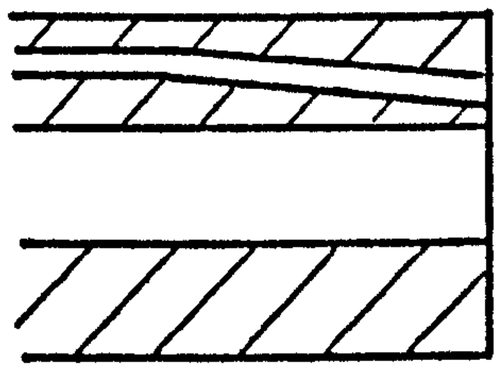

XX' view showing base tapping.

Upper surface				Lower surface	
Tapping No.	Distance from base in.	Tapping No.	Distance from base in.	Tapping No.	Distance from base in.
1	0·03	9	1·4	1	0·03
2	0·1	10	1·6	2	0·1
3	0·2	11	1·8	3	1·0
4	0·4	12	2·0	4	2·0
5	0·6	13	2·5	5	3·25
6	0·8	14	3·25	6	5·25
7	1·0	15	4·25		
8	1·2	16	5·25		

FIG.20. PRESSURE TAPPING ARRANGEMENT.

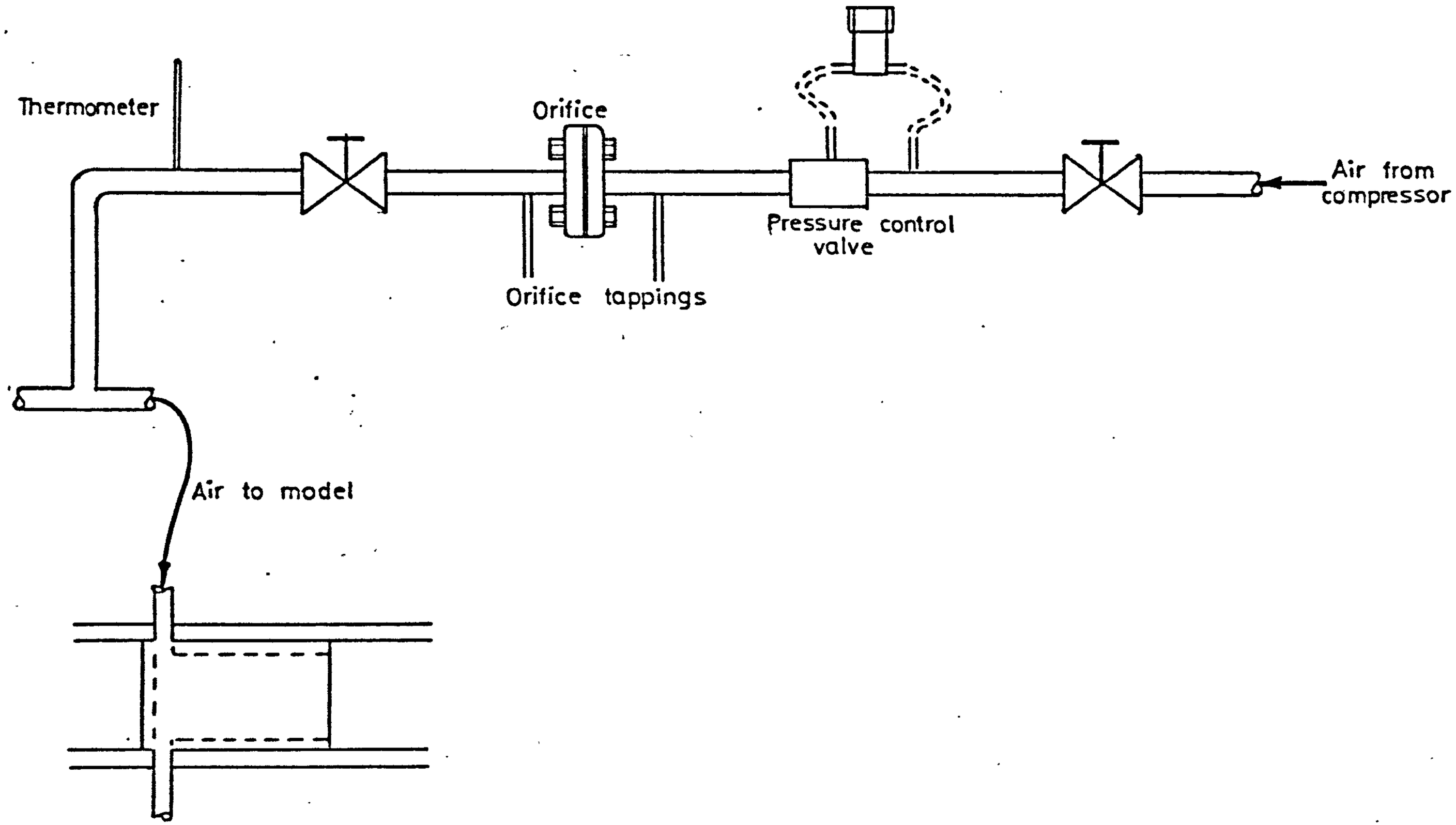

FIG.21. AIR BLEED CIRCUIT.

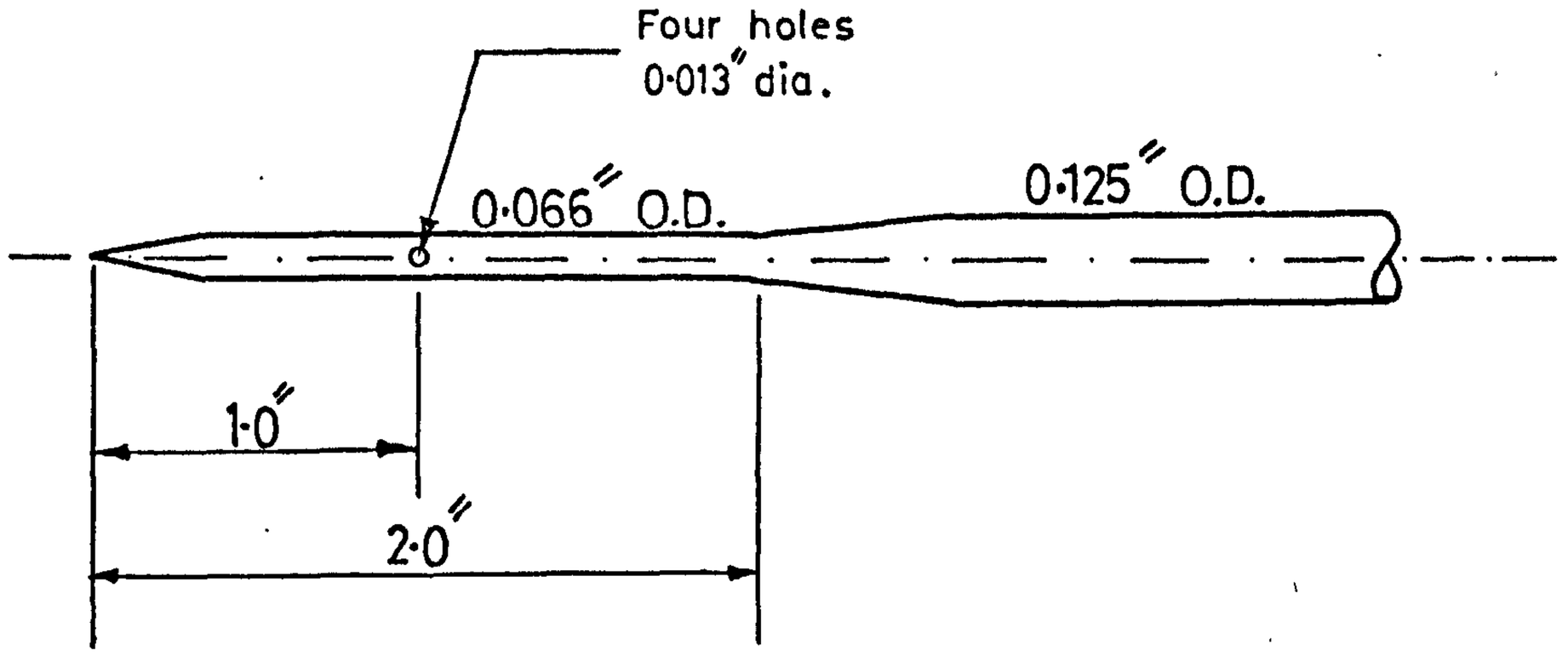

FIG. 22.a. STATIC-PROBE.

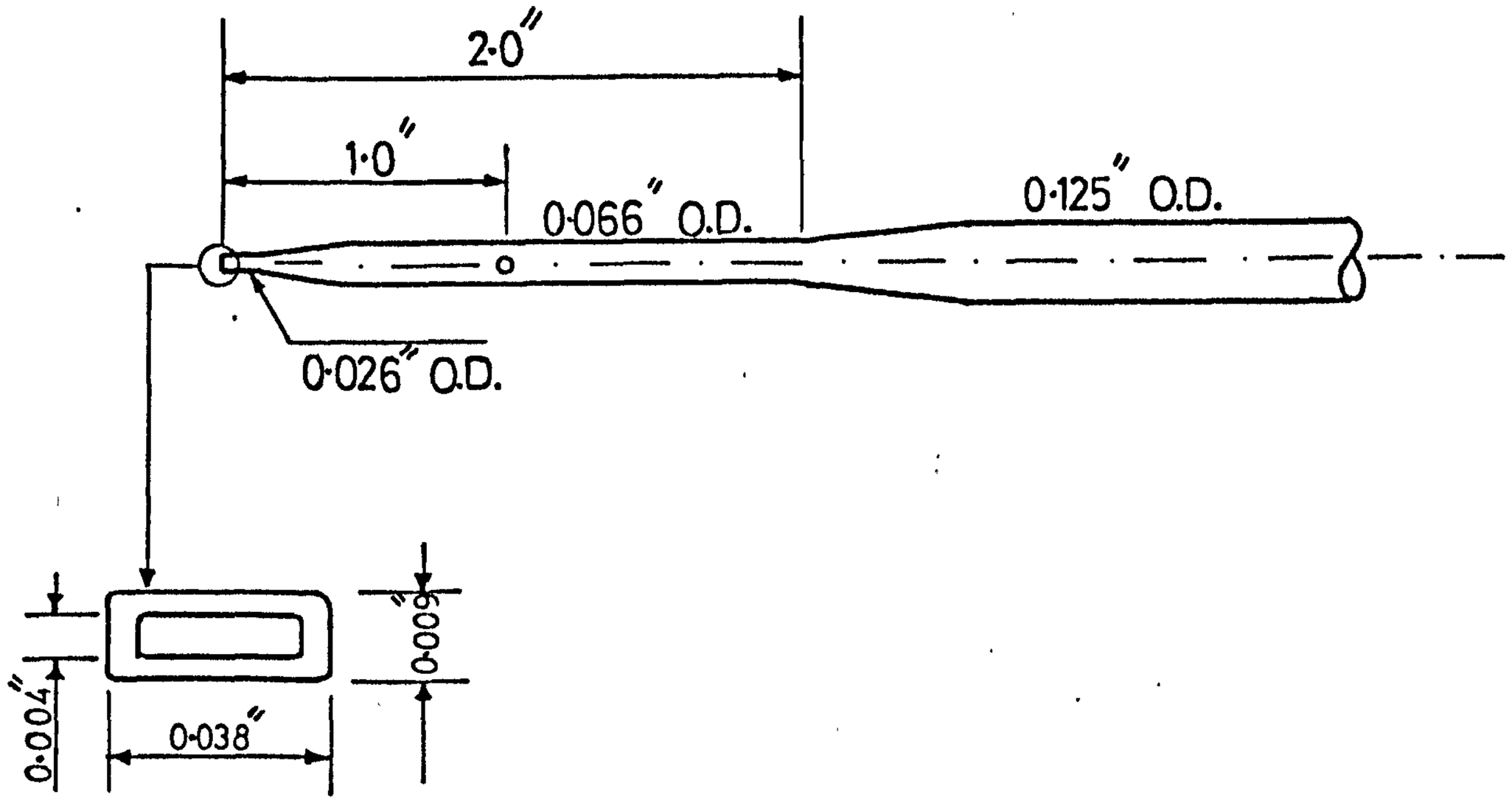

FIG. 22.b. PITOT-STATIC PROBE.

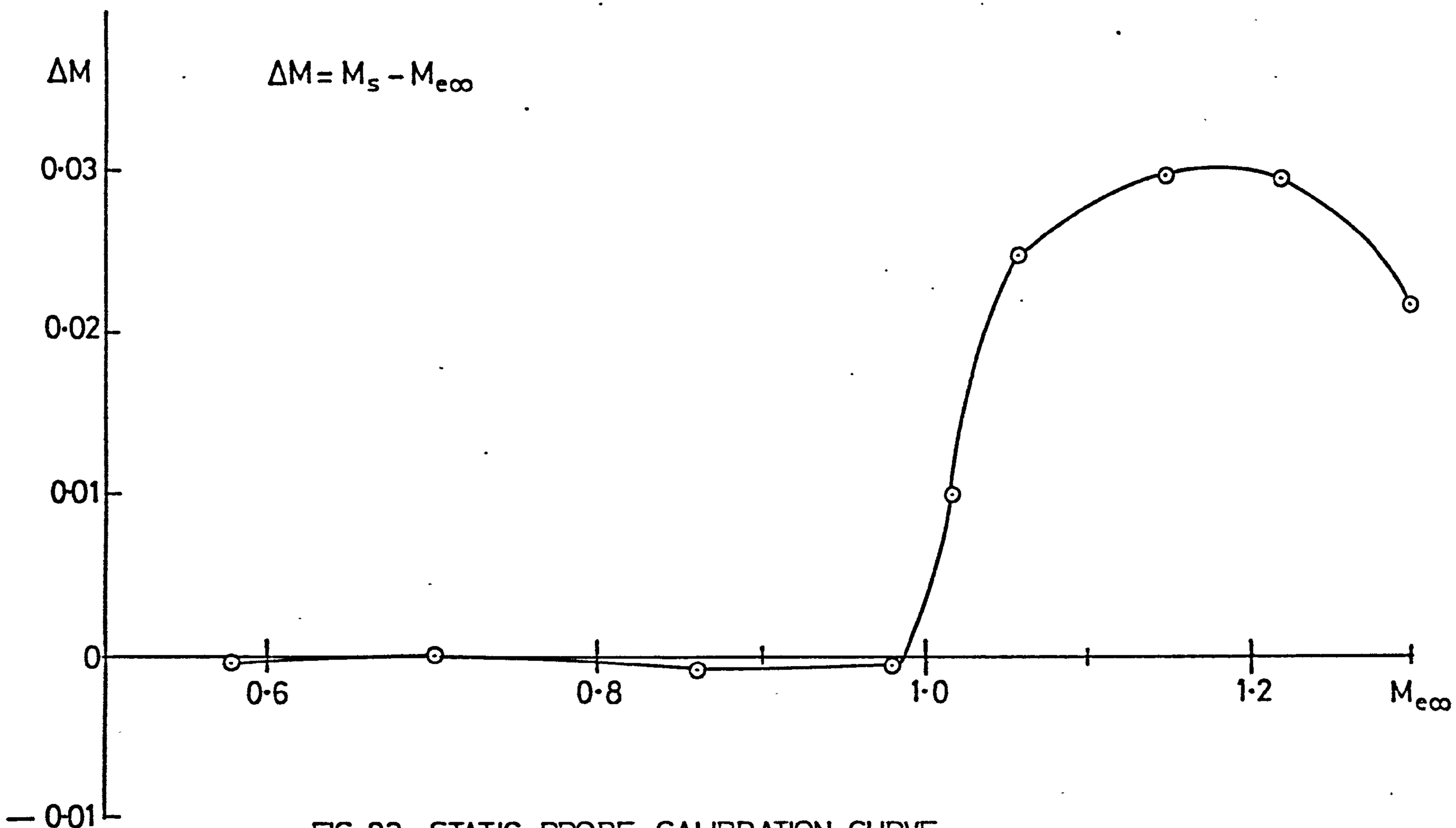

FIG. 23. STATIC PROBE CALIBRATION CURVE.

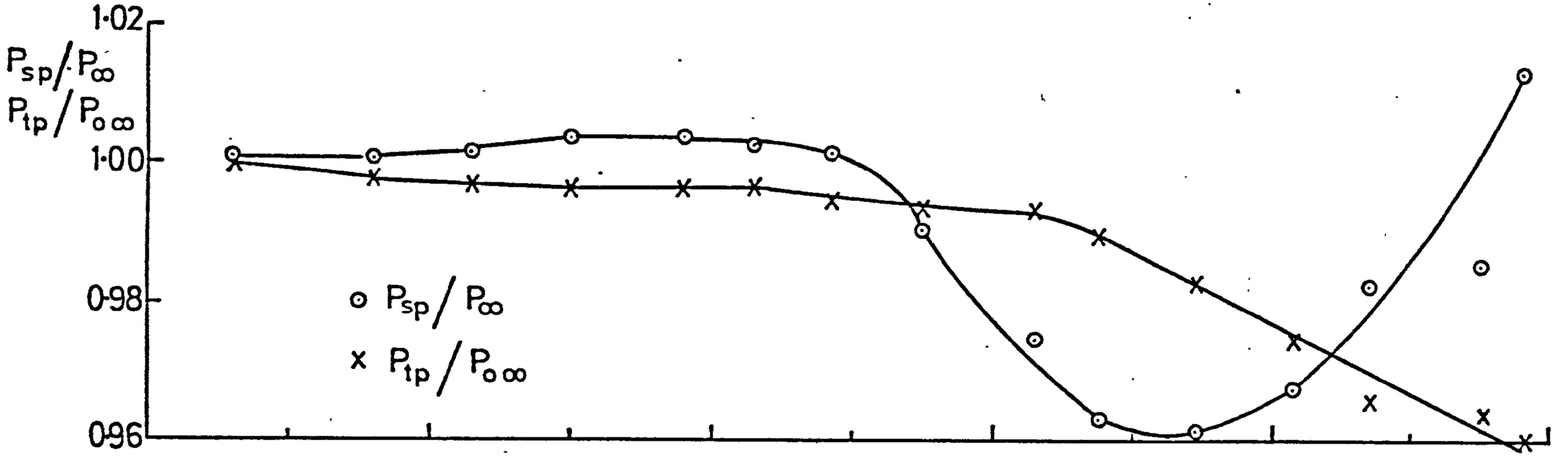

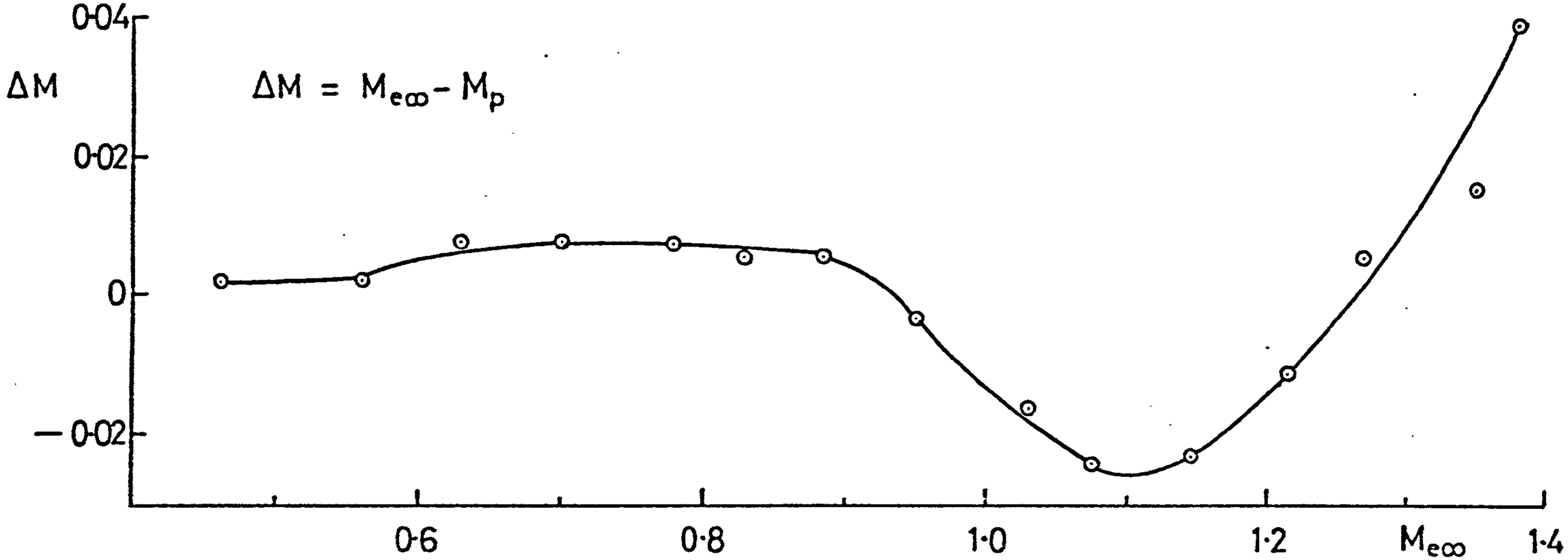

FIG. 24. PITOT-STATIC PROBE CALIBRATION CURVE.

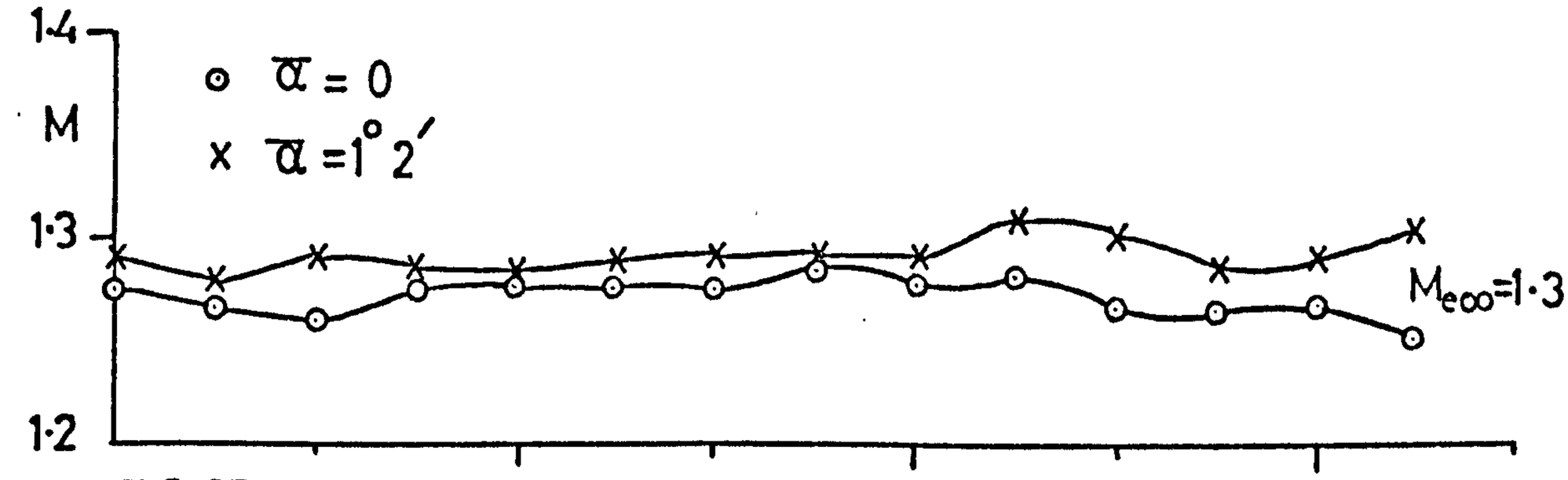

FIG.25.a. EFFECT OF WALL DIVERGENCE ANGLE.

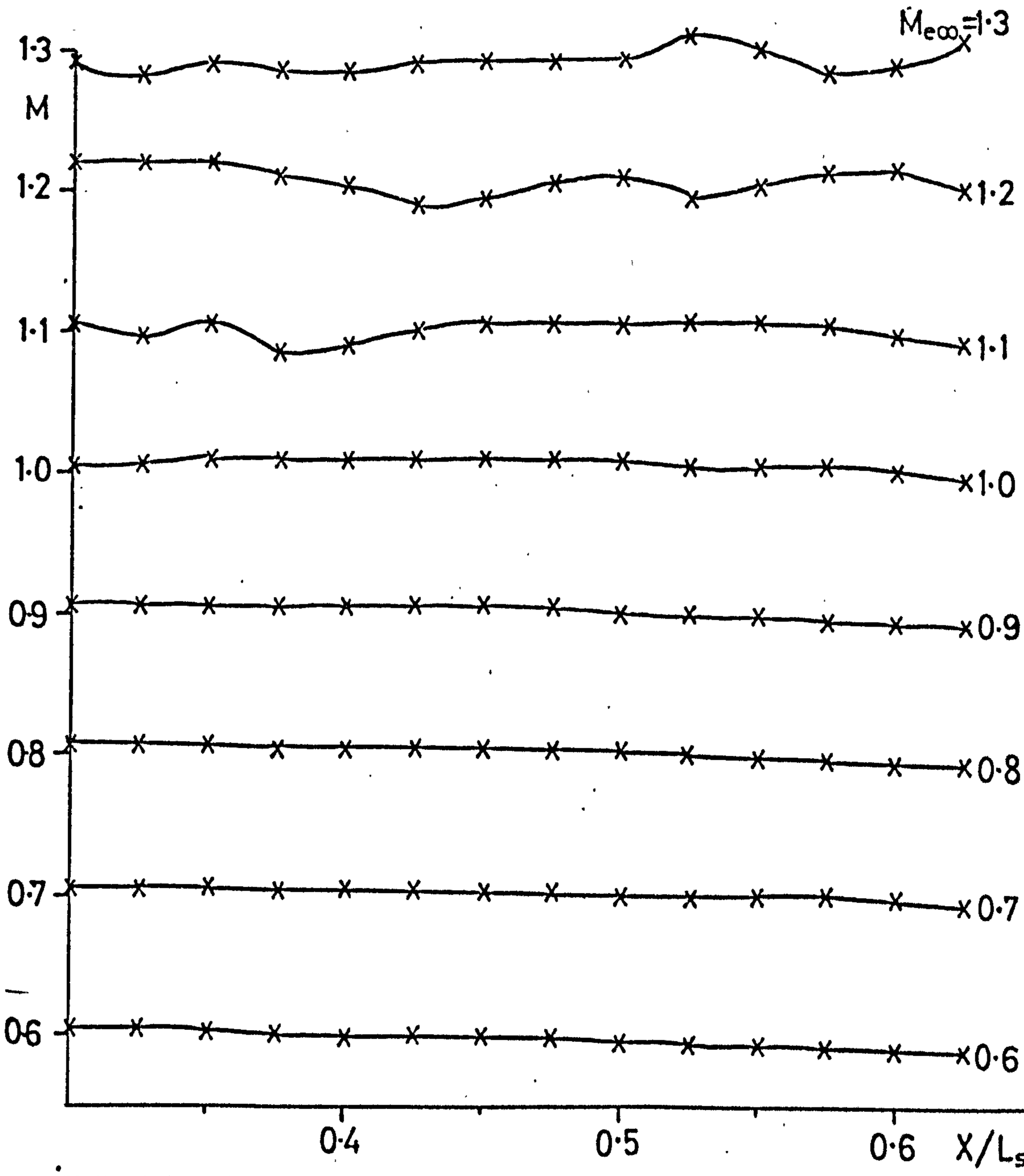

FIG.25.b. CALIBRATION CURVE OF THE WIND TUNNEL WORKING SECTION.

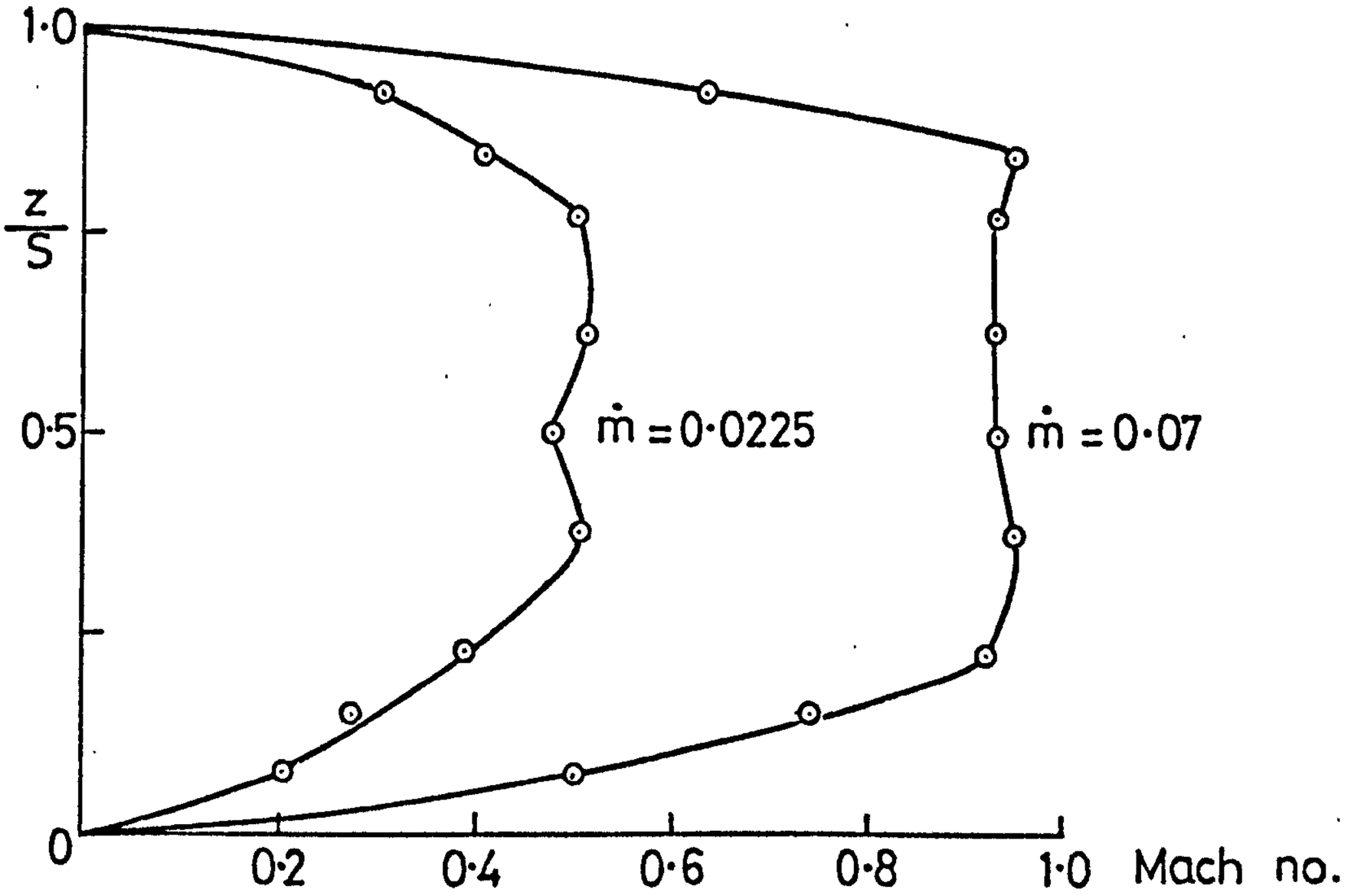

FIG. 26. TYPICAL BASE BLEED SPANWISE DISTRIBUTION.

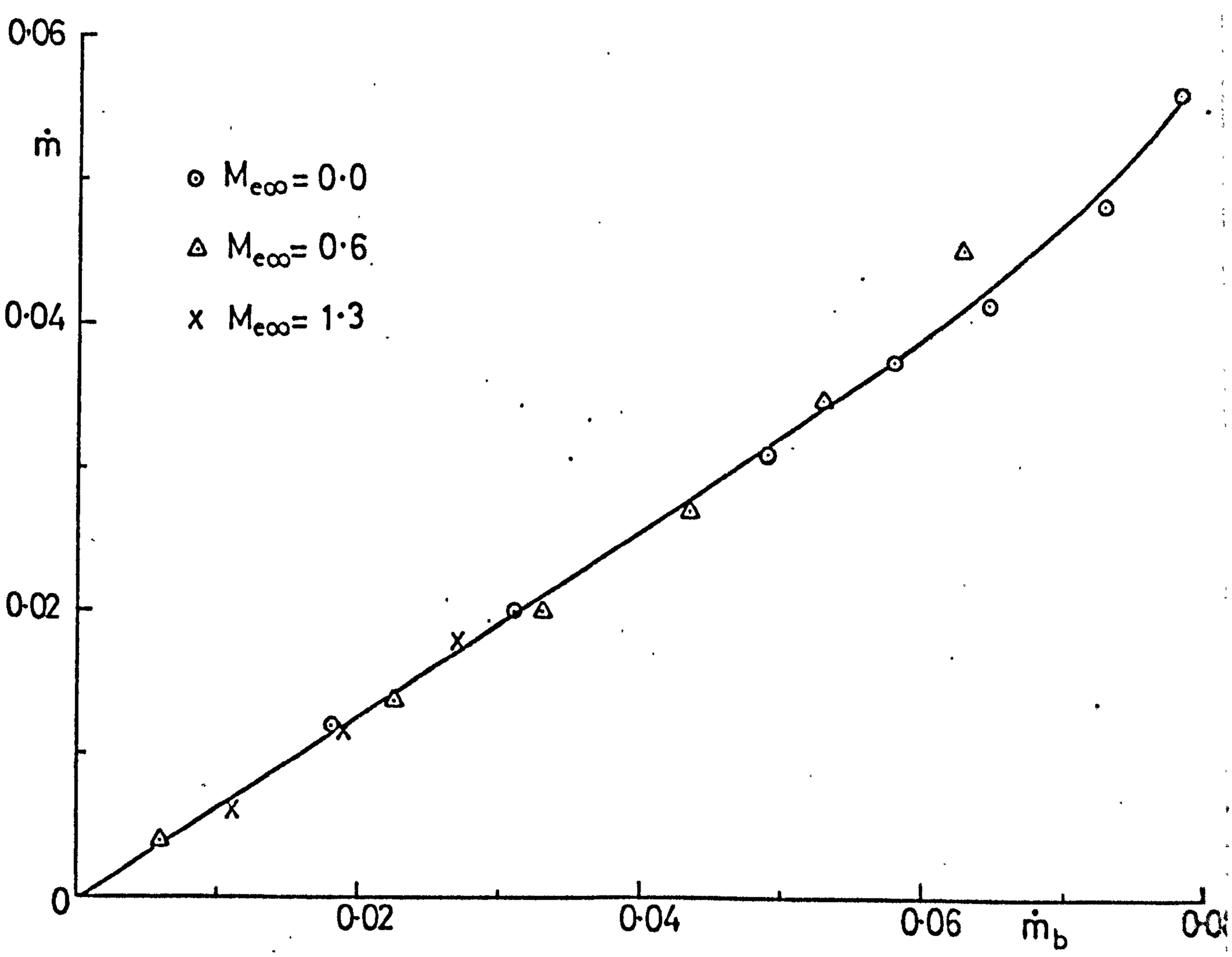

FIG. 27. RATE OF BASE BLEED CALIBRATION.

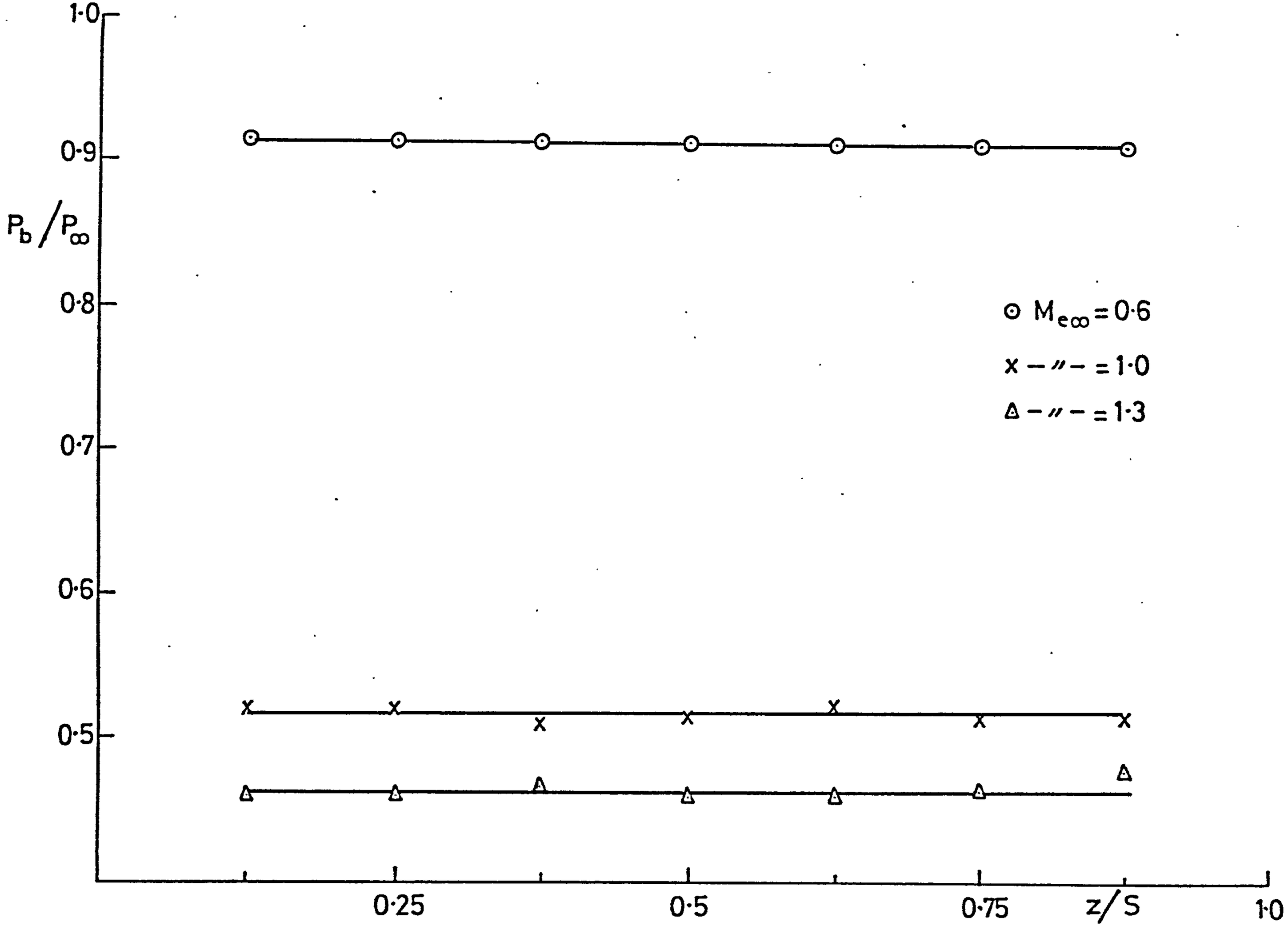

FIG.28. BASE PRESSURE ACROSS THE SPAN. ($\dot{m}$ = 0, d = ·024")

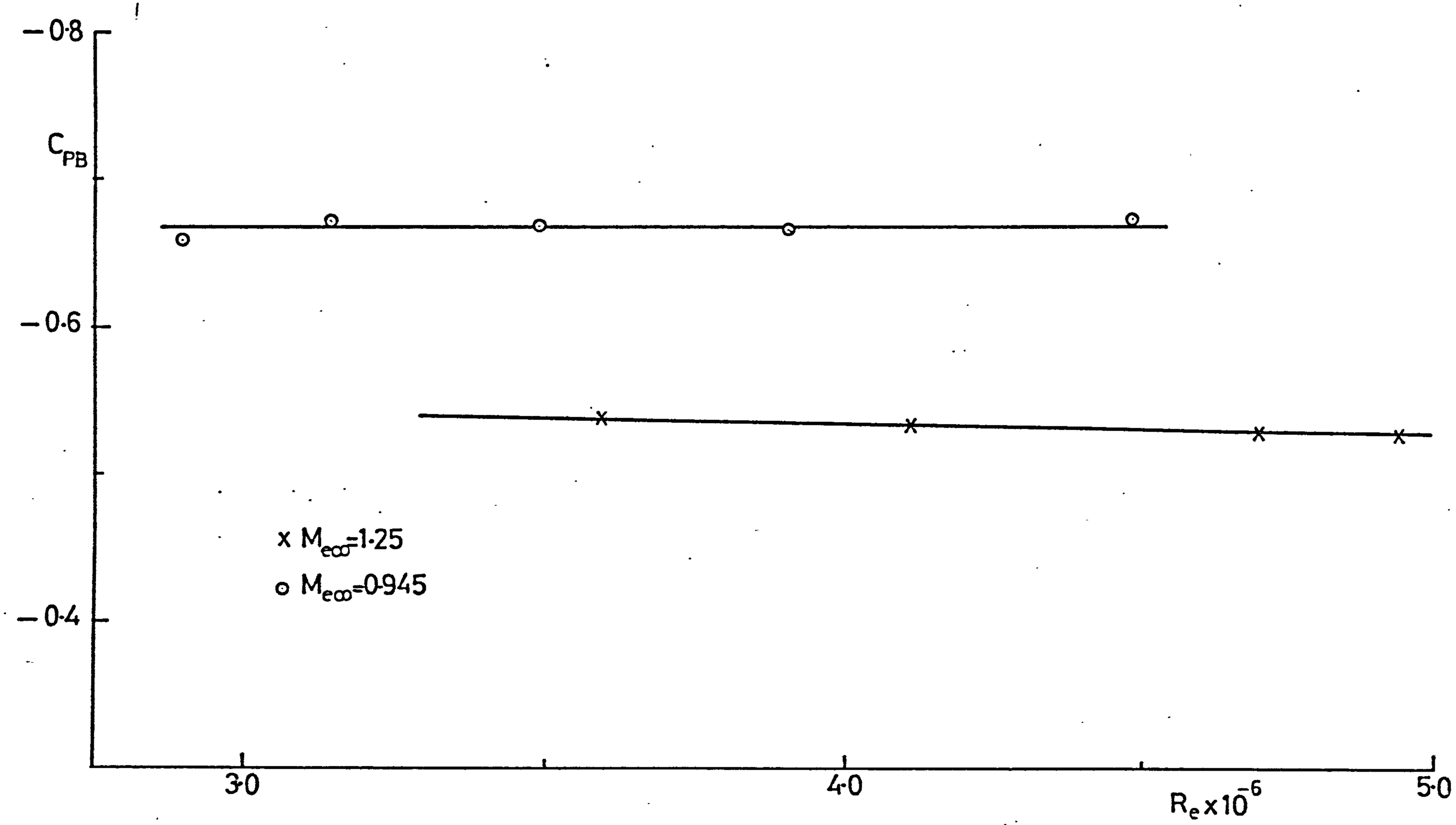

FIG.29. EFFECT OF REYNOLDS Nº. ON BASE PRESSURE. (d = ·007")

FIG.30. UPPER SURFACE MACH Nº DISTRIBUTION α=0
(m=0, d=0·024")

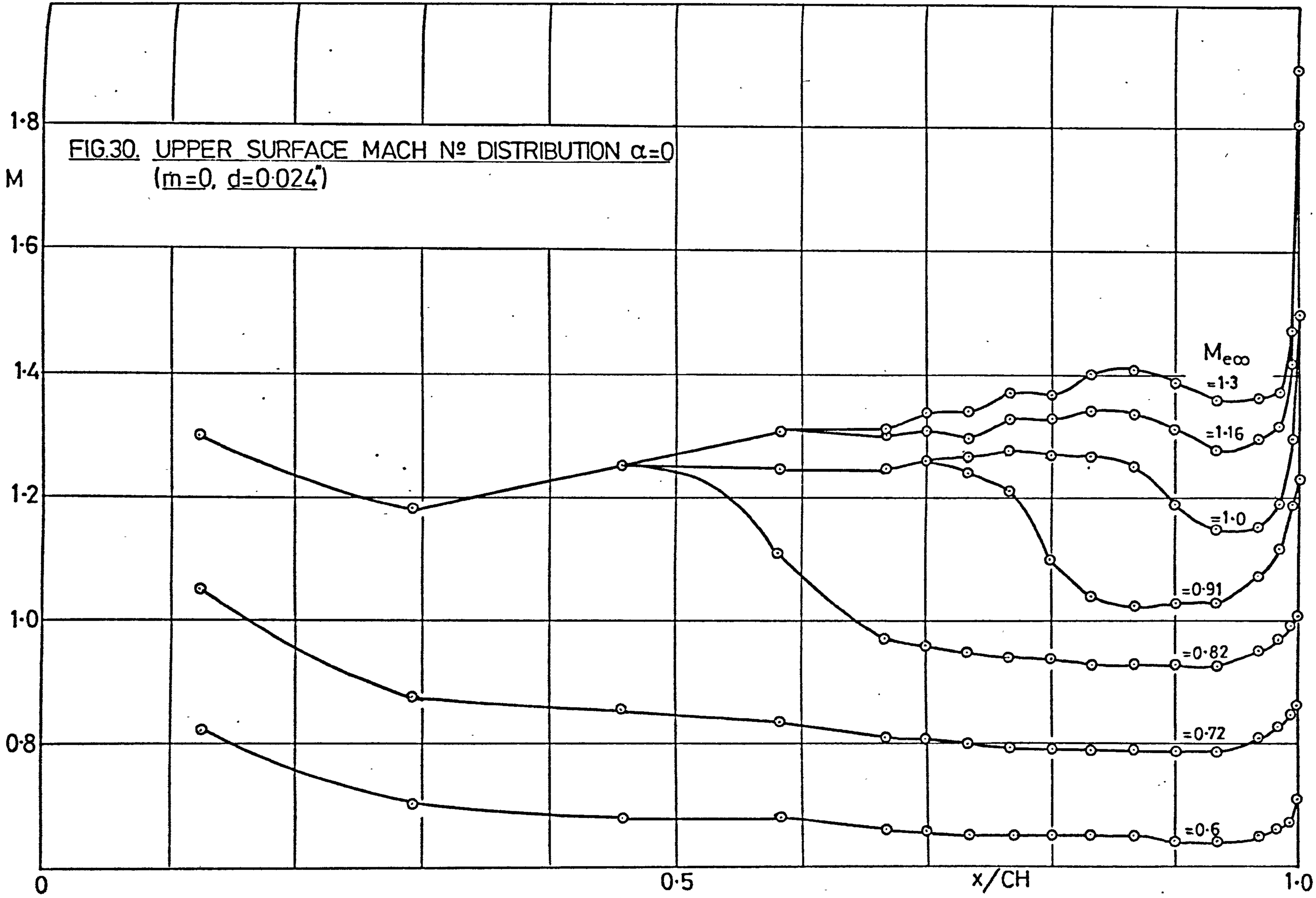

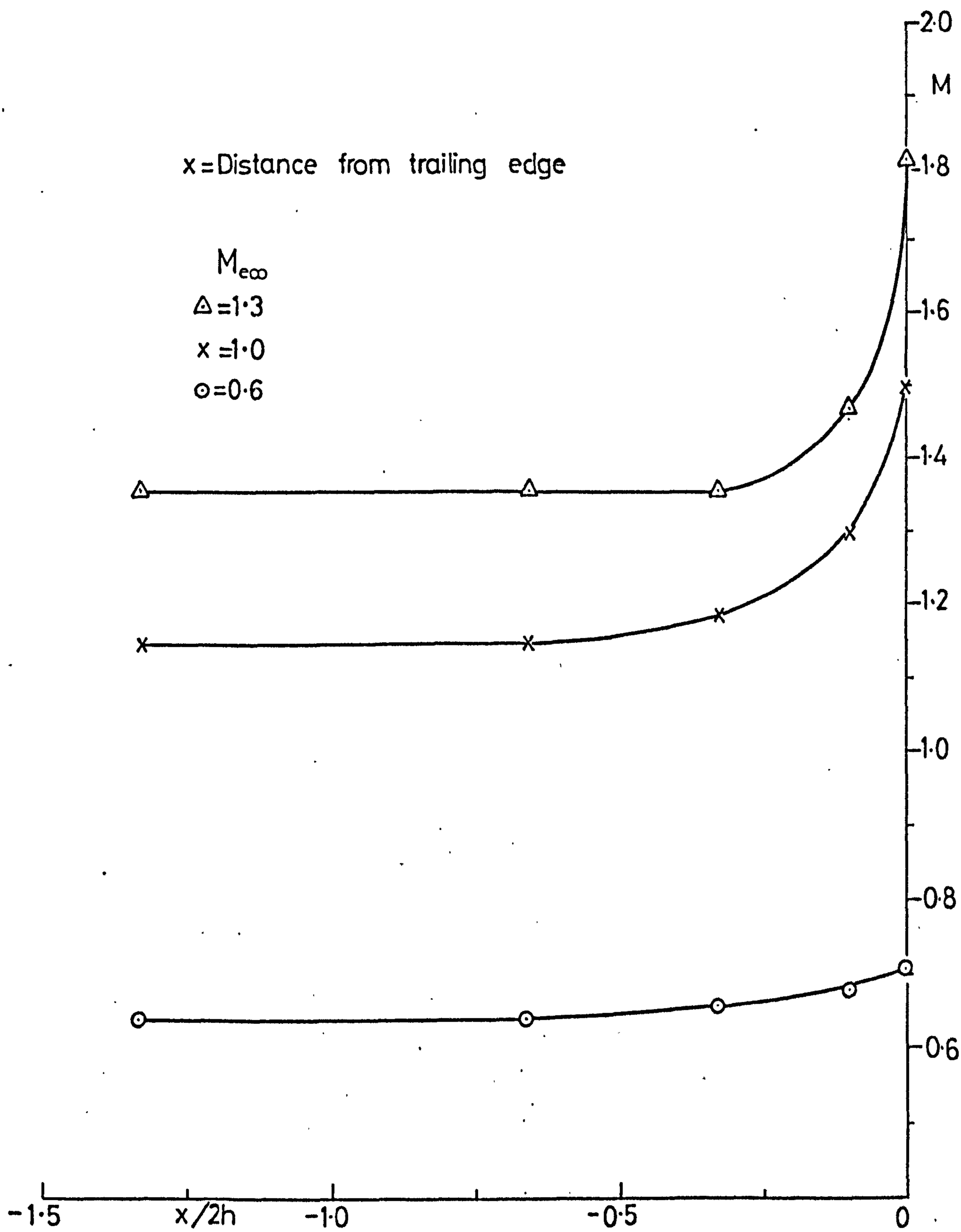

FIG.31. EFFECT OF BASE PRESSURE ON THE PRESSURE DISTRIBUTION UPSTREAM THE TRAILING EDGE. ($\alpha = 0$, $\dot{m} = 0$, d=·024")

FIG.32. EFFECT OF MACH Nº ON BASE PRESSURE

$\alpha = 0$, $\dot{m} = 0$, $d = \cdot 024"$.

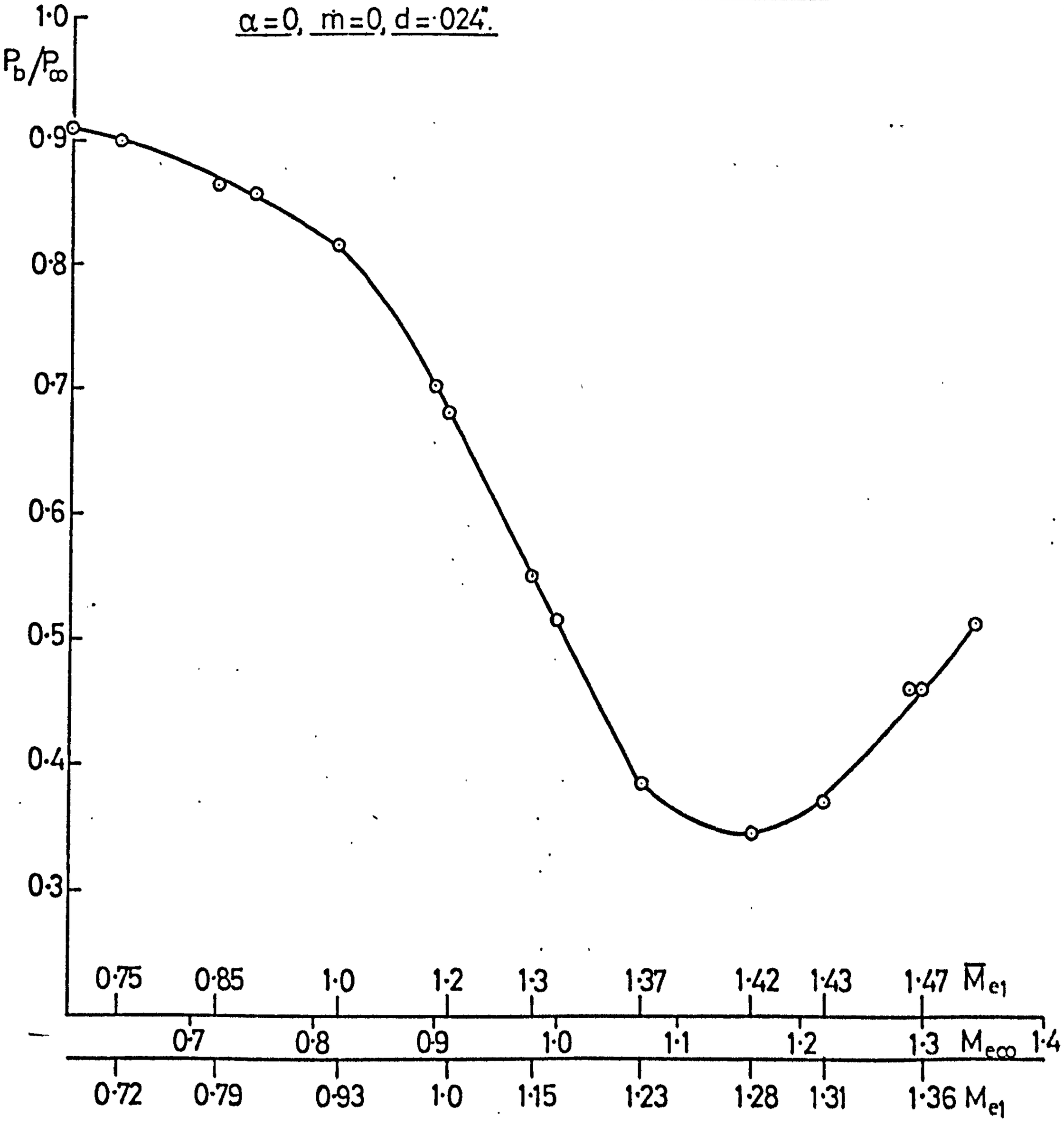

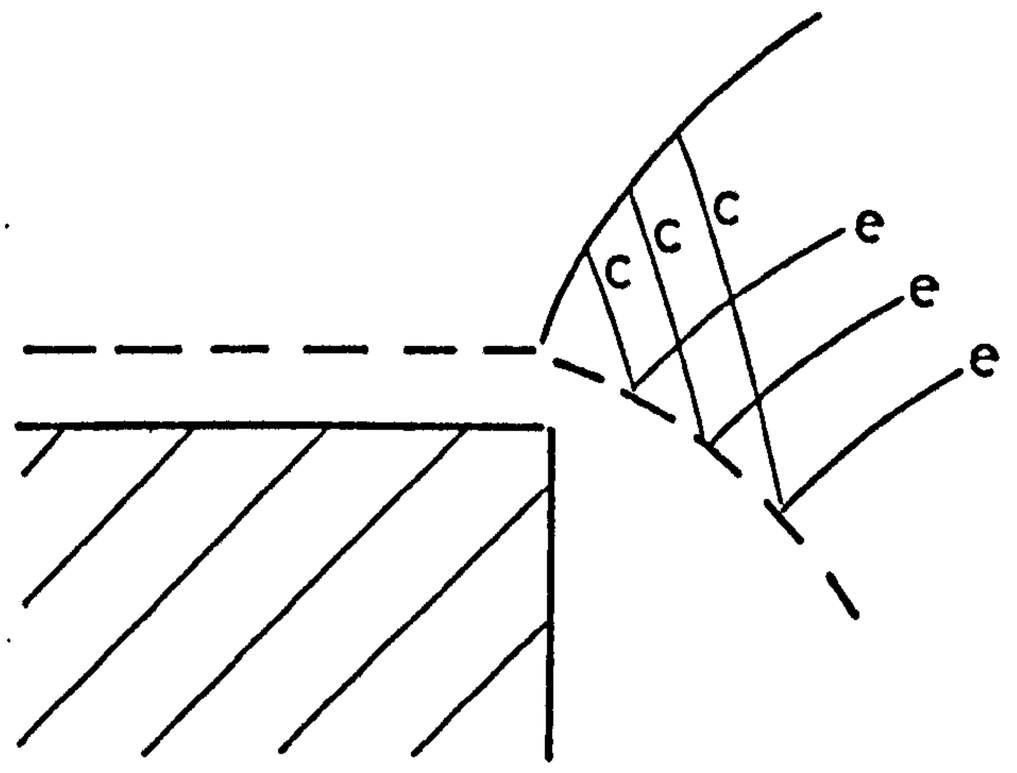

(A) $M_i < \sqrt{2}$

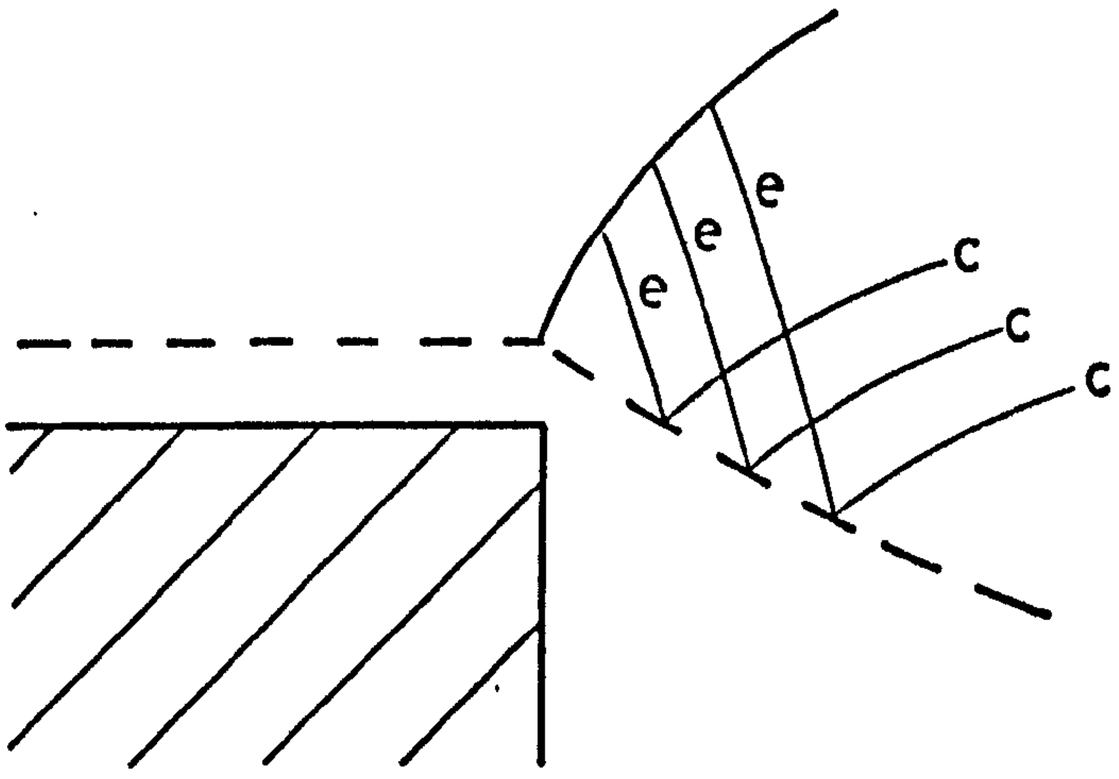

(B) $M_i > \sqrt{2}$

— — — Sonic line

c Compression wave

e Expansion wave

FIG.33. SCHEMATIC DIAGRAM OF THE EFFECT OF THE REFLECTED WAVES ON THE SHAPE OF THE SONIC LINE.

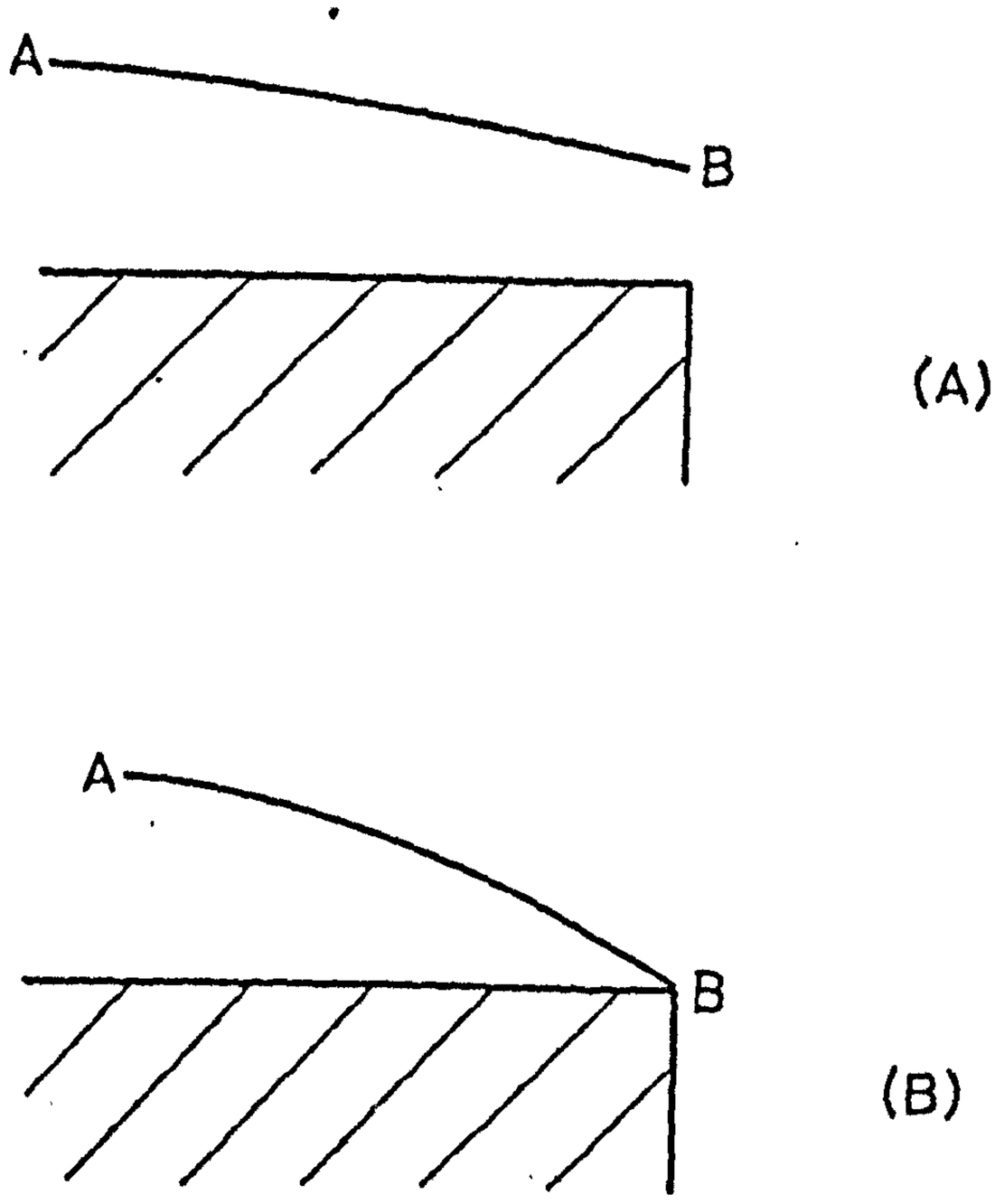

FIG. 34. THE SONIC LINE.

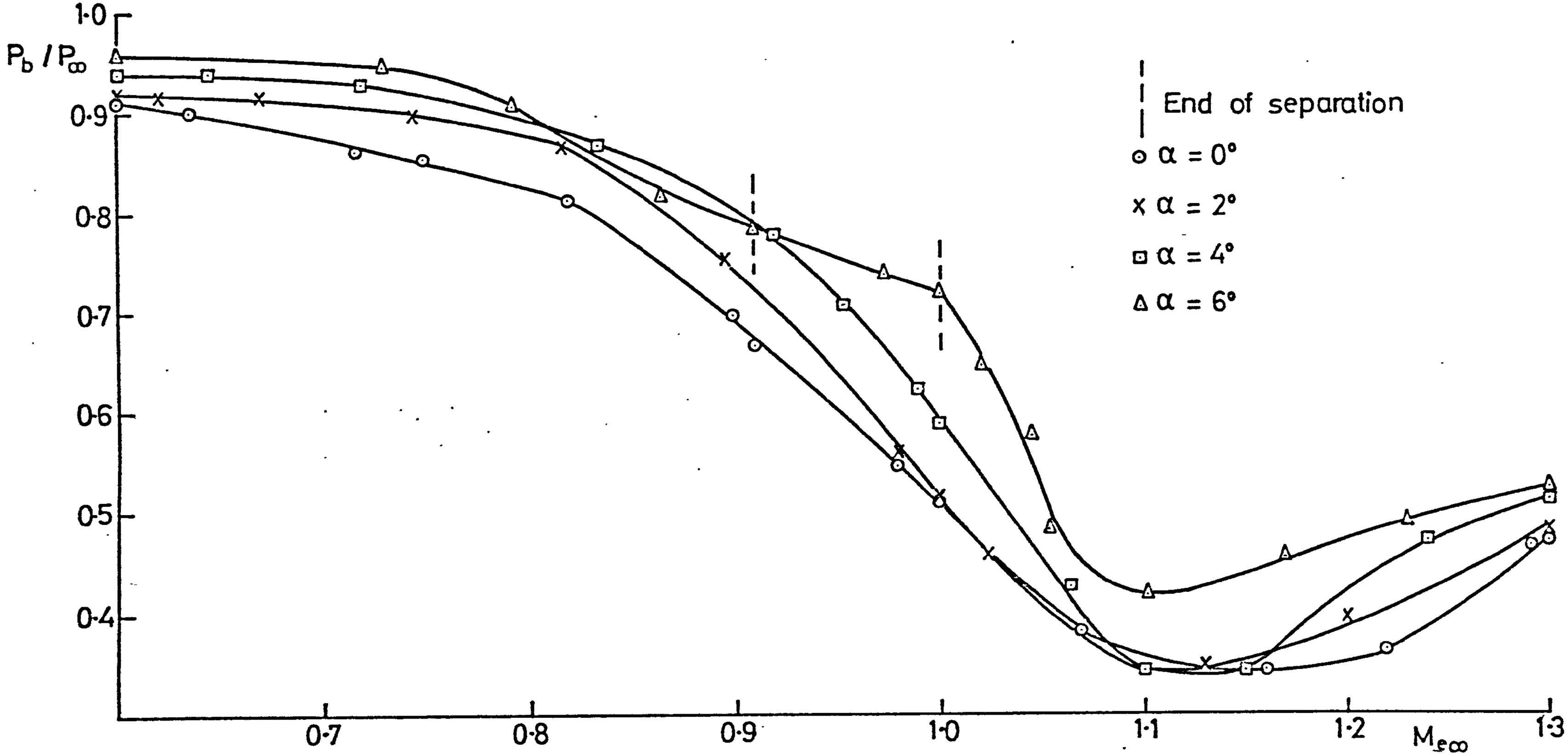

FIG. 35. VARIATION OF BASE PRESSURE WITH MACH Nº (m = 0, d = ·024")

FIG.36a. UPPER SURFACE MACH Nº DISTRIBUTION $\alpha = 2°$ ($\dot{m} = 0$, $d = \cdot 024$")

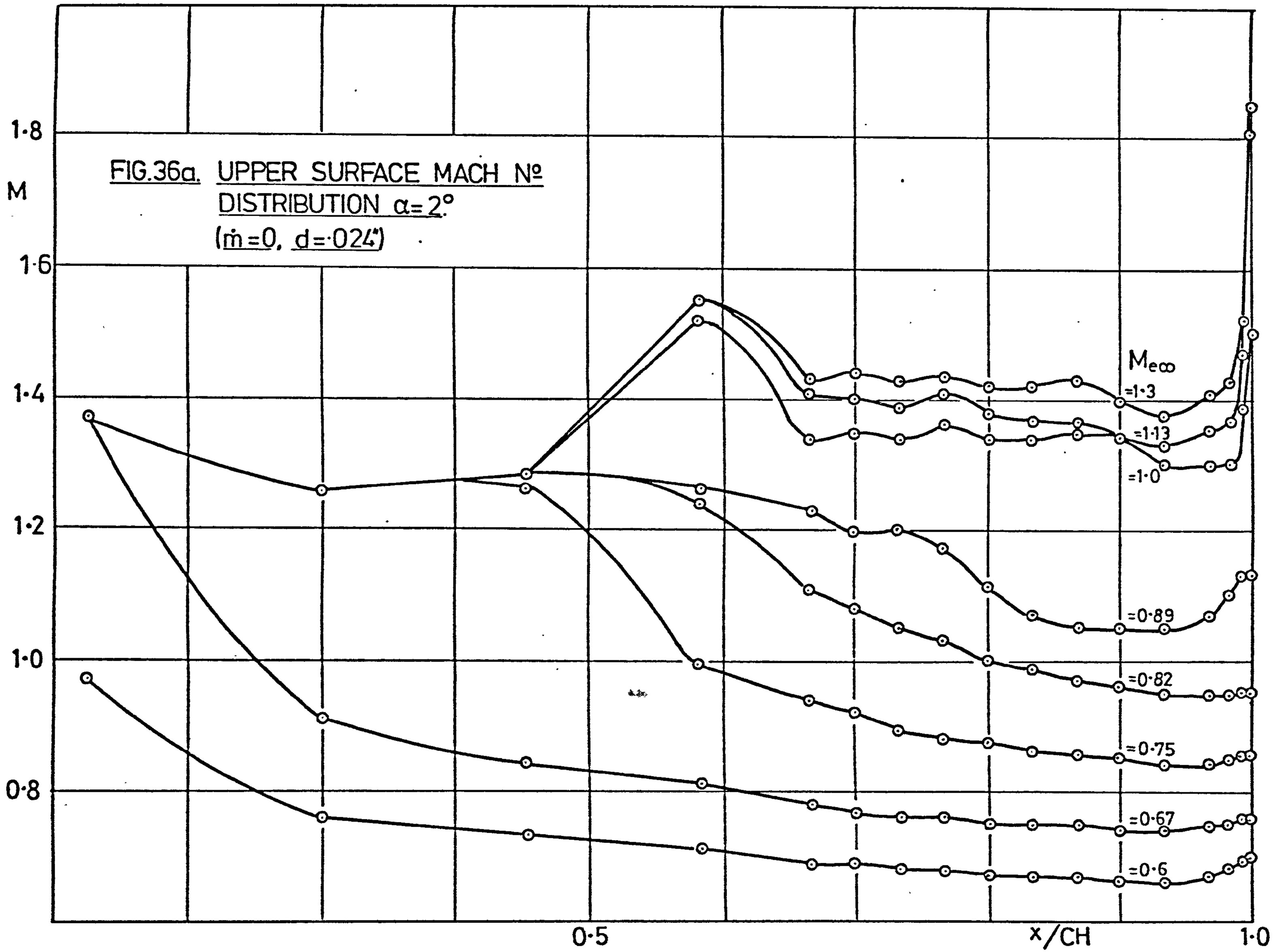

FIG.36b. UPPER SURFACE MACH Nº DISN
$\alpha = 4°$ ($\dot{m} = 0$, $d = .024"$).

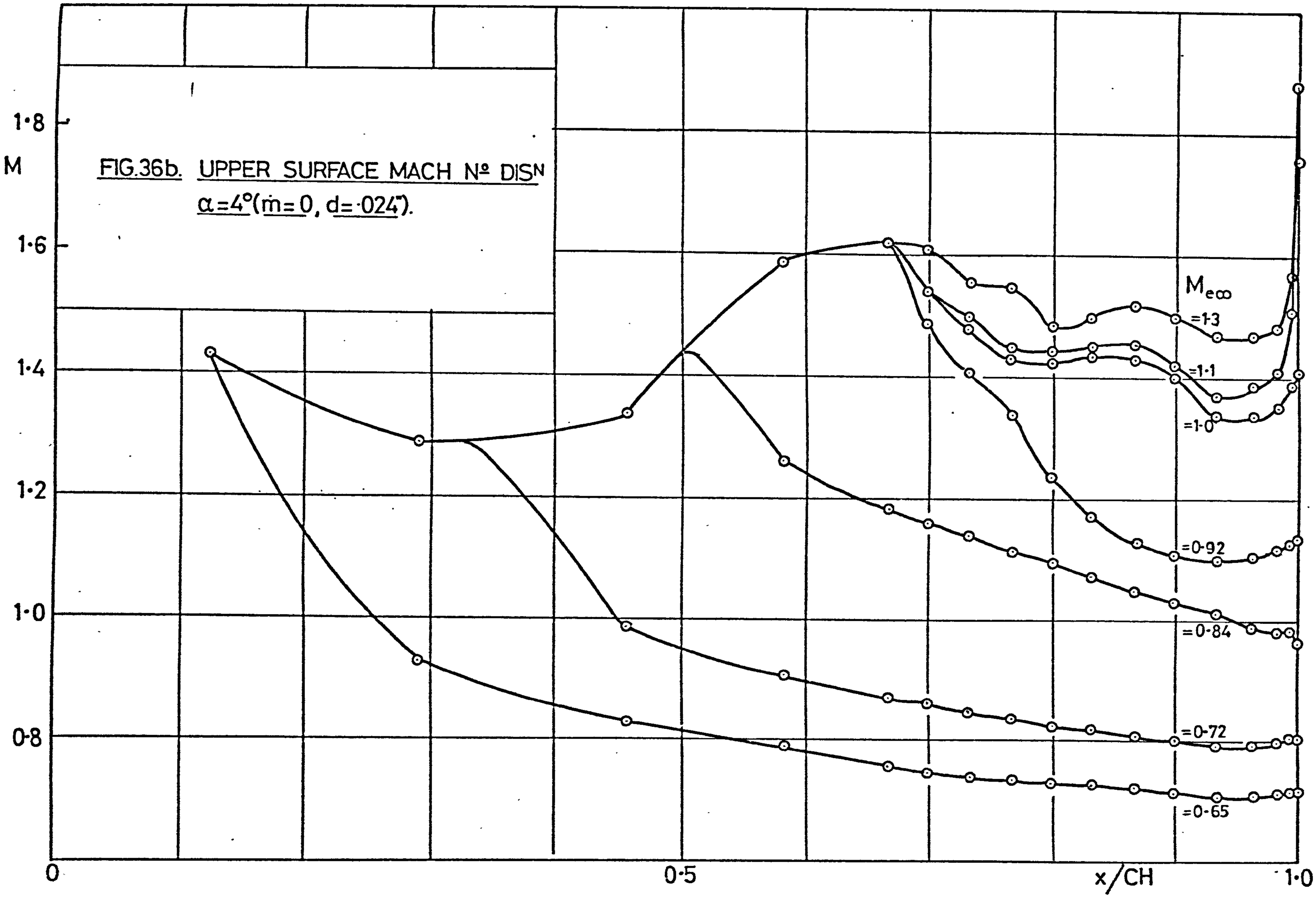

FIG.36c. UPPER SURFACE MACH Nº DISN
$\alpha = 6°$ ($\dot{m}=0$, $d=\cdot024"$).

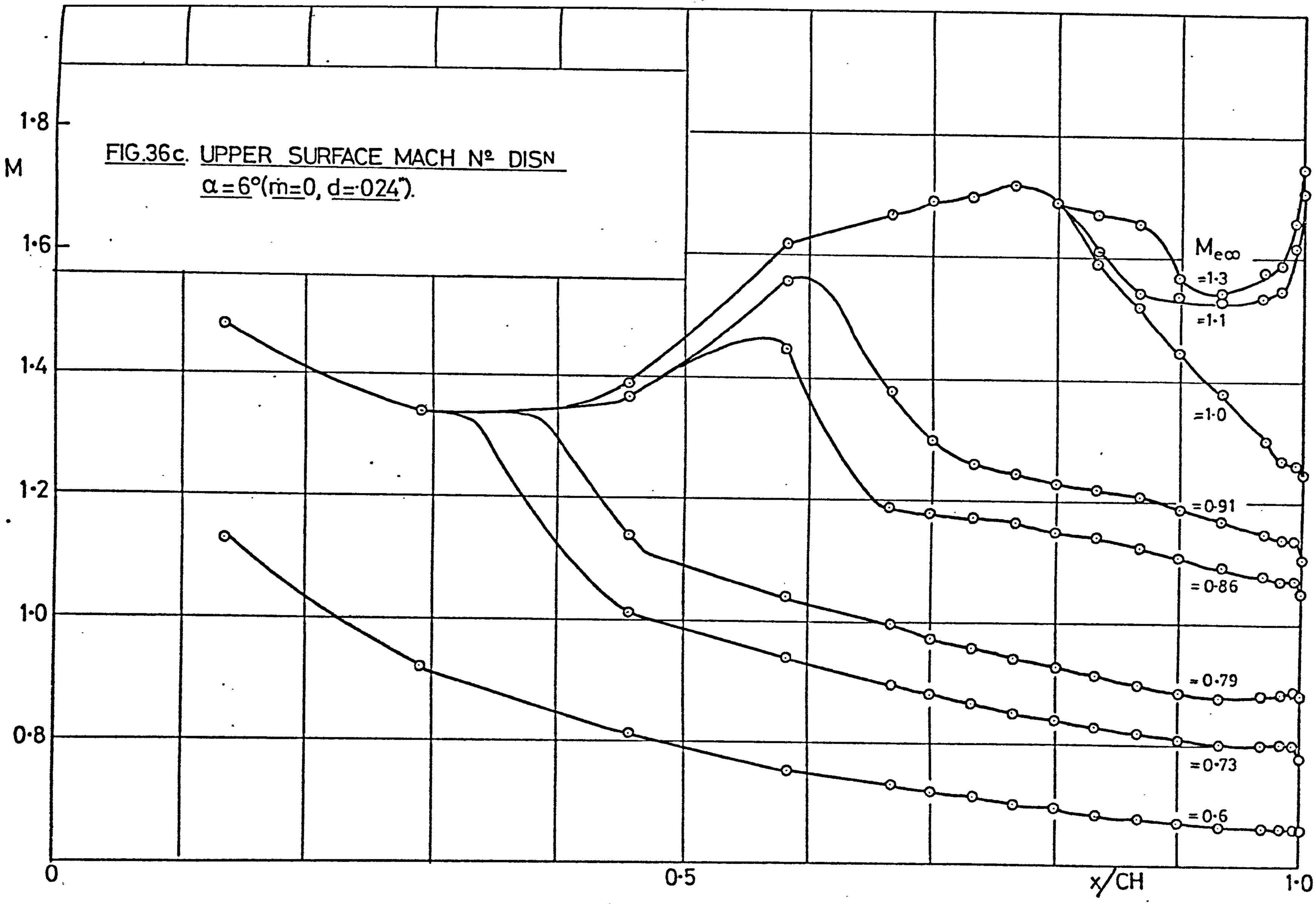

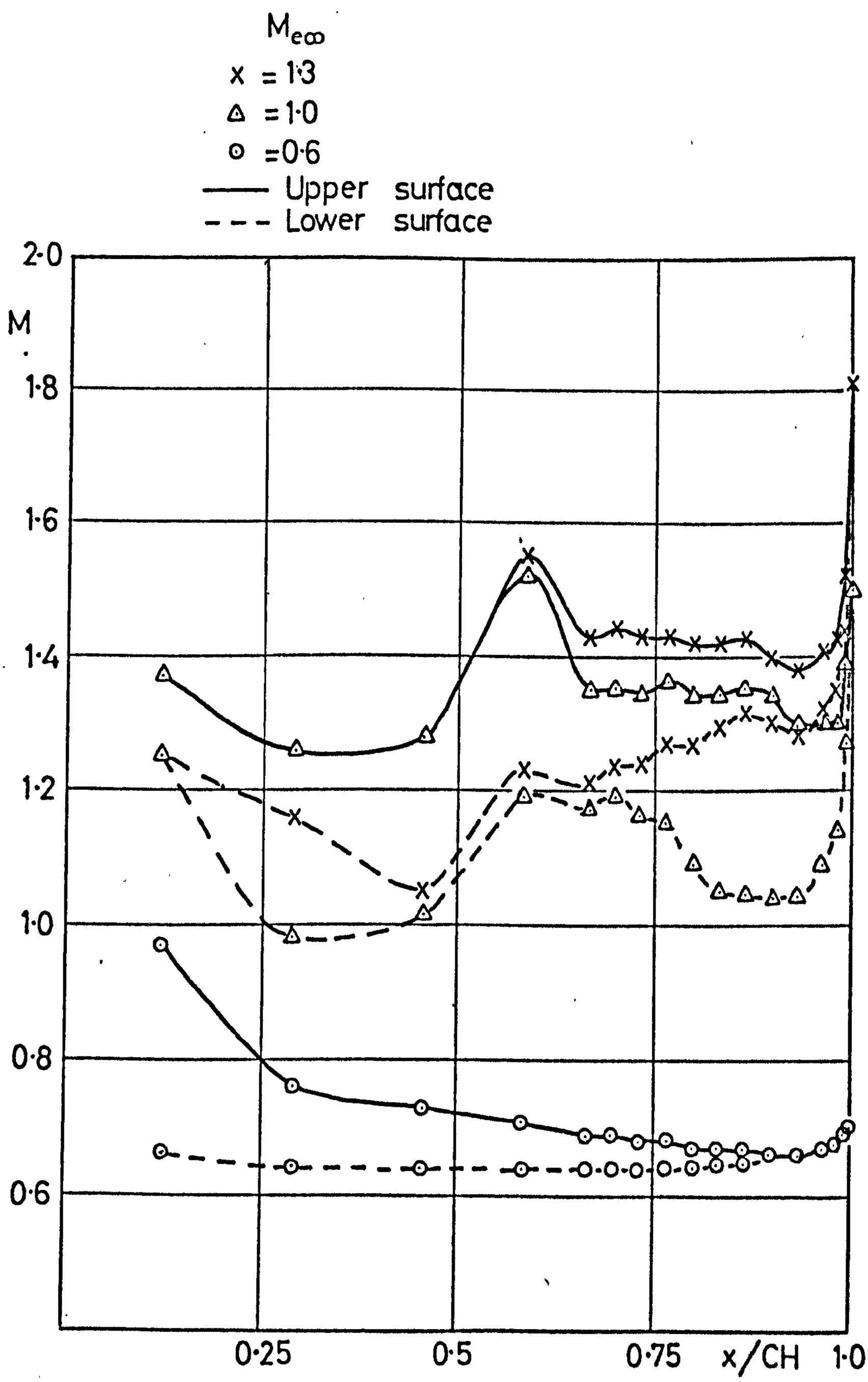

FIG.37a. MACH Nº DISTRIBUTIONS ON THE UPPER & LOWER SURFACES $\alpha = 2°$ ($\dot{m} = 0$, d = ·024").

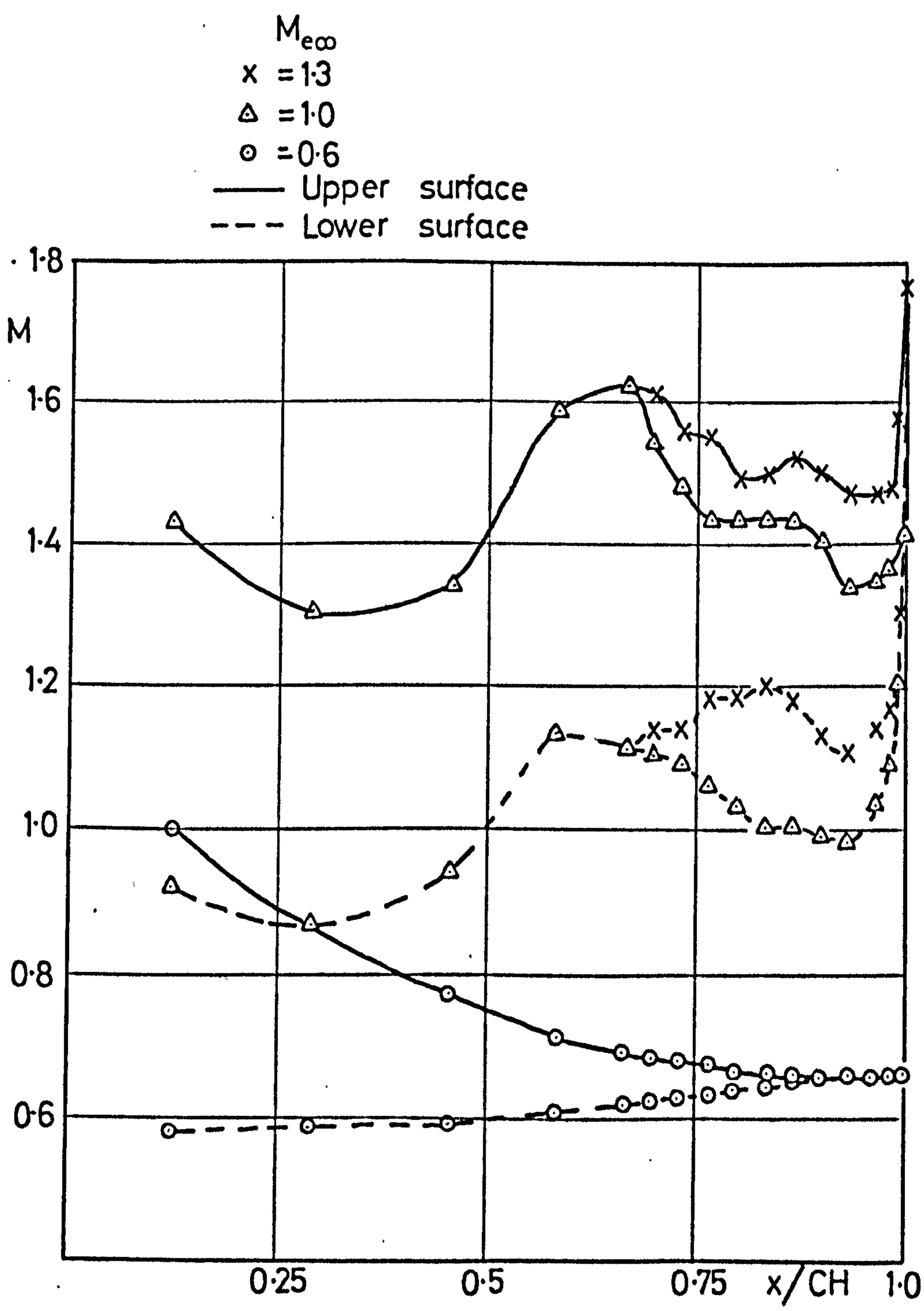

FIG.37b. MACH Nº DISTRIBUTIONS ON THE UPPER & LOWER SURFACES $\alpha = 4°$ ($\dot{m} = 0$, d=·024").

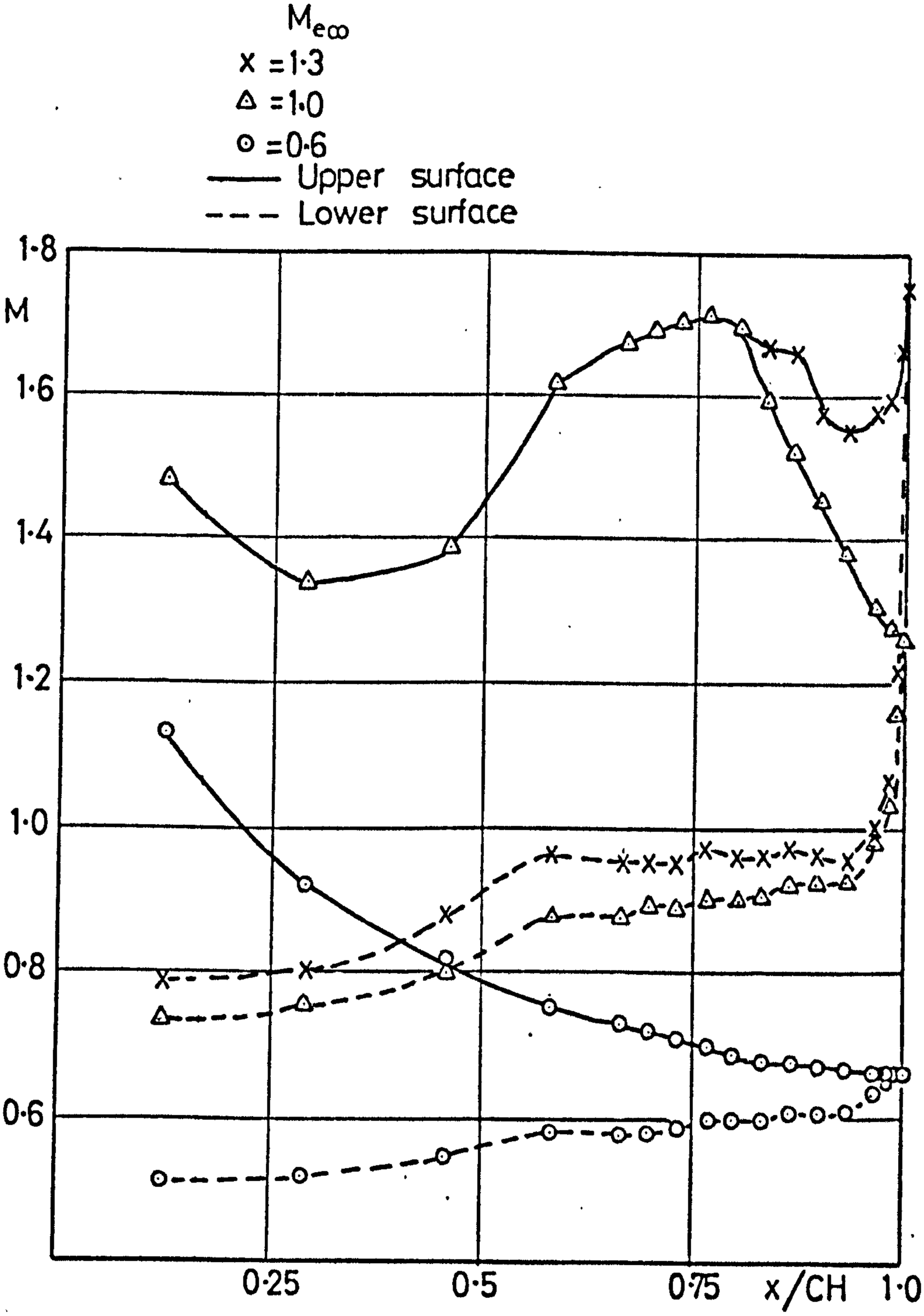

FIG.37c. MACH Nº DISTRIBUTIONS ON THE UPPER & LOWER SURFACES $\alpha = 6°$ ($\dot{m}=0$, d=·024")

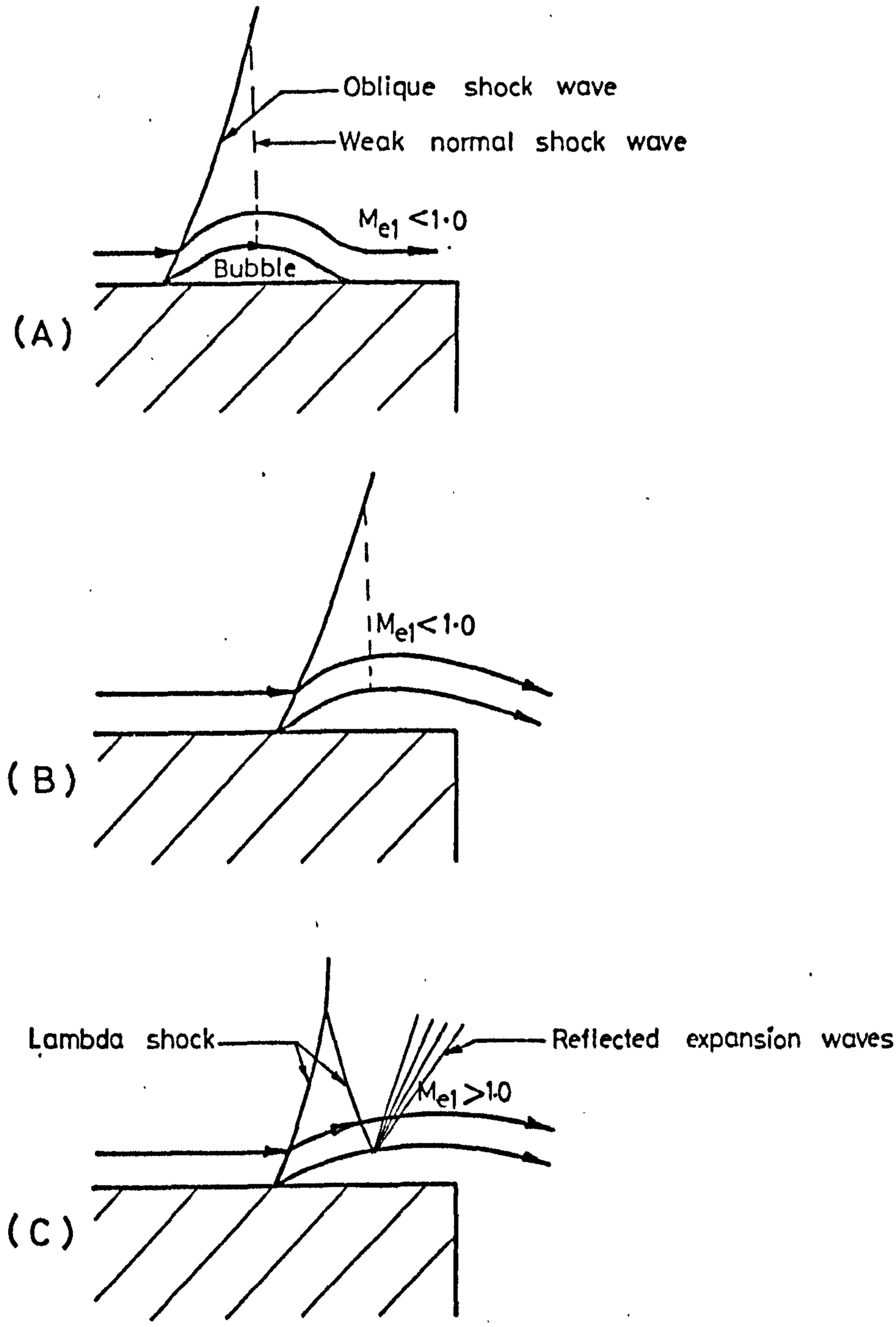

FIG.38. SCHEMATIC DIAGRAM OF THE FLOW POSSIBILITIES WITH SEPARATION ON THE UPPER SURFACE.

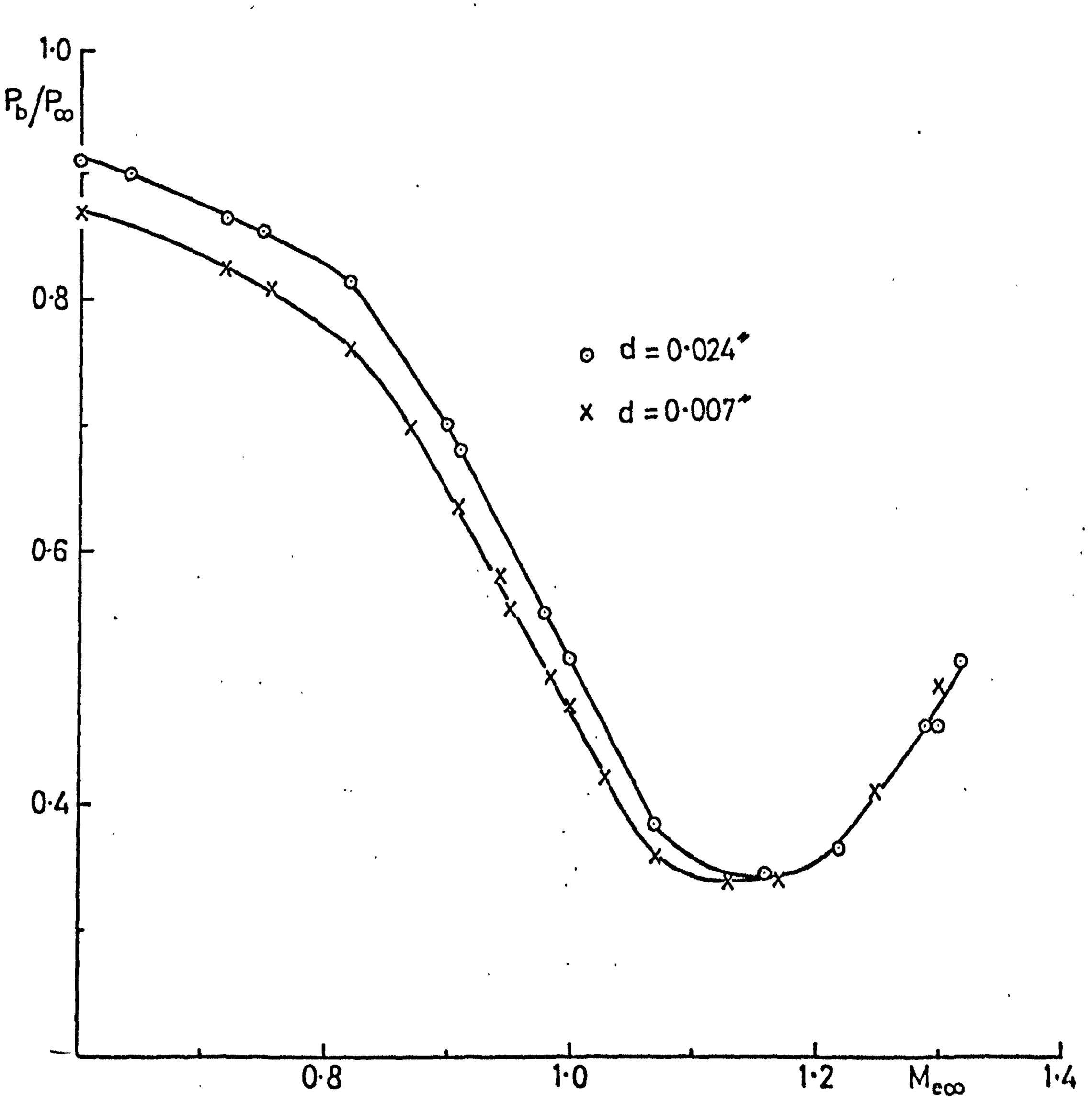

FIG. 39a. EFFECT OF TRANSITION WIRE SIZE ON THE VARIATION OF P_b/P_∞ WITH $M_{e\infty}$ WITHOUT BLEED (α=0).

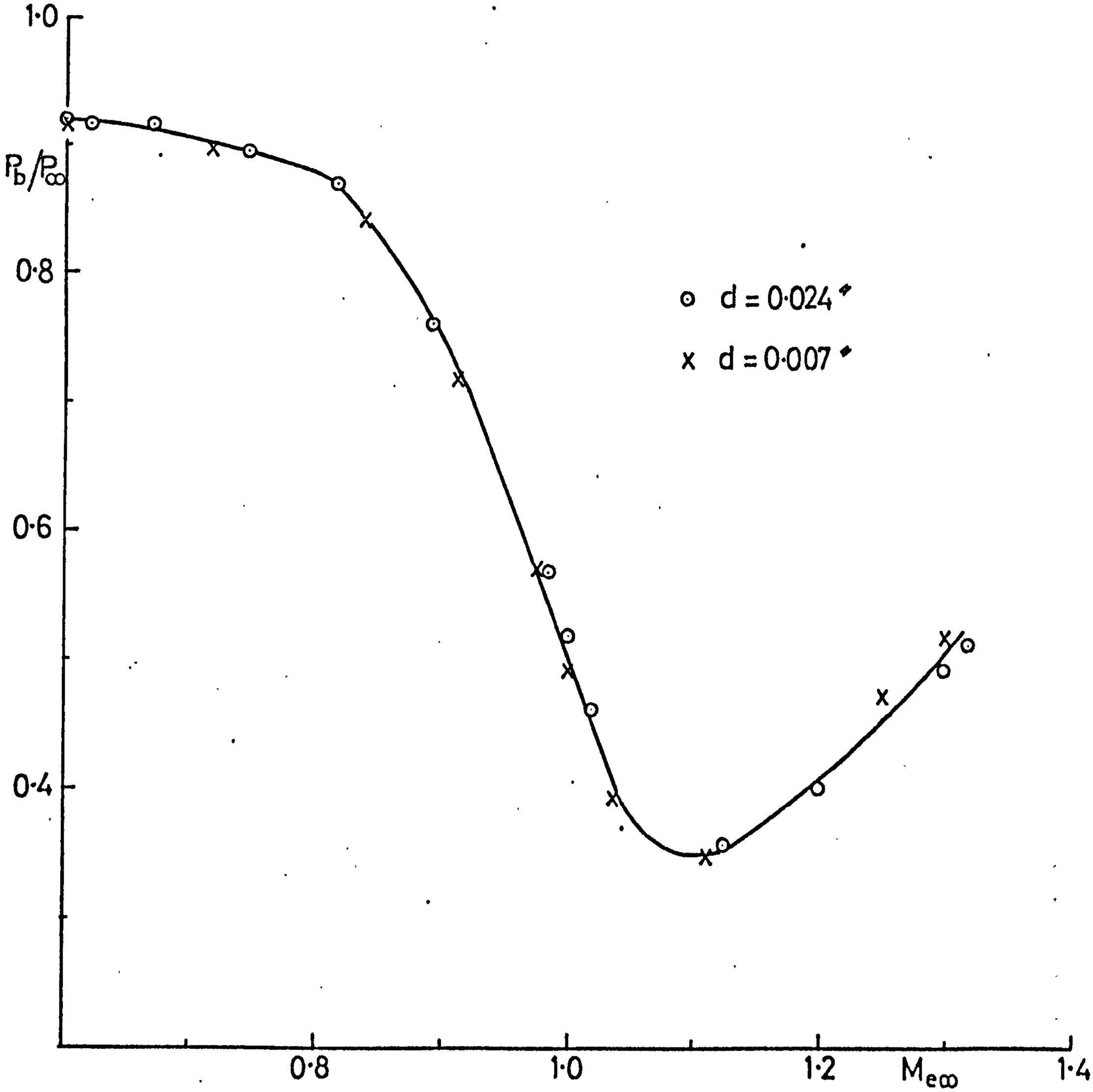

FIG.39b. EFFECT OF TRANSITION WIRE SIZE ON THE VARIATION OF P_b/P_∞ WITH $M_{e\infty}$ WITHOUT BLEED ($\alpha=2^\circ$).

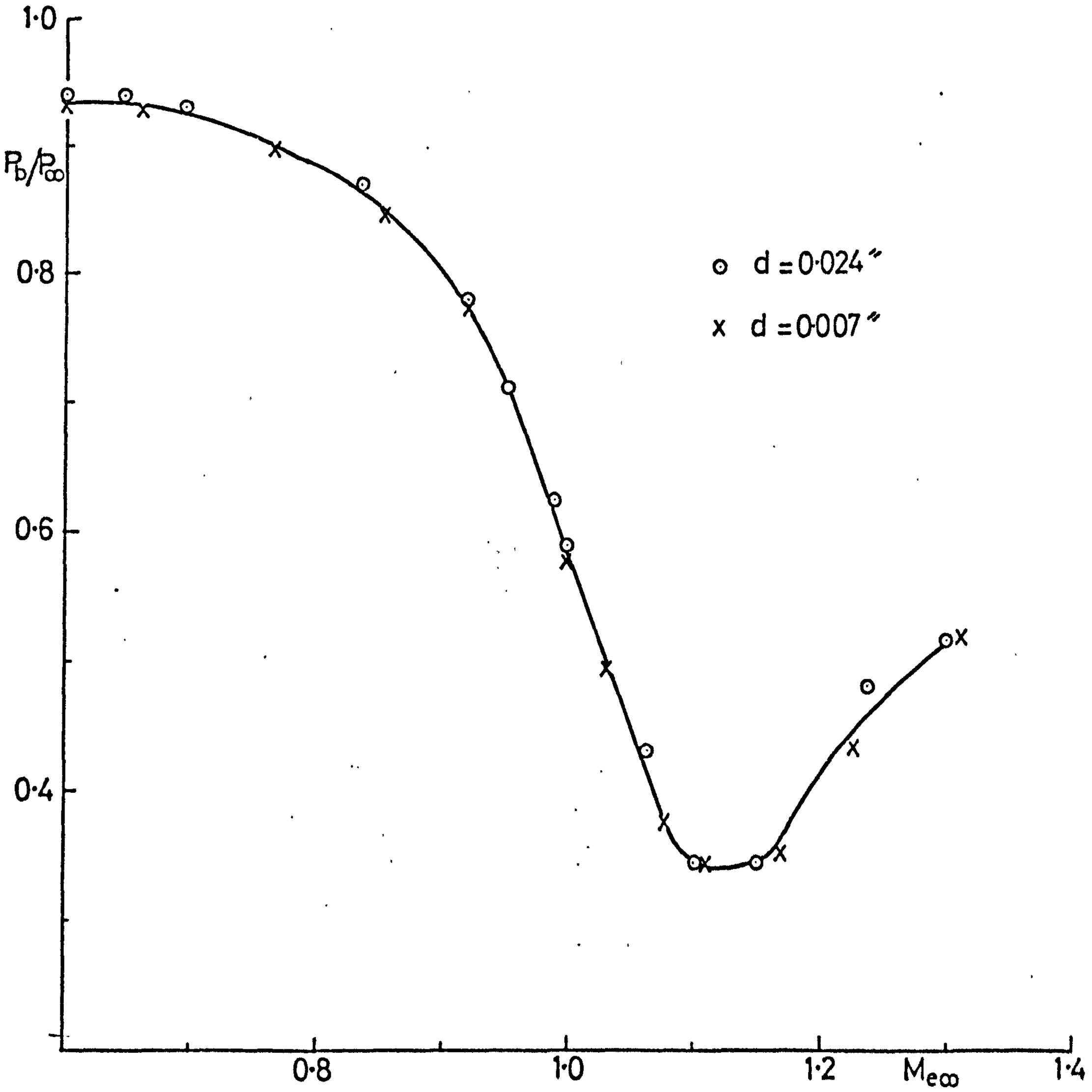

FIG.39c. EFFECT TRANSITION WIRE SIZE ON THE VARIATION OF P_b/P_∞ WITH $M_{e\infty}$ WITHOUT BLEED ($\alpha=4°$).

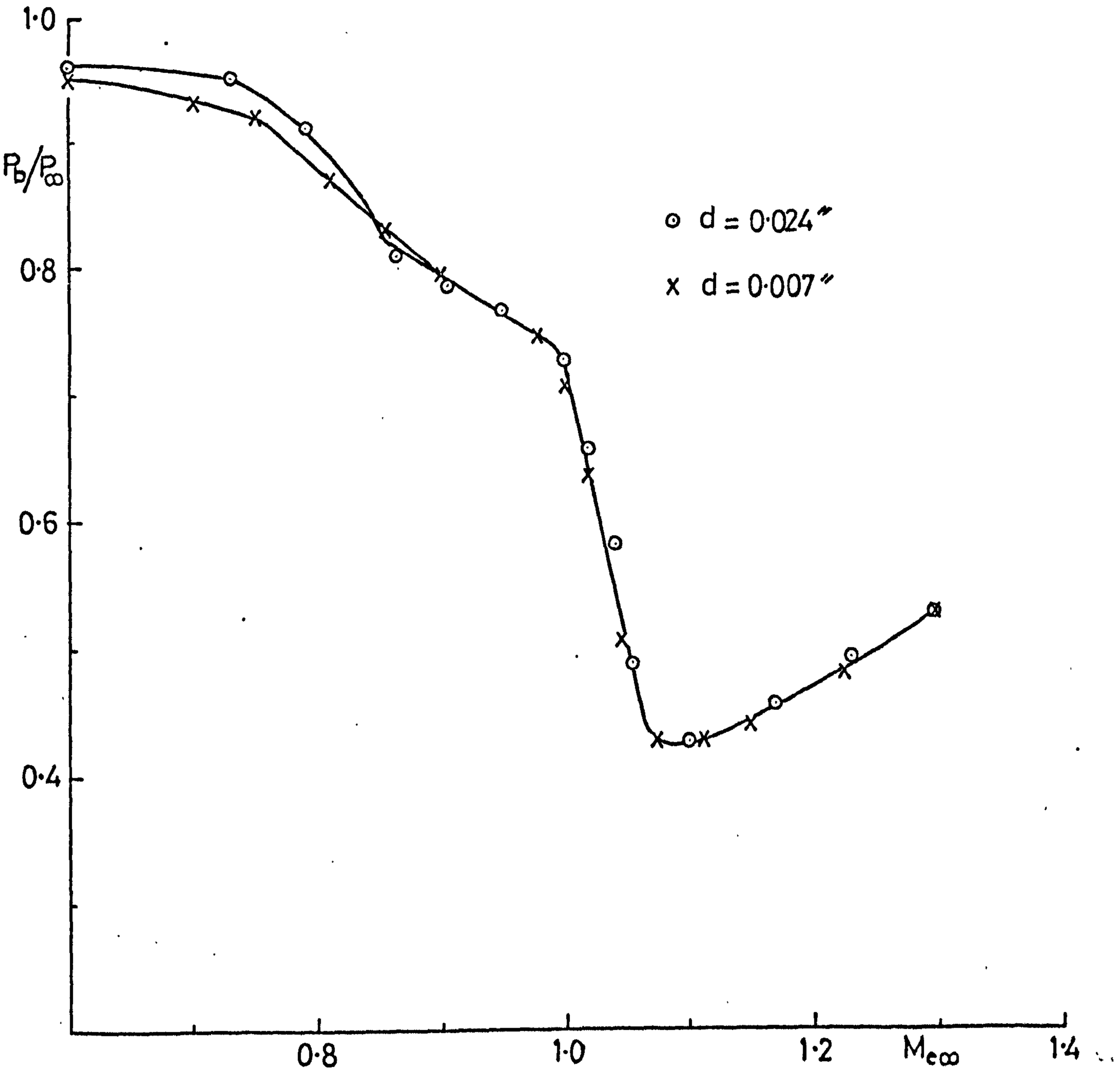

FIG.39d. EFFECT OF TRANSITION WIRE SIZE ON THE VARIATION OF P_b/P_∞ WITH $M_{e\infty}$ WITHOUT BLEED ($\alpha = 6°$).

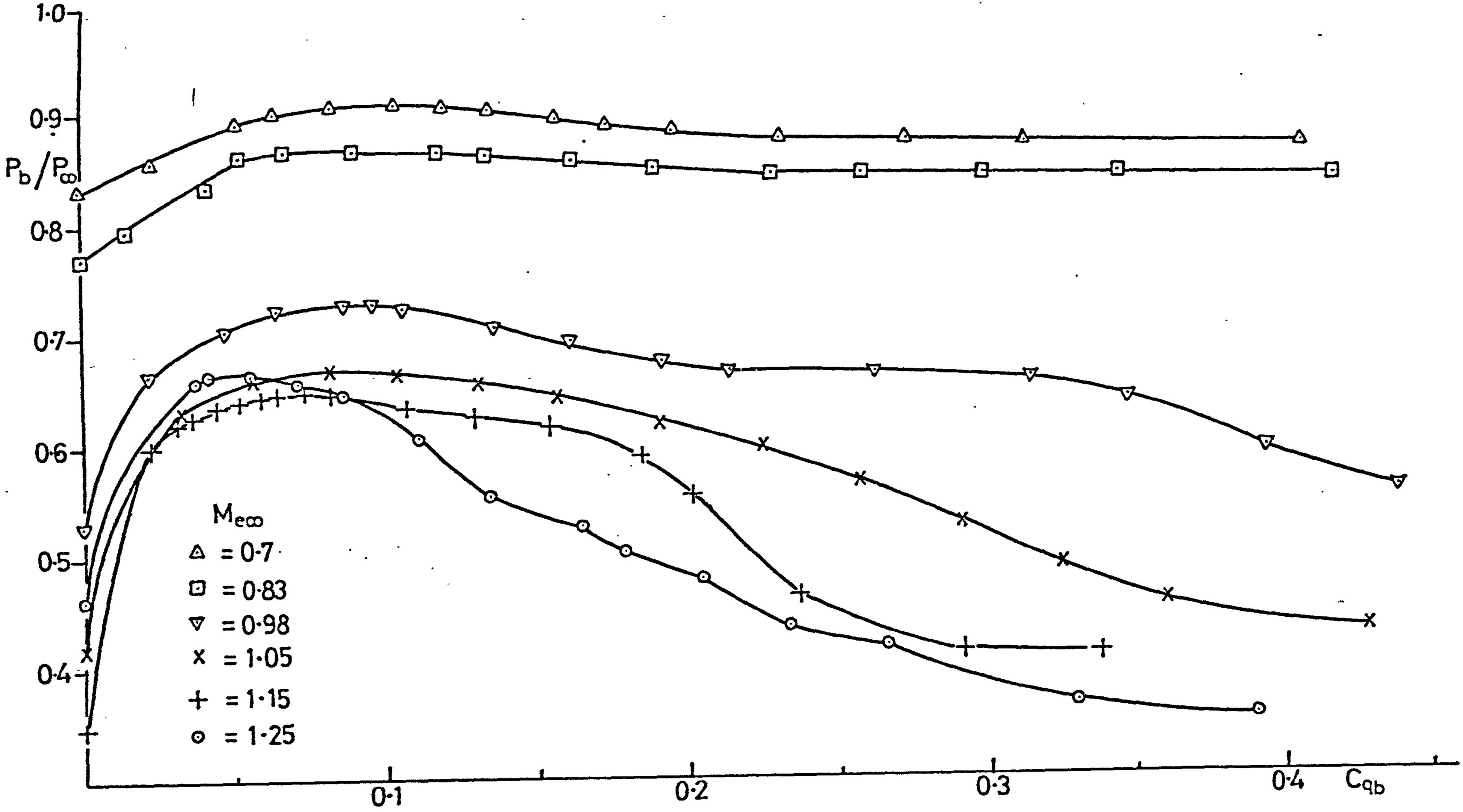

FIG.40. EFFECT OF BASE BLEED ON BASE PRESSURE $\alpha=0$ (d=·007")

FIG.41a. EFFECT OF α ON THE VARIATION OF P_b/P_∞ WITH BASE BLEED FOR M_{e_∞}=0·6 (d=·024").

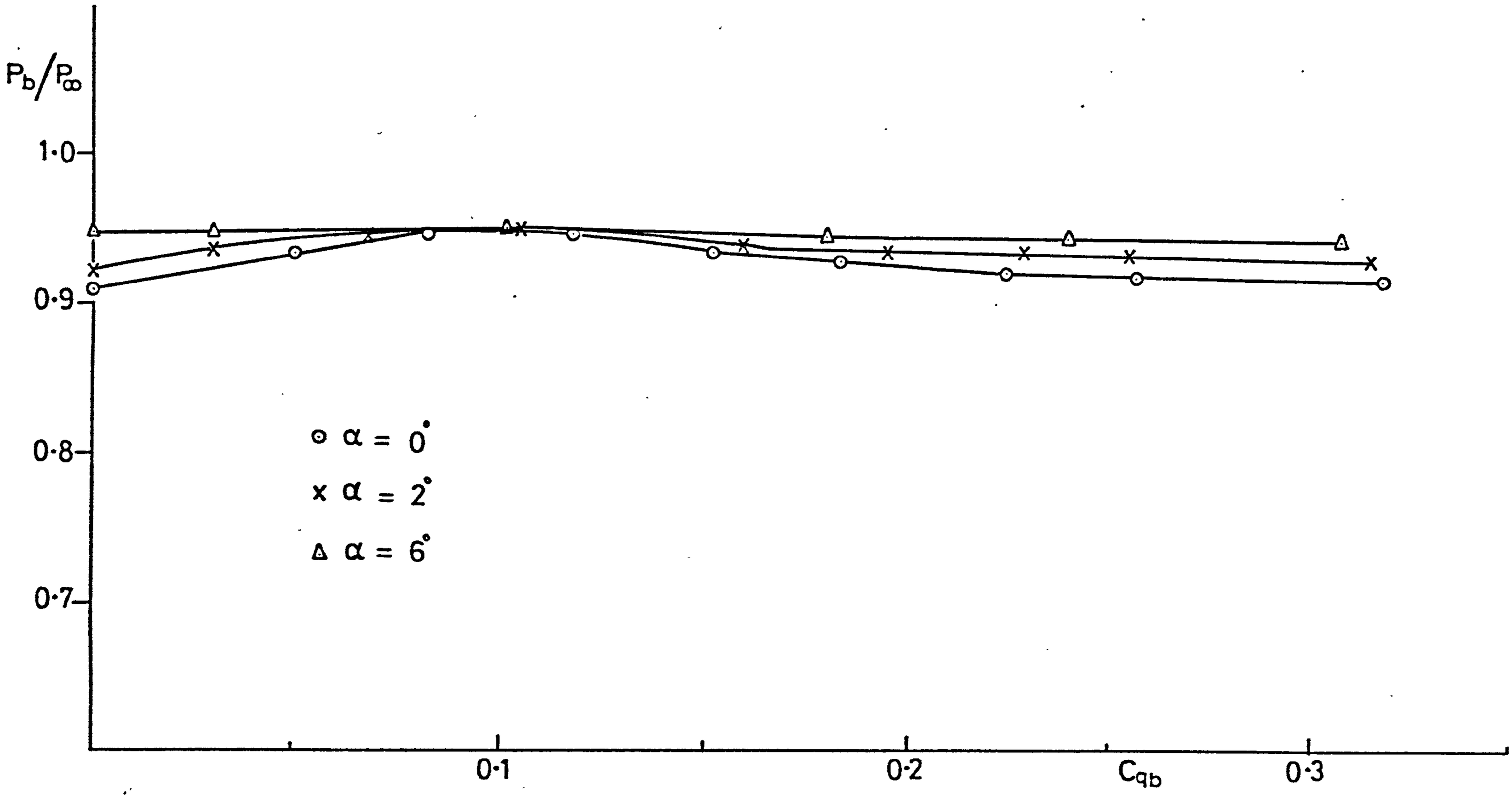

FIG.41b. EFFECT OF α ON THE VARIATION OF P_b/P_∞ WITH BASE BLEED FOR M_{e_∞}=1·0 (d=·024").

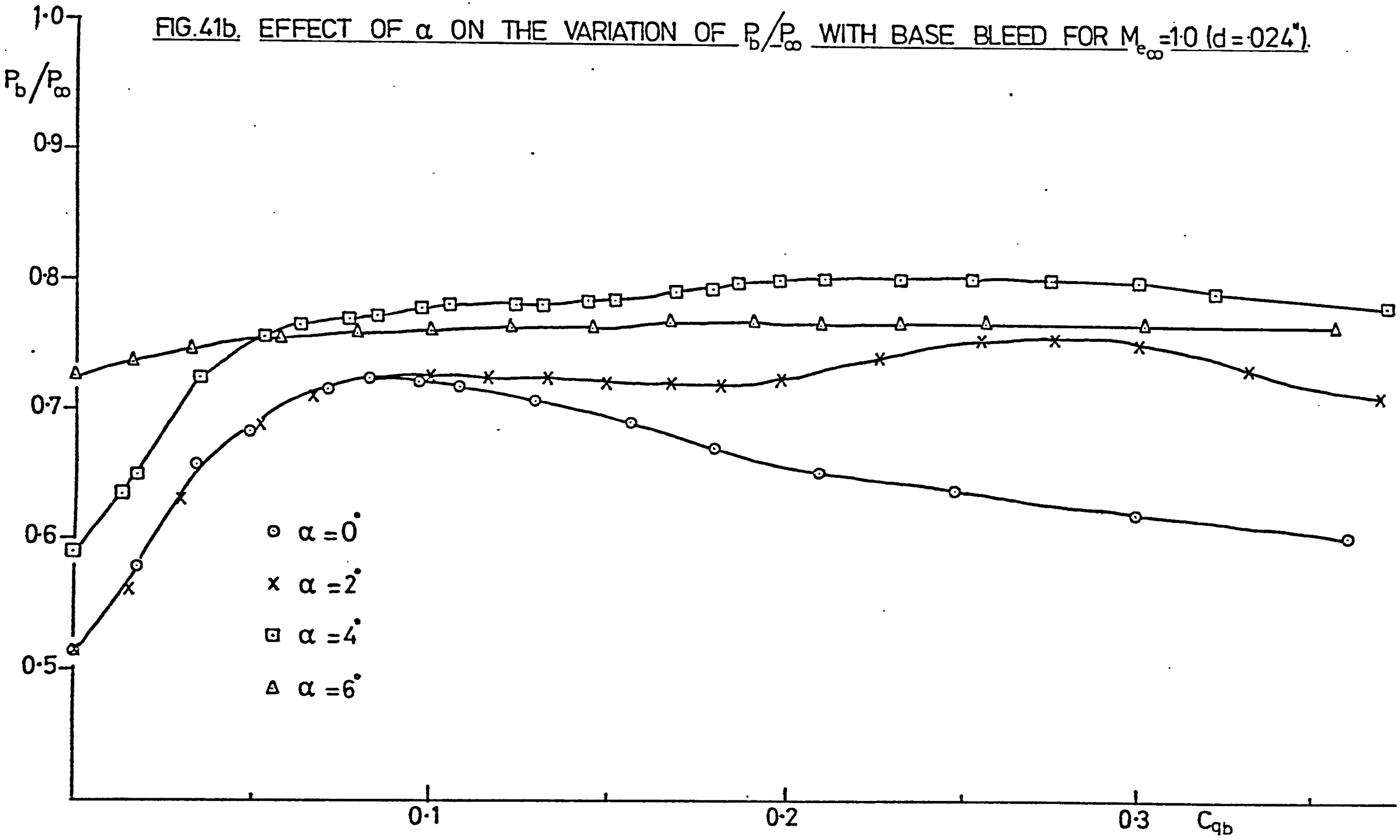

FIG.41c. EFFCT OF α ON THE VARIATION OF P_b/P_∞ WITH BASE BLEED FOR $M_{e\infty}=1.3$ ($d=.024"$)

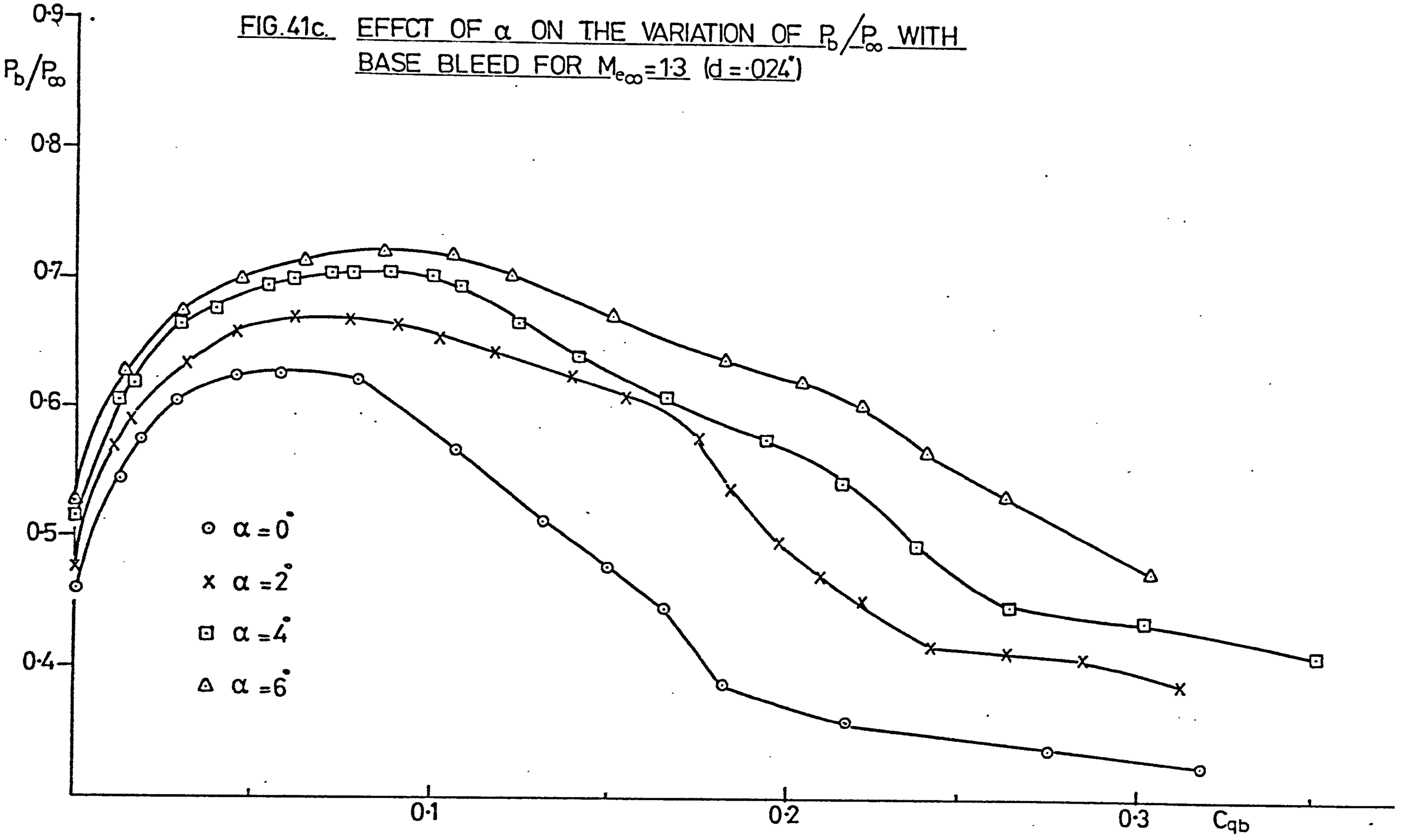

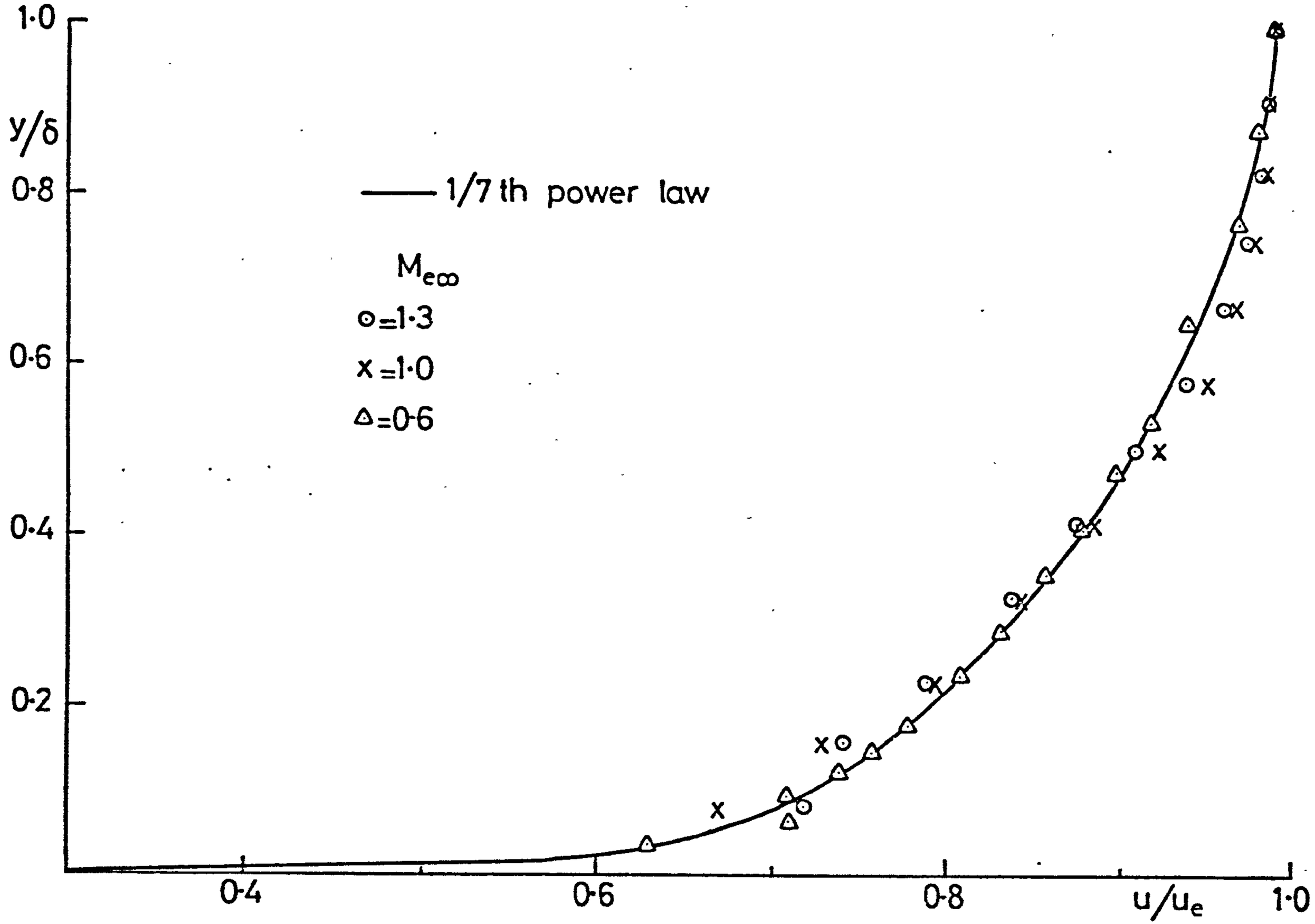

FIG.42. BOUNDARY LAYER TRAVERSE AT 0·4" BEFORE T.E. ($\alpha = 0$, d = ·024")

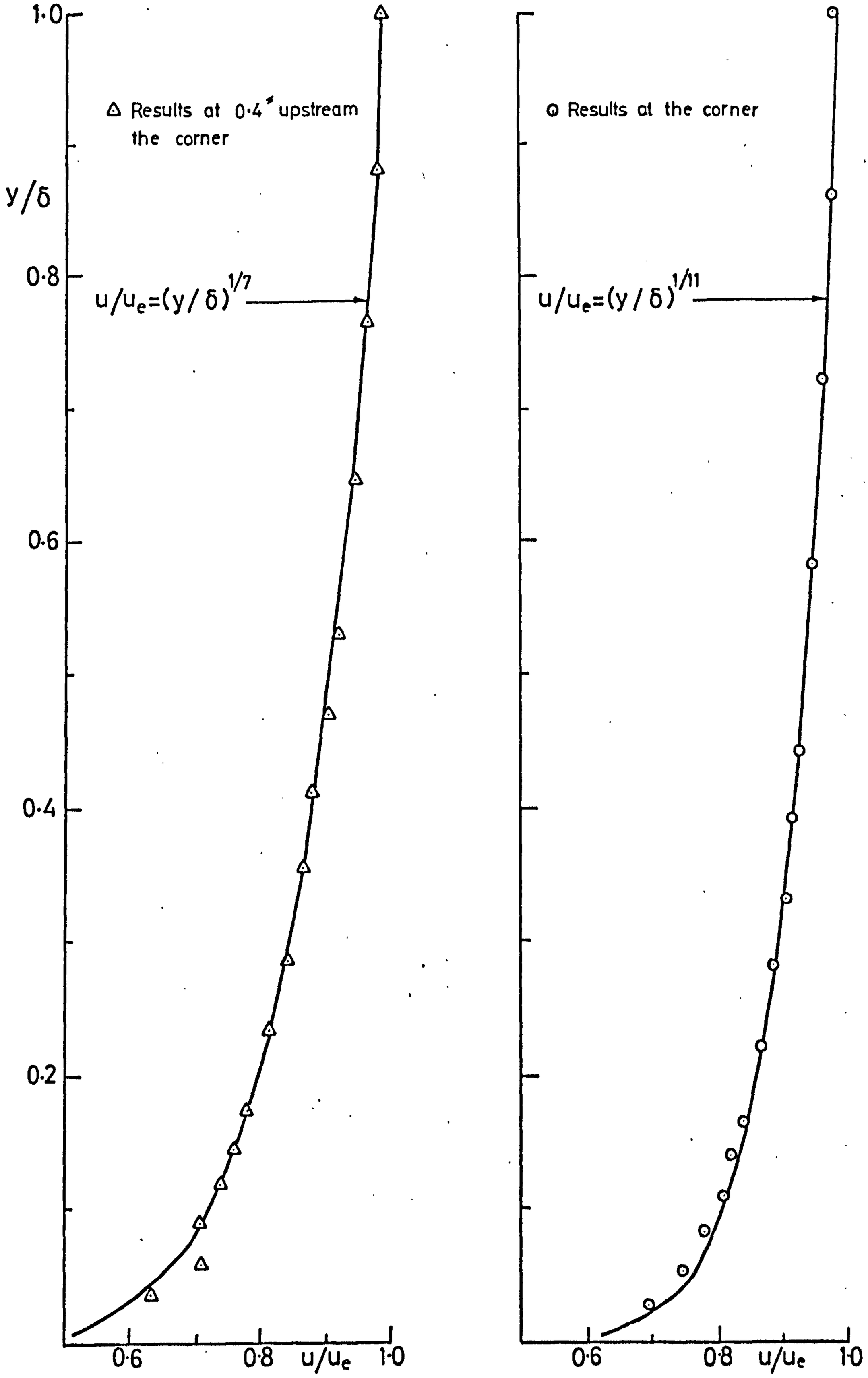

FIG. 43. BOUNDARY LAYER VELOCITY PROFILE BEFORE & AFTER EXPANSION FOR M_∞=0·6 (d =024")

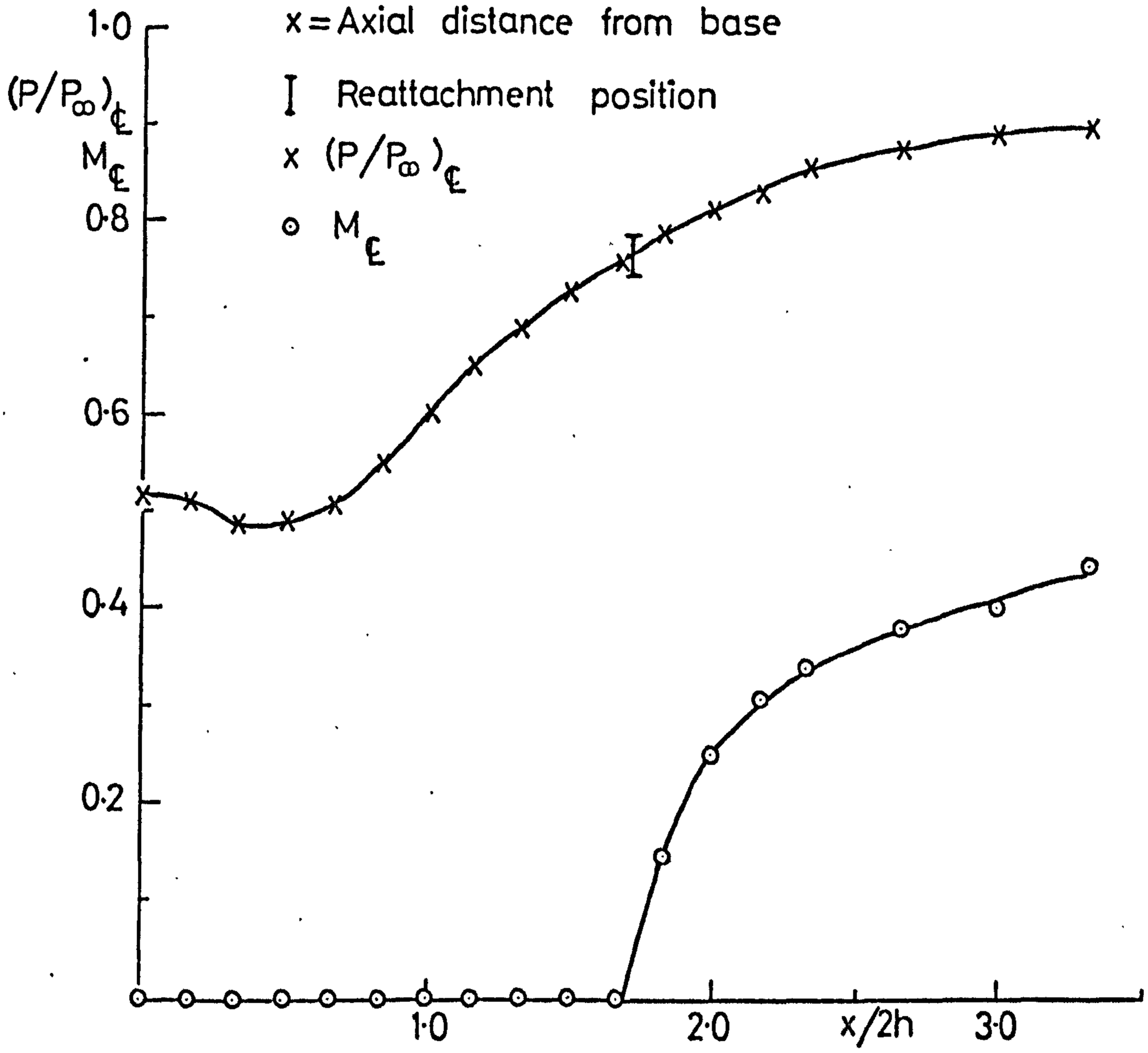

FIG.44. AXIAL PRESSURE AND MACH Nº DISTRIBUTION FOR M_{e_∞}=1·0 (d=·024", $\dot{m}$=0, α=0)

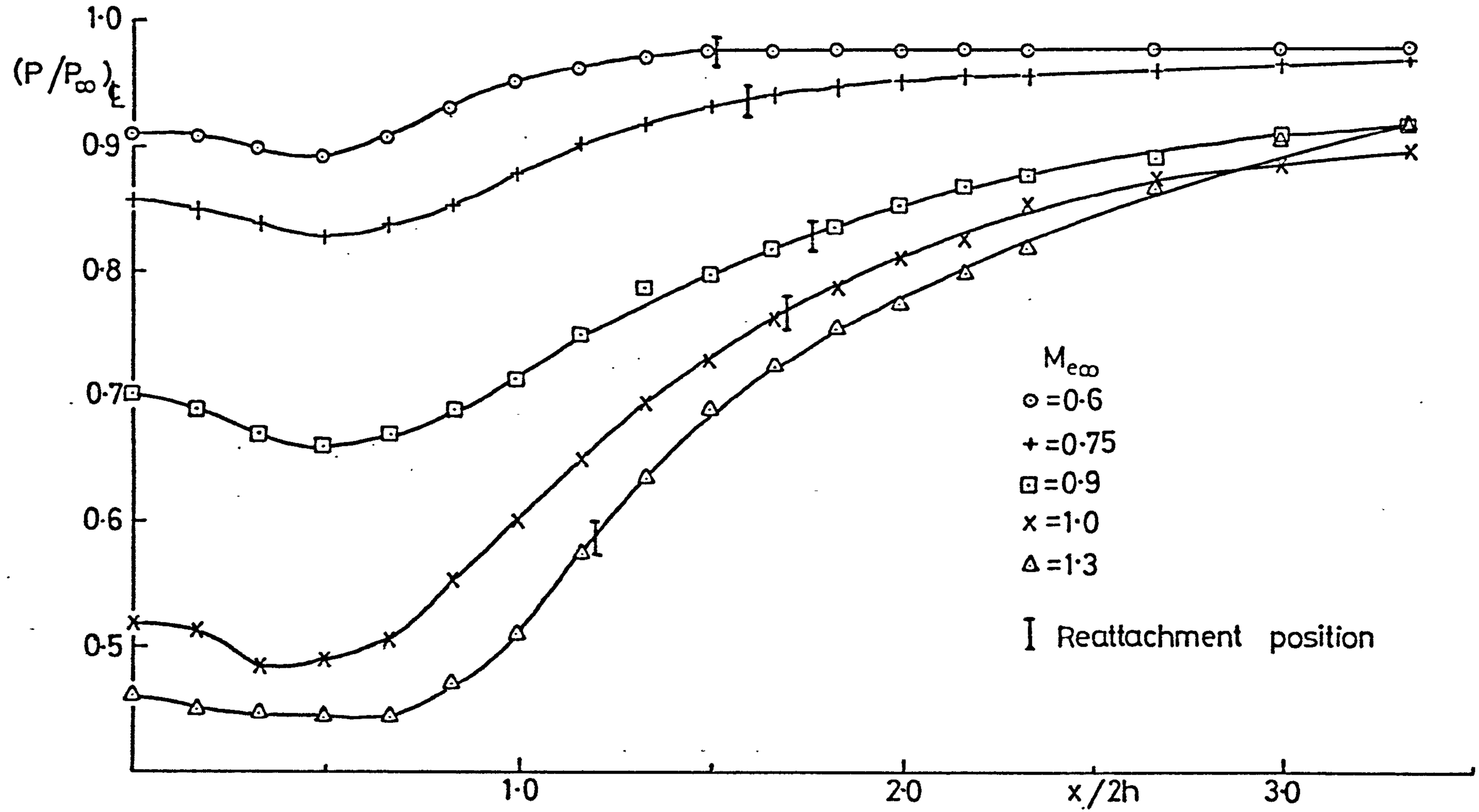

FIG.45. AXIAL PRESSURE DISTRIBUTION (d = ·024, ṁ=0, α=0)

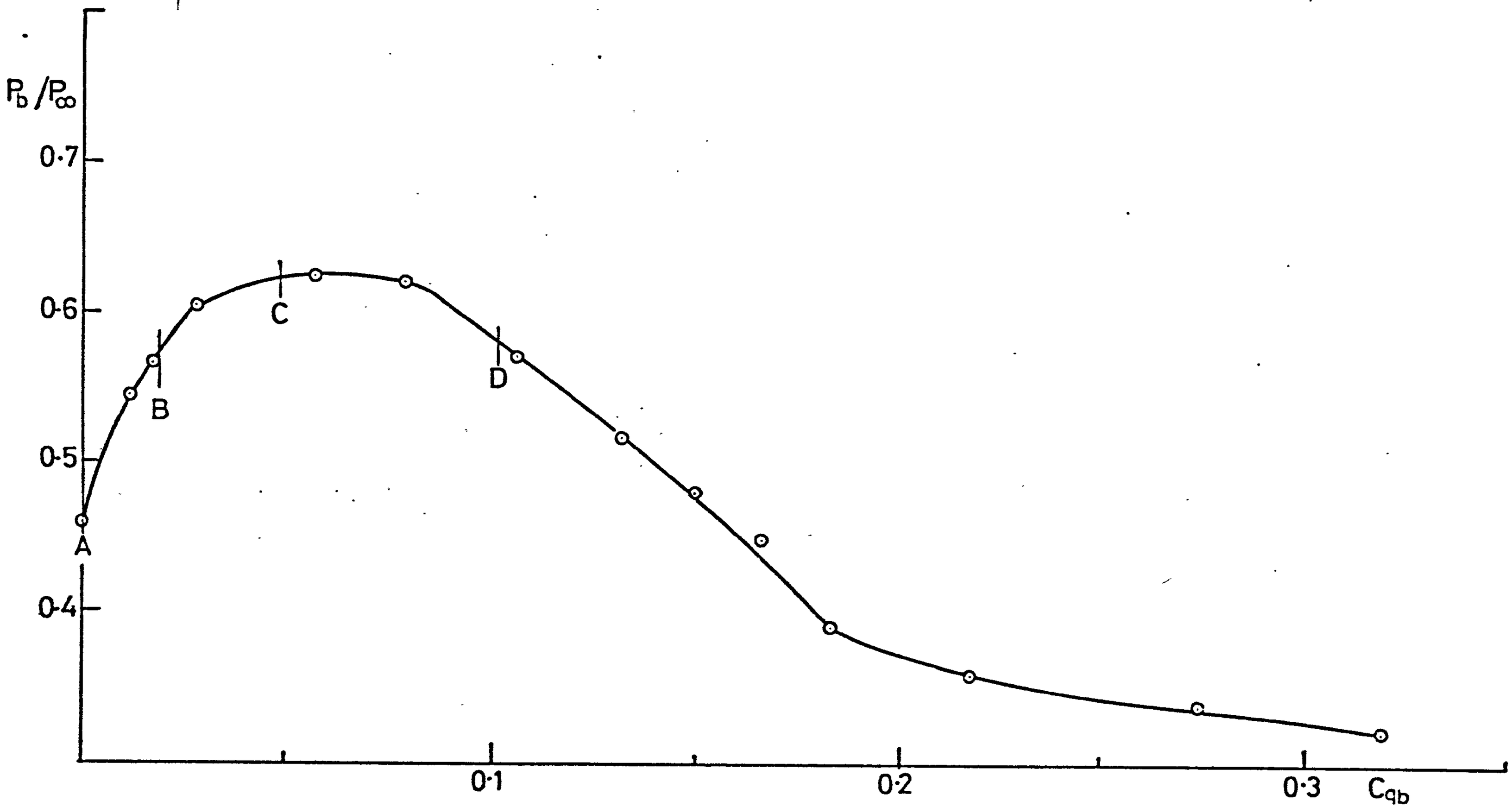

FIG.46. VARIATION OF BASE PRESSURE WITH BASE BLEED FOR M_{e_∞}=1·3 (α=0, d=024")

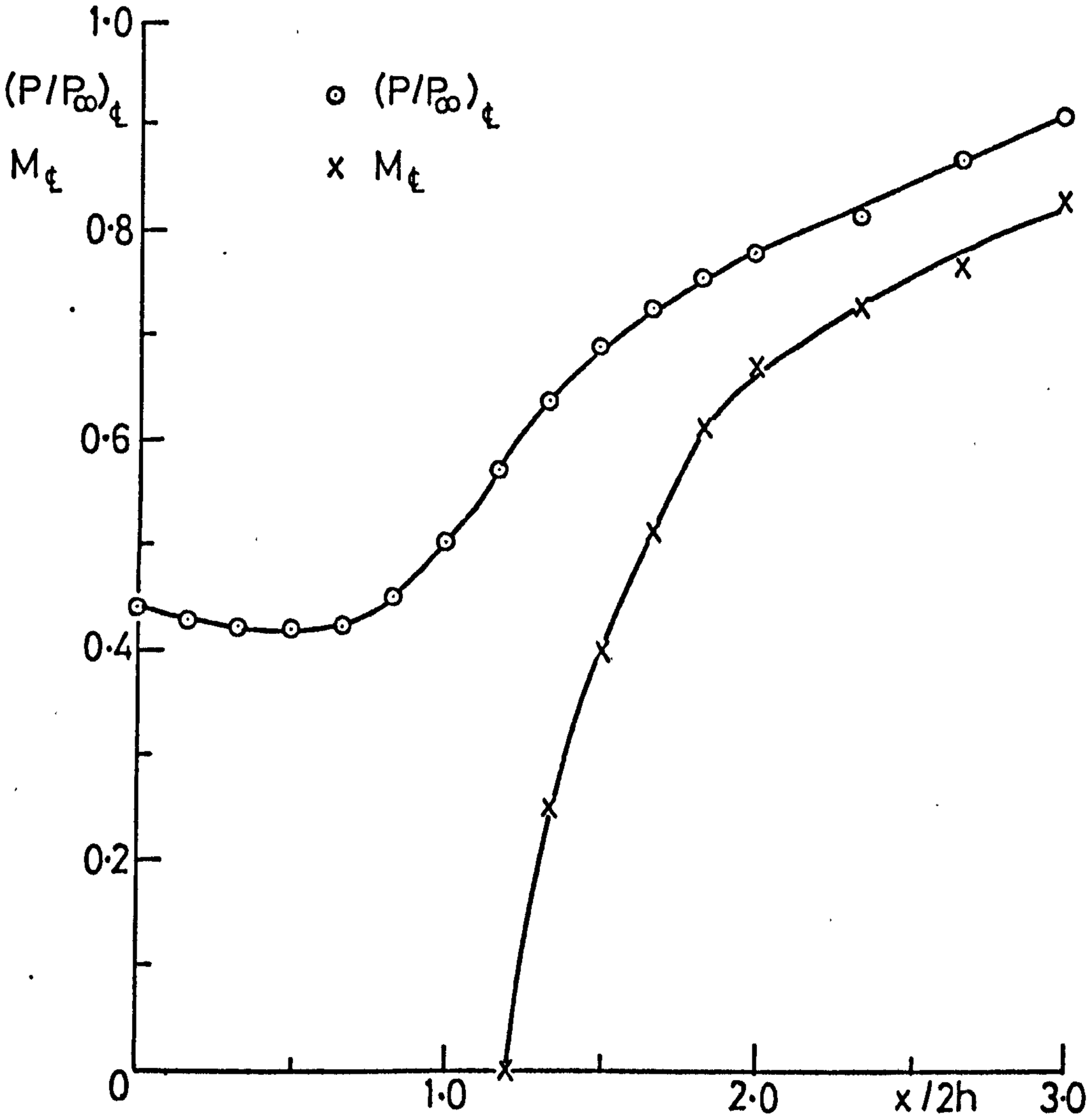

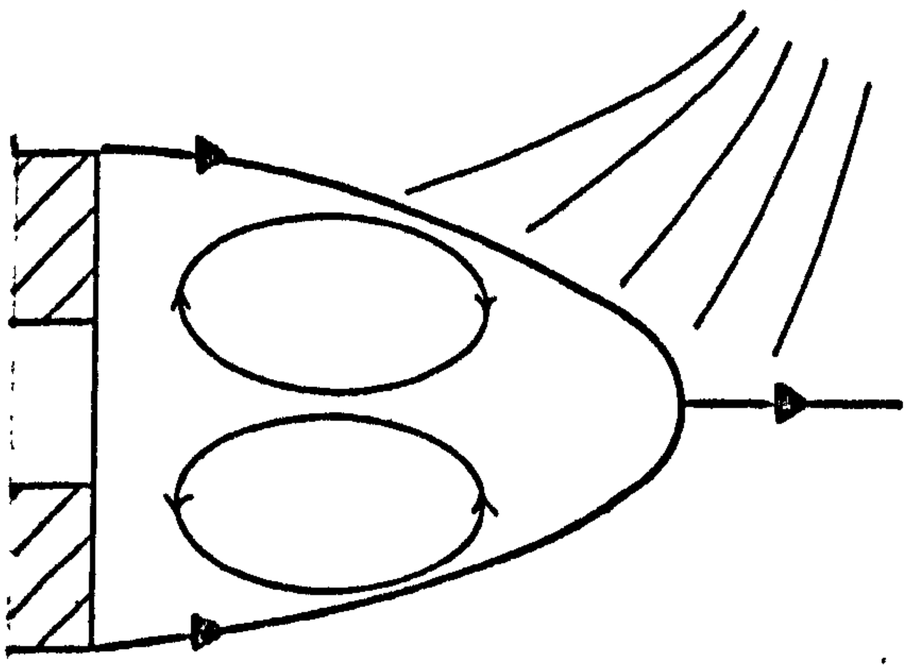

(a) $C_{q_b}=0$

FIG.47. P_ℓ AND M_ℓ DISTRIBUTION FOR $M_{e\infty}=1.3$ WITH BLEED ($\alpha=0$, $d=.024$)

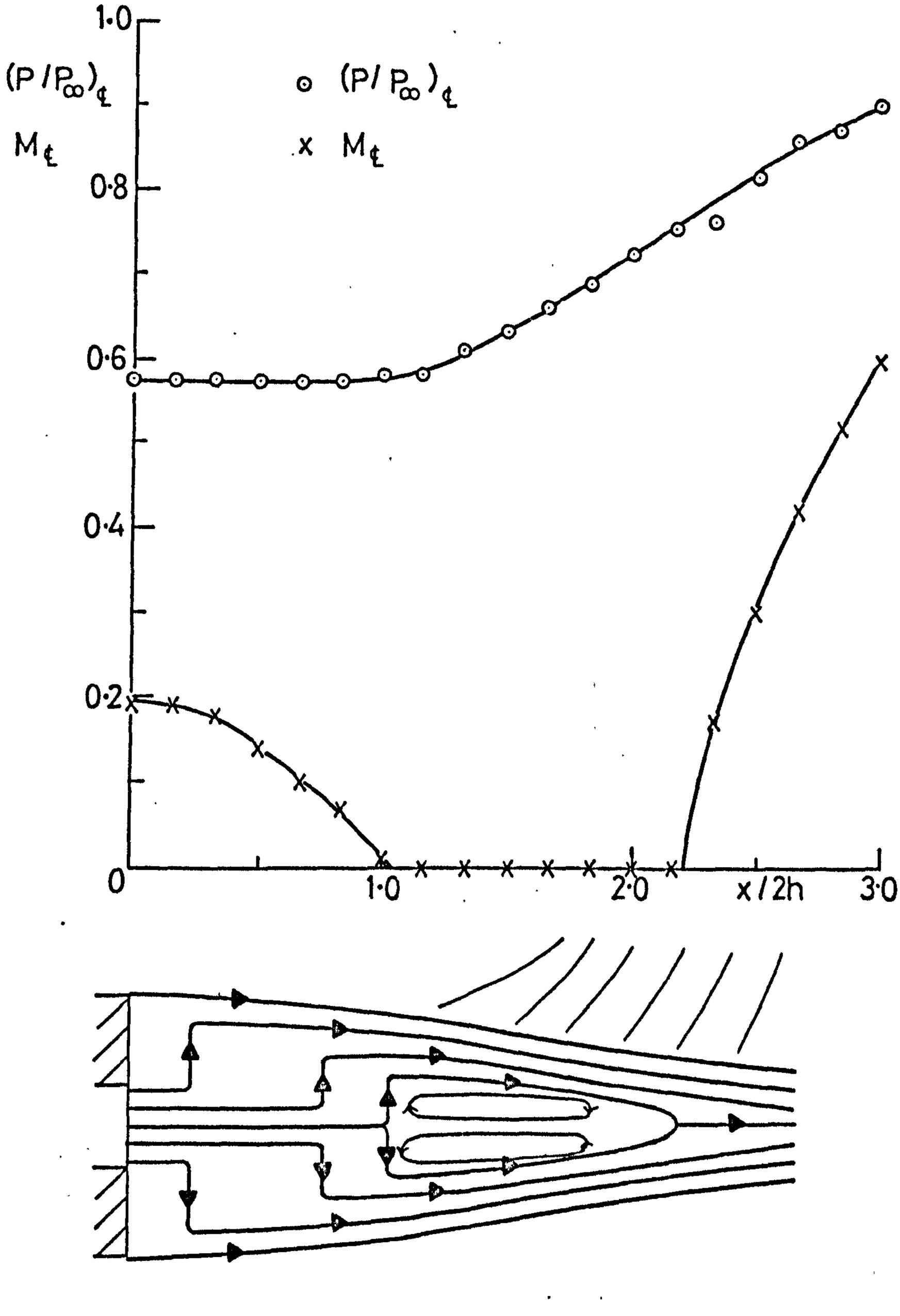

FIG. 47. (CONTINUED) (b) $C_{qb} = 0{\cdot}019$

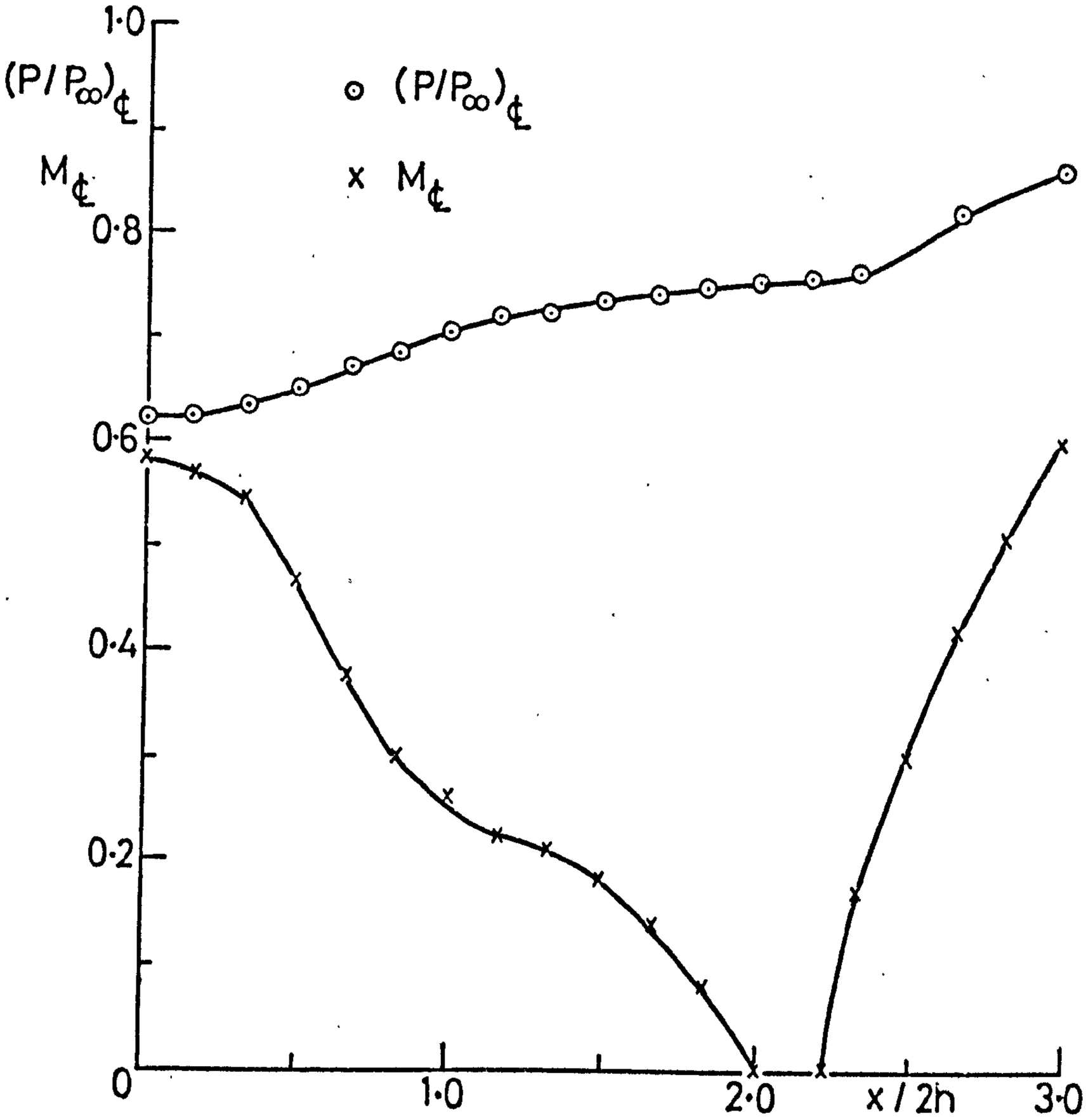

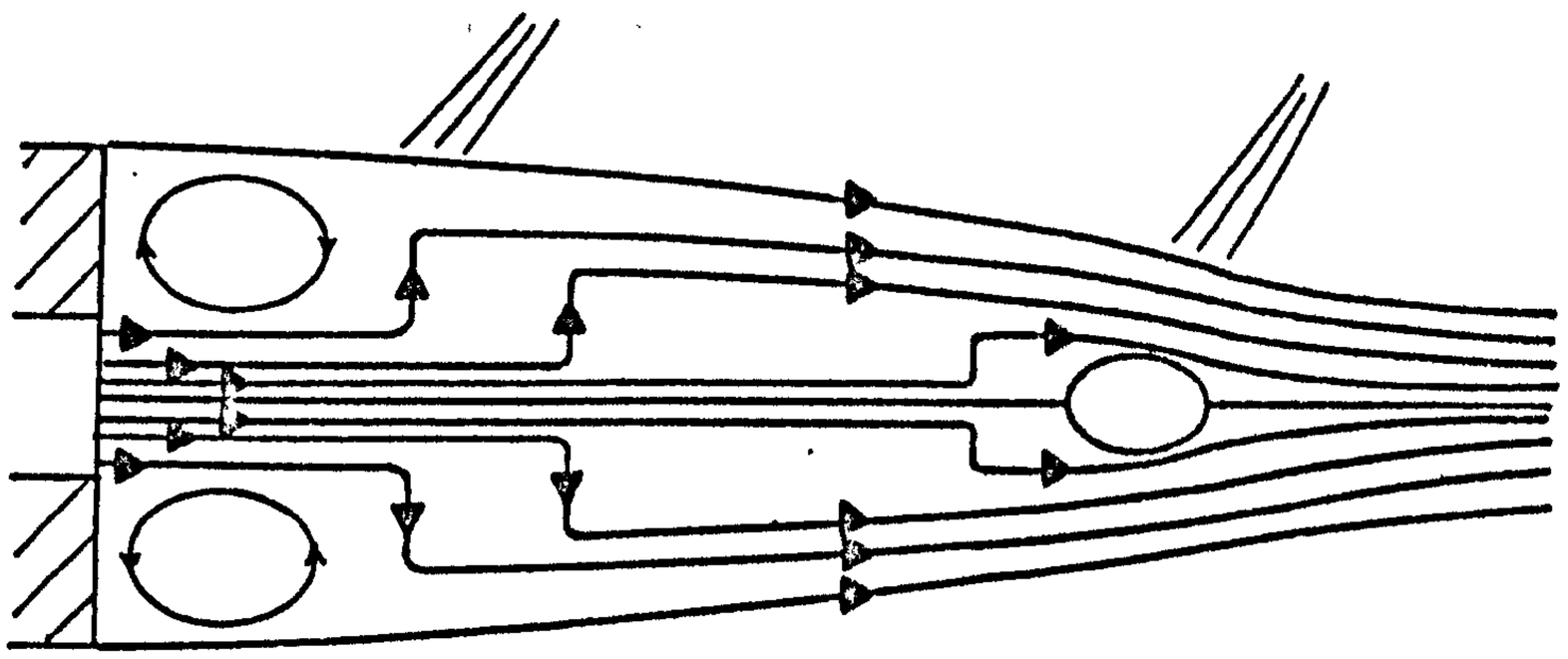

FIG. 47. (CONTINUED) (c) $C_{q_b} = \cdot 049$

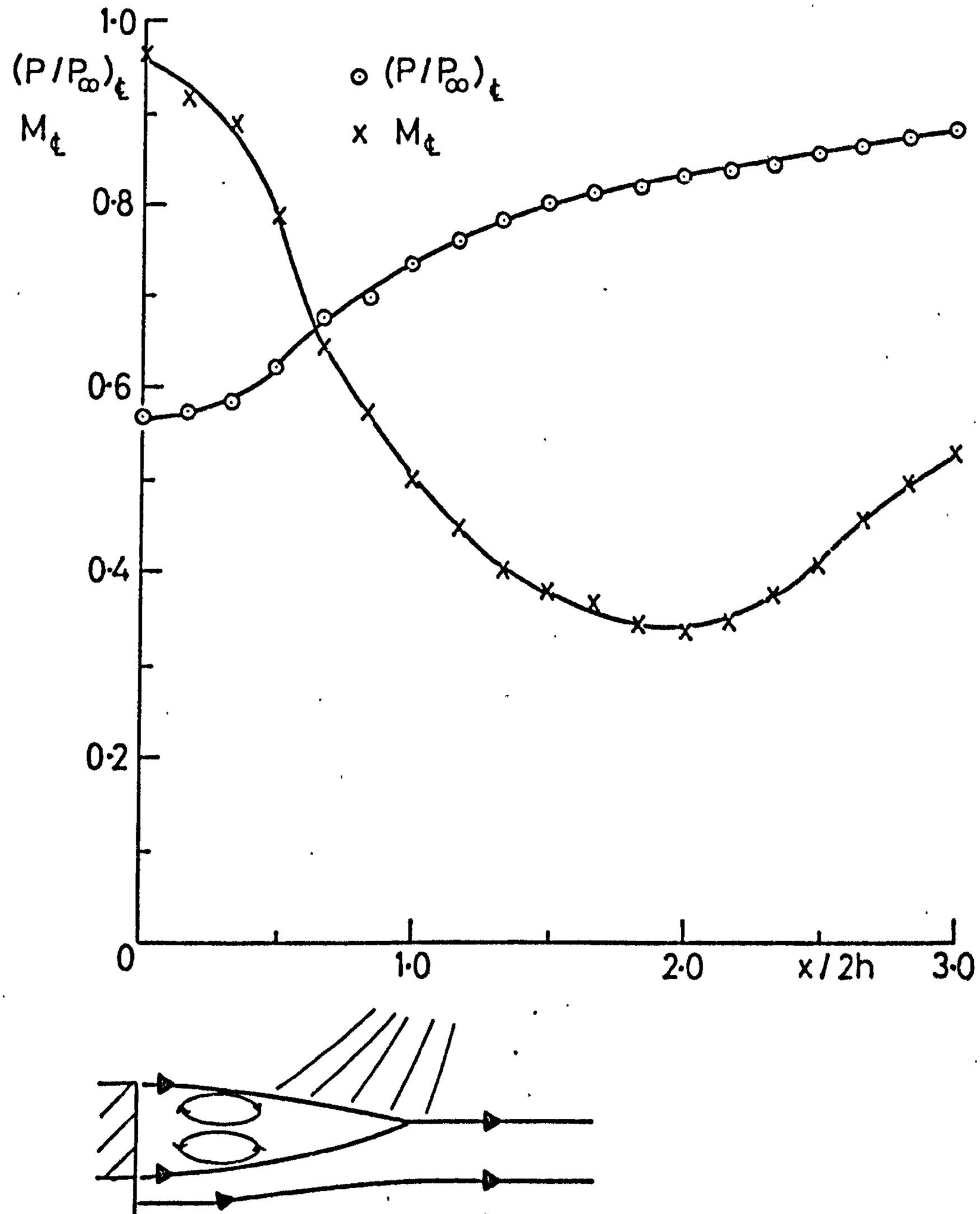

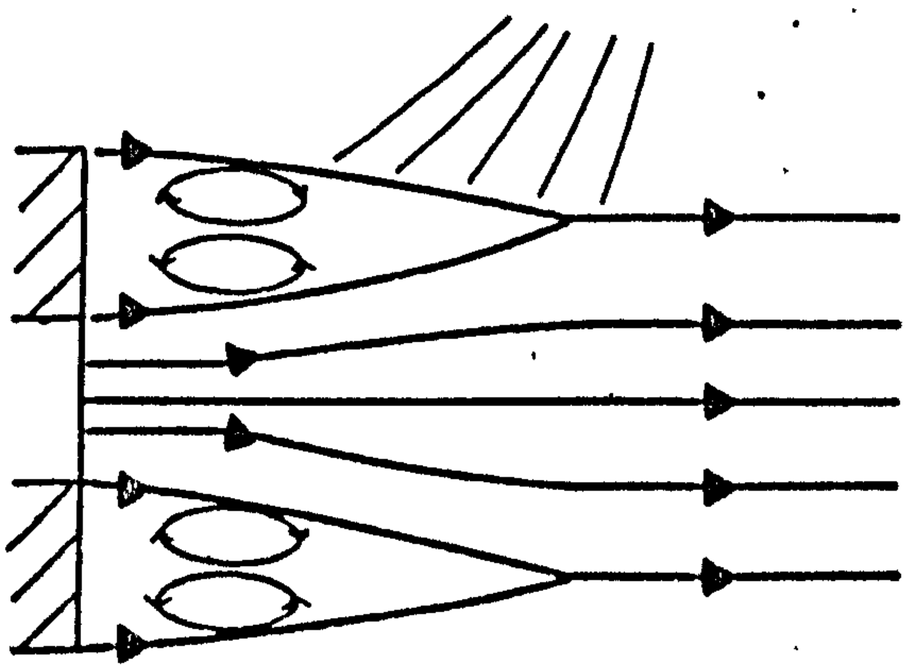

FIG. 47. (CONCLUDED) (d) $C_{qb} = 0{\cdot}10$

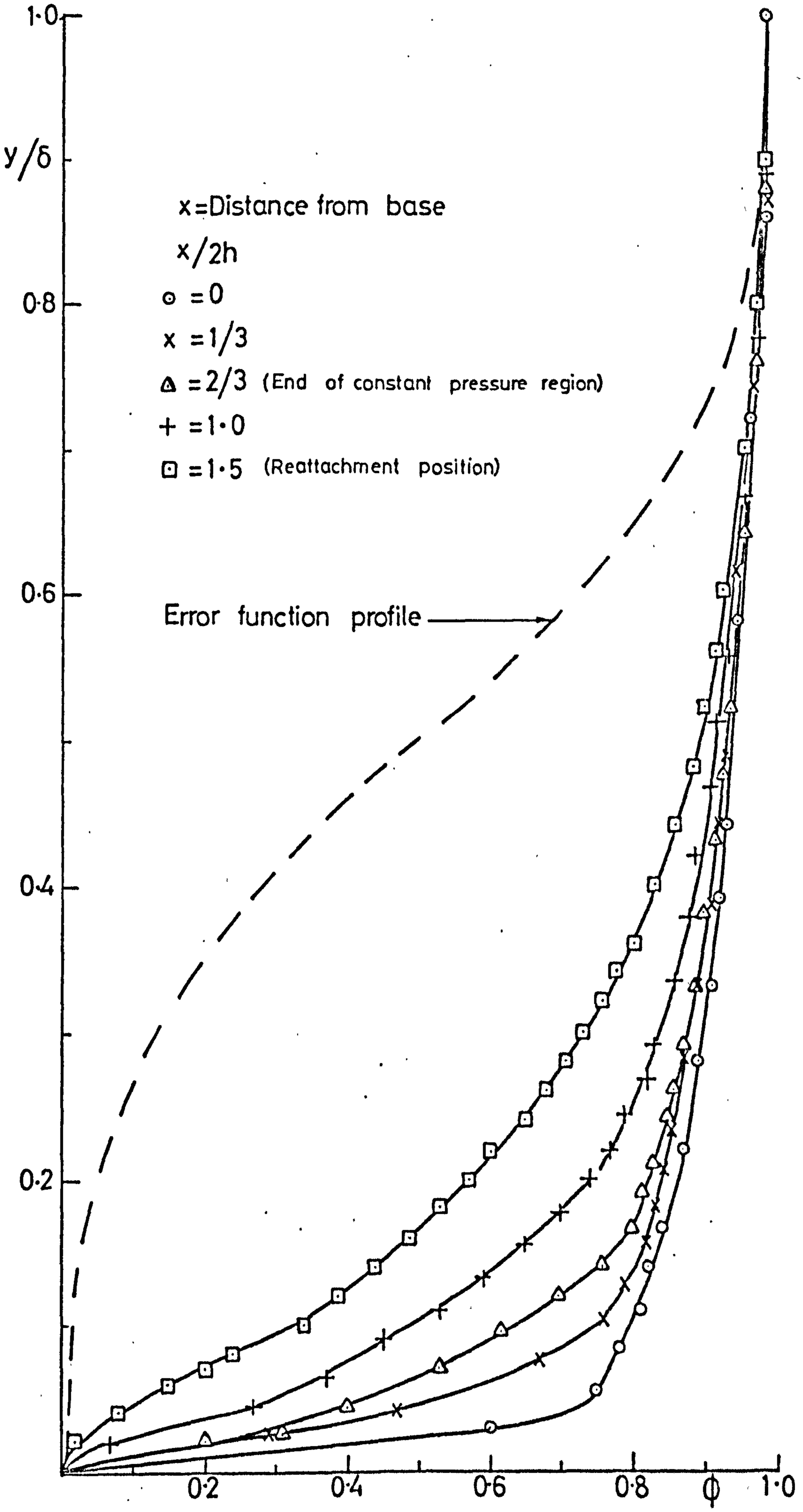

FIG.48a. FREE SHEAR LAYER VELOCITY PROFILE FOR $M_{e\infty}$=0·6 (α=0, m=0, d=·024)

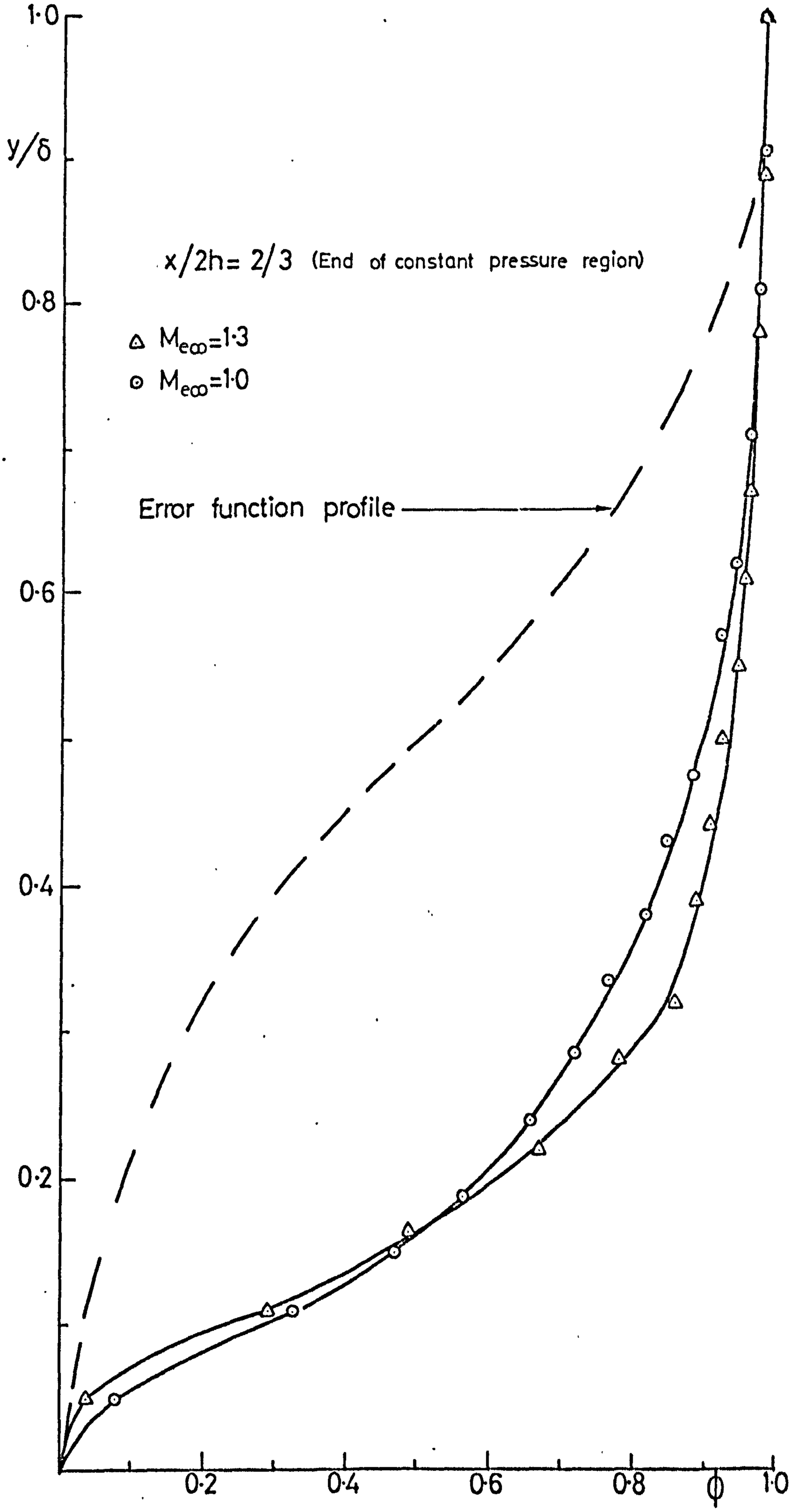

FIG.48b. FREE SHEAR LAYER VELOCITY PROFILE FOR $M_{e\infty}$=1·0 & 1·3 (α=0, $\dot{m}$=0, d=·024")

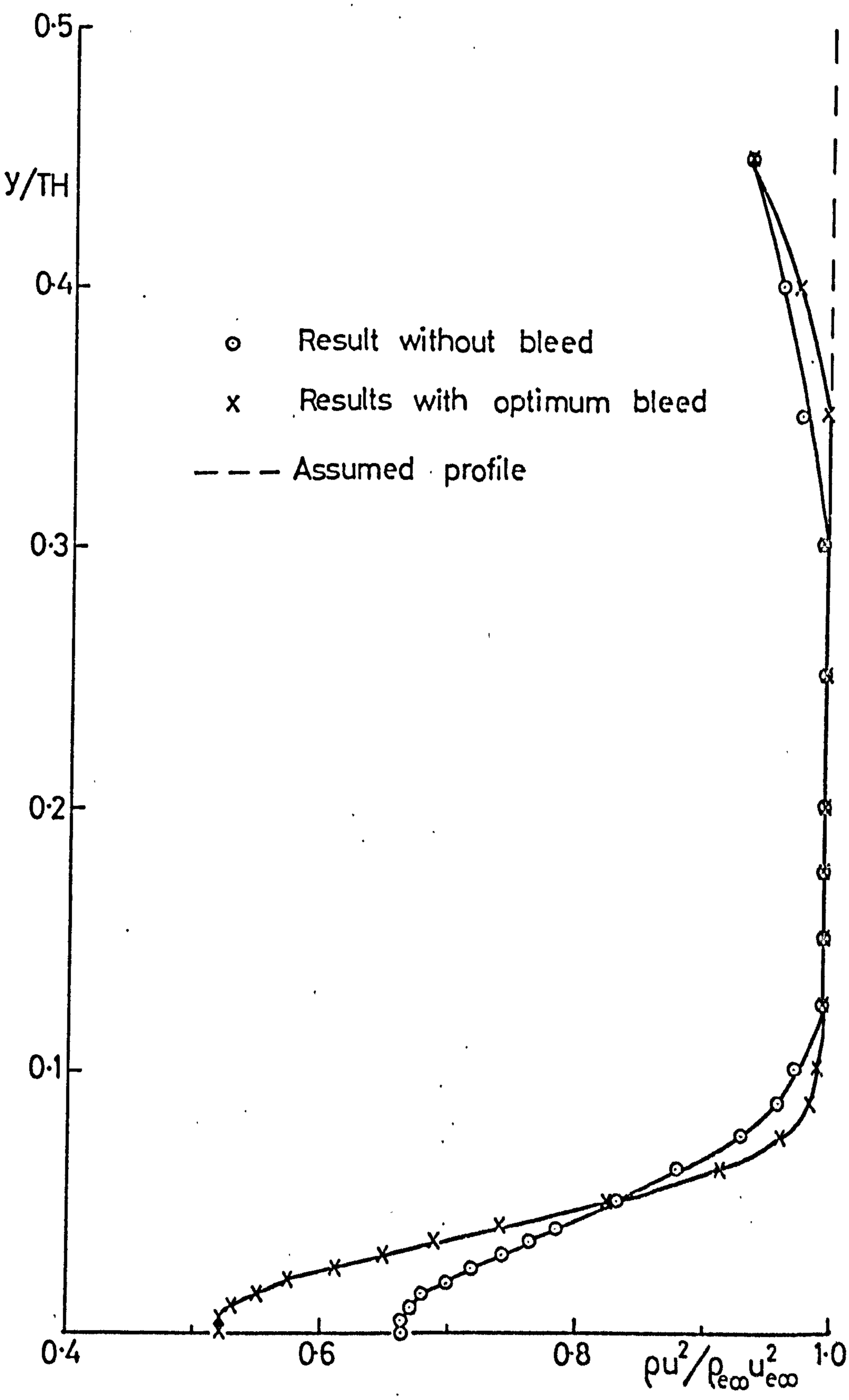

FIG.49a. WAKE PROFILE $\alpha=0$, $M_{e\infty}=0.6$.

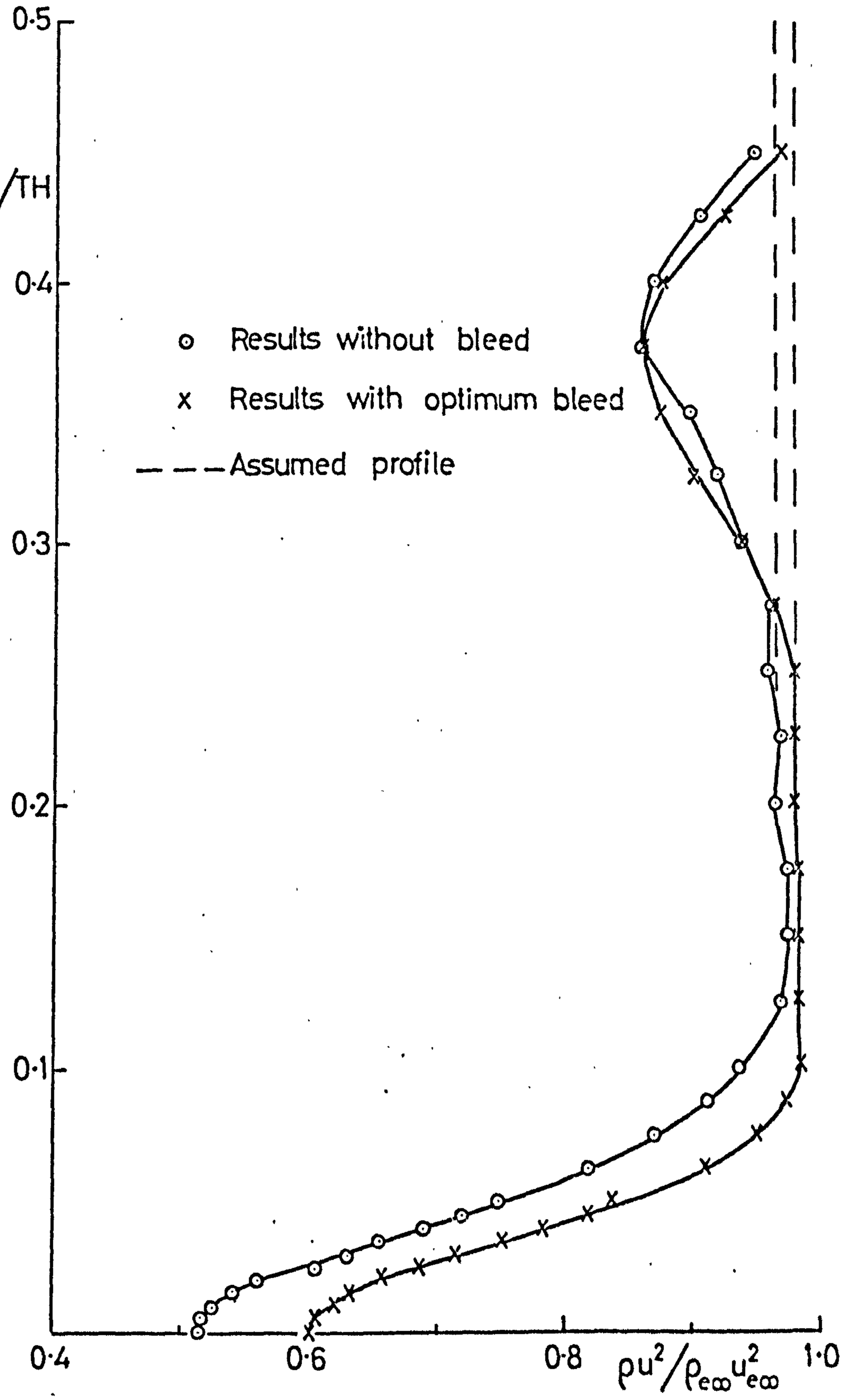

FIG.49b. WAKE PROFILE $\alpha = 0$, $M_{e_\infty} = 1{\cdot}0$.

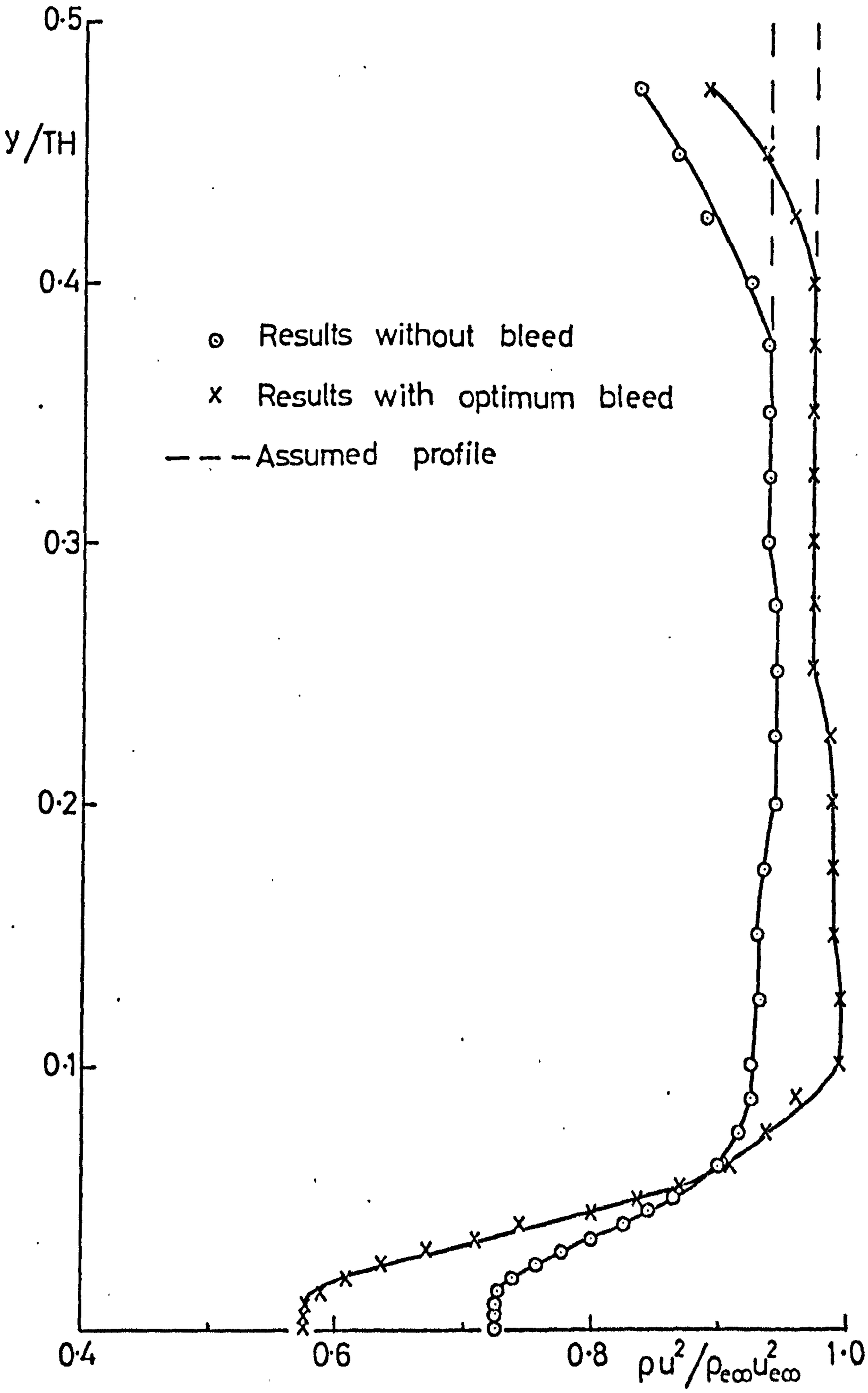

FIG. 49c. WAKE PROFILE $\alpha = 0$, $M_{e\infty} = 1{\cdot}3$.

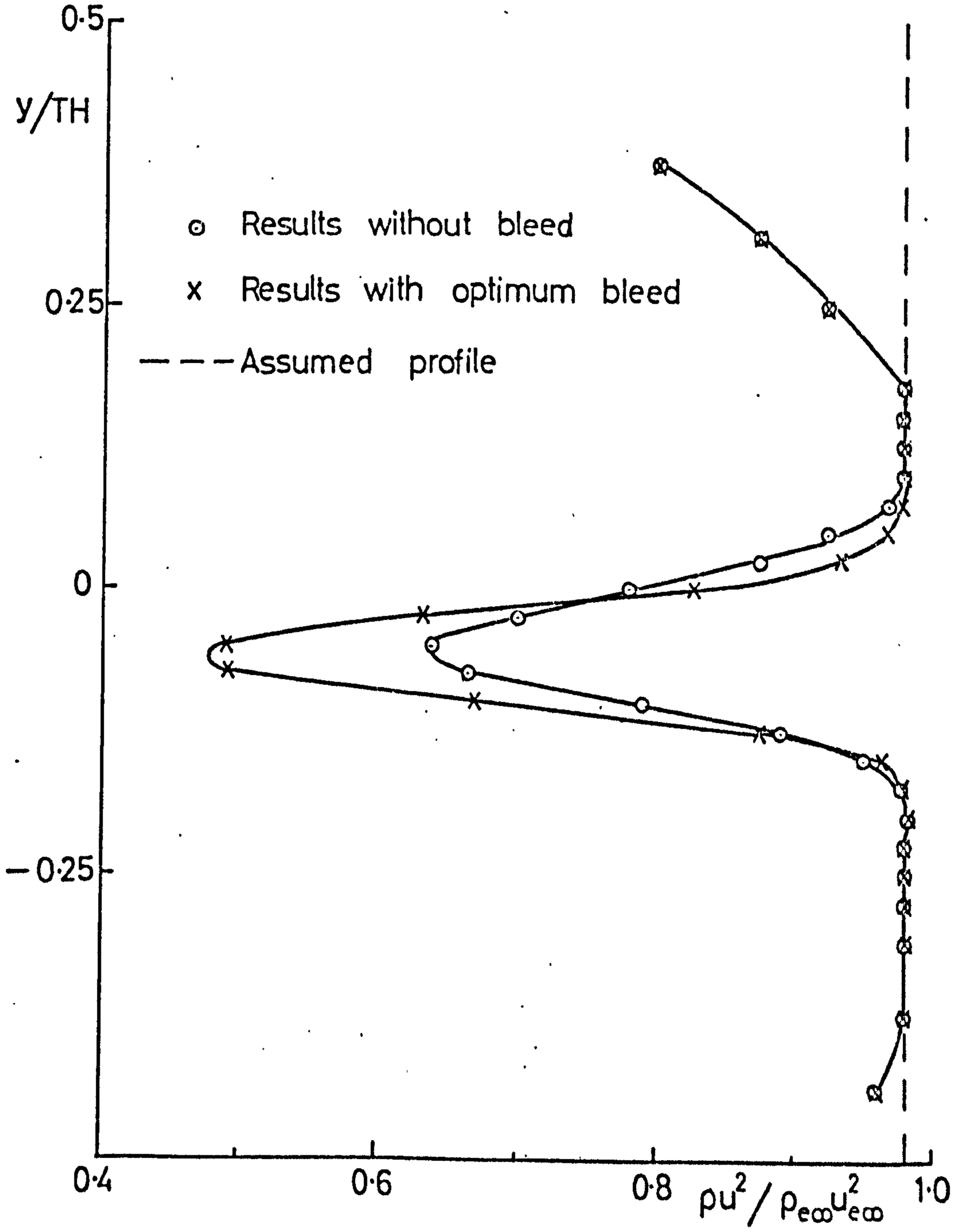

FIG.50a. WAKE PROFILE $\alpha = 2°$. $M_{e\infty} = 0.6$.

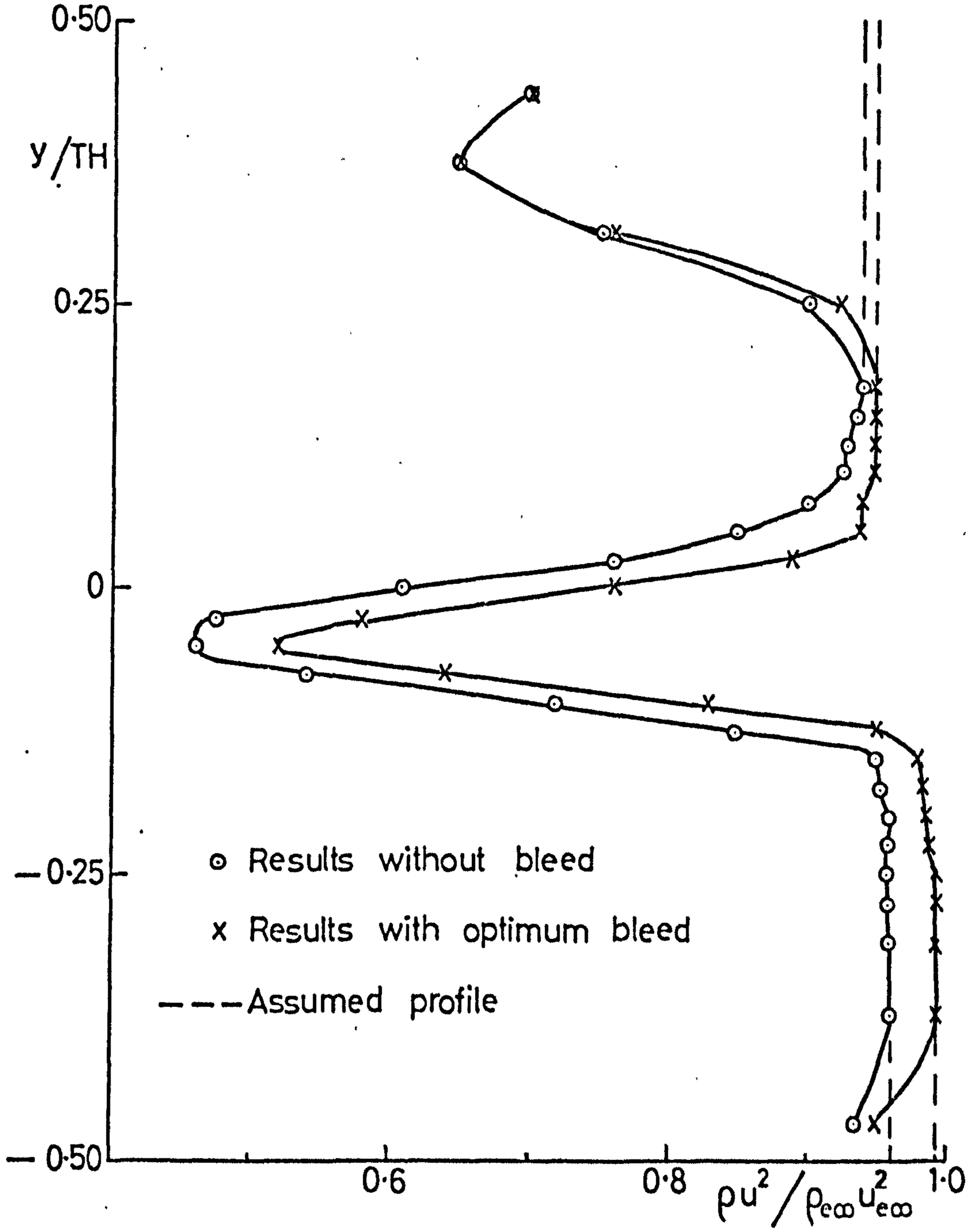

FIG.50b. WAKE PROFILE $\alpha=2°$, $M_{e\infty}=1.0$.

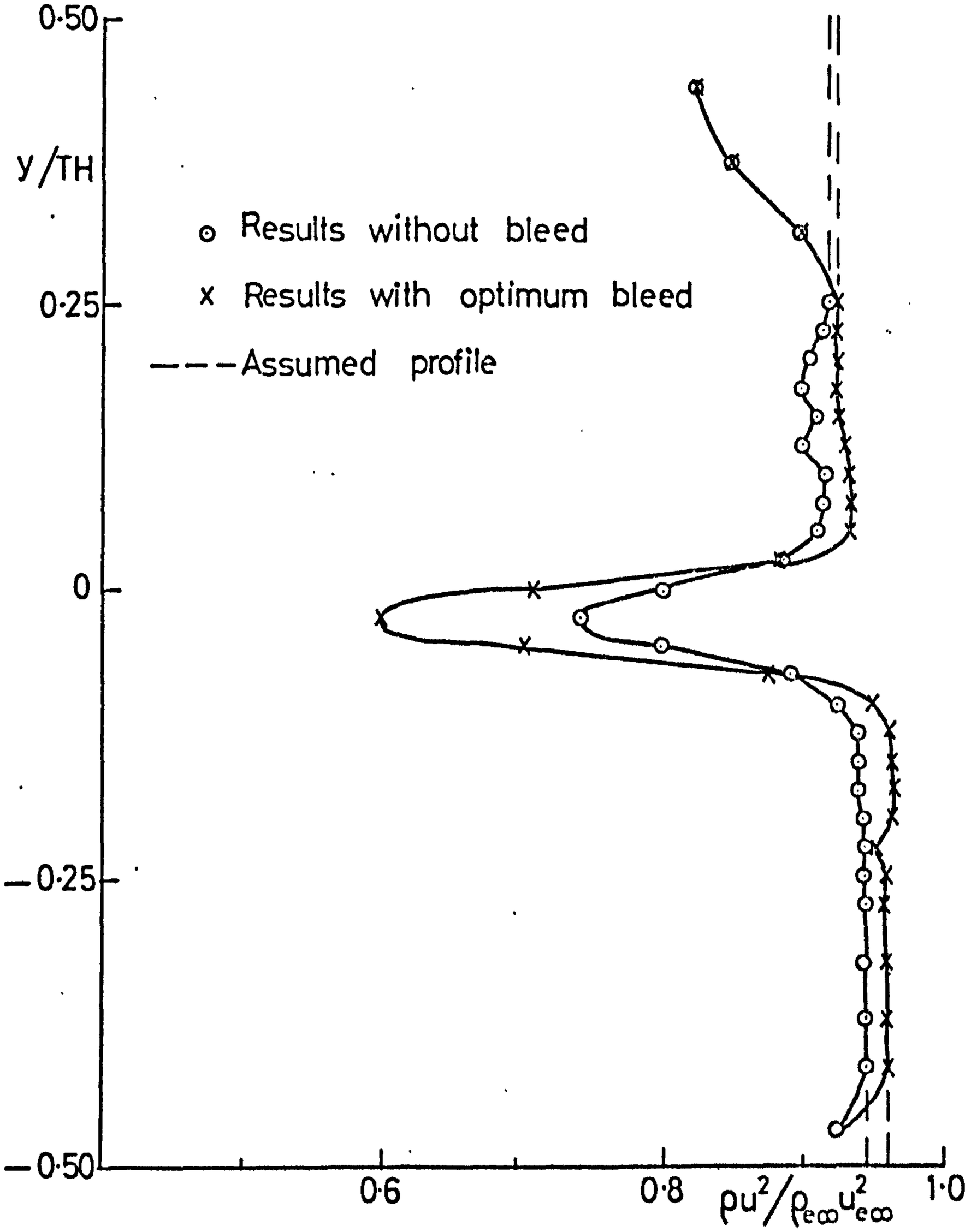

FIG. 50c. WAKE PROFILE $\alpha=2°$, $M_{e\infty}=1·3$.

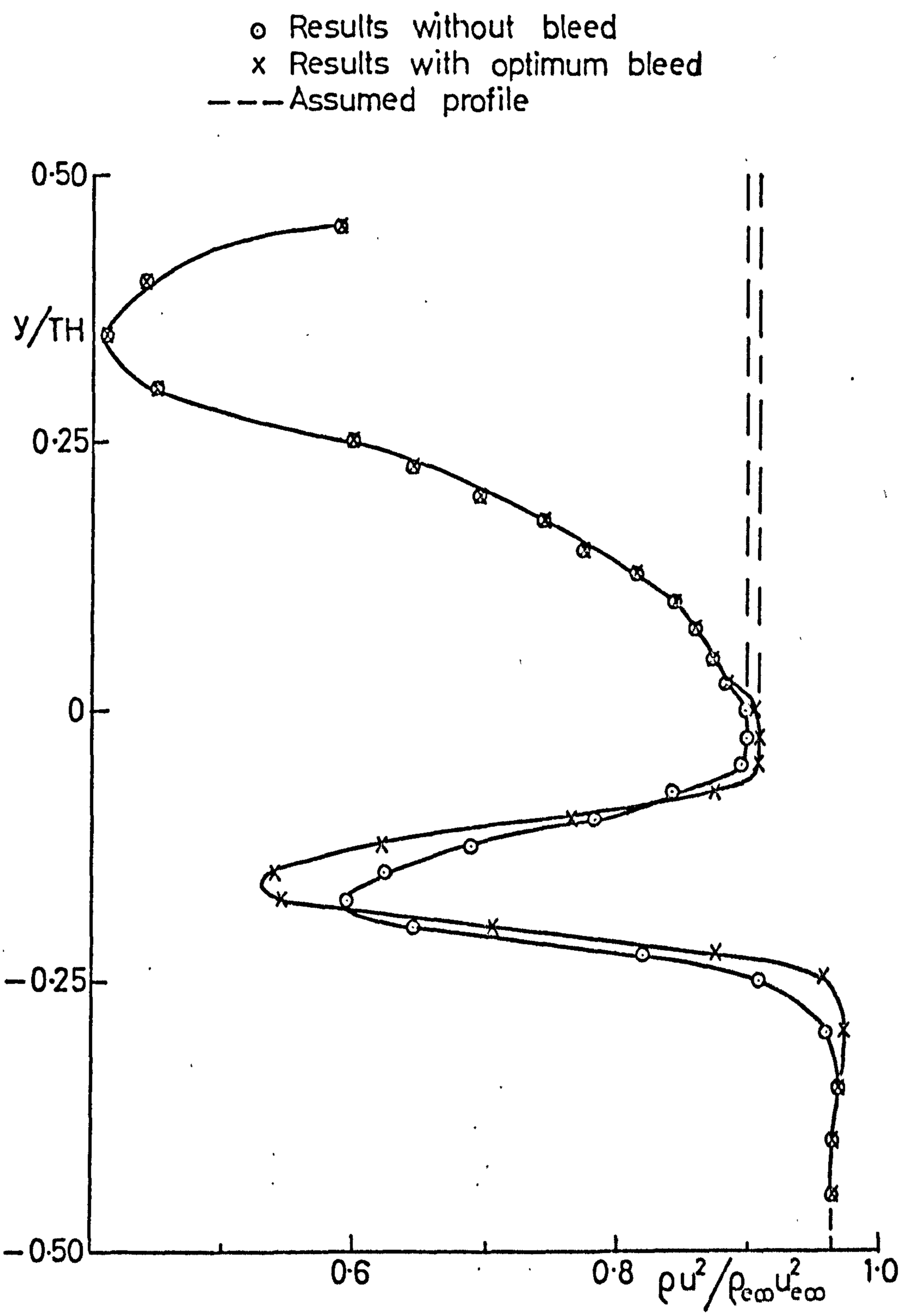

FIG. 51a. WAKE PROFILE $\alpha = 6°$, $M_{e\infty} = 0.6$.

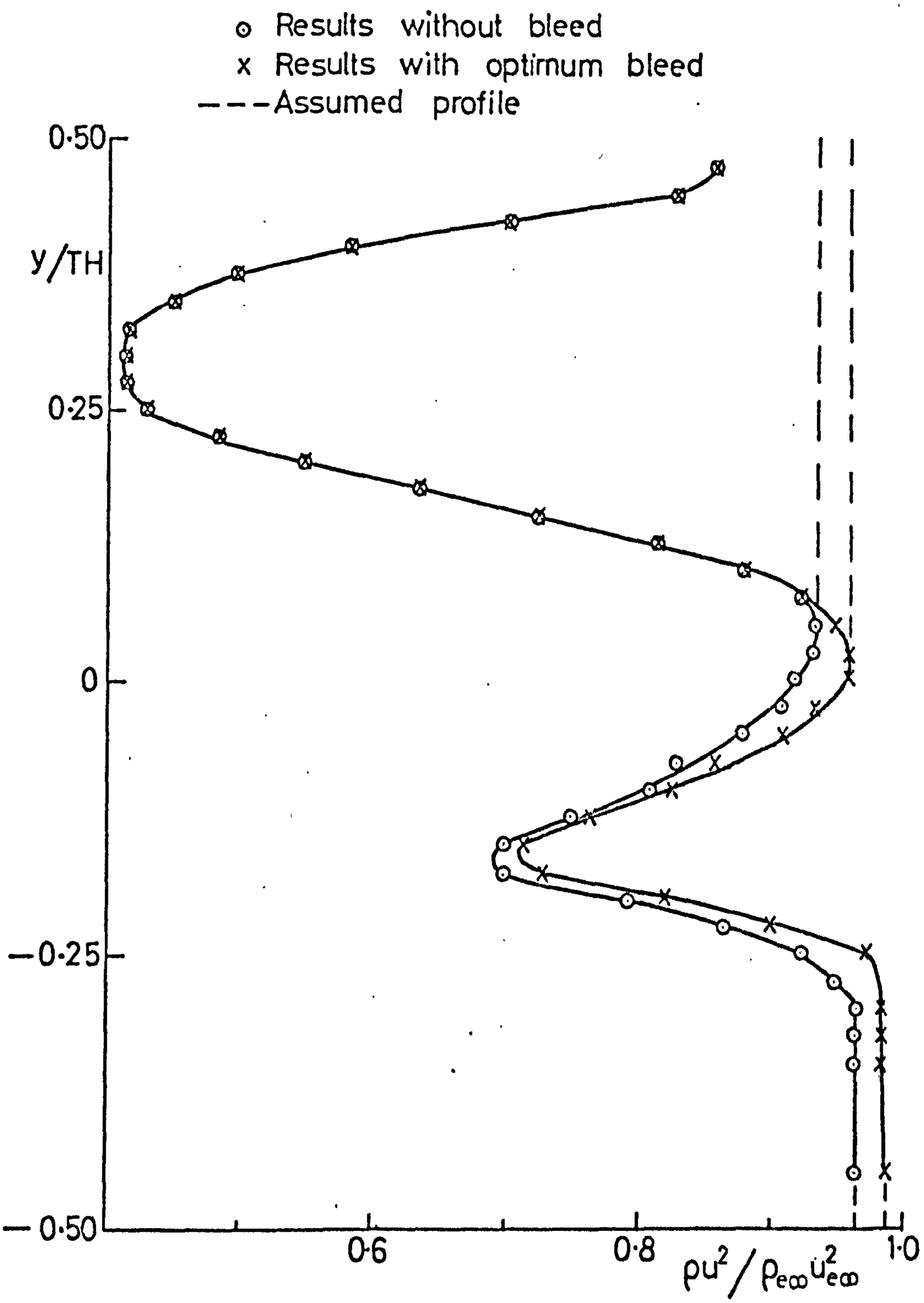

FIG.51b. WAKE PROFILE $\alpha=6°$, $M_{e\infty}=1·0$.

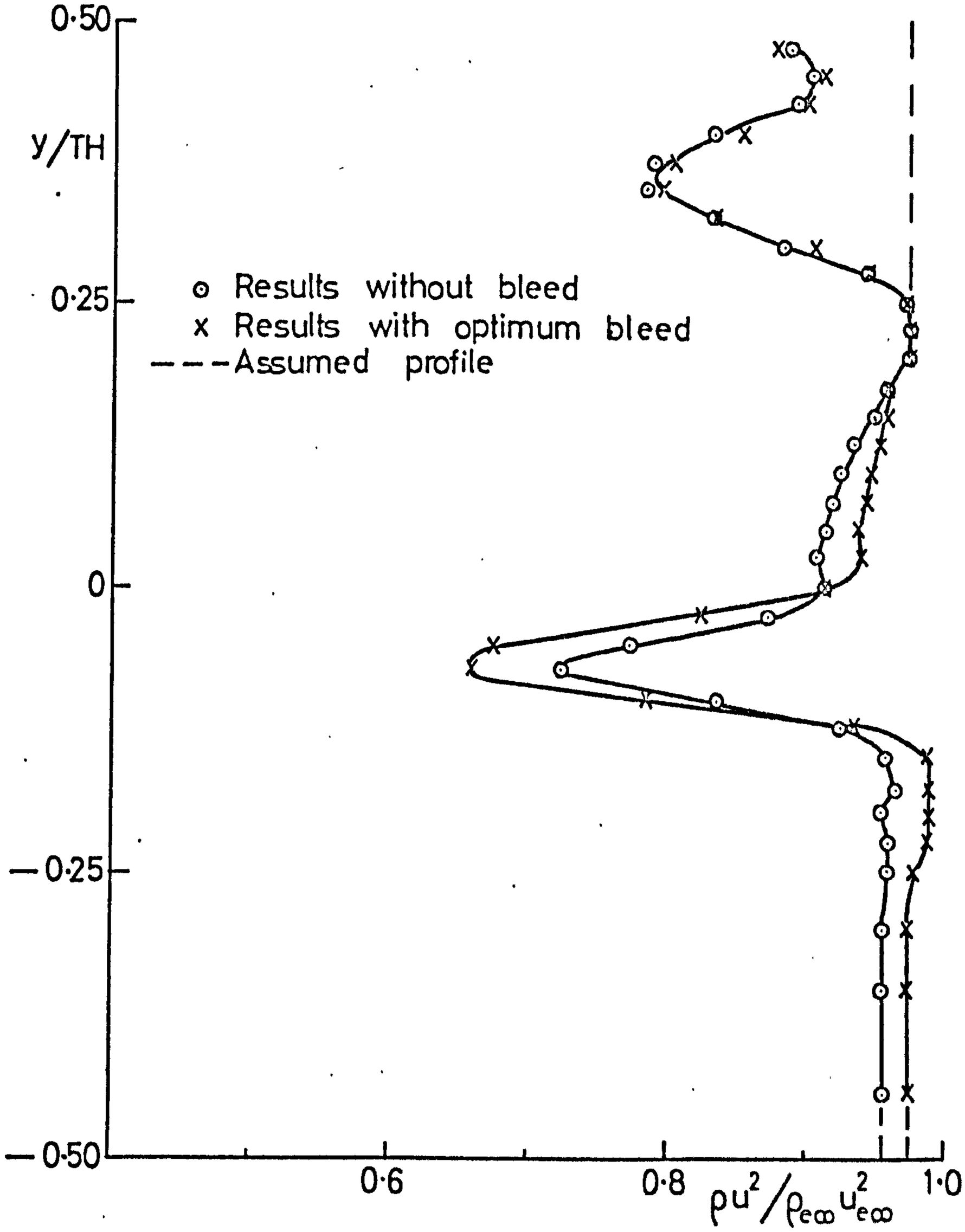

FIG. 51c. WAKE PROFILE $\alpha = 6°$, $M_{e\infty} = 1{\cdot}3$

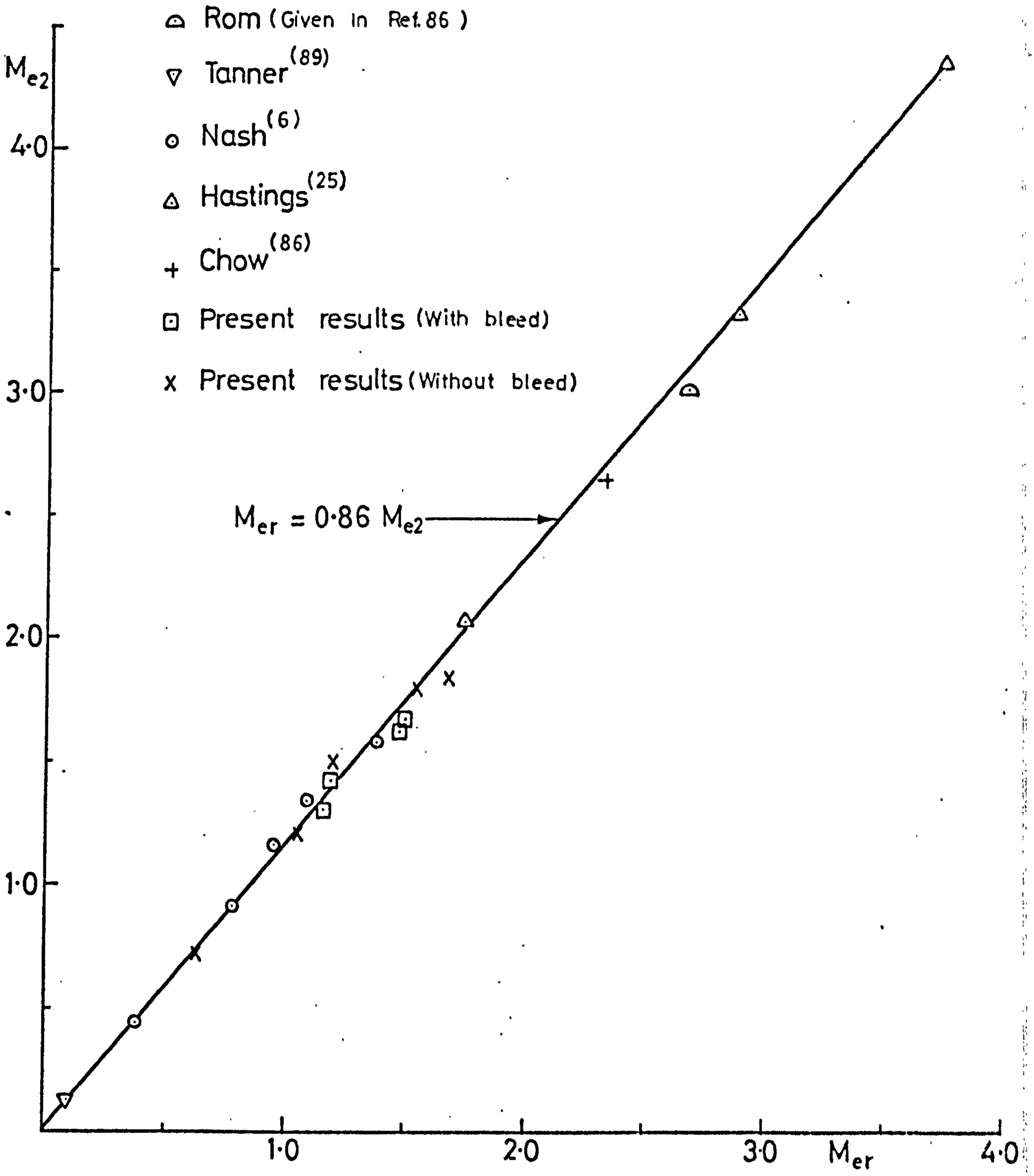

FIG. 52. VARIATION OF REATTACHMENT PRESSURE WITH BASE PRESSURE. (SEE TABLE 7)

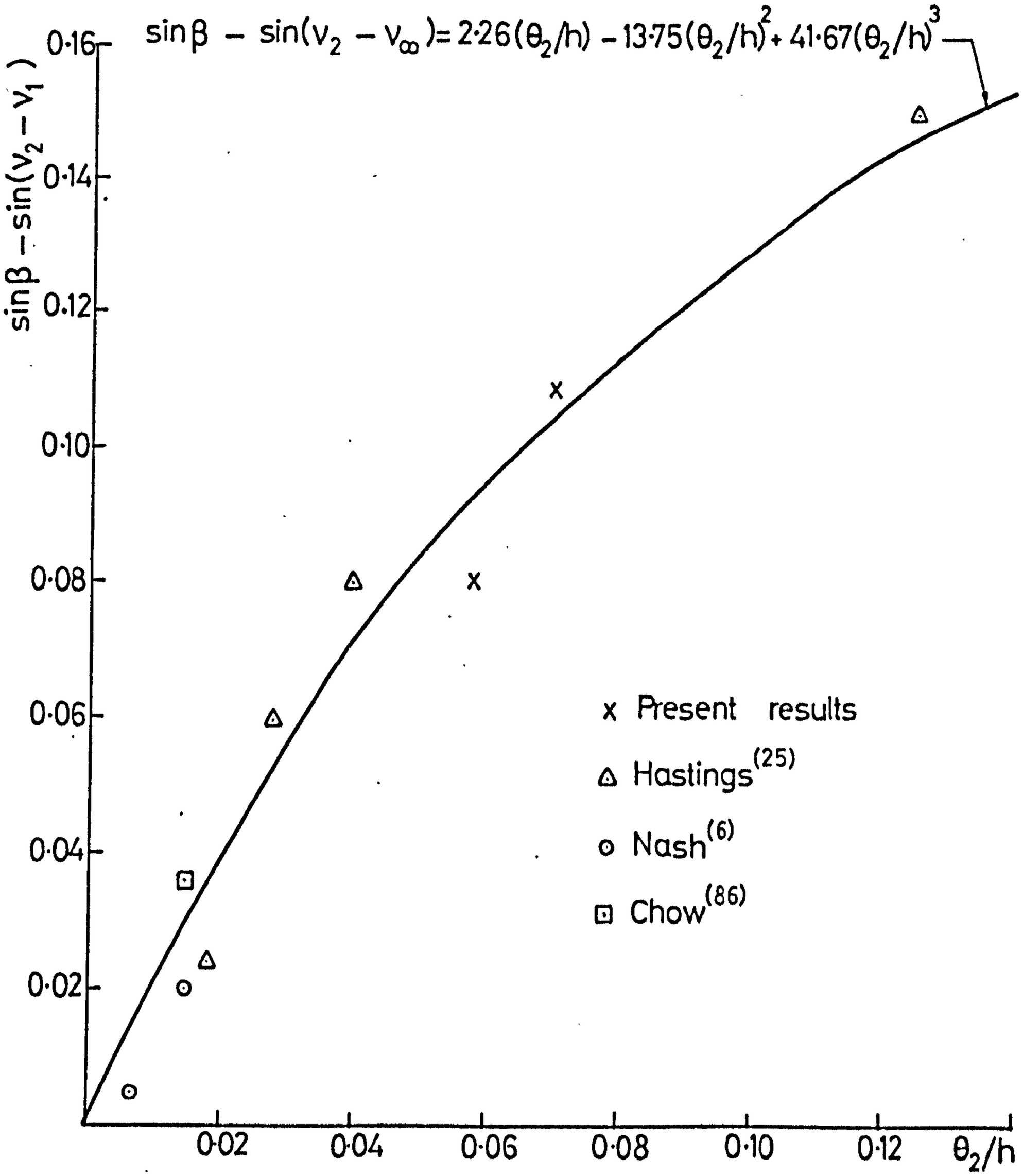

FIG.53. EFFECT OF THE BOUNDARY LAYER THICKNESS ON THE POSITION OF THE REATTACHMENT POINT.

FIG.54. VARIATION OF $(P_b/P_\infty)_{opt}$ WITH INITIAL P_b/P_∞.

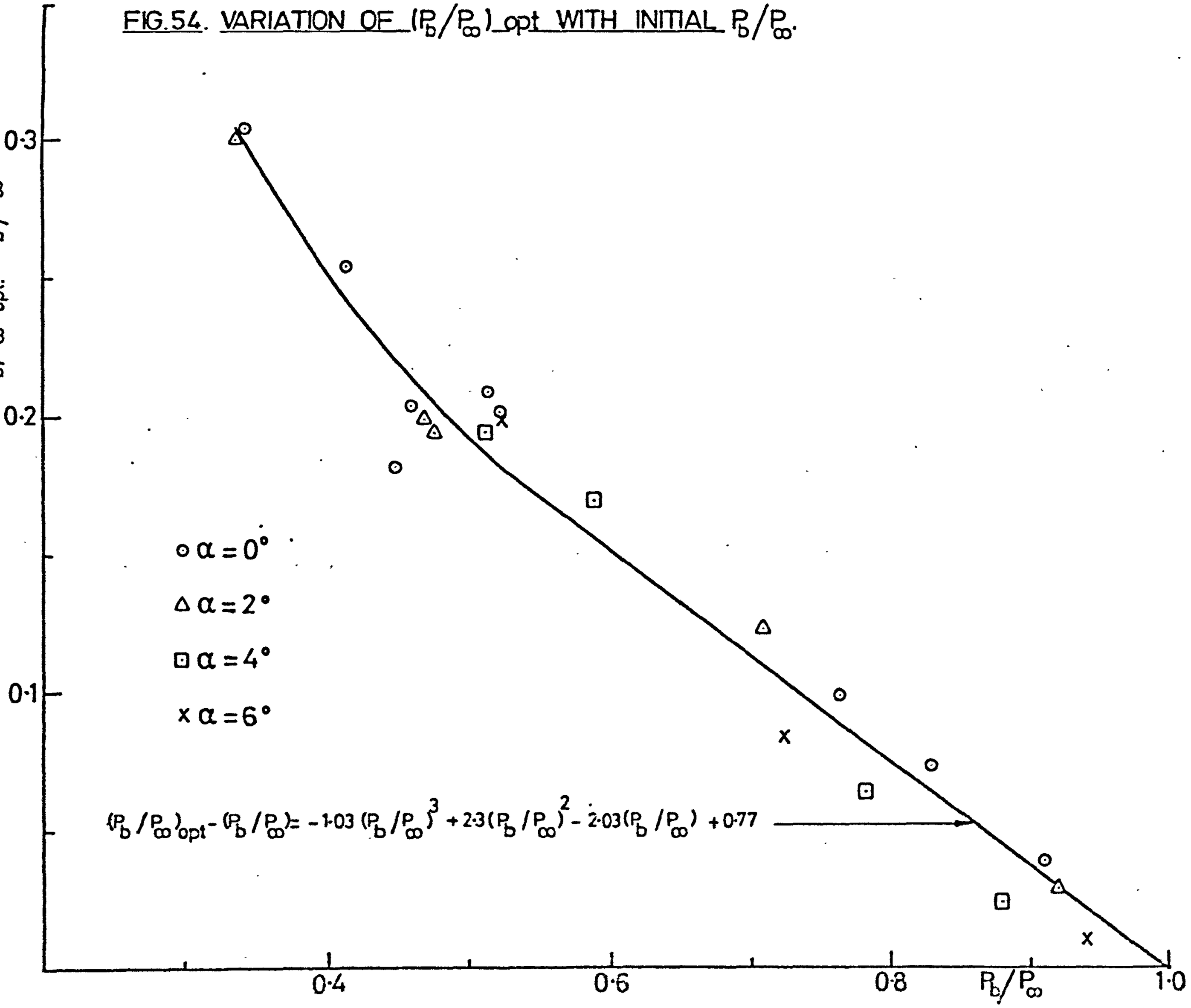

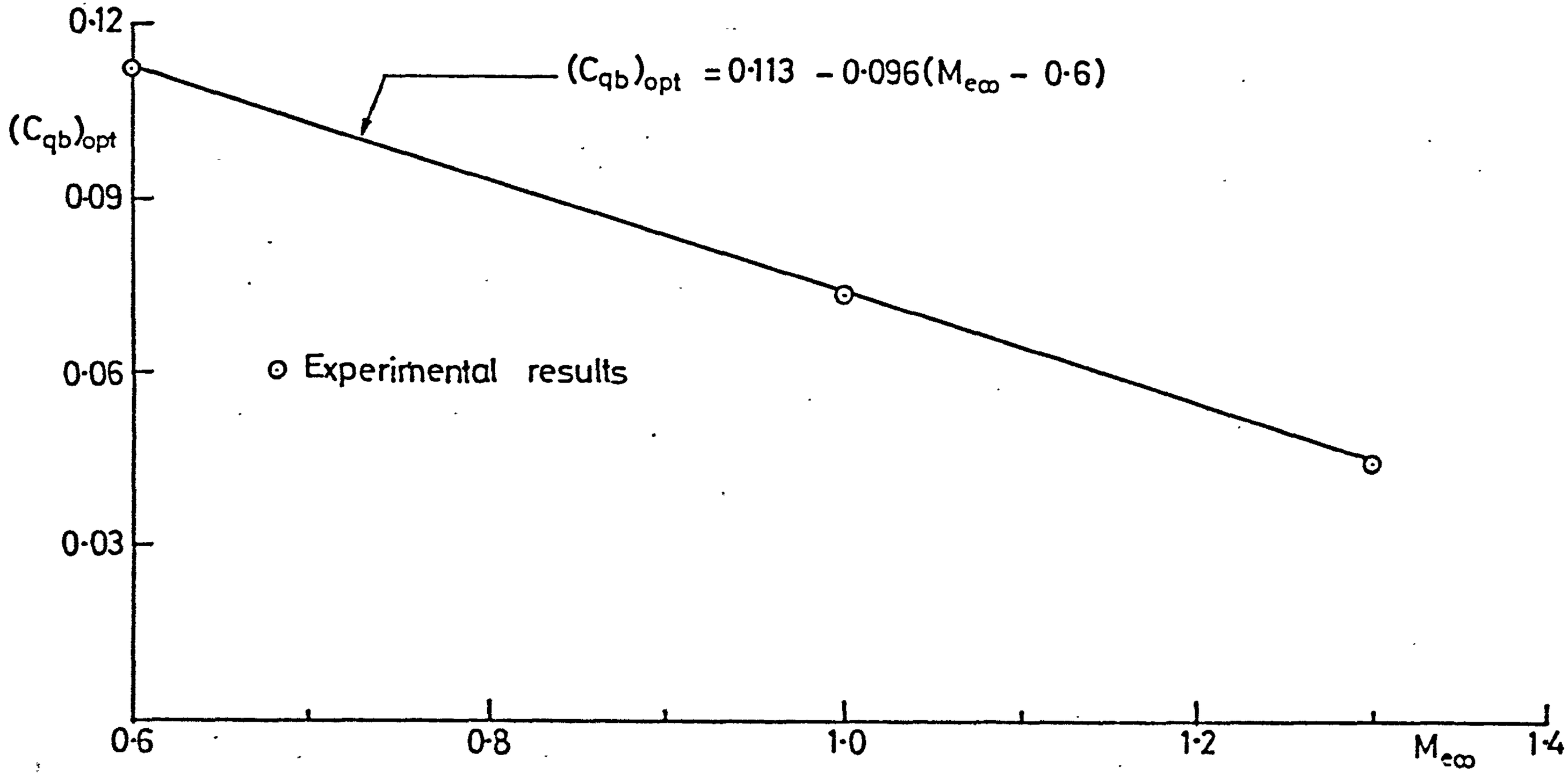

FIG.55. VARIATION OF $(C_{qb})_{opt}$ WITH $M_{e\infty}$.

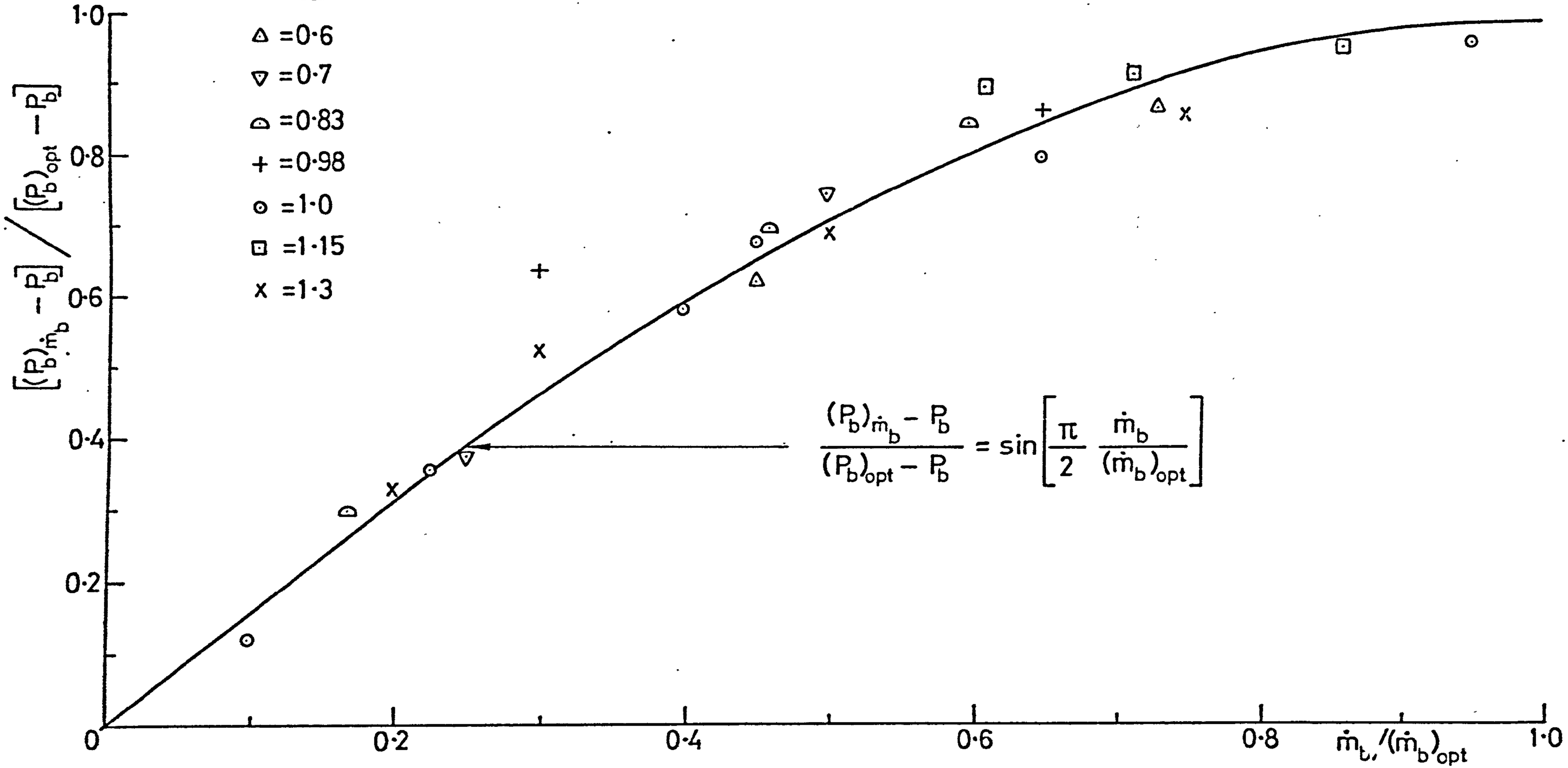

FIG.56. VARIATION OF BASE PRESSURE WITH MASS INJECTION ($\alpha=\phi$)

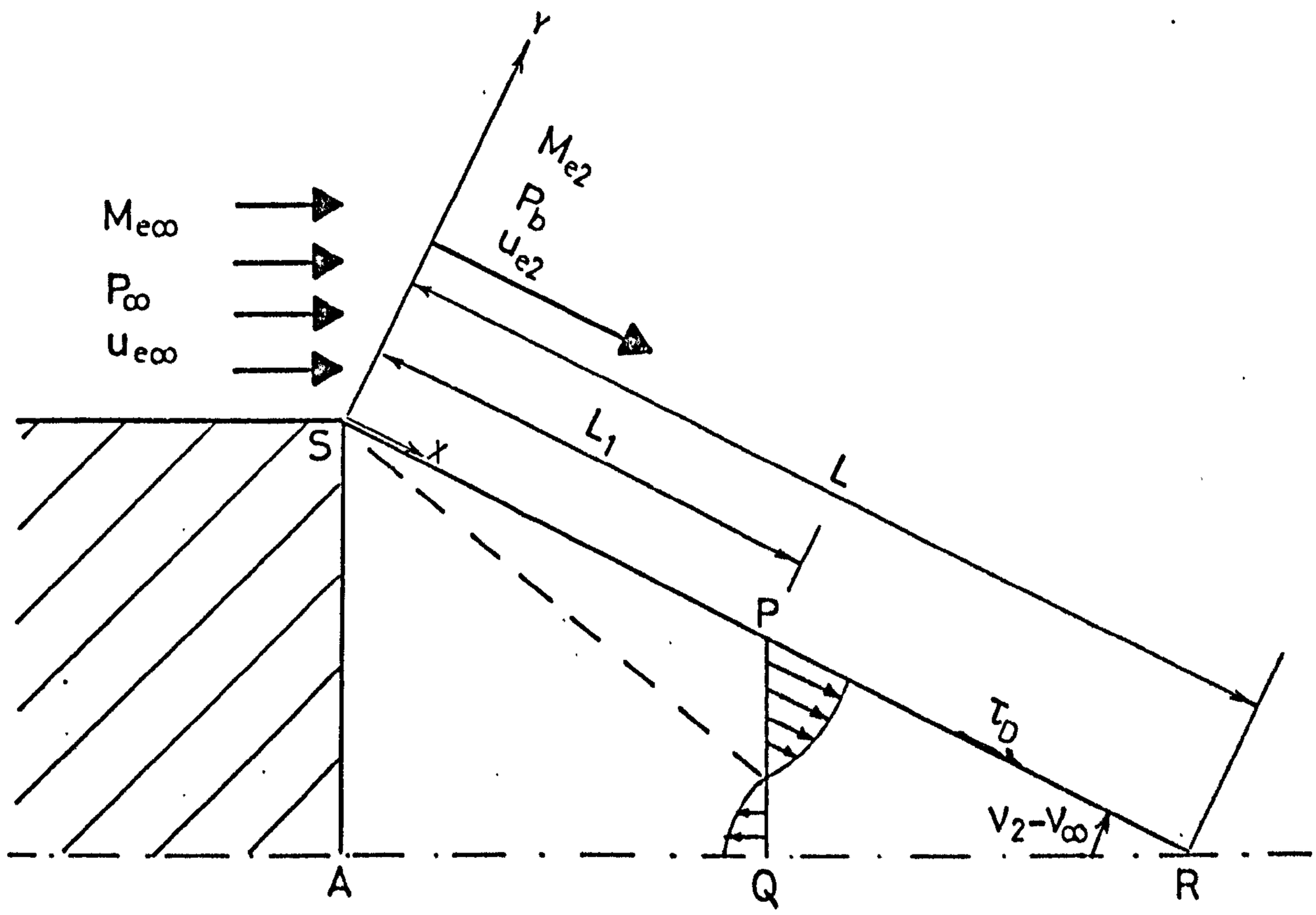

FIG.57. SKETCH OF BASE FLOW WITH ZERO BOUNDARY LAYER THICKNESS AT SEPARATION.

FIG.58. VARIATION OF LIMITING BASE PRESSURE COEFFICIENT WITH $M_{e\infty}$

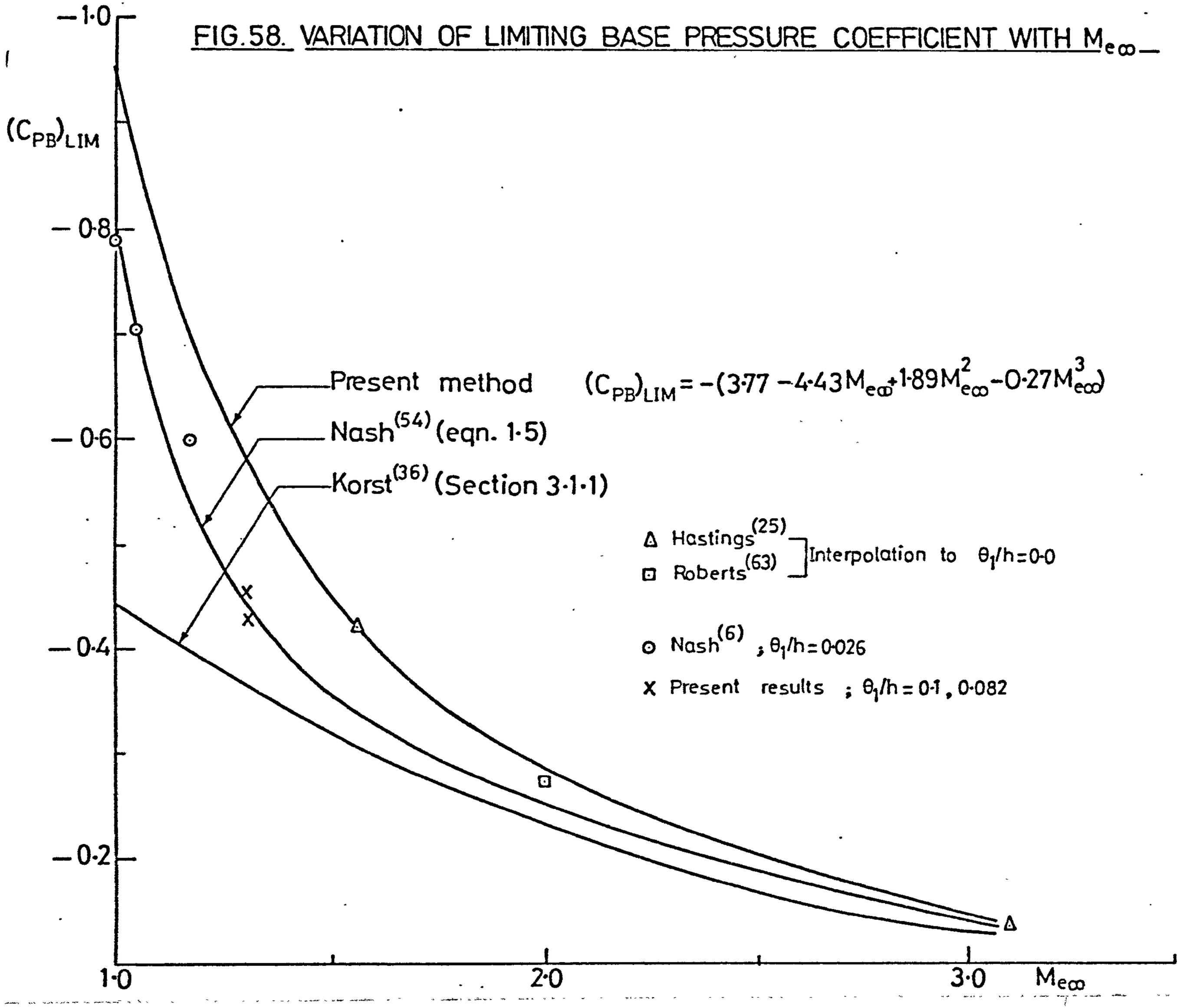

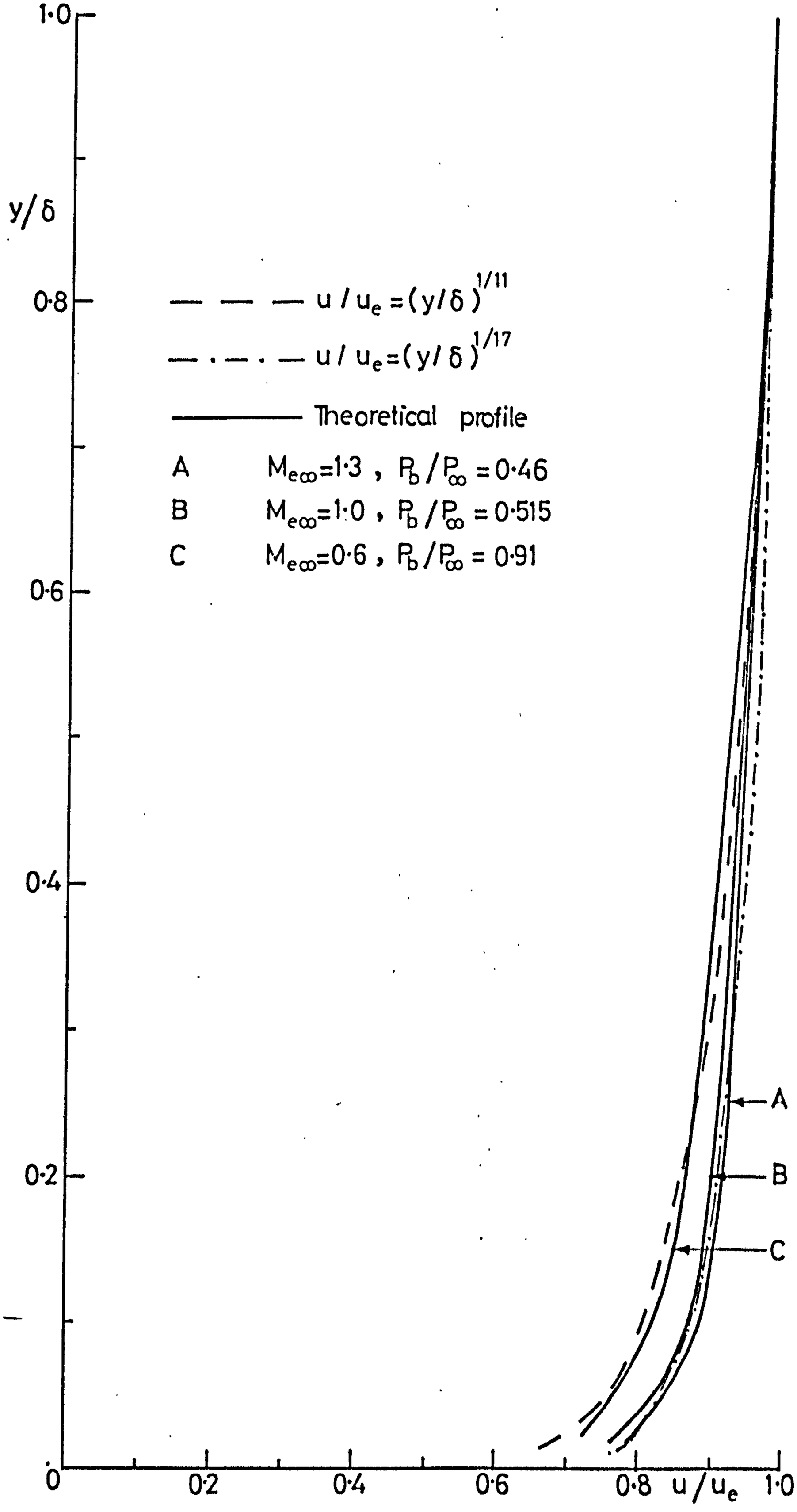

FIG.59. THEORETICAL BOUNDARY LAYER PROFILE AT THE CORNER.

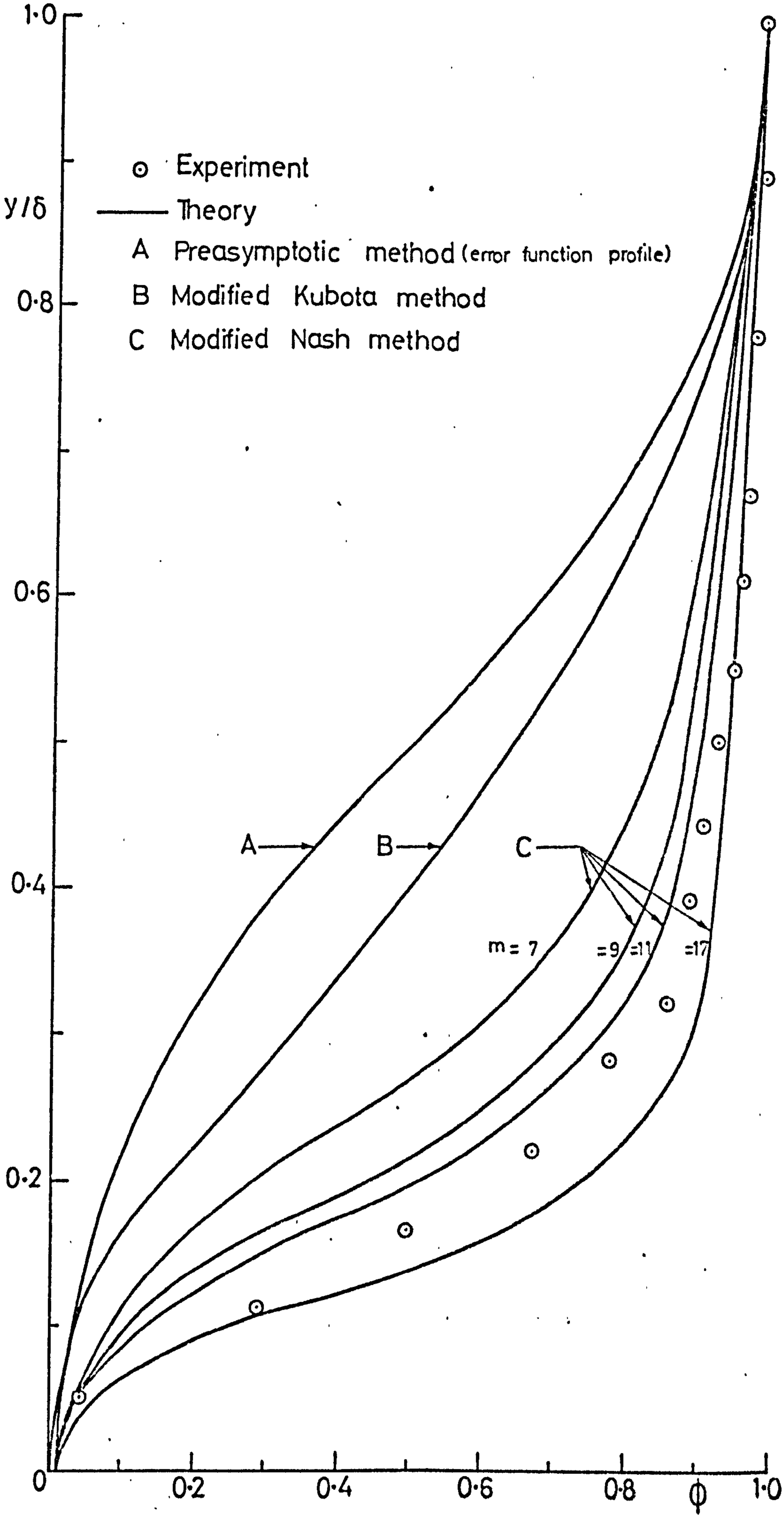

FIG. 60. FREE SHEAR LAYER VELOCITY PROFILE (M_{c_∞}=1·3, x/2h=2/3)

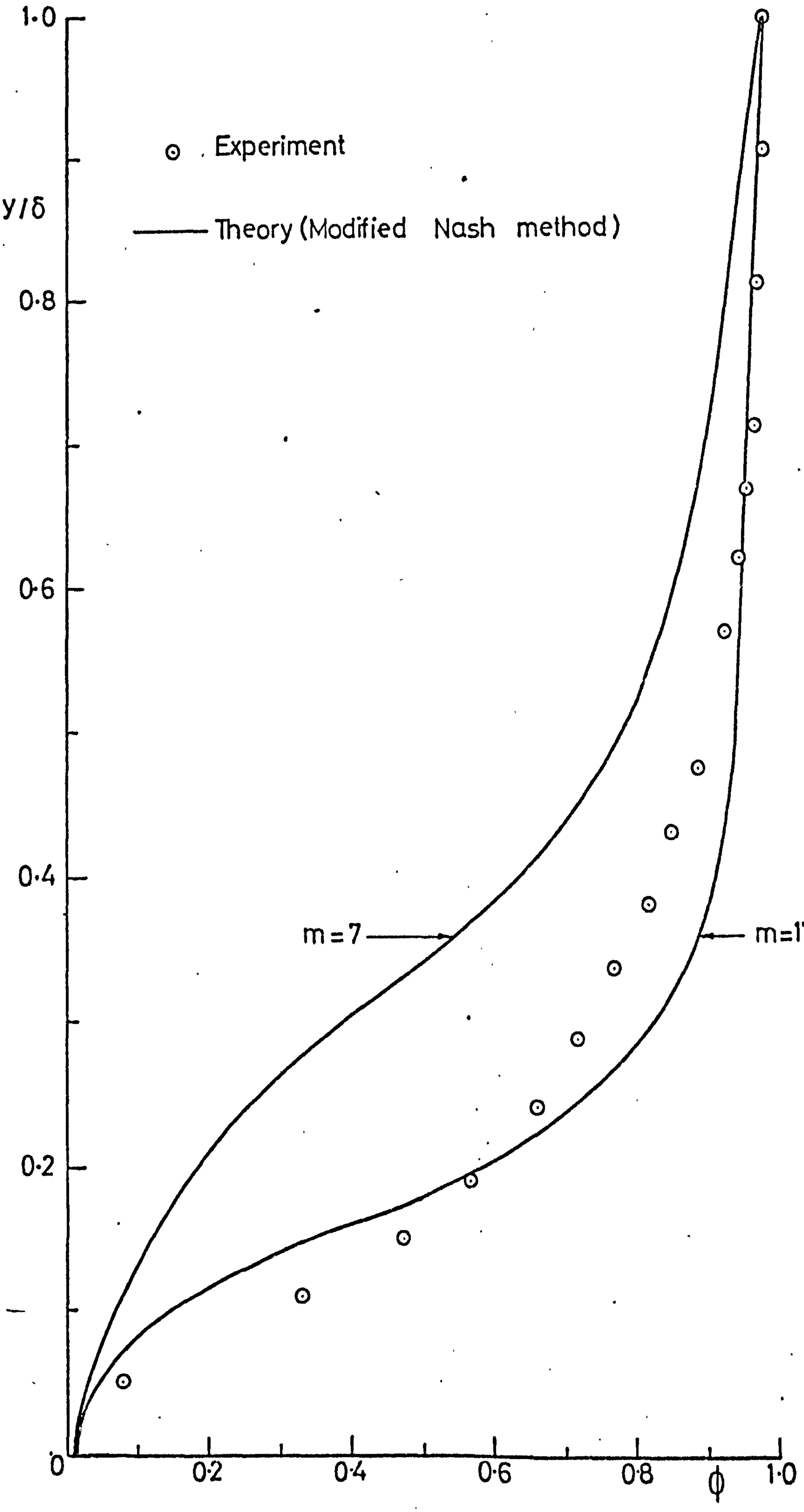

FIG.61. FREE SHEAR LAYER VELOCITY PROFILE ($M_{e\infty}$=1·0, x/2h=2/3)

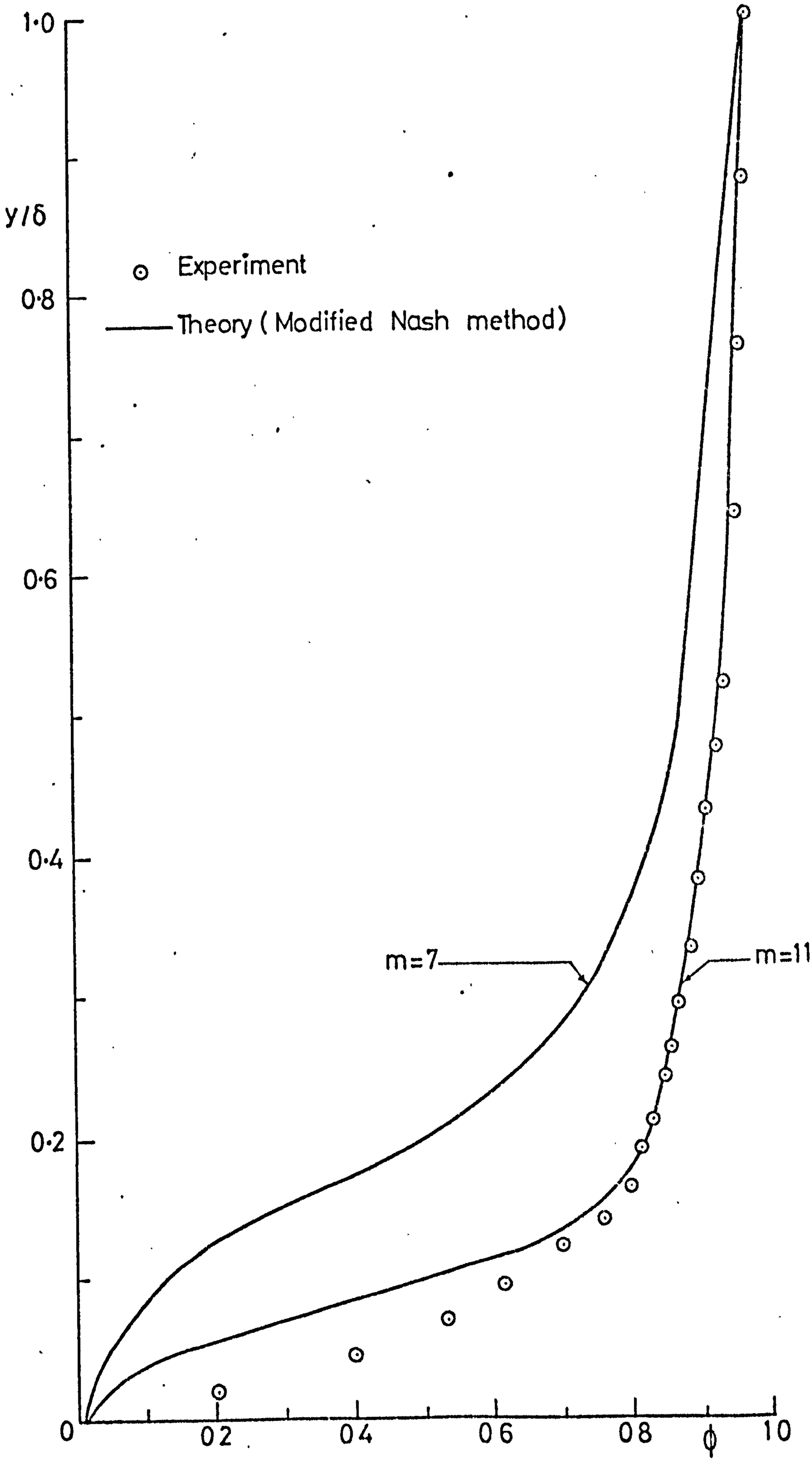

FIG.62. FREE SHEAR LAYER VELOCITY PROFILE ($M_{e\infty}$=0·6, x/2h=2/3)

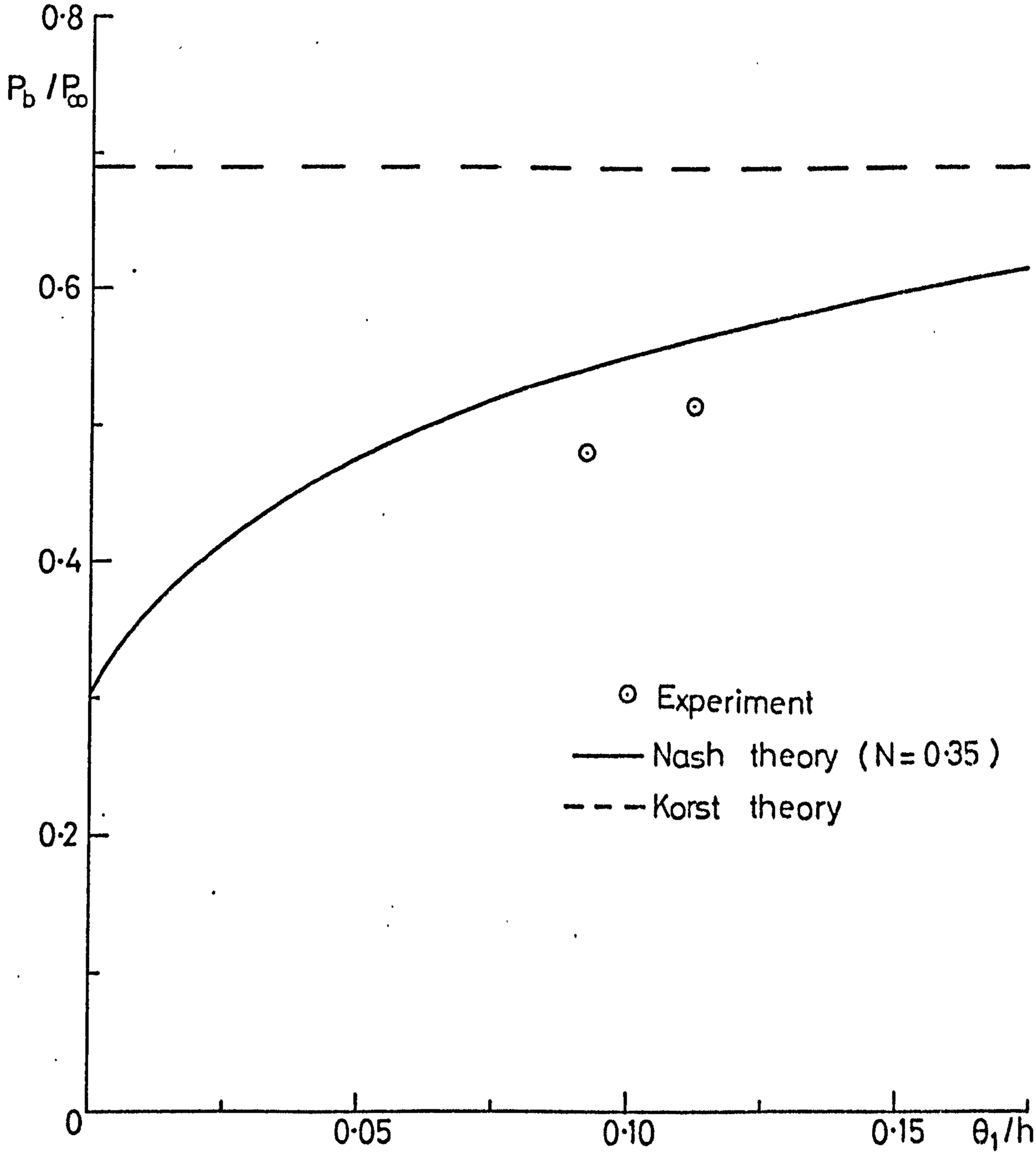

FIG.63. THEORETICAL VARIATION OF P_b/P_∞ WITH θ_1/h ($M_{e\infty}$=1·0).

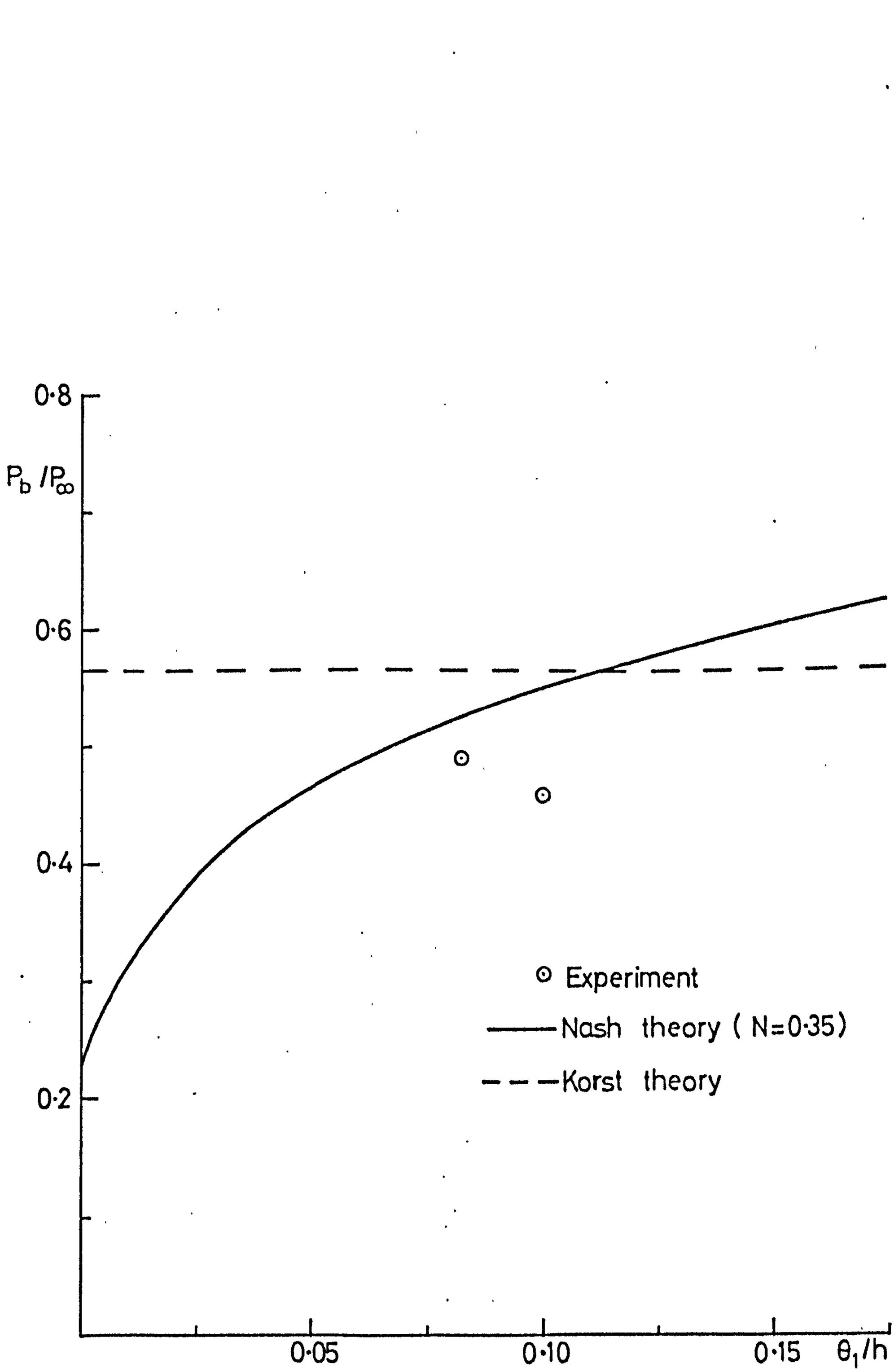

FIG.64. THEORETICAL VARIATION OF P_b/P_∞ WITH θ_1/h ($M_{e\infty}$=1·3).

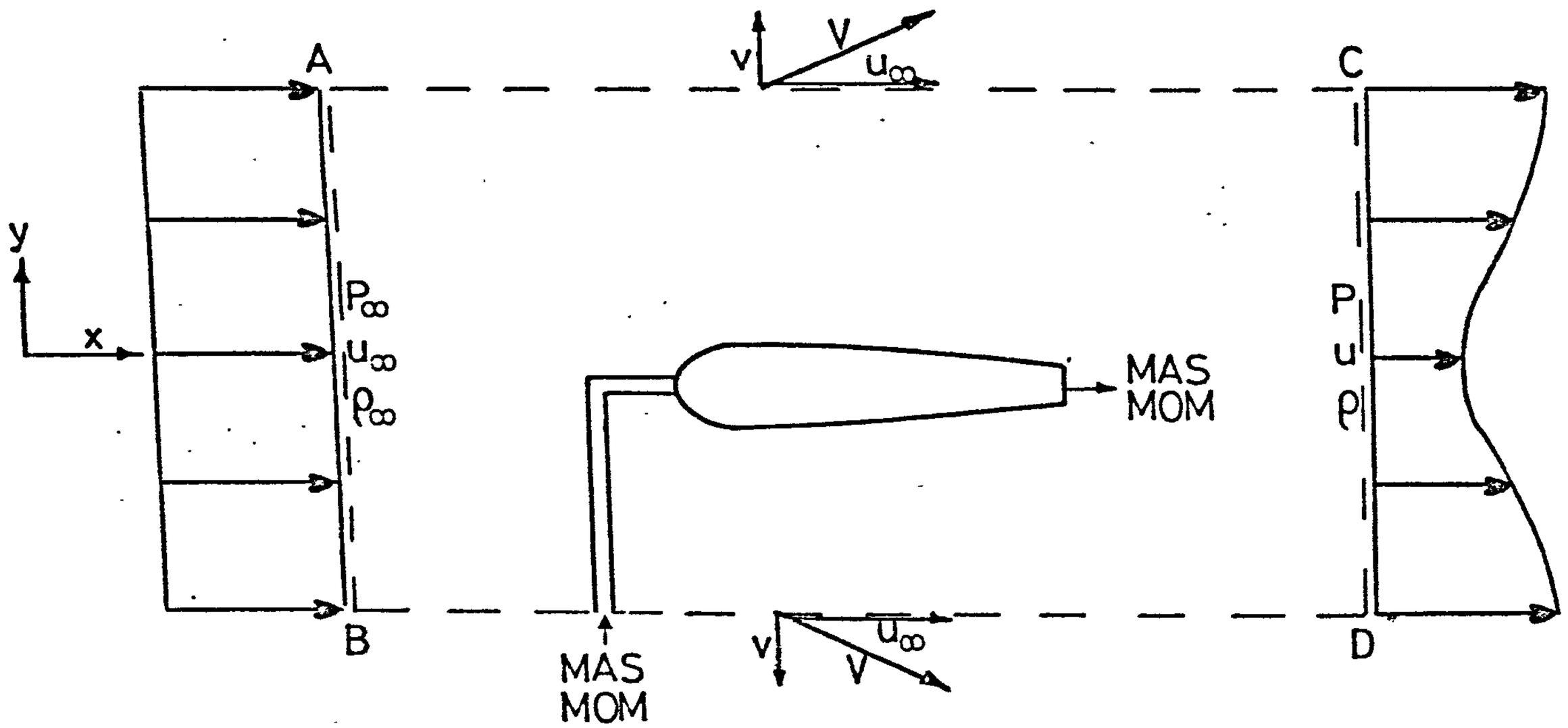

FIG.65. CONTROL VOLUME FOR DRAG ANALYSIS.

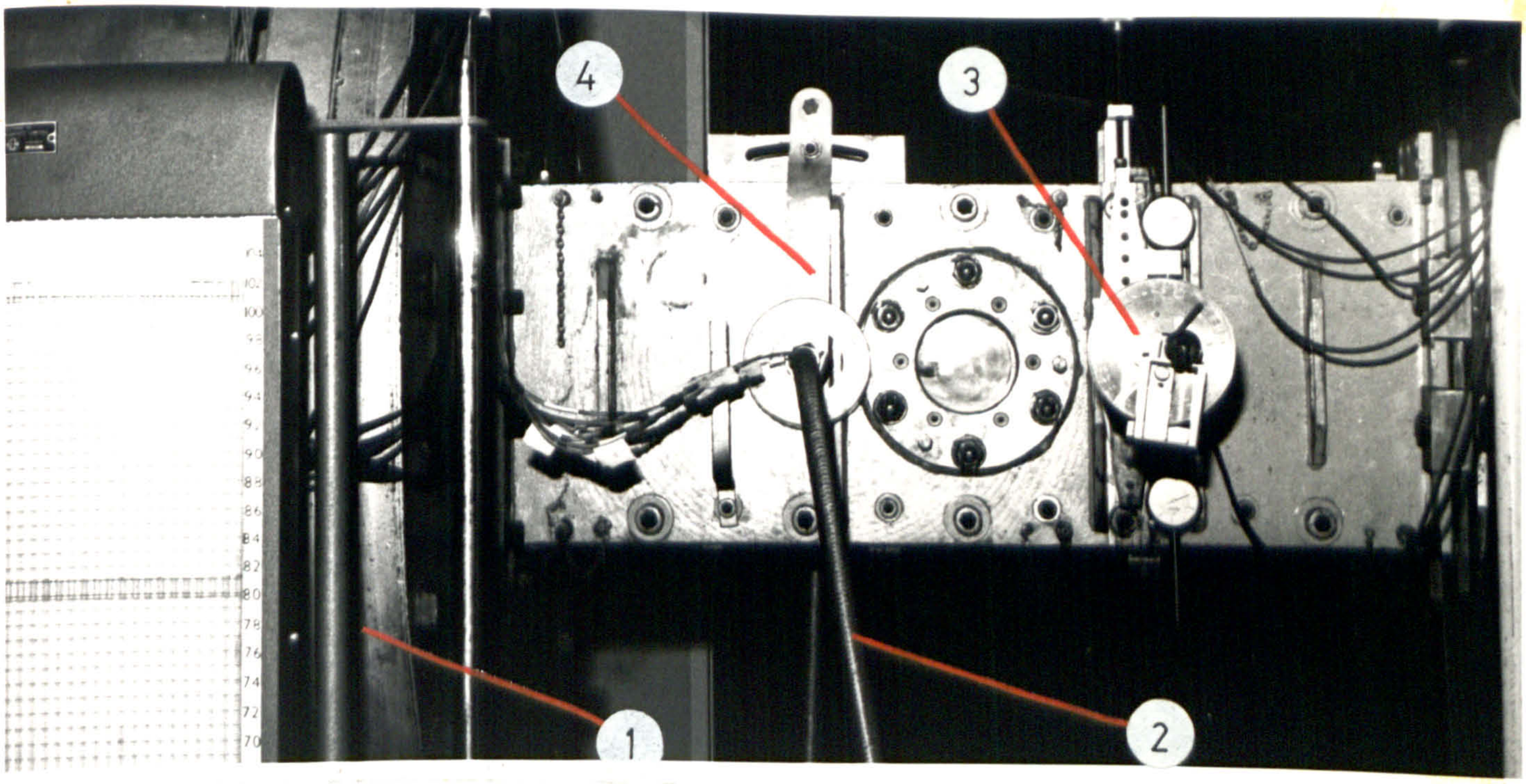

(A) Side A

PLATE 1 GENERAL VIEW OF THE TRANSONIC WIND TUNNEL (Continued)

1) Settling chamber
2) Air supply for base bleed
3) Traverse gear
4) Angle of incidence adjustment gear
5) Pitot-static probe
6) The model

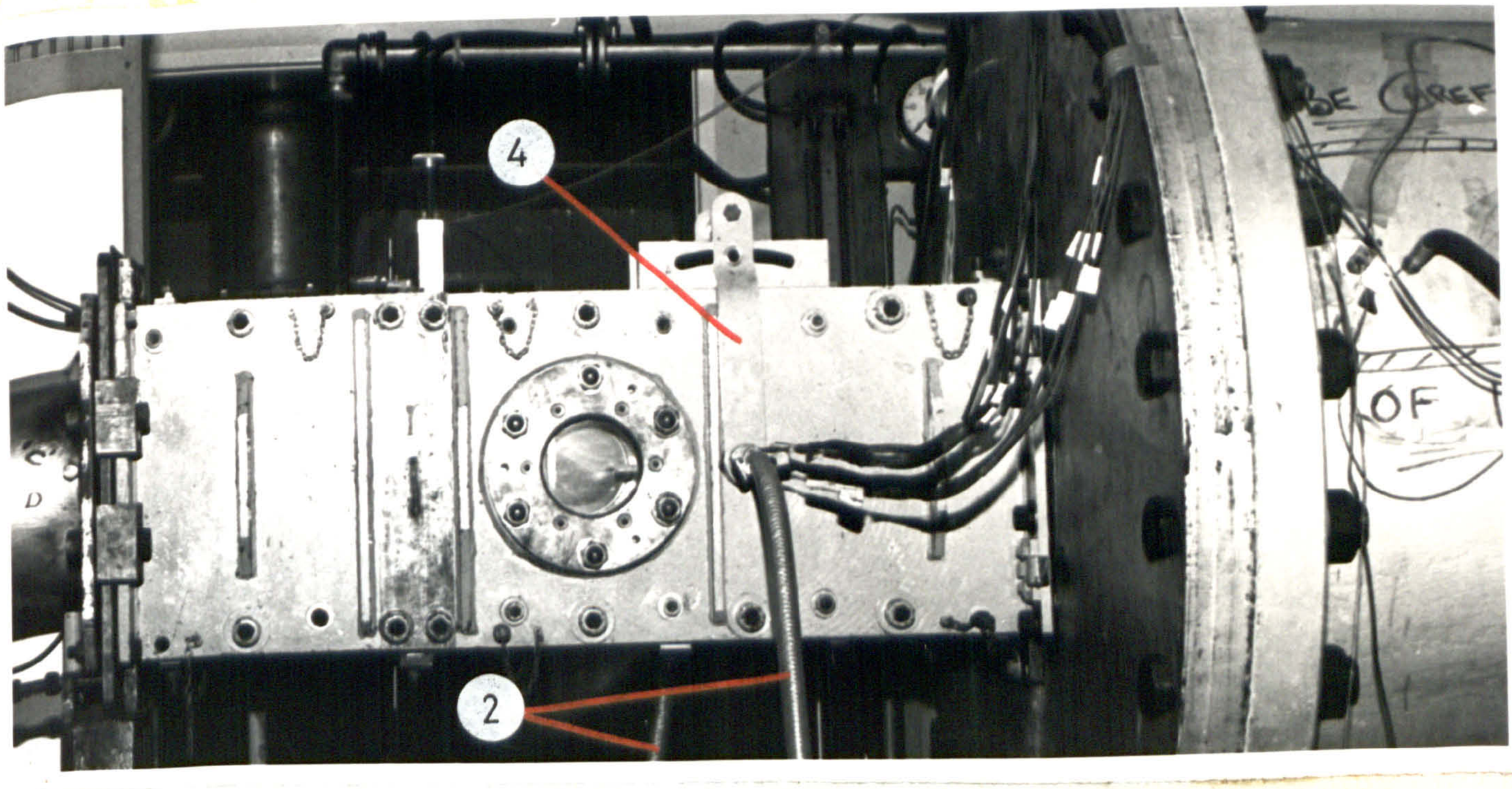

(B) Side B

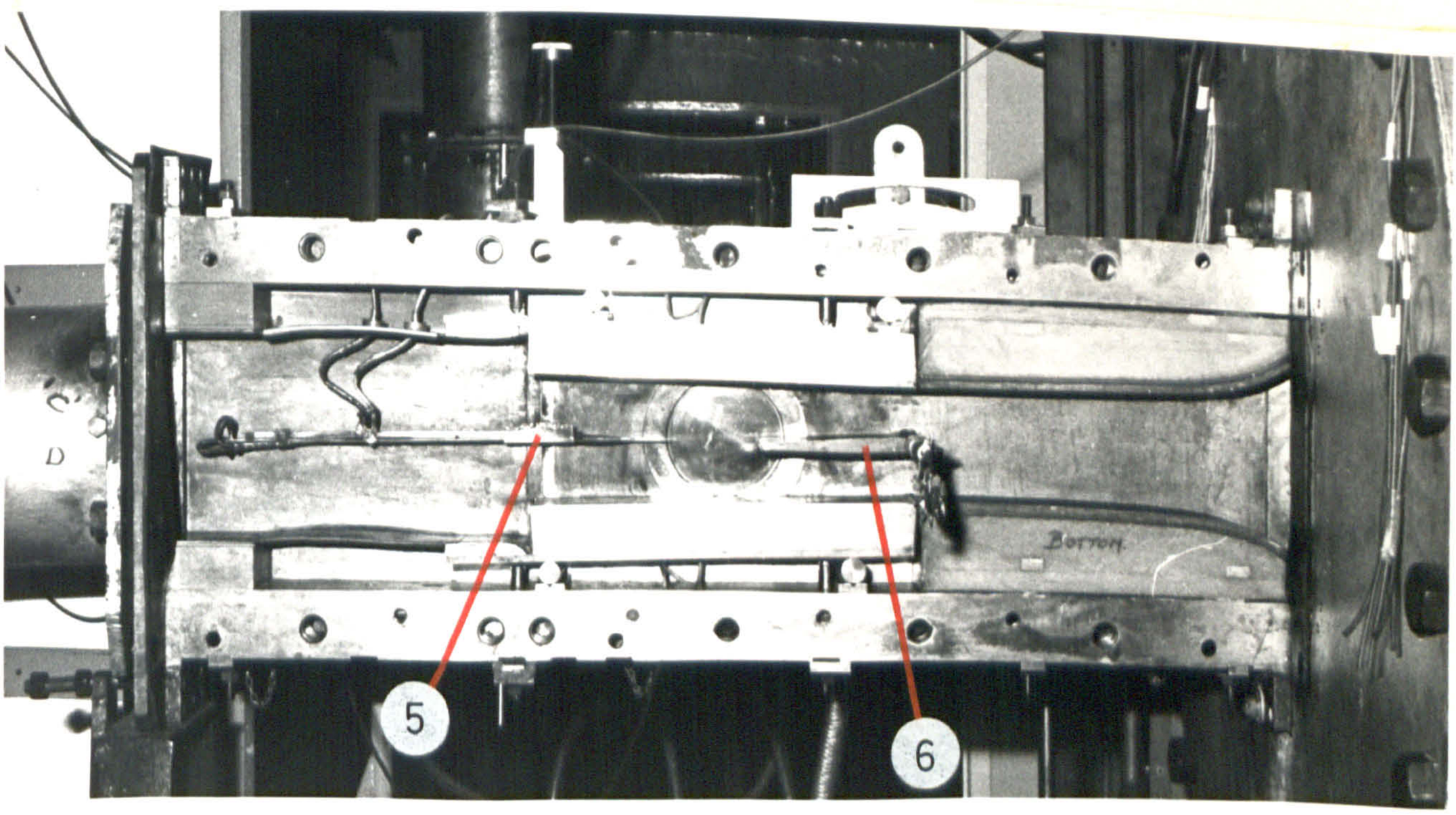

(C) Side B (With the Side Wall Removed)

PLATE 1 GENERAL VIEW OF THE TRANSONIC WIND TUNNEL

1) Settling chamber
2) Air supply for base bleed
3) Traverse gear
4) Angle of incidence adjustment gear
5) Pitot-static probe
6) The model

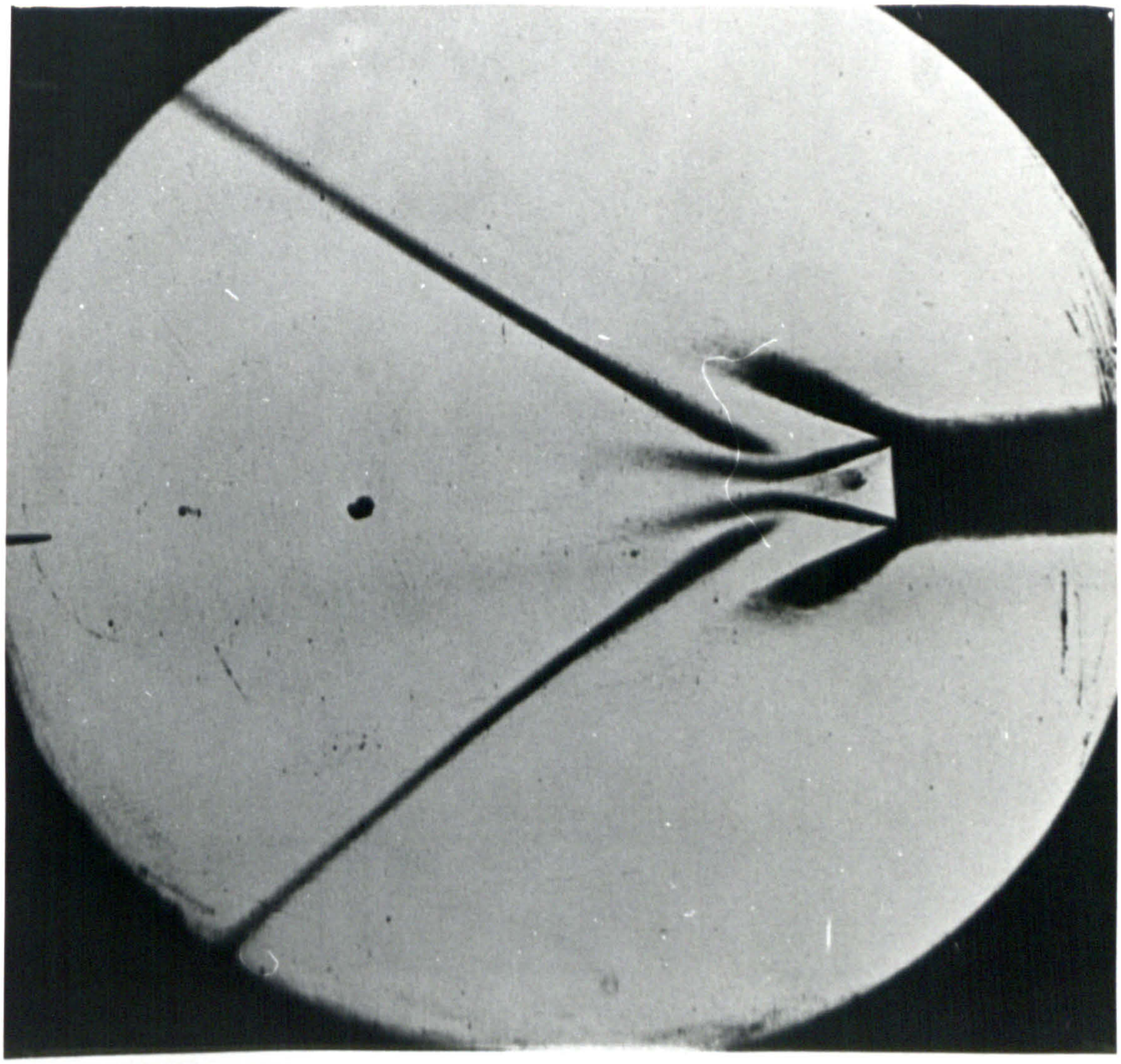

(A) Without Base Bleed

PLATE 2 BASE FLOW WITH THE MODEL AT ZERO INCIDENCE

($M_{e\infty}$ = 1.3)

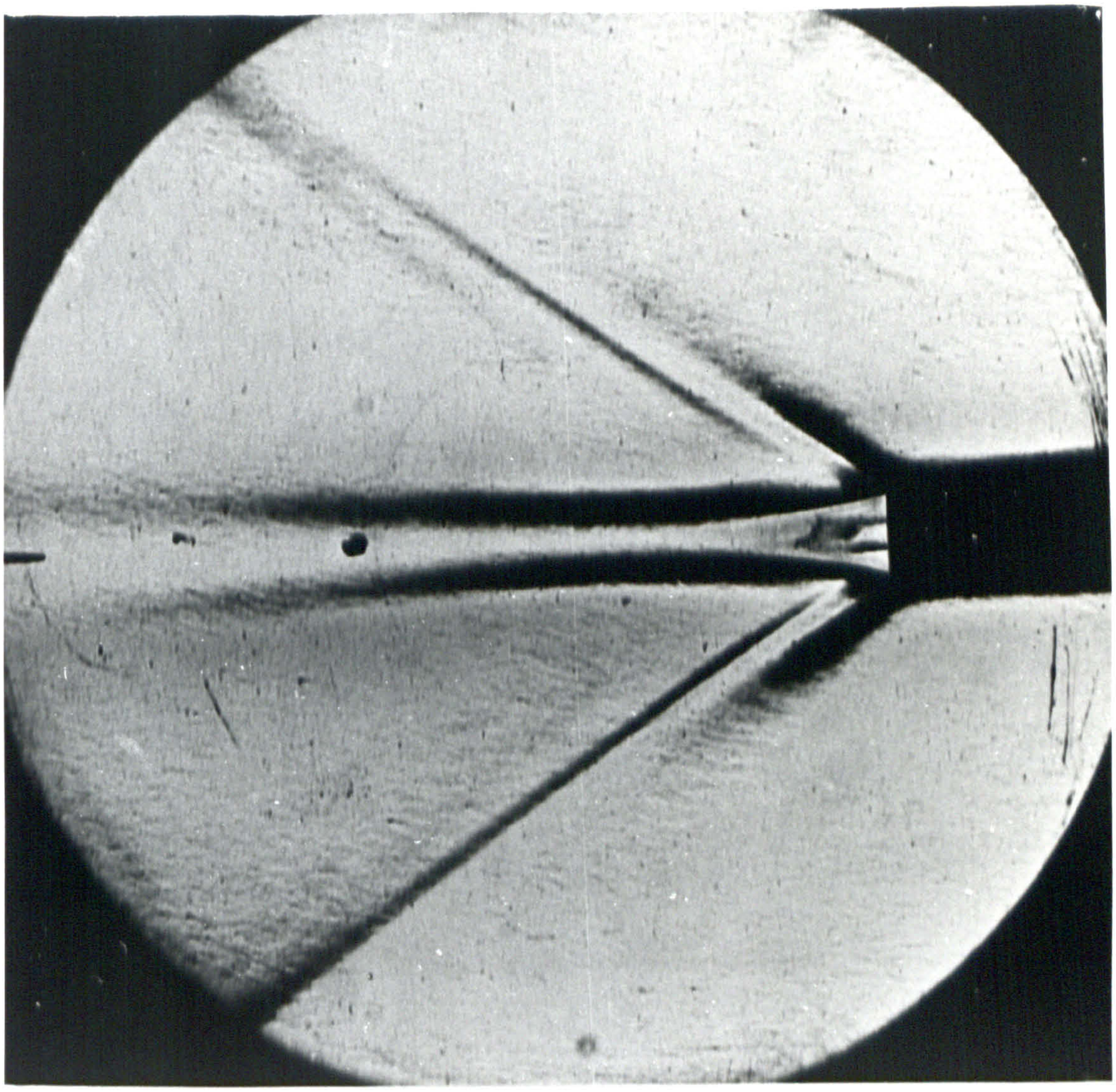

(B) With Base Bleed (C_{qb}=0.049)

PLATE 2 BASE FLOW WITH THE MODEL AT ZERO INCIDENCE

($M_{e\infty}$ = 1.3)

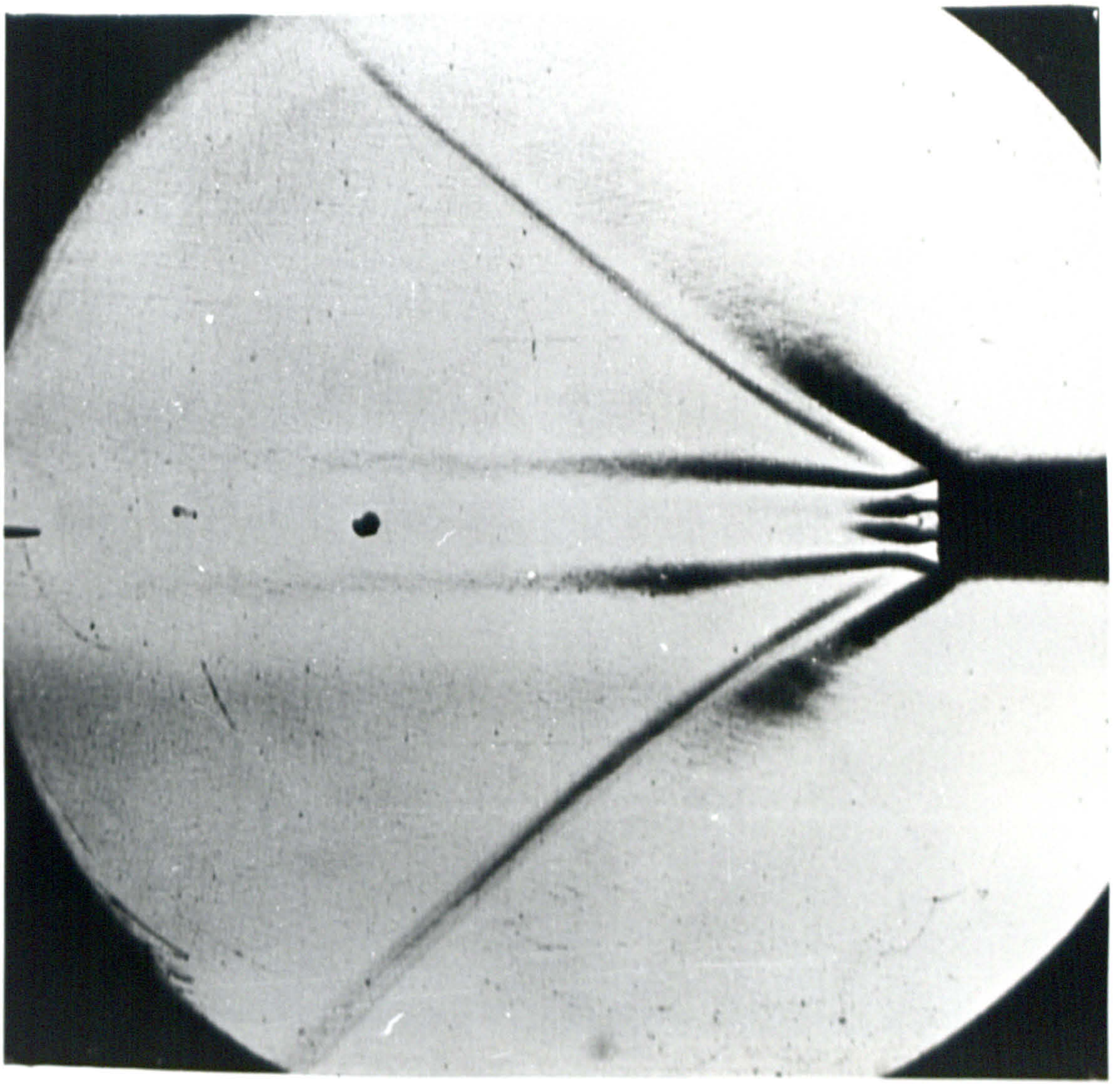

(C) With Base Bleed (C_{qb}=0.10)

PLATE 2 BASE FLOW WITH THE MODEL AT ZERO INCIDENCE ($M_{e\infty}$ = 1.3)

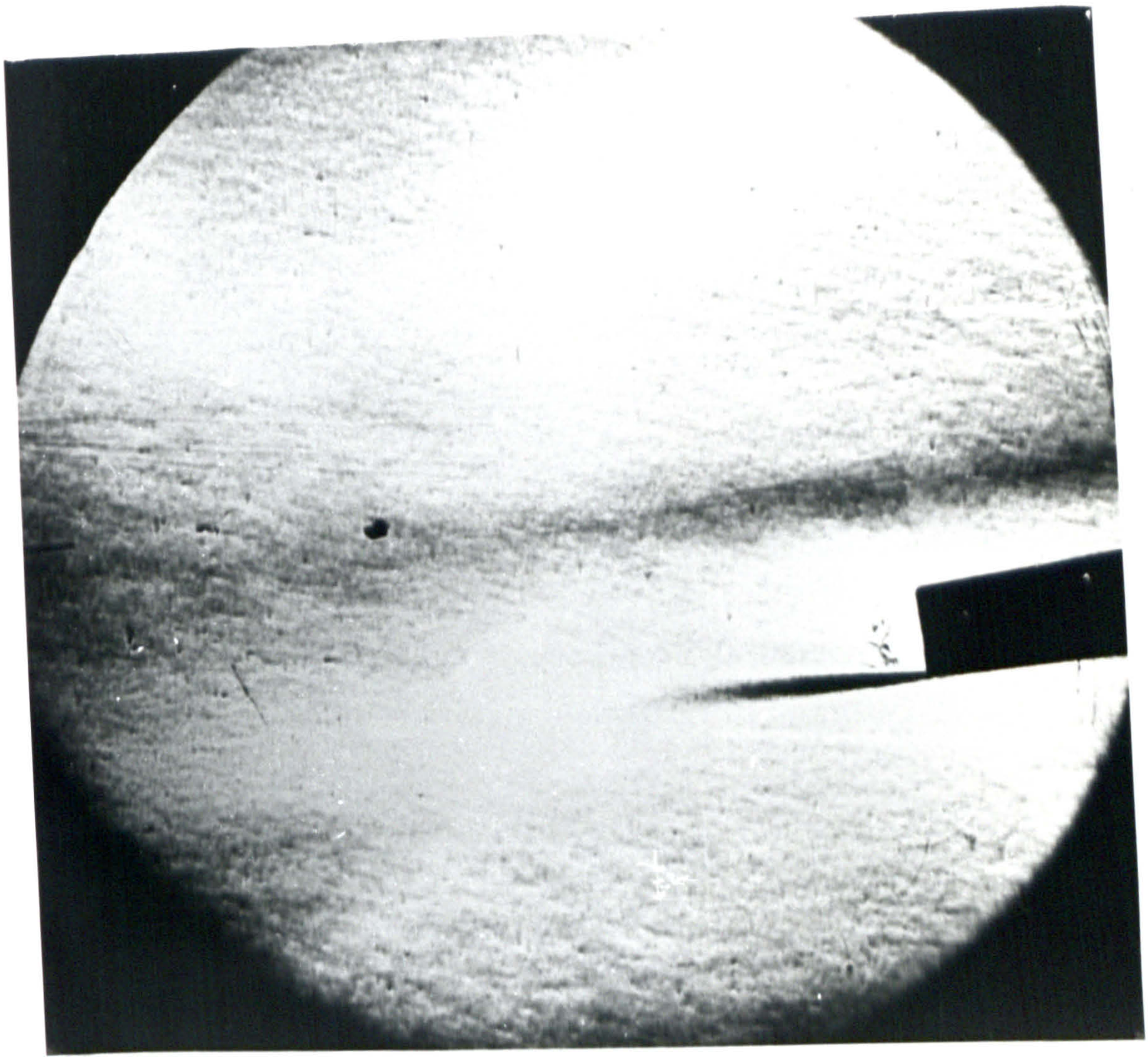

(A) ($M_{e\infty}$ = 0.79). The flow is separating on the upper surface and reattaching downstream of the base. The separation point is out of view.

PLATE 3 BASE FLOW WITH THE MODEL AT 6^{o} INCIDENCE AND WITHOUT BASE BLEED

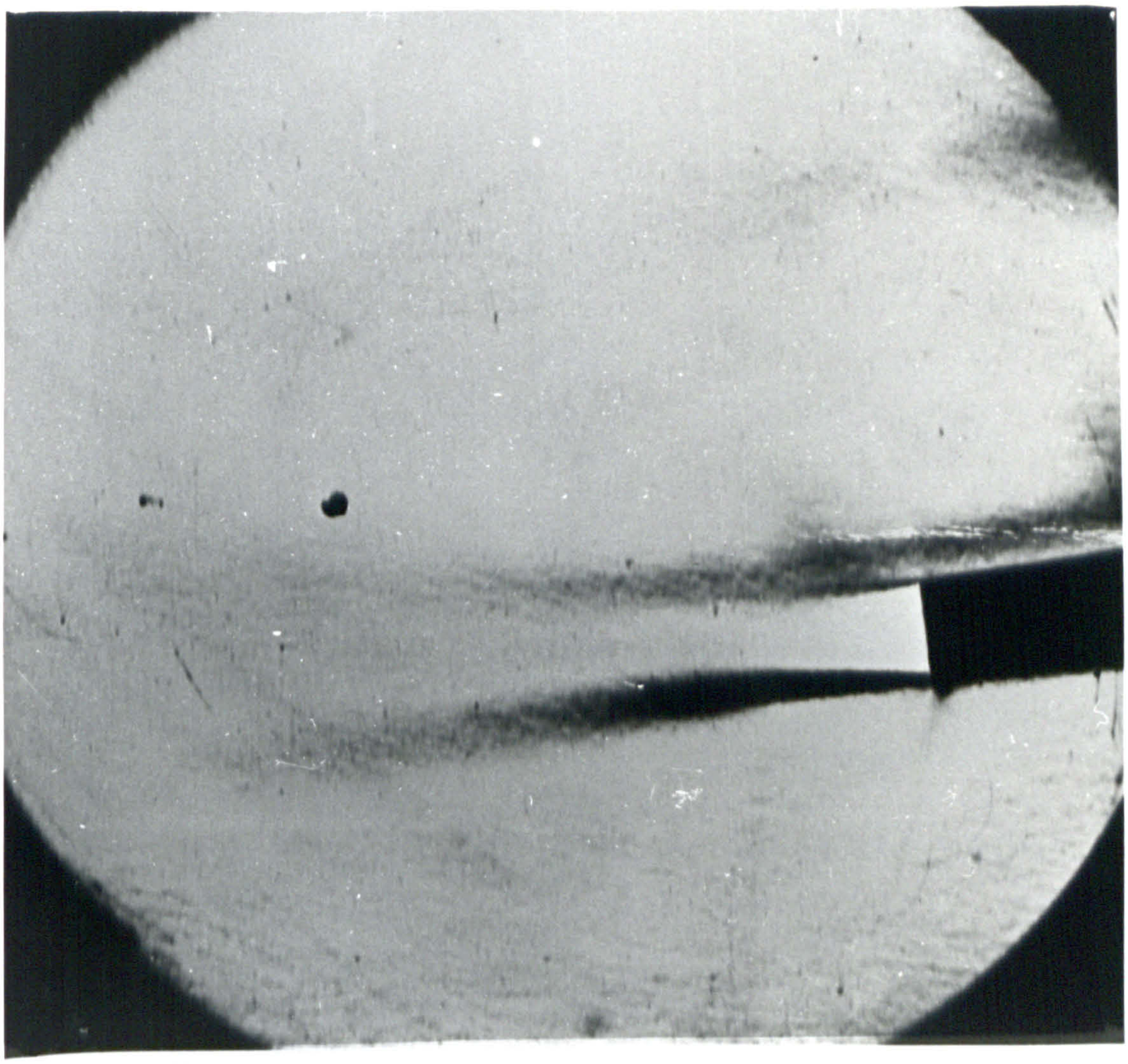

(B) ($M_{e\infty}$ = 0.92). The separation point has moved downstream towards the base.

PLATE 3 BASE FLOW WITH THE MODEL AT 6^{o} INCIDENCE AND WITHOUT BASE BLEED

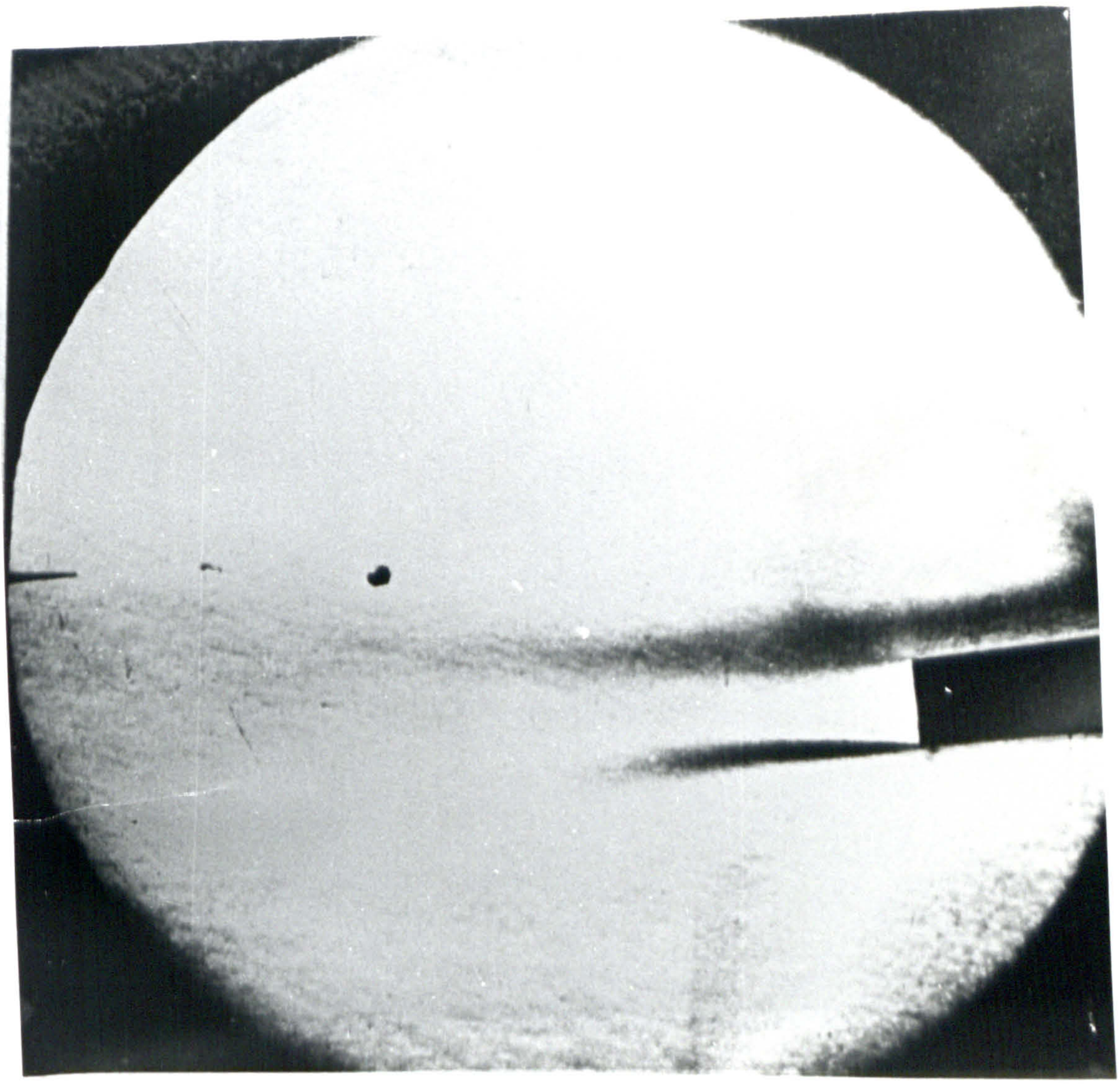

(C) ($M_{e\infty}$ = 0.93)

PLATE 3 BASE FLOW WITH THE MODEL AT 6^{o} INCIDENCE AND WITHOUT BASE BLEED

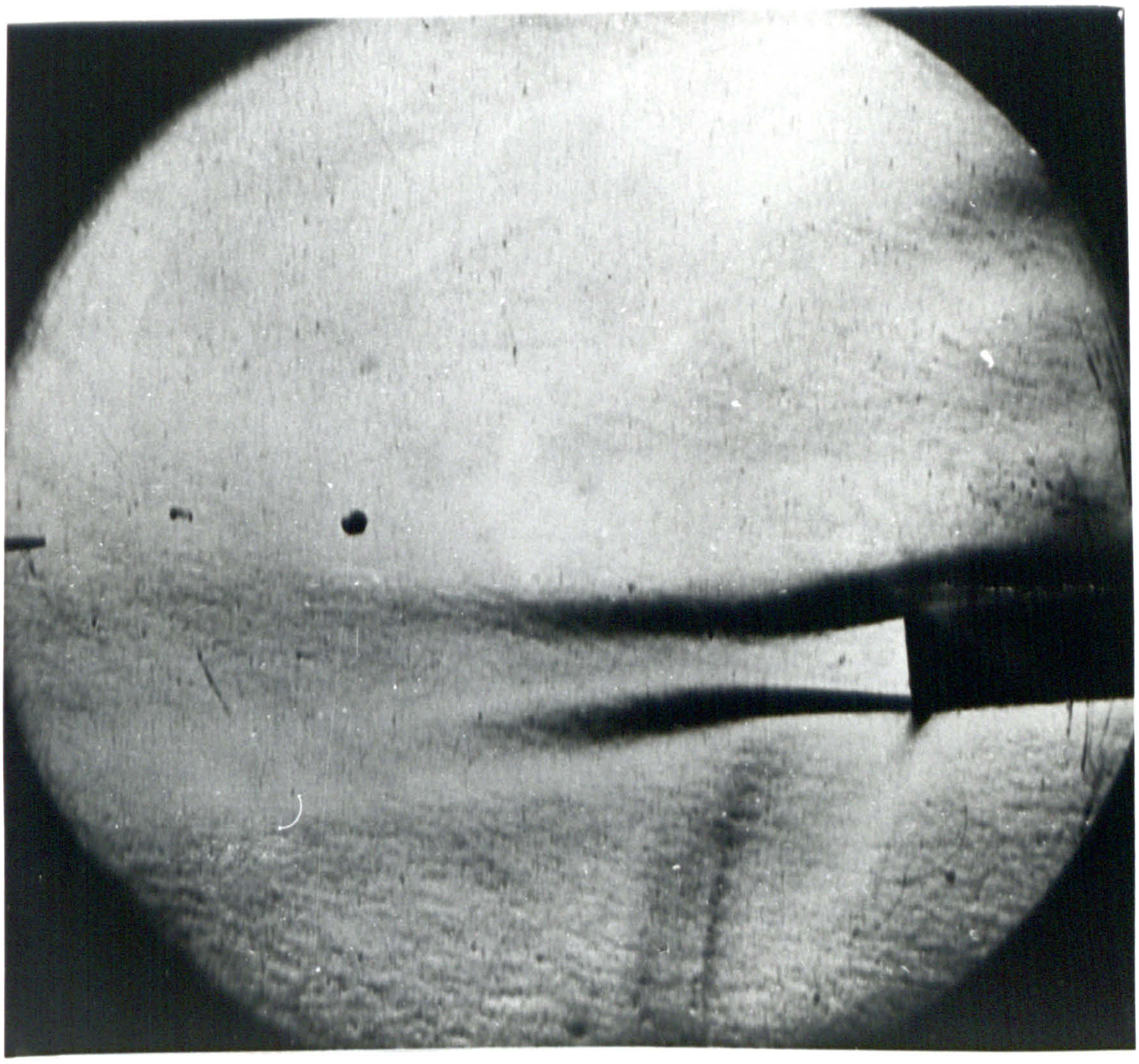

(D) ($M_{e\infty}$ = 0.965). The separation point is just visible on the extreme right-hand side.

PLATE 3 BASE FLOW WITH THE MODEL AT 6^{o} INCIDENCE AND WITHOUT BASE BLEED

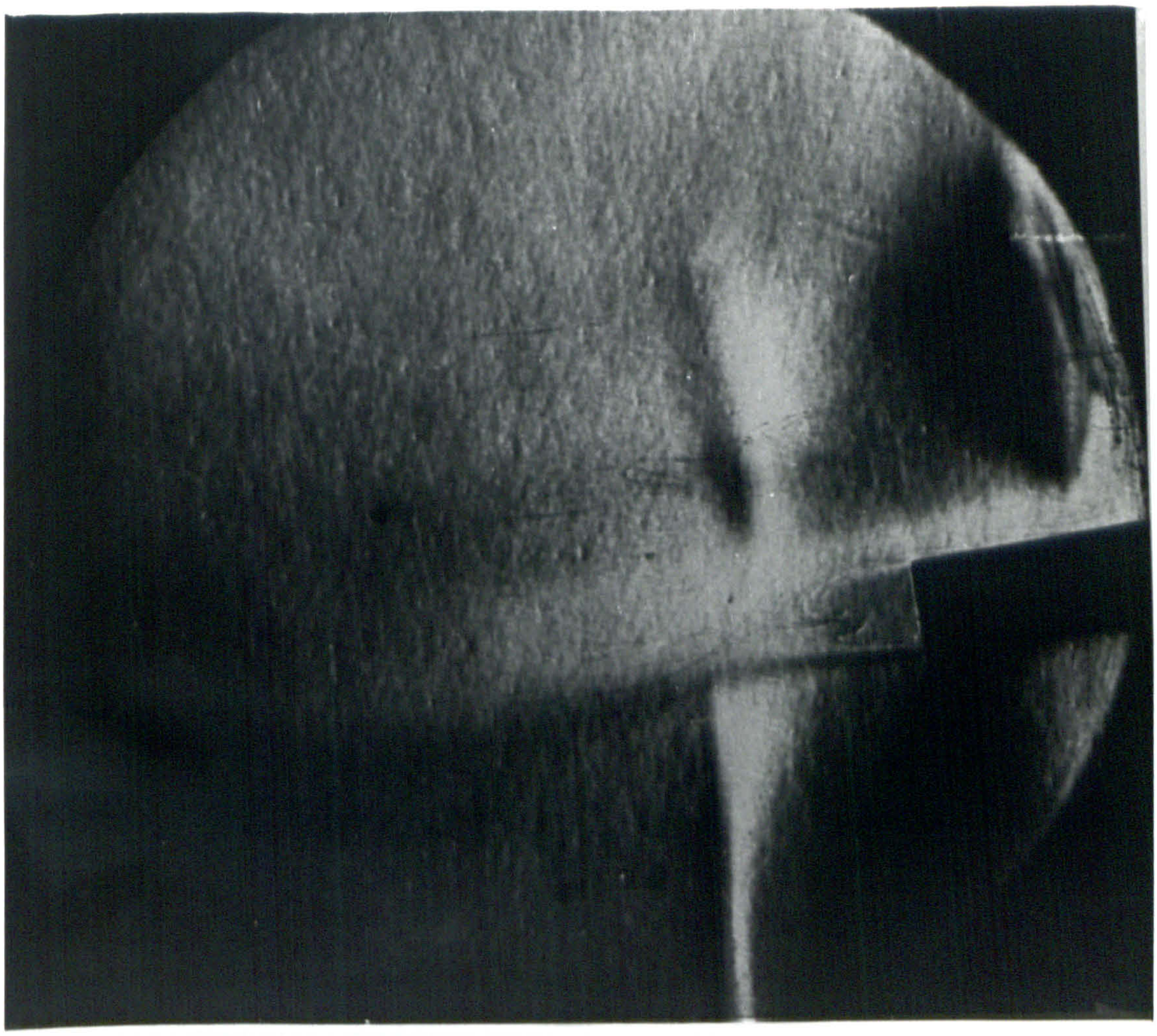

(E) ($M_{e\infty}$ = 0.965). The knife-edge is set in the vertical position and Plate 3D is repeated to show the shock and expansion waves.

On the upper surface, note the lambda shock on the extreme right-hand side. At the free boundary of the separation bubble, the rear branch of the lambda shock reflects as an expansion wave (see Fig. 38C).

PLATE 3 BASE FLOW WITH THE MODEL AT 6^{o} INCIDENCE AND WITHOUT BASE BLEED

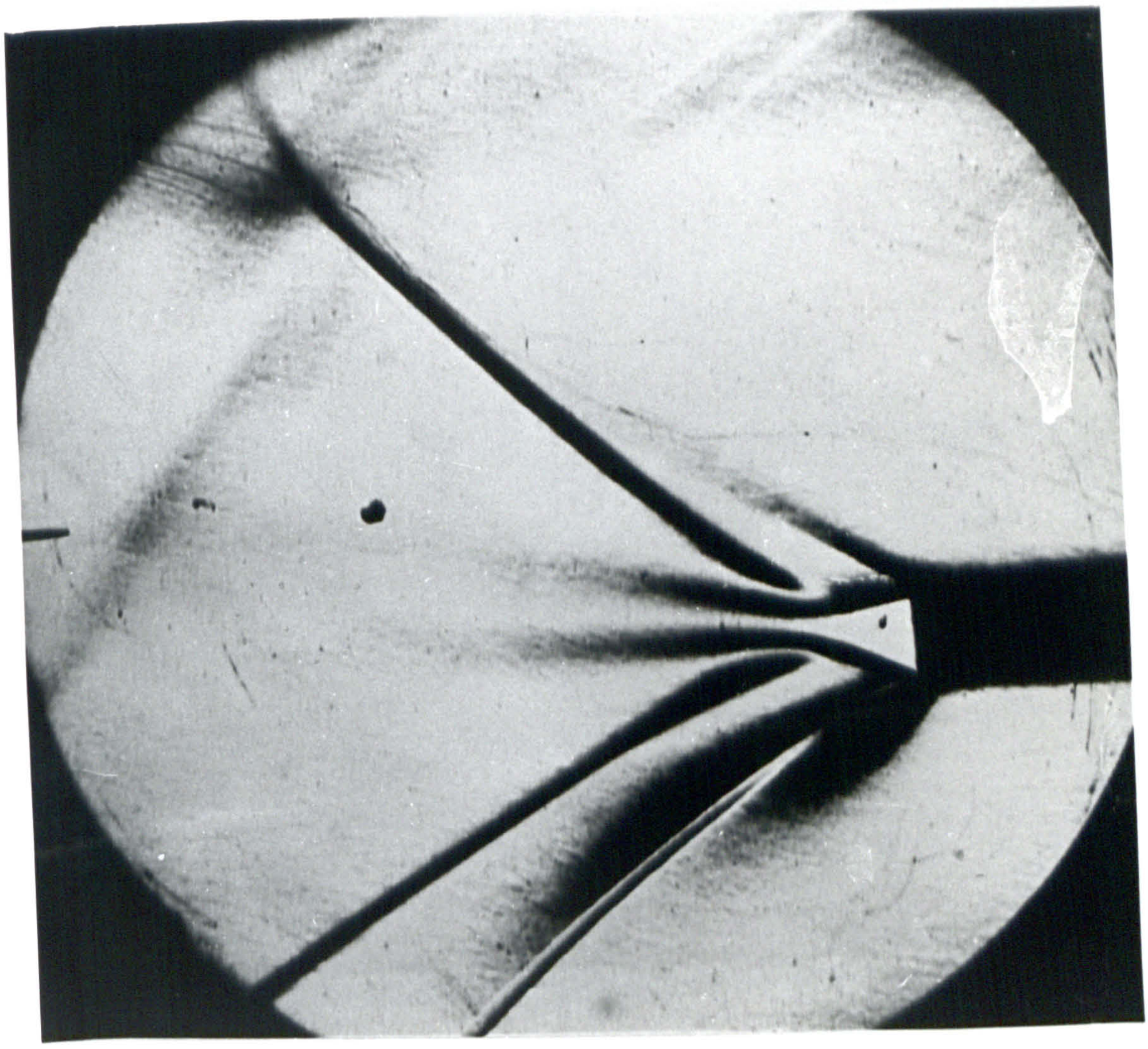

(F) ($M_{e\infty}$ = 1.3). The flow is attached on the upper surface. Note the two shock waves and the two expansion waves that follow the corner separation at the lower surface.

PLATE 3 BASE FLOW WITH THE MODEL AT 6^{o} INCIDENCE AND WITHOUT BASE BLEED

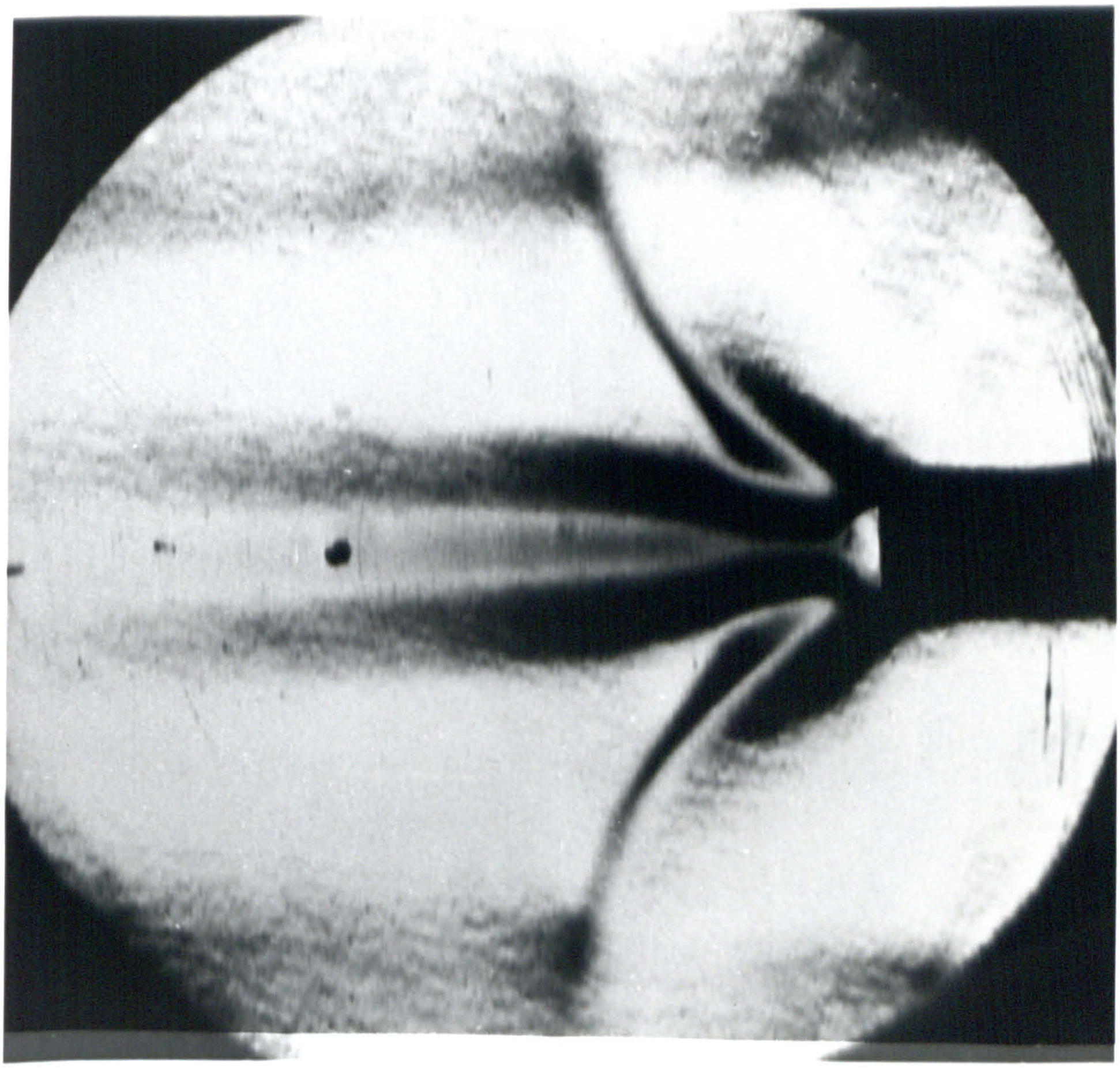

(A) α = 0, M_{e_∞} = 1.0

PLATE 4 THE MIXING OF THE AIR LEAVING THE PLENUM CHAMBER WITH THE MAIN FLOW DOWNSTREAM OF THE MODEL IN THE WAKE

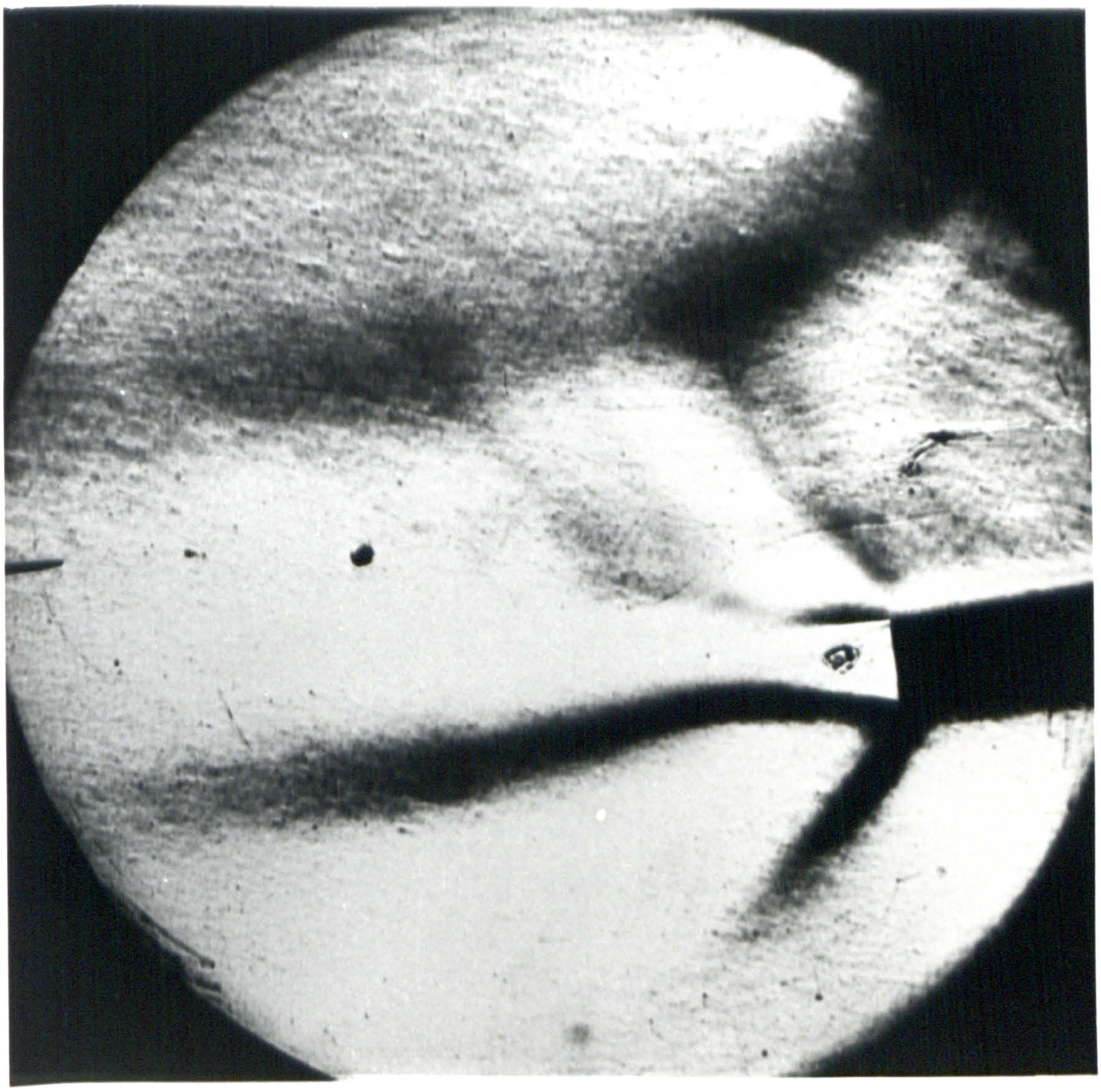

(B) $\alpha = 6^{o}$, $M_{e\infty} = 1.0$

PLATE 4 THE MIXING OF THE AIR LEAVING THE PLENUM CHAMBER WITH THE MAIN FLOW DOWNSTREAM OF THE MODEL IN THE WAKE